



University  
of Glasgow

Ankersen, Jesper (1999) *Quantifying the forces in stabbing incidents*.  
PhD thesis.

<http://theses.gla.ac.uk/2798/>

Copyright and moral rights for this thesis are retained by the author

A copy can be downloaded for personal non-commercial research or  
study, without prior permission or charge

This thesis cannot be reproduced or quoted extensively from without first  
obtaining permission in writing from the Author

The content must not be changed in any way or sold commercially in any  
format or medium without the formal permission of the Author

When referring to this work, full bibliographic details including the  
author, title, awarding institution and date of the thesis must be given

# **Quantifying the Forces in Stabbing Incidents**

by

Jesper Ankersen

Thesis submitted in partial fulfilment for  
the degree of Doctor of Philosophy

Ballistics and Impact Group  
Department of Mechanical Engineering  
University of Glasgow  
Scotland

May 1999

## Abstract

Stab wounds are an increasingly common cause of death or serious injury and the high-risk groups in society are growing both in size and number. These facts make the study of mechanics of knife penetration more relevant than ever.

The aim was to quantify the penetration force needed to inflict a certain stab wound by modelling knife penetration via the Finite Element Method. Case studies of stabbing incidents were carried out to give some insight into the nature and type of problem to be modelled. It was decided to work with an idealised stab-penetration model including a section of target tissue simulants. This stab-penetration test could yield repeatable and comparable results both experimentally and computationally. Suitable target simulants were identified by the stab-penetration test and also by uniaxial tensile tests. Pig skin was found to roughly match the mechanical properties of human skin with gelatine as a realistic flesh simulant.

Computational modelling of knife penetration was attempted by use of Abaqus/Explicit, a nonlinear FEA package which features modelling of contact-impact problems. A true to scale finite element model of the stab-penetration test set-up was built including a material model of the target simulant. The computed penetration force was found highly mesh dependent for sharp blades and too high forces were predicted. Blunt penetrators were also tested both by experiment and computationally. By refining the constitutive model for skin computed values were obtained in reasonable agreement with the experiments for blunt penetrators. Mesh dependency was minimal in the computational model with blunt penetrators. It was concluded that modelling of knife penetration via finite element method is possible but analysis is time consuming due to the high mesh refinement required. Accuracy of the predicted penetration force is still too low for typical blade sharpnesses to be of practical use. Adjustments to the material model and further studies of penetration mechanics are needed to be able to obtain complete experimental and computational agreement.

## Acknowledgements

Thanks are due to the following:

My supervisor Dr Ron Thomson for good guidance, inspiration, and for keeping me on the tracks during the critical stages of this project.

Professor John Hancock for professional advice and for providing funding.

Technician Alan Birkbeck for assisting with the practical side of the experimental work and to the many other departmental staff who helped in one way or another.

Tim Lucas, my “fellow soldier”, for the many discussions and good friendship.

On the financial side, the Danish Government and University of Glasgow for funding me throughout the study.

I dedicate this work to Glenda Favor who provided invaluable personal support, helped me through the difficult periods, and made it all worthwhile.

Finally thanks to my parents for making it all possible.

## List of contents

Abstract .....	2
Acknowledgements .....	3
List of contents.....	4
List of figures .....	7
List of tables.....	13
1 Introduction .....	14
1.1 Background and motivation.....	14
1.2 The nature and assessment of stab wounds.....	15
1.3 The engineering approach to stab wound assessment .....	16
1.4 The structure and properties of skin.....	18
1.4.1 Physical structure .....	18
1.4.2 Mechanical testing.....	19
1.4.3 Characteristics and properties .....	22
1.5 The finite element method.....	26
1.5.1 Finite element modelling of skin.....	26
1.5.2 Penetration mechanics .....	27
1.5.3 Constitutive modelling.....	29
1.6 Case studies of stabbing incidents .....	31
1.7 Proposed scope of work .....	34
1.7.1 Tensile test programme.....	34
1.7.2 Stab-penetration test.....	35
1.7.3 Computer simulation .....	35
2 Mechanical tests of tissue simulants .....	36
2.1 Pilot tensile tests on skin simulants.....	36
2.1.1 Uniaxial tensile test programme .....	37
2.1.2 Results and evaluation .....	39
2.2 Detailed tensile tests on selected skin simulant .....	41
2.2.1 Test programme .....	41

2.2.2	Results and evaluation .....	46
2.3	Additional tests on selected skin simulant.....	60
2.3.1	Notch tests .....	60
2.3.1.1	Test programme .....	60
2.3.1.2	Results and evaluation .....	61
2.3.2	The effect of cyclic loading.....	62
2.3.2.1	Test programme .....	63
2.3.2.2	Results and evaluation .....	63
2.3.3	Through-thickness compression test .....	65
2.3.3.1	Test programme .....	65
2.3.3.2	Results and evaluation .....	66
3	Stab-penetration test using sharp blades.....	67
3.1	Experimental programme.....	67
3.1.1	Results and evaluation .....	73
3.2	Computational simulation .....	75
3.2.1	Material modelling.....	76
3.2.2	Mesh design and analysis .....	82
3.2.3	Results and evaluation .....	85
4	Stab-penetration test using blunt penetrators.....	92
4.1	Experimental programme.....	92
4.1.1	Results and evaluation .....	94
4.2	Computational simulation .....	101
4.2.1	Material modelling.....	101
4.2.2	Mesh design and analysis .....	102
4.2.3	Results and evaluation .....	103
5	Stab-penetration test with revised material models .....	105
5.1	Revised material models .....	105
5.1.1	Material model with gradual failure.....	107
5.1.2	Material model with abrupt failure .....	113

5.2	Test and verification .....	114
5.2.1	Single element .....	114
5.2.2	Multi element model .....	117
5.3	Application to axisymmetric stab-penetration model .....	120
5.3.1	Mesh design and analysis .....	120
5.3.2	Results and evaluation for gradual failure .....	121
5.3.3	Results and evaluation for abrupt failure .....	124
6	Discussion and conclusions .....	126
6.1	Characteristics of tissue simulants .....	126
6.2	Experimental stab-penetration tests .....	127
6.3	Computational modelling .....	128
7	Recommendations and future work .....	131
7.1	Experimental work .....	131
7.2	Continuum modelling .....	131
7.3	Alternative approaches .....	132
	List of references .....	134
	Appendices .....	140

## List of figures

- 1.1. The wound length ( $L$ ) is typically less than the width ( $W$ ) of the knife blade.
- 1.2. Principal layers of the human skin.
- 1.3. Experimental set-up used by Peura (1993) for biaxial loading of skin specimens.
- 1.4. Skin model framework proposed by Daly (1966).
- 1.5. Stress-strain response of human abdominal skin under uniaxial tensile load recorded by: 1) Kenedi et al (1964), 2) Jansen and Rottier (1958), 3) Ridge and Wright (1966).
- 1.6. Penetration modes for projectiles for different materials.
- 1.7. Distribution of stab wounds in anatomical regions of the human body.
- 2.1. Rectangular tensile test specimen used in pilot tests. Dimensions in mm. Drawing not to scale.
- 2.2. Self tightening grips used in pilot tensile test.
- 2.3. Stress-strain curves for synthetic chamois from pilot tensile test.
- 2.4. Stress-strain curve for pig skin from pilot tensile test.
- 2.5. Dumbbell shaped tensile specimen used for detailed tests on pig skin. Dimensions in mm. Drawing not to scale.
- 2.6. Grip for dumbbell shaped pig skin tensile specimen.

- 2.7. Test set-up for dumbbell shaped pig skin specimen.
- 2.8. Plan view of pig skin showing regions used for experiments.
- 2.9. Average stress-strain failure values for pig skin obtained from dumbbell shaped specimens. L) Longitudinal direction. T) Transverse direction.
- 2.10. Tensile test on dumbbell shaped pig skin specimen - frozen back - longitudinal direction.
- 2.11. Tensile test on dumbbell shaped pig skin specimen - frozen back - transverse direction.
- 2.12. Tensile test on dumbbell shaped pig skin specimen - frozen back - transverse direction.
- 2.13. Tensile test on dumbbell shaped pig skin specimen - fresh belly - longitudinal direction.
- 2.14. Tensile test on dumbbell shaped pig skin specimen - fresh belly - transverse direction.
- 2.15. Tensile test on dumbbell shaped pig skin specimen - fresh back - longitudinal direction.
- 2.16. Tensile test on dumbbell shaped pig skin specimen - fresh back - longitudinal direction.
- 2.17. Tensile test on dumbbell shaped pig skin specimen - fresh back - transverse direction.

- 2.18. Tensile test on dumbbell shaped pig skin specimen - fresh back - transverse direction.
- 2.19. Dumbbell shaped specimen used for notch test.
- 2.20. Notch test on dumbbell shaped pig skin specimen with various notch lengths.  
Notch length / specimen width ratio:  $a/w$ .
- 2.21. Load-extension response of pig skin under cyclic loading (single cycle).
- 2.22. Load-extension response of pig skin under cyclic loading (5 cycles).
- 2.23. Load-displacement curves obtained for pig skin under compressive load.
- 3.1. Test set-up for pilot stab-penetration test.
- 3.2. Maximum entry forces on standard knife blades for various target simulants.
- 3.3. Maximum withdrawal forces on standard knife blades for various target simulants.
- 3.4. Entry and withdrawal force on blade 3B at 2 mm/s. Three repetitions on Roma Plastilina.
- 3.5. Entry and withdrawal force on blade 3B at 4 mm/s. Three repetitions on Roma Plastilina.
- 3.6. Entry and withdrawal force on blade 3B at 8 mm/s. Three repetitions on Roma Plastilina.
- 3.7. Pilot stab-penetration test on pig skin and chamois using knife blade 3B.

- 3.8. Bi-linear idealisation of pig skin for computational material model based on pilot tensile tests.
- 3.9. Boundary conditions on FE quarter model.
- 3.10. Computational stab-penetration test using 60 membrane elements and knife blade 3B (pointed tip and sharp edges). Bias values 1.00 to 0.75.
- 3.11. Computational stab-penetration test using 60 membrane elements and knife blade 3B (pointed tip and sharp edges). Bias values 0.70 to 0.45.
- 3.12. Computational stab-penetration test using 5 x 60 solid elements and knife blade 3B (pointed tip and sharp edges). Bias values 1.00 to 0.75.
- 3.13. Computational stab-penetration test using 5 x 60 solid elements and knife blade 3B (pointed tip and sharp edges). Bias values 0.70 to 0.50.
- 3.14. Maximum penetration force for membrane elements and solid elements with different mesh bias.
- 4.1. Skin specimen fixture for stab-penetration test using rounded penetrators.  
Plates: 110 x 110 x 12 mm with  $\varnothing$ 70 mm hole.
- 4.2. Hemispherical penetrators and adaptor used in stab-penetration test on pig skin.
- 4.3. Maximum experimental penetration force versus penetrator diameter. Straight best fit line based on average values for each penetrator.
- 4.4. Experimental stab-penetration test on pig skin - Penetrator A (D=3.2mm).
- 4.5. Experimental stab-penetration test on pig skin - Penetrator B (D=4.8mm).

- 4.6. Experimental stab-penetration test on pig skin - Penetrator C (D=6.4mm).
- 4.7. Experimental stab-penetration test on pig skin - Penetrator D (D=7.9mm).
- 4.8. Radial plane defining the axisymmetric computational stab-penetration model.
- 4.9. Computational stab-penetration test using axisymmetric model.  
Penetrator: A (D=3.2mm), B (D=4.8mm).
- 5.1. Constant strain rate loading to complete failure at different strain rates for gradual failure model.
- 5.2. Single membrane element stretched to yield, compressed, and re-loaded to failure with gradual failure model.
- 5.3. Single membrane element stretched to failure with abrupt failure model.
- 5.4. Stress-time curves of biaxially loaded single membrane element showing synchronised failure.
- 5.5. Quarter mesh of dumbbell shaped tensile specimen.
- 5.6. Force-displacement curve for computational tensile test with dumbbell shaped specimen and gradual failure material model.
- 5.7. Force-displacement curve for computational tensile test with dumbbell shaped specimen and abrupt failure material model.
- 5.8. Computational stab-penetration test using axisymmetric FE model with orthotropic material model with gradual failure.

- 5.9. Computational stab-penetration test using axisymmetric FE model with orthotropic material model with abrupt failure.
- 5.10. Maximum penetration force from axisymmetric models plotted against straight line fit from experimental values.

## List of tables

- 1.1. Mean mechanical values characterising human abdominal skin. From Jansen and Rottier (1958).
- 2.1. Pig skin specimens tested on the Lloyd LR30 Universal Testing Machine.
- 2.2. Average values of Poisson's ratio at the intermediate point and at failure for each specimen category.
- 2.3. Nominal failure stress for notched specimens.
- 3.1. Target simulants subjected to stab-penetration test.
- 3.2. Key values used in the computational material model.
- 4.1. Maximum experimental penetration force and penetrator displacement at failure for penetrator A, B, C, D.

# 1 Introduction

## 1.1 Background and motivation

In the UK the ownership of firearms is tightly controlled and even today their criminal use is unusual. Stabbings account for more than 50% of the recent homicides in the Strathclyde Region of Scotland and by 1993 the frequency of knife attacks was sufficient to merit a focused campaign by the police (Operation BLADE) to reduce the incidence of knife-carrying in the streets. This continues and has met with some success but knife attacks remain a problem, with a police officer stabbed to death in July 1994 in Glasgow and, more recently, in October 1997 in London. The murders of a medical practitioner in his surgery and a physiotherapist in her clinic, and the horrific attack on a Surrey woman travelling alone by train on the evening of 3 March 1997, highlight the vulnerability of particular occupational and social groups.

The lack of quantitative knowledge of the force needed for a sharp instrument to penetrate human tissue (and clothing) makes it impossible to model stabbings mathematically with any degree of confidence. This presents a problem in forensic pathology, since it is impossible to infer, after the event, whether a specific wound was necessarily the result of a deliberate blow. The common defence “he fell upon the knife” then becomes difficult to challenge in cases where evidence suggests otherwise. The requirement is for a quantitative method of assessing the force used in any stabbing incident. This will reduce the margin of doubt, both in single stabbing “alleged accidental” cases and in multiple stabbings where the effort required, and hence the speed of repetition of the blow, is often a critical factor. A quantitative force assessment method should therefore lead to speedier resolution of cases and, by reducing the subjectivity of expert opinion, improve the soundness of the verdict. In addition, sounder knowledge of the forces involved in the production of stab wounds, in relation to location on the body and likely damage to underlying structures, would enable clinicians to make a more rapid and appropriate assessment of the severity of injury. This is important since unnecessary deaths still occur from time to time in cases where the stab wound track length and the severity of trauma to the underlying structures had not been fully appreciated.

Most experimental attempts to measure knife penetration forces have been initiated by forensic pathologists. However recent developments in computational mechanics have enabled simulation of contact, impact and penetration in a number of engineering contexts. The aim of the present work is (hopefully) to adopt a symbiotic approach which combines the pathological and engineering approaches to develop a useful analytical tool. This requires an assessment of those significant factors that determine penetration forces and development of a computational model for prediction of these forces. Such factors include the type of weapon, the physical characteristics of the wound, the weight of the assailant and of the victim, etc. The desired outcome is a computational model which can help solve for one unknown factor, in any particular stabbing incident, if others are given.

## **1.2 The nature and assessment of stab wounds**

Stab wounds are frequently encountered in forensic medicine and a large amount of experience in assessing stab wounds has been built over time. Stab wounds are very different from incised or slashed wounds and are therefore classified separately in the forensic literature. Stab wounds usually involve a pointed object (knives, ice picks, sharpened screwdrivers) which penetrate deep into the victim causing internal damage to vital organs. The entry force, and hence the wound, is confined to a very small area on the victim's body. Slashed wounds are inflicted with the sharp edge of a knife rather than by the tip. The wounds tend to be larger and not as deep as stabbed wounds and are therefore less likely to be fatal. Blood loss is more likely to be the cause in fatal cases involving slashings.

Assessment of the force used to create a stab wound is subjective and extremely difficult. The physically observable and measurable characteristics of wounds are fairly limited and include the depth and width of the wound and the type of tissue cut. When it comes to matching a possible weapon to the wounds these measurable characteristics are important but a number of additional factors should be taken into account. For example, a typical single stab wound will have a length which is slightly less than the width of the blade used (Figure 1.1). This occurs due to stretching of the skin. However, repetitive stabbing without complete withdrawal may increase the length of the entry wound. Similarly, if muscle fibres are cut, the wound will gape but if the wound

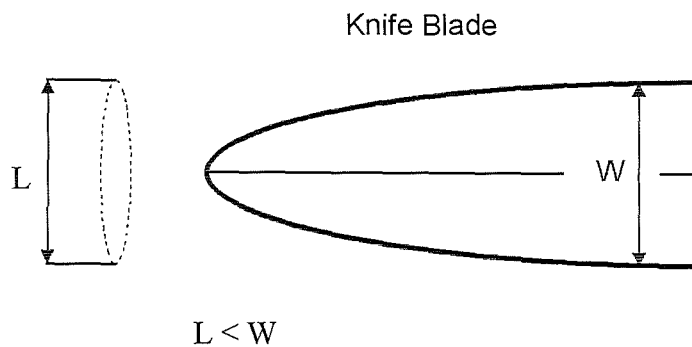


Figure 1.1. The wound length (L) is typically less than the width (W) of the knife blade.

follows the direction of the fibres it may close. Such factors add to the uncertainty of establishing how the incident might have taken place but assessment of the force exerted still remains the most difficult and uncertain task.

In addition to the wound characteristics, force assessment must take account of the sharpness of the weapon and the thickness and nature of any clothing (Camps & Cameron (1971)). Assessment of the force exerted by an assailant is further hampered by the presence of additional forces such as counter-pressure by the victim. Indeed, Simpson (1979) states that “accident may do anything” and that wounds with unnatural features might have been caused accidentally. This alone means that any contention that a wound was a result of a deliberate blow must be to some extent subjective and probabilistic. However, it is believed by the present author that more detailed knowledge of the force required to inflict a certain wound will be of value in most cases.

### 1.3 The engineering approach to stab wound assessment

“Wound Ballistics” is a well established science which combines biomedical science with engineering dynamics (Jason and Fackler (1990)). Naturally, this subject has been thoroughly researched by the military and a large corpus of experiential, experimental and analytical knowledge exists here. However, as the title implies, wound ballistics restricts its attention to the penetration of tissue by high-speed ballistic projectiles such as bullets or small, fast-moving fragments. In such cases, tissue damage caused is determined and indeed dominated, by the hydrodynamic and inertial forces which develop as the deformable projectile passes through soft tissue.

In stark contrast, stab wound damage appears to be dominated by the behaviour of skin and bone and the penetration mechanics has only been explored to a limited extent in work usually initiated by forensic pathologists. It does not appear to have been approached from a rigorous, “engineering” viewpoint. This would aim to develop a quantitative model of the system and to improve our understanding of the dynamics of knife penetration. Specifically, such an approach would seek to isolate the relevant mechanical properties of skin and would subsequently include these in a mathematical or computational simulation of the penetration of the knife. Penetration forces were recorded on cadavers immediately before routine medicolegal autopsy in the classic study by Knight (1975), who used a knife attached to a special dynamometer. Quasi-static load on the knife was increased until penetration occurred and it was noted that once the skin was penetrated, no additional force was required to obtain full penetration provided bone was not hit. Similar experiments were conducted by Green (1978) who, instead of using a spring loaded knife, placed the cadavers on a force platform measuring deflection of the platform during knife penetration. Both Knight and Green found the blade-tip sharpness to be predominant in determining the penetration force, although other factors have an effect. Pretensioning of the skin, for example, reduces the penetration force, with tight intercostal (ie between the ribs) spaces more easily penetrated than slack abdominal skin.

The effect of momentum was also investigated and Knight found blade velocity important as much lower penetration forces were obtained with a fast moving blade. Green, however, concluded that momentum had only little effect on the recorded force. This disagreement is thought, by the present author, to be due to the different measuring methods used, as in Greens case the response of the cadaver and force table was too slow to pick up any force transients caused by a fast travelling knife blade. Indeed, both the capability of Green’s apparatus and of Knight’s spring loaded knife to simulate the mechanics of “real” stabbing incidents is questionable. There is an ongoing discussion concerning which measures are the most significant when determining penetration ability of projectiles (Hetherington (1995)). The measures in question are momentum and kinetic energy which are both dependent on the mass and velocity of the impacting object but are also mutually dependent. When considering momentum and kinetic energy it must be assumed that the impacting object behaves as a projectile, that is, no external

forces must act during impact. This is seldom the case in stabbing incidents where the weapon is held by the assailant and relatively high follow through forces are encountered. The lower penetration forces recorded at higher velocities by Knight and Green could therefore simply be due to rate dependence of the human skin. Green also tested clothed bodies and found that the penetration force rose up to tenfold that found for exposed skin. Unfortunately neither the type of clothing nor the number of layers was stated.

#### **1.4 The structure and properties of skin**

Skin is a highly complex biomaterial which has been widely studied. The present study is not intended as a detailed study of skin, thus only a brief description is given of the structure and mechanical properties. Skin is the largest single body organ in humans and most animals, with a typical area of 1.7 m<sup>2</sup> and weight of 3 kg in humans. Hairy skin covers most of the body whereas smooth skin, which has thicker epidermis, more nerves, and no oil glands, covers palms and soles. Apart from serving as a containment for the underlying anatomic structures it has a number of important functions, for example, in the control of body temperature through evaporation and in protecting the body against bacterial, chemical, and physical attack. Stabbing incidents naturally fall under physical attack and the mechanical characteristics of skin become relevant in this context.

##### **1.4.1 Physical structure**

Skin can be divided into two main functional layers, the dermis and the epidermis (Figure 1.2). The epidermis is a thin protective layer providing almost no structural strength but which has a stiffening effect on the complete skin if dried out. The epidermis is formed by cells growing from the dermis and, as new layers of cells appear, the older cell layers are pushed outwards where they gradually die and eventually are shed. This outermost layer of cells is known as the stratum corneum. The dermis is the main structural loadbearing layer and consists of a dense randomly interwoven mesh of collagen fibres, a similar mesh of very fine elastin fibres, and a viscoelastic gel (ground substance) which permeates the collagen and elastin networks. Collagen fibres are stiff and strong acting as reinforcement in skin. Collagen molecules are structural proteins which form a triple helix with a length of 280 nm. The molecules form fibrils (with a typical diameter of

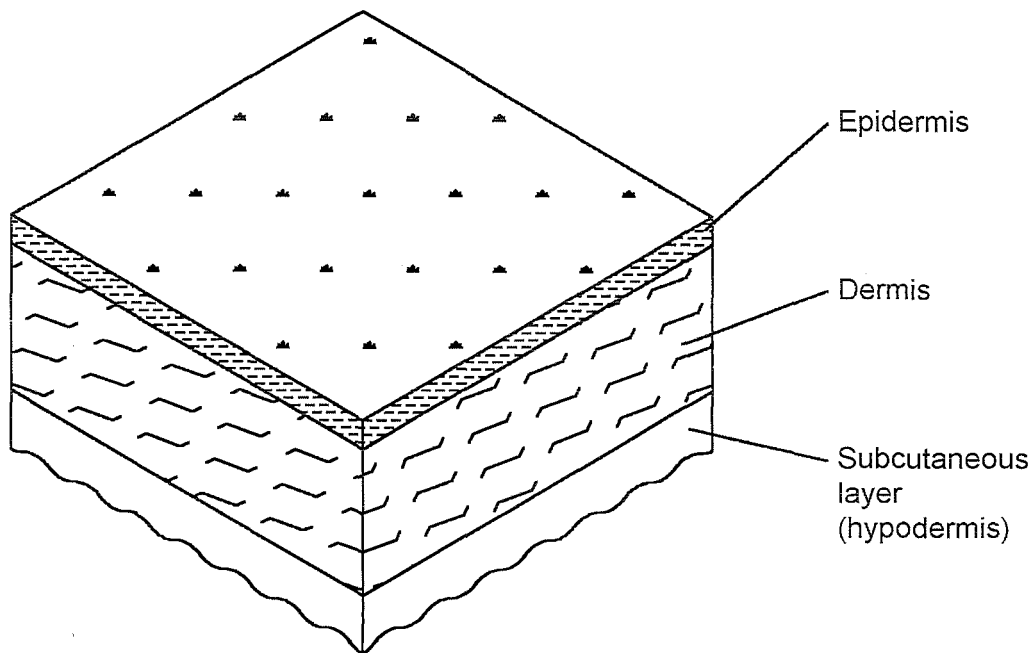


Figure 1.2. Principal layers of the human skin.

100 nm) which collect side by side forming fibres. Fibres are bundled in collagen networks ranging in width from 1 to 40  $\mu\text{m}$  (Wilkes et al (1973)). Elastin fibres are capable of large deformation without loss of elasticity. Apart from water, collagen is the main constituent and makes up approximately 72% of the dry weight of skin. A typical composition of fresh skin by weight is according to Daly (1966):

Water	62 - 70%
Collagen	29 - 37%
Elastin	0.7 - 1.4%
Reticulin	0 - 12%

#### 1.4.2 Mechanical testing

Human skin has been mechanically tested using different methods which can be grouped as *in vitro* and *in vivo* tests.

*In vivo* tests are performed on the skin in its original place and usually involve live individuals. This limits the test to relatively small strain levels. The influence of underlying and surrounding tissue cannot be avoided and it is then difficult to isolate any

single mechanical property and measure a precise value. However, suction cup tests have been found useful in comparative tests in clinical medicine where changes in skin properties can be used as diagnosis for various skin related diseases. Torsion tests have been used to derive mechanical properties at low strains (Barbenel (1973)).

*In vitro* testing implies specimens being excised from a donor typically during post-mortem examination. This type of test is used for studying tensile behaviour of the skin under different loading conditions and, since the skin is detached from underlying tissue, the stress-strain behaviour can be obtained directly. With some reservations such as extension rate, normalised results are broadly comparable. Destructive testing is also possible, and is indeed necessary for obtaining failure stresses and strains. Uniaxial and biaxial tensile tests are commonly used for *in vitro* testing.

Uniaxial tensile testing is the simplest material test and is routine for conventional engineering materials. A number of investigators have used the uniaxial tensile test for testing human skin specimens (Daly (1966), Jansen and Rottier (1958a, b), Kenedi et al (1964), Ridge and Wright (1966a)). In most cases the specimens are either waisted or dumbbell shaped to avoid premature failure due to the stress concentration at the grips. Sizes vary from 4 x 10 mm to 10 x 38 mm measured at the waisted gauge section. Rectangular specimens (90 x 5 mm) were used by Jansen and Rottier who apparently did not encounter any end effects from the grips. The preparation of specimens is generally done by first excising a piece of skin from the donor. As specimens are removed they tend to shrink due to relaxation of the natural *in-situ* tension which amounts to 10 - 30 % change in length. Subcutaneous tissue is removed but a method for this is only described by Ridge and Wright; After freezing the specimen with the epidermis downward on a block the specimen was shaved to a thickness of 0.1 inch. All dumbbell shaped specimens were stamped out with a die similar to a cookie cutter. The rectangular shape used by Jansen and Rottier was probably cut by scalpel along a ruler but this is not made clear in their communication. Tests were usually performed at constant extension rate ranging from 0.05 mm/min to 78 mm/min except Kenedi et al who used a stepwise incremental loading profile. A period of 5 minutes was allowed for stabilisation between each load increment. From such uniaxial tensile tests, the failure stress and strain have been determined and a mathematical expression for the stress-strain relationship developed by curve fitting.

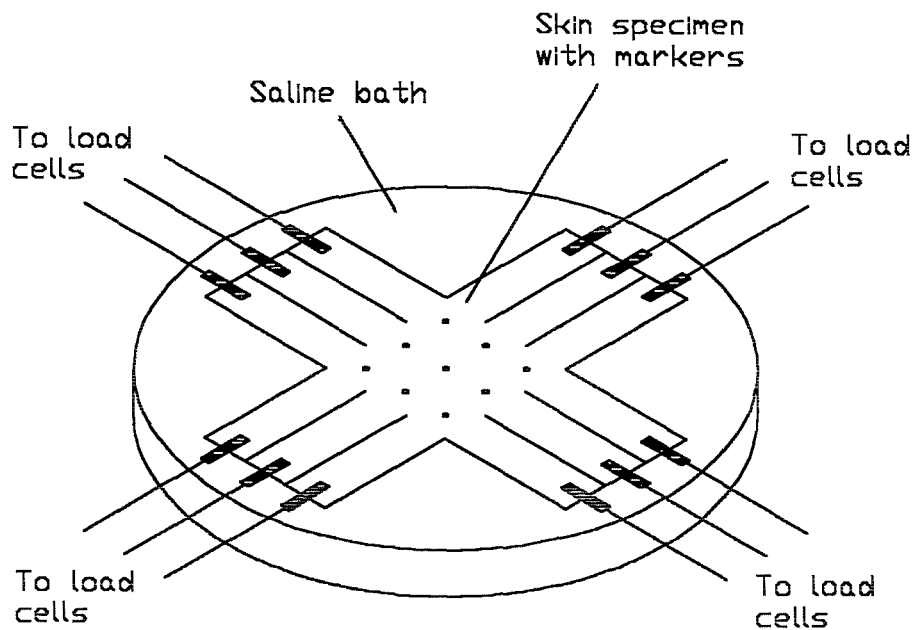


Figure 1.3. Experimental set-up used by Peura (1993) for biaxial loading of skin specimens.

Biaxial tests have been performed by Lanir and Fung (1974a, b) on rabbit skin, Schneider (1982) and Peura (1993) on human skin, all using an almost identical test set-up. Square specimens were tested in a temperature controlled saline bath. Peura also cut tabs in the specimen to allow shearing strains to be applied via surgical sutures attached to load cells (see Figure 1.3). The test protocols involved keeping the strain constant in one direction while extending the specimen in the other direction at a constant strain rate. In Peura's case, strains in the square specimen were recorded via one video camera and a video screen grabber while Lanir and Fung as well as Schneider used two video cameras and a video dimensional analyser (VDA). Results from these rather complicated experiments were used for a more accurate determination of stress-strain relationship for soft tissues but since the aim of these investigations was to clarify the stress-strain behaviour in near natural condition, far below the failure level, the equipment was not designed for large extensions and the results are valid only at relatively small strains.

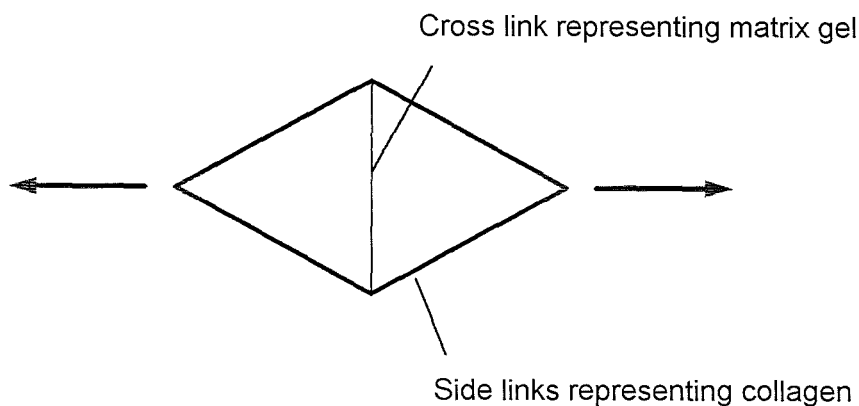


Figure 1.4. Skin model framework proposed by Daly (1966).

### 1.4.3 Characteristics and properties

Skin is sometimes described in the literature as a rubber-like material but this is not an accurate engineering description since rubber has a sigmoid shaped stress-strain curve (Atkins and Mai (1988), Marks (1983)). In contrast, while skin is indeed non-linear, it shows a two-phase response. Initially it is very compliant, large strains being obtained for low loads but it then shows a marked increase in stiffness, developing high loads for small additional strain increments. This characteristic J-shaped stress-strain curve for soft tissue is responsible for the remarkably high resistance to tearing. Fibres re-align perpendicularly at the crack tip in a viscoelastic manner. There is very little communication of strain energy between stressed parts and it is difficult to feed energy into potential crack sites (Vincent (1982)). It has been argued that the moderate work of fracture for skin is not directly related to the high tearing resistance (Atkins and Mai (1988)). The non-linear behaviour can be explained by the skin structure. The initial compliant response occurs while the randomly orientated collagen fibres are being realigned in the load direction and is dominated by elastin fibres. Once the collagen fibres are fully aligned, the stress-strain response for the whole skin matches that of the stiff collagen fibres alone. To describe this, Daly proposed a skin model based on a diamond shaped framework with stiff side links representing collagen fibres and a weaker cross link representing matrix gel (Figure 1.4). In both uniaxial and biaxial loading this model gives a realistic stress-strain response. The diamond shape also results in anisotropic behaviour where a square arrangement of the side links would give an in-plane isotropic behaviour.

Simple analytical expressions have been proposed by most investigators. Ridge and Wright described the two phases by the following equations where extension is a function of load:

$$\text{1st phase: } E = x + y \log L \quad (1) \qquad \text{2nd phase: } E = c + kL^b \quad (2)$$

where  $E$  = extension,  $L$  = load, and  $b, c, k, x, y$  = constants. These constants were evaluated by curve fitting using the experimentally obtained load-extension curves. In a similar manner Kenedi et al proposed an exponential expression covering both phases where stress is a function of strain:

$$\sigma = A\varepsilon^n \quad (3)$$

where  $\sigma$  = nominal stress,  $\varepsilon$  = strain, and  $A, n$  = constants. Other authors have also used a power law expression to describe overall stress-strain response of skin but stress was in all cases based on initial cross-section and so measured as nominal rather than true stress (Daly (1966), Fung (1993), Jansen and Rottier (1958a, b), Schneider (1982)). Failure modes are not treated in detail but are typically described as abrupt. Also a gradual failure mode, in which the collagen fibres are thought to fail one by one and then be pulled out of the matrix gel, was observed by Daly (1966). Fibre slippage is described by Wilkes et al (1973) as an explanation to the sometimes large strains associated with yield and failure of skin. Typical stress-strain curves obtained by uniaxial tensile tests are shown in Figure 1.5. Rather different curves were obtained by the authors (Jansen and Rottier (1958a), Kenedi et al (1964), Ridge and Wright (1966a)). It should be taken into account that the results presented by Ridge and Wright are from a two-day old human child whereas the other two curves represent skin taken from adults of the same age group. This highlights the fact that skin properties change dramatically during the early years, but also that skin properties vary much between individuals.

Skin is generally considered anisotropic in the in-plane directions. The directional effects of skin were studied by Ridge and Wright (1966b) with reference to "Langer's lines", visible markings which correspond to the directions of principal tension. It was found that the general shape of the load-extension curve is similar when measured along

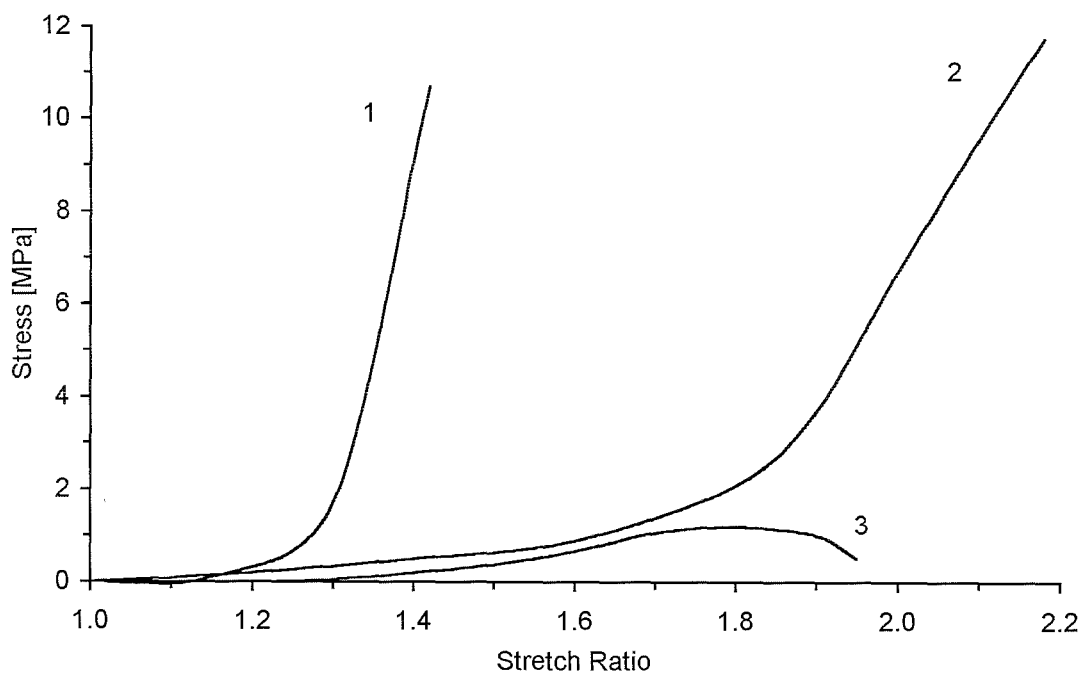


Figure 1.5. Stress-strain response of human abdominal skin under uniaxial tensile load recorded by: 1) Kenedi et al (1964), 2) Jansen and Rottier (1958a), 3) Ridge and Wright (1966a).

and across Langer's lines but there is a considerable difference in the actual extension for a given load. This corresponds to the constant  $b$  in equation (2) being the same both across and along the Langer's lines while the constant  $k$  is much higher across than along (Ridge and Wright (1966a)). It is, however, also evident from their work that the influence of age and location on the body is just as significant as the directional effects.

Hysteresis and rate dependence are also observed in the response of skin, further complicating its mechanical characterisation. During cyclic loading, hysteresis is minimised and a pseudo-elastic state is reached after a number of cycles. Some investigators have used this as a means of preconditioning the specimens prior to testing (Kenedi et al (1964), Lanir and Fung (1974a, b), Schneider (1982)). Schneider found that skin is rate-dependent with a ten-fold increase in load rate causing a two-fold increase in the load at a given strain. This is somewhat contradicted by Fung (1993) who states that the stress-strain relationship can be regarded as essentially independent of the strain rate.

The effect of storage, handling, and environment during testing has been discussed extensively but little hard evidence has been presented. Schneider noted that swelling

Age group Years	Strength at rupture [kg / mm <sup>2</sup> ]		% elongation at rupture	
	Male	Female	Male	Female
0 - 9	1.1 ± 0.9	(1.0 ± 0.2)	102 ± 42	(104 ± 46)
10 - 19	0.3 ± 0.2	0.8 ± 0.8	85 ± 36	125 ± 82
20 - 29	0.9 ± 1.3	1.3 ± 1.7	96 ± 53	100 ± 25
30 - 39	1.4 ± 1.0	0.6 ± 0.8	88 ± 35	76 ± 32
40 - 49	0.5 ± 0.3	1.2 ± 0.4	79 ± 50	67 ± 10
50 - 59	0.8 ± 0.8	0.9 ± 1.9	69 ± 22	52 ± 28
60 - 69	0.8 ± 1.0	0.4 ± 0.6	70 ± 9	58 ± 35
70 - 79	0.6 ± 0.4	0.5 ± 0.8	65 ± 28	58 ± 38
80 - 89	0.6 ± 0.7	0.8 ± 1.5	64 ± 31	51 ± 34
90 - 99	(0.4 ± 0.3)	-	(70 ± 17)	-

- Double standard deviation is stated after the ± sign.
- Single values in parenthesis.

Table 1.1. Mean mechanical values characterising human abdominal skin.  
From Jansen and Rottier (1958a).

occurs mainly during the first two hours when a skin specimen is immersed in normal saline solution. A maximum thickness increase of approximately 20% was observed. Freezing and storage are thought to have some effect on mechanical properties and some investigators point out the importance of humidity and temperature control during testing. The effect of exsiccation (drying out) was demonstrated by Jansen and Rottier (1958b). After just one hour exposure to open air the failure load had increased three fold and four fold after two hours. Elongation at failure was reduced by exsiccation.

In summary, skin is characterised as being nonlinear, anisotropic, viscoelastic, sensitive to humidity, and dependent on age, location, and direction. However this is not particularly helpful for modelling and some simplification is therefore necessary if progress is to be made. Anisotropy is generally accepted but has not been investigated at near-failure and could possibly be confused with the in-situ predominant tension lines, the Langer's lines. Actual failure values have been stated by Jansen and Rottier (1958a)

whose work covered 89 cadavers providing more than 267 stress-strain curves. These are summarised in Table 1.1 but even with this relatively high number of specimens the double standard deviation indicates that there are significant differences in properties between individuals.

### **1.5 The finite element method**

Finite element modelling or finite element analysis (FEA) has been applied to many different types of problem in areas as diverse as engineering, geology, mathematics, biology and medical research. Fundamentally, it is a technique for solving partial differential equations whose domains are geometrically too complicated to admit analytic solutions. The domain is divided into sub-domains, into a “mesh” of “finite elements” connected at “nodes”. Each element is small enough for the field variable, commonly displacement or temperature, to be approximated by a simple function of position. In principle then, FEA can be used to solve almost any problem which can be modelled by differential equations and it has indeed been described as the most powerful analysis technique ever made available to engineers.

Contact modelling is a rather specialised and relatively recent development of FEA and enables the analysis of the interaction between two deforming surfaces or bodies. Special contact algorithms are required to monitor the making or breaking of contact and to evaluate the resulting interaction forces between the surfaces. Certain parameters such as contact algorithm and element size determine how efficient the contact simulation works and as a general rule, the finite element model of a contact problem should use a more refined mesh for the more flexible material (Zhong (1993)). Better results are also obtained when the elements actually in contact are of broadly similar sizes. A reliable model of the contact between a rigid, sharp point and a softer target material then requires a very fine mesh in the contact zone. Furthermore, large angles between element faces in the two contact surfaces are known to cause problems.

#### **1.5.1 Finite element modelling of skin**

At the macroscopic scale, skin behaves as a membrane and both experimental and computational work is mostly based on two-dimensional membrane theory where it is assumed that no stresses in the thickness direction exist. An example of a finite element

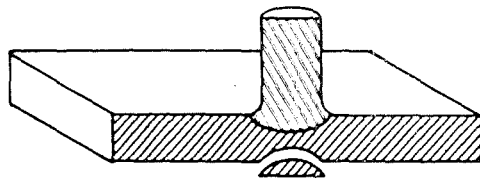
based model of skin is given by Flynn (1989) whose work was continued and refined by Peura (1993). Similar work was also presented by Nielsen et al (1991). Here the properties of soft tissue were investigated by a two-dimensional approach using four-noded and nine-noded membrane elements. Latex rubber from surgical gloves and rat skin were used as benchmark test materials. An experimental set-up provided biaxial incremental load-displacement data which was used as input to the FE-model. From the FE-model the nonlinear and anisotropic material compliance values could be extracted. A material failure model was not implemented as only low strains were imposed on the test specimens. Provided a failure criterion could be developed, membrane elements appear to be good candidates for realistic modelling of skin. These admit only in-plane stresses but this is likely to be the predominant factor in determining when a membrane element fails. This simplifies the failure model in comparison to that of, say, a full 3-d continuum element in which the stress in the thickness direction could not be ignored.

### **1.5.2 Penetration mechanics**

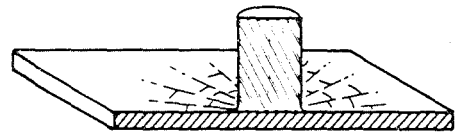
As noted in section 1.1, the mechanics of stab-penetration have not been extensively treated in the literature. In contrast, ballistic penetration has been well covered both in the areas of wound ballistics and in the penetration of hard and soft armours. The latter include modern lightweight textiles while the former include both traditional rolled homogeneous (steel) armour (RHA) and modern engineering ceramics.

Sharp, hard projectiles initiate penetration of metal by causing internal separation at the tip (Backman and Goldsmith (1978)). Further penetration can occur either by a continuous enlargement of the hole along the direction of the projectile, or by petalling where fractures propagate radially from the initial hole (Figure 1.6). Ceramics respond in a different way by shattering along a conical front as the stress wave travels through the brittle material (Figure 1.6). Penetration of thicker targets usually occurs by plugging as the shattered cone is detached from the surrounding material. Plugging also occurs in metal punching processes where a cylindrical punch is used and failure is determined mainly by shear stresses.

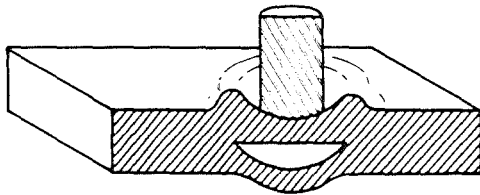
The response of textile structures to bullet penetration has been computationally modelled by Roylance and Wang (1980) and Shim et al (1995), but not in continuum FE terms. A woven panel was idealised as an assemblage of pin-jointed flexible fibre



(a) FRACTURE DUE TO INITIAL STRESS WAVE



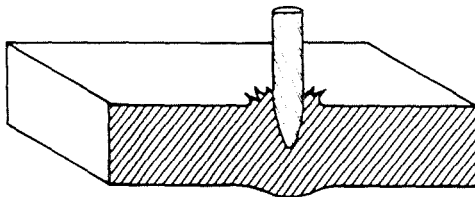
(b) RADIAL FRACTURE BEHIND INITIAL WAVE IN A BRITTLE TARGET



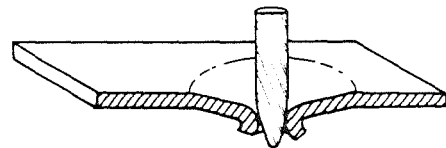
(c) SPALL FAILURE (SCABBING)



(d) PLUGGING



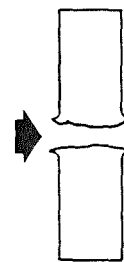
(e) PETALING (FRONTAL)



(f) PETALING (REARWARD)



(g) FRAGMENTATION



(h) DUCTILE HOLE ENLARGEMENT

Figure 1.6. Penetration modes for different materials. From Backman and Goldsmith (1978).

elements characterised by a material model including viscoelastic behaviour and failure. An initial projectile velocity was imposed on a single node on the target. Wave propagation through the target material was simulated with a number of material models and with different projectile velocities. Good agreement with experimental results was reported. Although this model looks a promising basis from which to begin modelling knife penetration, there are a number of serious problems. The greatest of these concerns the sharp tip of the knife. The existing model can not take this factor into account as load is applied to only a single node which will result in similar forces in the target structure independent of the actual penetrator tip radius. Another question is whether human skin is better represented as a fibrous mesh or as a homogeneous membrane. The former is more appropriate at the microstructural scale since skin is, structurally, a fibre mesh with randomly orientated fibres in the unloaded state. However this is problematic to model and the homogeneous membrane is often used as an idealised model at the macroscopic scale. Finally there is an obvious difference in the velocities involved in bullet and knife penetration, the latter being almost quasistatic.

Computational penetration mechanics are far from being fully developed. Numerical instabilities, constitutive modelling, and friction affects are mentioned by Oden (1983) as areas posing difficulties. Development of constitutive models is difficult particularly with respect to plasticity and failure. Microstructural influences are often ignored for the sake of simplicity although they can play an important role in the description of material failure.

### **1.5.3 Constitutive modelling**

The basic purpose of a constitutive model or material model is to form a connection between stresses and strains in any material used in a structural analysis. Almost any material can be described mathematically provided complexity is not a limiting factor. To be of practical use it is, however, necessary to keep complexity within limits yet maintain realistic accuracy as highlighted in the quote from Wilkins (1984): "The objective of the material models is to provide a theoretical description applicable to a wide class of practical problems, but using simple idealizations of the outstanding features of the real phenomenon". Below is given a brief review of material modelling

relevant to soft tissue which essentially is a composite and which can be regarded as a subgroup of composites used in a conventional engineering context.

### *Composites*

A composite material consists of two or more distinct materials which typically are present as a fibre phase and a matrix phase respectively. The matrix binds the fibres which act as reinforcement. Glass fibre Reinforced Polyester (GRP) is an example of a man-made composite widely used in eg boat building. Also carbon fibre composites are becoming more frequently used in high performance engineering applications where high strength to weight ratio is required. Modern materials for high temperature applications are often composites of metal and ceramic which in combination can give the required temperature resistance yet maintain the mechanical strength and some ductility.

Constitutive modelling of composites for FEA is mostly based on average mechanical properties measured over an area of the material. Macromodelling is relatively simple in the elastic range while modelling of damage and failure complicate matters. Micromechanical data from destructive mechanical testing is often used for derivation of a damage evolution law applied at a global level. Macromodelling of composites generally requires a complicated material model while the rest of the FE model can be meshed as a homogeneous material (Hamouda and Hashmi (1996)). Another approach is micromechanical modelling where a unit cell containing a single fibre is meshed with interface elements at the matrix-fibre boundary. The interface transfers load along, normal to, and tangential to the fibres by means of friction and above a certain traction, debonding and slipping occurs (Lissenden and Herakovich (1995)). Micromechanical modelling allows a relatively simple constitutive model as each material is described separately. Meshing, on the other hand, is rather complex and the analysis is expensive due to the high number of elements combined with contact surfaces between fibres and matrix material. Macromodelling is therefore by far the most common approach to FEA involving composites.

### *Hyperelasticity and soft tissue*

Computational models directly applicable to soft tissues and like materials have been proposed by a number of authors. A 2-d model using a stiffening finite strain extremum

principle was proposed by Flanagan et al (1995). An example is given for a single finite element using constants derived from experiments on rabbit abdominal skin by Tong and Fung (1976). A stress-strain plot is given showing 2nd Piola-Kirchoff stress (Bathe (1982) p.319) versus total strain. The stress derived computationally increases linearly to a certain point where the stiffness becomes infinitely high. This graph is compared with experimental results from Tong and Fung (1976) which also show near linear response at low strains and significant stiffening at higher strains. The computational stiffening is facilitated by a single locking constituent causing the sudden change in stiffness. A more complex formulation was proposed by Park and Youn (1997) allowing full 3-d anisotropic behaviour but with a multitude of constants to be experimentally determined.

Any computational treatment of failure of soft tissue has not been found in the literature. A low demand for failure modelling of skin might partly explain why this is the case as material models admitting failure are well developed for traditional engineering materials such as steel. Another part of the explanation might be difficulties in modelling the substantial strain energy release during failure encountered in hyperelastic materials such as skin.

### **1.6 Case studies of stabbing incidents**

In order to give some insight into the nature and type of problem to be modelled, a detailed survey was carried out of cases brought to the attention of the Department of Forensic Medicine at the University of Glasgow. Access was given to 34 cases including stabbing incidents where the weapons were known. The information recorded was:

- The date of incident.
- Personal details of the victim (sex, age, etc).
- The locus (place of the incident).
- The actual cause of death.
- The number of layers of clothes penetrated by the weapon.
- Whether bone was penetrated by the weapon.
- Wound characteristics (number, location, length, depth).
- Weapon characteristics (length/width of blade, shape).

These data are tabulated in Appendix 1.1. and 1.2. The results may be summarised as follows:

Cause of death. In all 34 cases the knife attack proved fatal. In two cases death was caused by other circumstances than stabbing and in another two cases the cause of death was combined with stabbing.

Personal details. The incidents included 82% male victims and 16% female victims. The average age was found to be 31 years for both the male and female group. The typical victim is then a male about 30 years old.

Locus. In 9 of the 34 examined cases the incident took place inside a building or house. 7 incidents took place on open street. The rest are unknown. It should be noted that the nature of attack can vary according to the locus, eg domestic attacks are more likely to be confrontational.

Clothing. The number of clothing layers cut through was recorded. However, detailed information was only present in very few cases. It is not then possible to derive any empirical conclusions from the clothing on eg penetration depth.

Bone tissue. In almost 60% of the cases bone was cut. The type of bone cut was in all cases costal (rib) bone. There is not, however, any significant correlation between the width of the knife blade and the frequency with which bone was cut.

Wound location. The majority of wounds were inflicted in the chest region. The remainder of the injuries were found in (in descending order) the neck/head, the back, the abdomen and, finally, extremities such as limbs. Injuries on extremities are usually caused by defensive movements but are not usually, in themselves, fatal.

Wound characteristics. It was confirmed that full penetration of the knife blade occurred in most cases. In some cases wounds were found to be longer than the knife blade, indicating that the victim's body was compressed. This is common during attacks

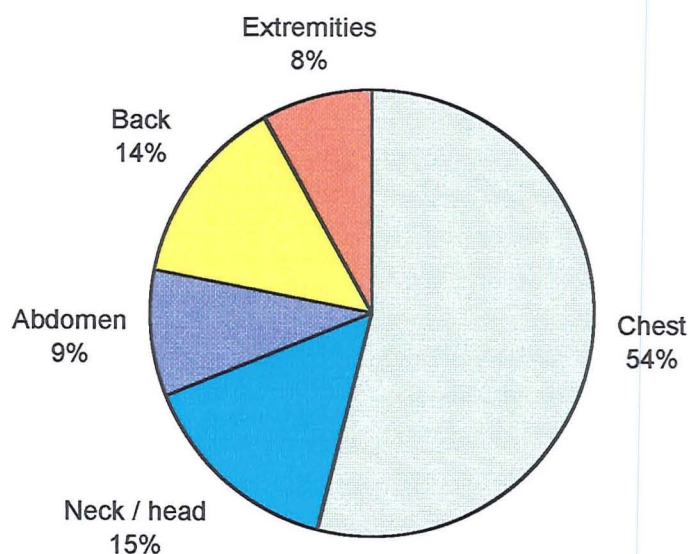


Figure 1.7. Distribution of stab wounds in anatomical regions of the human body. Original in colour.

where excessive force is applied to the knife. The width of the knife blade matched, in most cases, the wound length.

Weapon characteristics. A single edged kitchen knife is the predominant weapon type. The length of knife blade varied from 76mm to 238mm with a typical length of 110 to 160mm. The width of the knife blade varied from 6mm to 50mm with a typical width of 15 to 25mm.

A recent comprehensive survey by Bleetman (1997), based on data collected over 30 years in the UK, shows a similar pattern regarding age of victim, location of wounds, and type of weapon. Records from Glasgow in 1985 also show that chest wounds accounted for 45% of stabbings, abdominal wounds 36%, limbs 33%, head and neck 15%, and buttocks in 5%. Multiple stab wounds are particularly common in the chest region. These studies also confirm that kitchen knives are the predominant weapon, accounting for 33% of attacks, with sheath knives accounting for 12%, and lockback knives 8%. It is significant to note that, contrary to public perception and recent media coverage, purpose made weapons and combat knives are not commonly involved in homicides. The conclusions from the author's study of 34 cases are therefore

considered representative of the general nature and severity of stabbing incidents. The distribution of stab wounds in anatomical regions of the human body as found in the author's case studies is as shown in Figure 1.7.

### **1.7 Proposed scope of work**

The aim of the current work is to quantify the forces in stabbing incidents. However, as the surveys and case studies show, by their very nature stabbing incidents are rather complex and it would be unrealistic to consider all aspects of an incident. A number of simplifications must be made in order to make any progress whatever. Any particular stabbing incident is a unique event involving a multiplicity of variables such as the weight and age of both the victim and the assailant, the "style" of attack (eg high or low swing, thrust or sweep), the type of weapon and the clothing worn by the victim. The author's detailed case study then provides some insight into the more "typical" features of stabbing attacks and so points towards the most critical features to be modelled. It is, for example, counterproductive to attempt to model the type of weapon specified in the Home Office's Police Scientific Development Branch publication on stab-resistant armour (Parker (1993)). A simplified and, to some extent, idealised model is therefore required to quantify the force required for a knife blade to penetrate human tissue.

Skin provides much more resistance to penetration than the underlying tissues (apart from bone) and thus provides the major focus for the current work. The effect of bone is not underestimated, especially since costal bone is often cut through in stabbing incidents and so plays an important role in determining the required force to inflict the wound. This is however being investigated in a parallel project and is outwith the scope of the present work (Soh (1998)).

#### **1.7.1 Tensile test programme**

Uniaxial tensile tests are simple to perform and are readily analysed. It was decided to carry out such tests to determine the properties of both skin and skin simulants. The test programme therefore comprised two phases:

- 1) Pilot tests to identify a suitable human skin simulant. This simulant should be readily available and have mechanical characteristics broadly similar to those of human skin.

2) More extensive tests on the material selected from the pilot test. These tests provided materials data needed for the computational material model. In this study, such data must include values for failure stress and strain and the uniaxial tensile test is particularly suited to obtaining such values.

### **1.7.2 Stab-penetration test**

The idealised model of a stabbing victim comprises a fixed target block which is to be penetrated by a series of purpose-made knife blades moving at a constant low velocity. This test protocol will be referred to as the stab-penetration test and was intended to yield the reaction force on a given blade, both on entry and on exit. The stab-penetration test was also carried out in two stages:

- 1) Pilot tests were used to investigate the important features of knife blades, eg edge and tip sharpness, and to evaluate the suitability of various skin simulants under stabbing actions.
- 2) Additional tests on the identified skin simulant. Such stab-penetration tests were carried out in parallel with FE modelling and both sharp blades and penetrators of various tip radius were used as benchmarking against computed values.

### **1.7.3 Computer simulation**

The stab-penetration tests were simulated computationally using Abaqus/Explicit, a nonlinear FEA package with particular features to admit modelling of contact-impact-penetration problems. The key variable to be extracted from the computational simulation of the stab-penetration test was the reaction force on the knife during penetration. This was obtained for various shapes of blade and blunt indenter and the results compared with the directly measured experimental values. A material constitutive model representative of skin was developed, based on the uniaxial tensile tests. Although many variables must be omitted in the computational simulations, key parameters identified from the literature and the preliminary test, such as blade tip sharpness, must be retained in the FE-model.

## **2 Mechanical tests of tissue simulants**

Mechanical tests are commonly used to characterise engineering materials but have also been used for determining mechanical properties of biological materials. In this study uniaxial tensile tests were used to identify a suitable simulant material for human skin as described in this chapter. The advantages of using such a simulant are various. Firstly, complete human cadavers as used by Knight (1975) and Green (1978) are not needed and the related practical and ethical problems are avoided. Bulky, purpose-built test equipment would also be necessary in whole-body tests for the stab-penetration test described in chapter three and four.

### **2.1 Pilot tensile tests on skin simulants**

Pilot tests were designed to identify suitable simulants for human soft tissue. The skin simulant should be readily available and have matching characteristics to those known for real human skin. A synthetic material was initially preferred to avoid the inconsistencies usually associated with biological materials. Synthetic chamois, commercially available as window-washing cloth, was suggested by Barbenel (1994). In this study “Easy Glide Chamois” supplied by Halfords Ltd. was used. This is a non-woven fabric consisting of a soft poly vinyl acetate foam matrix with orthogonal continuous reinforcement threads laid in a 0/90° pattern. The directionality of the reinforcement threads was not initially considered to be a problem.

Pig skin, a true biomaterial, is believed by the author to be more representative of human skin and is relatively easy to obtain. It is however likely to be less consistent. Initial work therefore focussed on synthetic chamois.

The mechanical properties of neither pig skin nor synthetic chamois could be found from the literature and so tests were needed to determine even basic material properties. A number of authors have argued that only a biaxial tensile test can yield the true stress-strain behaviour of skin (Cook (1975), Flynn (1989), Peura (1993)). This may be true, especially for low strain but such tests are more difficult to perform, particularly at the high strains associated with failure of the material. At this stage, it is then more appropriate to study the material via simple uniaxial tensile tests.

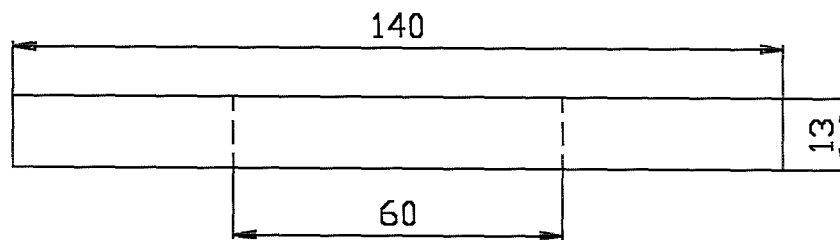


Figure 2.1. Rectangular tensile specimen used in pilot tests. Dimensions in mm. Drawing not to scale.

### 2.1.1 Uniaxial tensile test programme

#### *Test rig*

A similar test protocol was devised for both materials. A rectangular specimen shape was chosen with dimensions close to those used by Jansen and Rottier (1958) (Figure 2.1). This shape can be easily cut from the bulk material. Self-tightening wedge clamps with flat gripping surfaces were used to retain the specimen during testing (Figure 2.2). Initial tests were carried out on a Hounsfield Tensometer with a manual drive, via a winding wheel and a worm gear, and a manually operated load-extension plotter. Such tests are quick to perform and give a feel for the levels of the loads and displacements to failure. More accurate results were however obtained using a Lloyd LR30 Universal Testing Machine with displacement control of the crosshead. A measure of crosshead movement was available from the internal instruments in the machine while the corresponding loadtrain reaction force was measured via an electronic loadcell. The load-displacement data was displayed on an on-line PC and stored on disk. The PC was also used to control the crosshead movement via Lloyd's Instruments dedicated software.

#### *Specimen preparation*

Synthetic chamois specimens were cut from sheet with a note taken of the fibre orientation. The thickness was measured with Vernier callipers as 1 mm which should be regarded as an approximate value due to the material being very soft and easy to compress.

Complete pig skins were procured and patches measuring about 150 x 150 mm cut out. The fatty subcutaneous layers were removed using a purpose-made curved edged

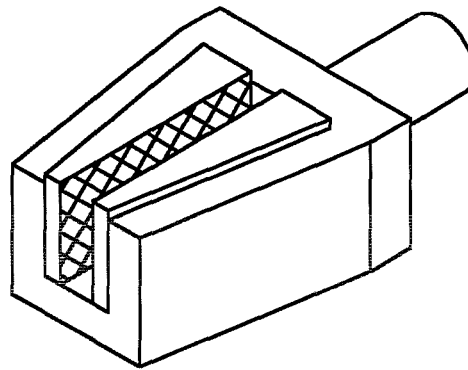


Figure 2.2. Self-tightening grips used in pilot tensile test.

knife. After cutting the individual specimens to the required dimensions (Figure 2.1) the thickness measured by Vernier callipers was found to be approximately 2 mm. Pig skin specimens not immediately required were stored frozen in self sealing bags and thawed at room temperature one hour prior to testing.

### *Test Protocol*

As noted previously, synthetic chamois is a non-woven fabric with orthogonal reinforcement threads. The material was tested both parallel to, and at 45° to, the threads. The material was tested both dry and wet to elicit any effect of moisture content on material properties.

Pig skin was, during the pilot tests, tested without any knowledge of the principal fibre orientation.

The pilot test protocol can be summarised as follows:

### Hounsfield Tensometer

- 3 pig skin specimens
- 3 dry synthetic chamois specimens, pulled parallel to the fibre direction
- 3 wet synthetic chamois specimens, pulled parallel to the fibre direction

### Lloyd LR30 Universal Testing Machine

- 3 dry synthetic chamois specimens, pulled parallel to the fibre direction
- 3 dry synthetic chamois specimens, pulled at 45° to the fibre direction
- 1 wet synthetic chamois specimen, pulled at 45° to the fibre direction

The procedure applied was to insert the specimen between the grips, pre-tighten the grips manually just to hold the specimen, and then extend the specimen up to failure. The extension rate was programmed to be 100 mm/min, resulting in a strain rate of 0.028 s<sup>-1</sup> for the Lloyd Universal Testing Machine but was indeterminate for the manually driven Hounsfield Tensometer.

#### **2.1.2 Results and evaluation**

The results from the uniaxial pilot tensile tests are given in the form of force-extension curves in Appendix 2. For comparison between materials, selected curves showing typical normalised results are also given in Figure 2.3 and Figure 2.4. In these the stress is nominal stress, ie force divided by the initial unstrained cross-section (here 1 mm x 13 mm = 13 mm<sup>2</sup>). Strain is presented as stretch ratio  $\lambda = L / L_0$ , where  $L$  is the current length and  $L_0$  is the initial gauge length (60 mm).

The results show that the tensile behaviour of synthetic chamois is highly dependent on direction. The nominal failure stress is indeed similar for the directions tested but the failure strain is two to three times greater in the 45° direction than in the parallel direction. This result is hardly surprising; when tested parallel to the fibre direction, a stiff and almost linear response is observed since practically all the load is carried by the longitudinally orientated fibres. The effect of the soft matrix material is negligible in this situation. In the 45° direction the situation is different as the web of reinforcement fibres has a very low shear modulus. The individual fibres are being re-aligned during the first, flat part of the stress-strain curve (Figure 2.3) but once this re-alignment is complete they start to take up the load and continue to do so until the point of abrupt failure.

These characteristics are qualitatively very similar to those observed in pig skin (Figure 2.4). A similar explanation for tension stiffening, based on re-alignment of load bearing fibres, has been given by Daly (1966) and other authors regarding the

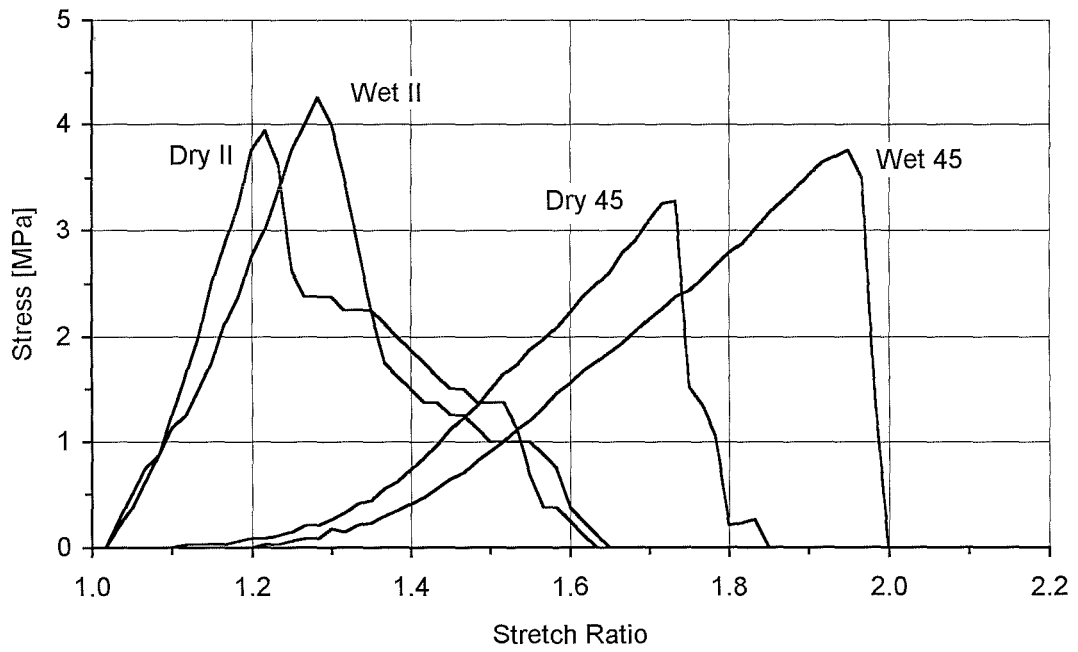


Figure 2.3. Stress-strain curves for synthetic chamois from pilot tensile test.

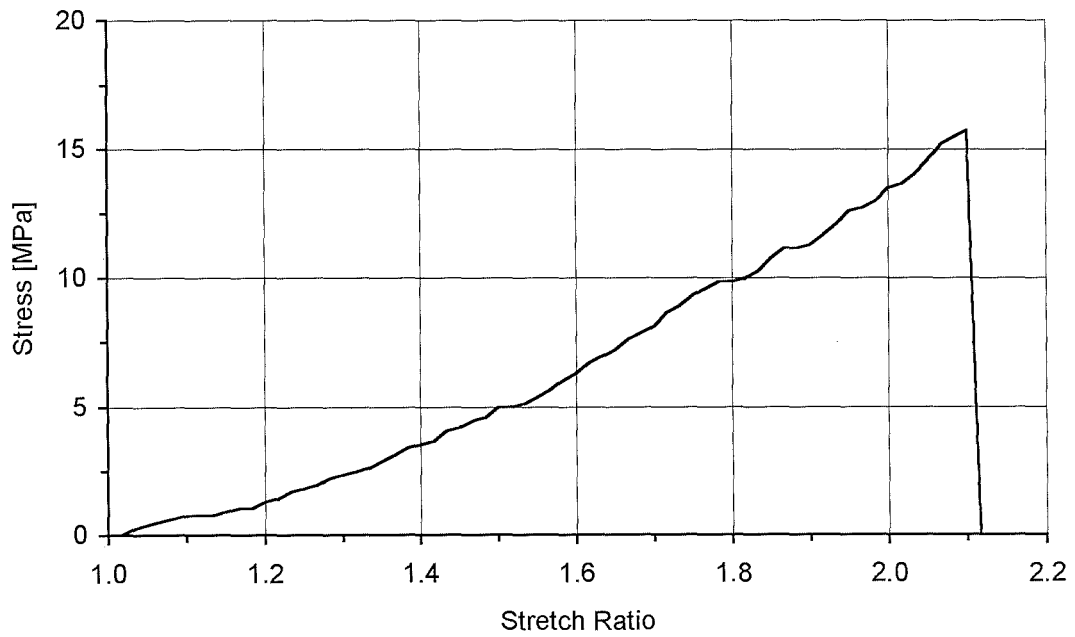


Figure 2.4. Stress-strain curve for pig skin from pilot tensile test.

stress-strain behaviour of human skin. Although the characteristics for chamois loaded at 45° to the fibre direction and for pig skin are similar, the absolute values of failure stress and strain are quite different for the two materials. Surprisingly, high moisture content in the synthetic chamois causes a slight increase in both failure stress and strain. This might be explained by an increase in internal fibre-to-matrix friction due to swelling.

In this pilot study, the tensile behaviour of pig skin was found close to that of human skin as recorded by other investigators. This also includes the actual nominal stress and strain at failure keeping in mind that these values can vary considerably between individuals. At this stage pig skin appears to be a realistic and the most suitable simulant for real human skin as opposed to the synthetic chamois which is too weak and directionally dependent. Since pig skin is a biological material inconsistencies may be encountered demanding a higher number of repetitive tests.

## **2.2 Detailed tensile tests on selected skin simulant**

To confirm the tentative conclusions from the preliminary tests and to provide more detailed information to help in constitutive modelling, more comprehensive tensile tests were performed. These focused on pig skin rather than synthetic chamois, since the growing opinion was that the latter showed features which were not in accord with the known behaviour of skin (eg increased strength when wet). In this phase, the tensile tests were repeated several times to provide greater statistical reliability. This in turn increased the requirement for test specimens. Additional specimens were also used to take account for the original location and orientation of the specimen on the individual animal. During the comprehensive tensile tests, the change in width was measured to evaluate Poisson's ratio.

### **2.2.1 Test programme**

#### *Test rig*

To avoid end-effects from the grips and to ensure that failure would not occur at the inevitable stress concentrations, it was decided to use a dumbbell shaped specimen with larger dimensions than was previously used. This also minimised damage during handling and clamping. The specimen dimensions are as shown in Figure 2.5. For the larger specimens a set of grips was designed and made as shown in Figure 2.6.

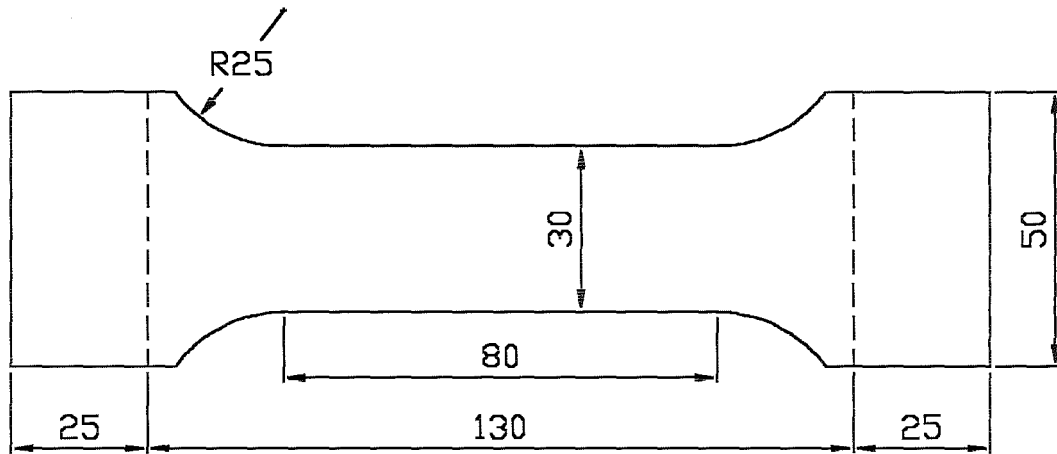


Figure 2.5. Dumbbell shaped tensile specimen used for detailed tests on pig skin. Dimensions in mm. Drawing not to scale.

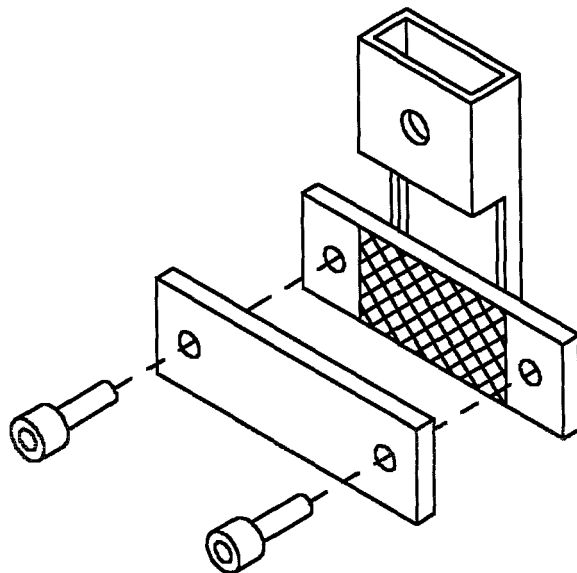


Figure 2.6. Grip for dumbbell shaped pig skin tensile specimen.

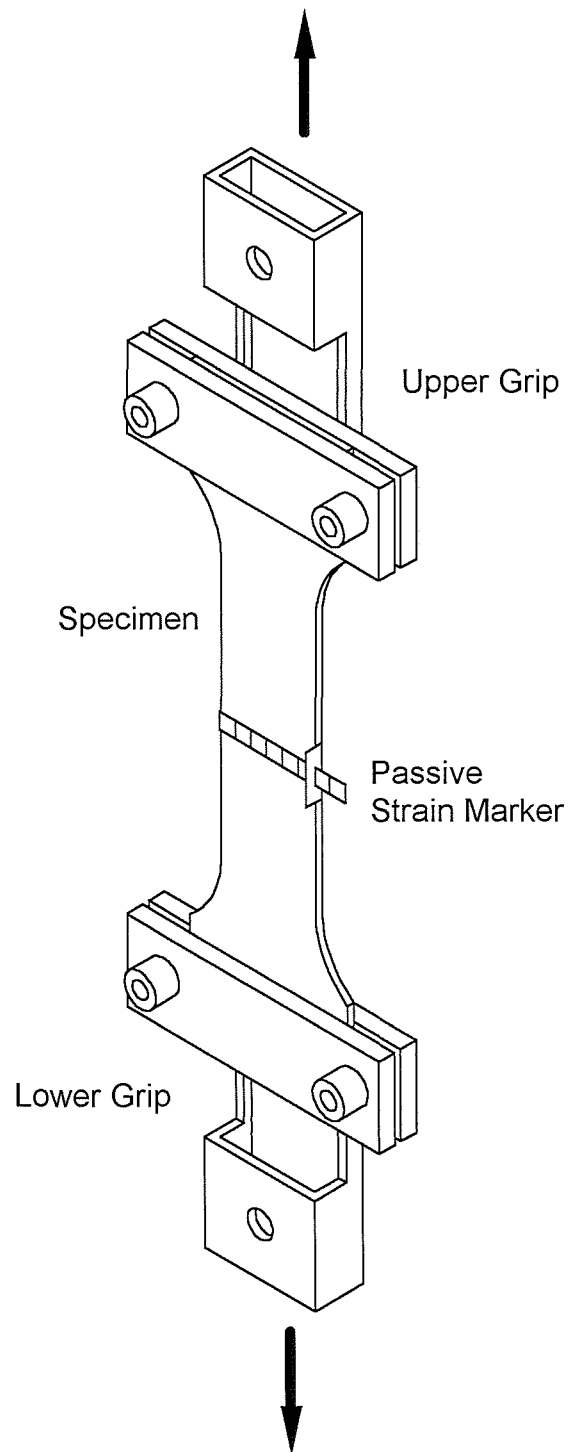


Figure 2.7. Test set-up for dumbbell shaped pig skin specimen.

These grips were formed by two roughened steel plates clamped together by two machine screws with the specimen held in between the plates. One of the steel plates was attached via an adaptor to the testing machine allowing the other steel plate to be removed when changing the specimen. To further increase friction, nylon scouring pads were inserted between the grip plates and the specimen. The change in width was measured by attaching a piece of graph paper to one side of the specimen and a reference marker to the other side (Figure 2.7). As the specimen necks down under elongation the scale moves relative to the marker. Scale and marker were attached by quick drying super-glue midway between the ends of the specimen. Only a small point on the specimen was covered by glue to ensure that the test results would not be affected. A piece of graph paper was used as a backdrop for general reference and each tensile test was recorded on video tape.

### *Specimen Preparation*

Pig skin was obtained from the abattoir in the form of whole skins, to provide the increased number of oversized specimens. The age of the pigs was between 7 months and 8 months. To ensure that the material was relatively fresh, one skin was procured at a time and cut into 4 large rectangular pieces, one from each side of the back and one from each side of the belly region (Figure 2.8). Location and orientation was marked on each piece. Fatty subcutaneous layers were removed from these pieces using a purpose-made curved edged knife. The dumbbell shaped specimens were cut to a steel template using a size 3/15 scalpel. The thickness was measured as  $2 \pm 0.5$  mm, the material being generally thicker at the back and thinner at the belly. Some batches were stored in airtight plastic containers and frozen for later use. Such frozen specimens were thawed in air at room temperature while others were soaked in water during thawing. These specimens will be referred to as "frozen", although they were thawed prior to testing. Other batches were tested immediately on receipt to avoid any possible effects of the freezing.

### *Test Protocol*

The pig skin specimens were cut from two orthogonal directions, longitudinal (parallel to the pig's spine) and transverse (normal to the spine). Some non-standard specimens

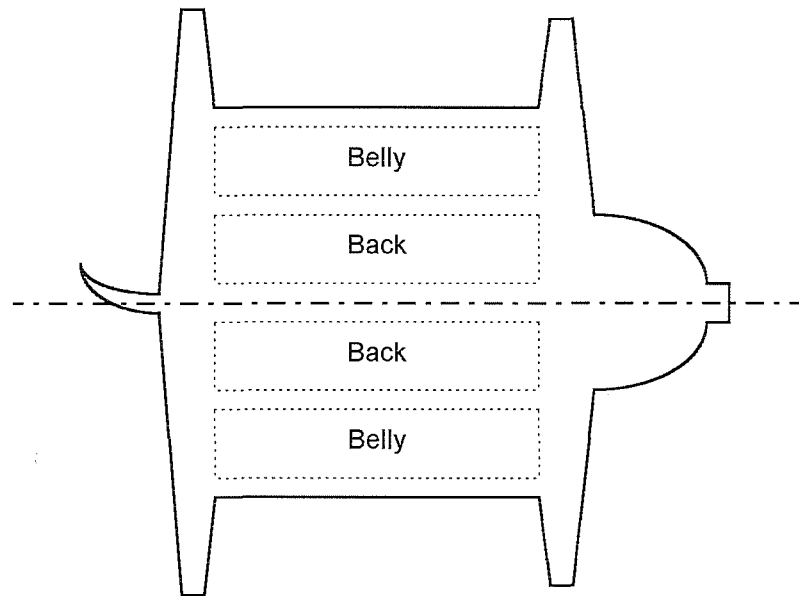


Figure 2.8. Plan view of pig skin showing regions used for experiments.

were prepared to allow investigation of the significance of moisture content and the loadbearing influence of the fatty subcutaneous layers. The distribution of specimens used for the uniaxial tensile tests is listed in Table 2.1.

The test procedure was commenced by inserting the specimen in the upper grips and tightening the screws. With the specimen hanging from the upper grips, the cross-head height was adjusted until the specimen was correctly positioned in the lower grips. The lower screws were then tightened. Under a constant extension rate of 50 mm/min the specimen was loaded until failure occurred. This lower cross-head speed was adopted to match the strain rate of  $0.01 \text{ s}^{-1}$  used by Jansen and Rottier (1958).

Number	Storage	Location	Orientation	Remarks
10	Frozen	Back	Longitudinal	1 soaked in water
14	Frozen	Back	Transverse	2 w/ fatty layer
3	Fresh	Belly	Longitudinal	
4	Fresh	Belly	Transverse	
11	Fresh	Back	Longitudinal	
12	Fresh	Back	Transverse	

Table 2.1. Pig skin specimens tested on the Lloyd LR30 Universal Testing Machine.

### 2.2.2 Results and evaluation

Results from the uniaxial tensile tests on the pig skin are presented in form of force-extension curves shown in Figure 2.10 to Figure 2.18. Specimens are organised in the figures by preparation (frozen/fresh), orientation, and batch, where the first letter in the legend code indicates orientation (Longitudinal / Transverse), the following two digits indicate batch number and the two last digits indicate specimen number. Curves represent the tensile force measured on the grips versus extension of the specimen measured as displacement of the grips. Specimens which slipped in the grips are excluded from the figures but are included in the complete lists of tensile test specimens in Appendix 3. From these lists it can also be seen that the majority of specimens failed at the transition between the narrow gauge section and the wide gripping area at the ends of the specimens. The rest of the specimens failed somewhere along the narrow gauge section but only a few failed right at the middle.

#### *Strain measurement*

The uniaxial tensile tests of pig skin yielded results on failure load, extension at failure, and change in width. To counteract end-effects, a dumbbell shaped specimen was used which has a disadvantage regarding measurement of active strain due to the non-linear specimen geometry. The Lloyd Universal Testing Machine measured displacement of the grips with an initial specimen length between grips of 130 mm. The waisted specimen section was only 80 mm long and using either of these values as initial specimen length in strain calculations would cause an unacceptable error. From the video recordings of the tests it was verified that an assumed initial length of 110 mm provided good agreement between strain calculations and the load-extension curves obtained from the testing machine. This approximation method is subject to specimen geometry and material.

#### *Directional effects*

Average failure values found for pig skin are shown in Figure 2.9 with nominal stress values and stretch ratios obtained from Appendix 3. Directional effects appear to be relatively small for back skin. The small degree of directional effects, which do exist, seem consistent for both fresh and frozen back skin with higher failure stress-strain

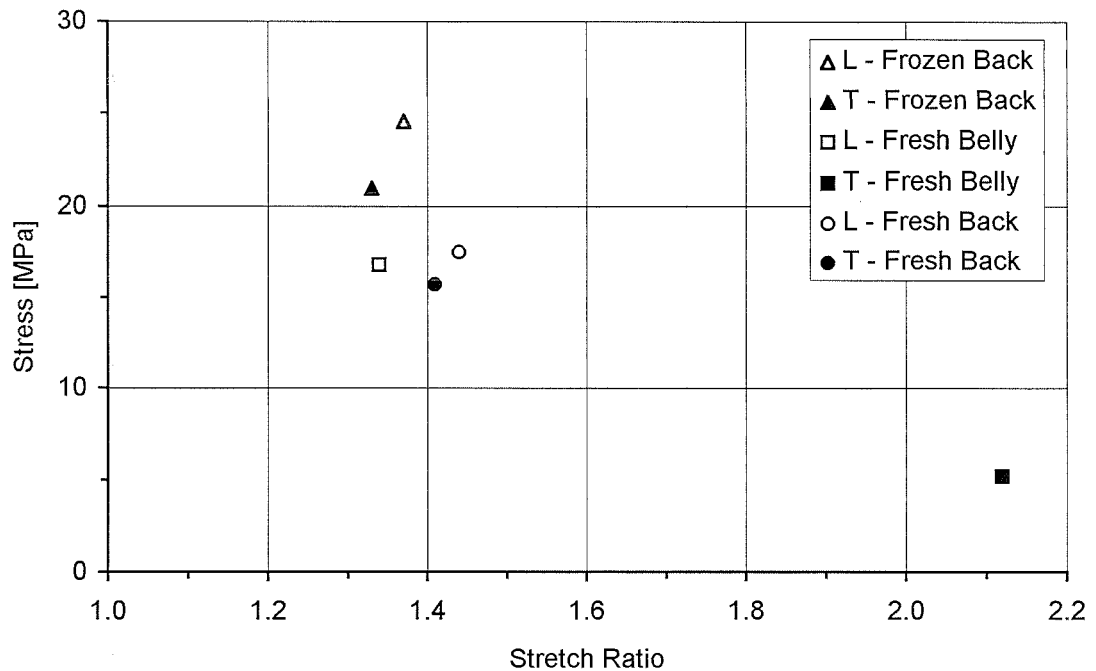


Figure 2.9. Average stress-strain failure values for pig skin obtained from dumbbell shaped specimens. L) Longitudinal direction. T) Transverse direction.

values in the longitudinal direction than in the transverse direction. This observation indicates that the strength of pig skin is slightly higher across Langer's lines than along these lines of principal tension, assuming that Langer's lines coincide for pigs and humans. Freezing of the skin specimens has a toughening effect which is thought to be due to loss of water content during freezing and thawing. Belly skin showed large directional effects and yielded generally more inconsistent results than the back skin. The stiffest and strongest direction is the longitudinal direction which is not in agreement with the findings of Ridge and Wright (1966b) who found the transverse direction, along Langer's lines, to have the stiffest response. The study by Ridge and Wright was on human abdominal skin which might explain part of the discrepancies. Due to the large inconsistencies in belly skin it was decided to concentrate on back skin which has been investigated using a higher number of specimens. The inconsistencies also associated with the back skin are thought to be due to the fact that properties do vary gradually from the spine down the sides towards the belly region. With the relatively large specimen sizes property variations will be encountered between specimens and even within the same specimen. It is still desirable to keep the specimen size quite large to minimise the influence of handling the specimen during testing. Errors caused by

specimen handling have been mentioned by most investigators who all used smaller specimens than used in the present work.

#### *Failure stress and strain*

The average uniaxial failure stress of around 22 MPa and stretch ratio of around 1.4 found for back pig skin is in quite good agreement with the failure stress values stated by Jansen and Rottier (see Table 1.1). It should be taken into account that Jansen and Rottier tested human abdominal skin which is supposed to be slightly weaker and more pliable than the back skin of a pig. Although the results from the belly skin are inconsistent they do show similar characteristics to the human abdominal skin that is weaker and more pliable compared to the back skin. Age of the pig will probably have some influence on the skin properties but that remains an unknown factor as the tested specimens were from animals of roughly the same age.

#### *Failure mode*

The failure mode of pig skin was typically abrupt with no “warning” prior to failure, however, some specimens did fail gradually by tearing from one edge. The abrupt failure is regarded as the ideal mode of failure where almost all fibres are stretched equally to their maximum just prior to failure. In reality one fibre must fail first, initiating general failure of the whole specimen, but this is happening too fast for observation in real time. High speed video recording might yield more information about this type of failure. Tearing occurs when material imperfections are present. Failure will initiate at the imperfection which can be either natural or imposed during specimen preparation and will propagate as a crack until failure is complete.

#### *The influence of moisture content*

Prior to testing, specimen T0102 (Figure 2.11) was soaked in water for 2½ hours and a 7% increase in thickness was measured. Such hydration had no apparent effect on the tensile behaviour of this, admittedly single, specimen. Fibre pullouts were more noticeable on the soaked specimen whereas these pullouts are barely visible on unsoaked specimens. Schneider (1982) noted a 20% increase in thickness for human skin after 2 hours submersion in saline solution. It is known that saturation of biological tissue

occurs faster and to a higher degree with saline solution than with water which will hardly be absorbed by the tissue, a point that should have been considered while the experiments were ongoing. This possibly explains the differences in thickness increase but Schneider did not test skin specimens to failure so the effect of moisture content on failure values is still to be investigated in detail. Based on the results from the frozen specimens which are likely to have been dried out during freezing and thawing it can be argued that a high moisture content will have a lowering effect on the failure stress and make the specimen more extensible.

#### *The effect of subcutaneous tissue*

Specimen T0201 and T0202 were prepared with the subcutaneous fatty layers remaining on the specimen. No usable results were obtained from these specimens as the first slipped out of the grips and the second exceeded the maximum load of 2 kN set for that particular test. Since the load for frozen back skin loaded in the transverse direction lies between 1.3 kN and 1.7 kN, this might indicate that fatty tissue has some influence on strength. This could not be pursued in the present work.

#### *Passive strain*

The width of the specimen is nominally 30 mm when cut to the template but it was noted that some specimens contracted slightly after cutting and so the initial width was measured accurately just prior to testing. From play back of the video taped tests it was possible to note the width and elongation at failure as well as width at half the elongation to failure (intermediate point). Values are shown in Appendix 3. The width measures were taken at the narrowest point on the specimen which was generally halfway between the grips. Based on these width measurements and the specimen elongation Poisson's ratio was evaluated as:

$$\nu = -\frac{\varepsilon_{22}}{\varepsilon_{11}} = -\frac{\Delta W/W_0}{\Delta L/L_0} \quad (4)$$

where  $\varepsilon_{11}$  is the active strain,  $\varepsilon_{22}$  is the passive strain,  $\Delta W$  is the change in width,  $W_0$  is the initial width,  $\Delta L$  is the change in length, and  $L_0$  is the original length. The small

changes in thickness were ignored which is common practise when dealing with sheet-like materials.

Average values of Poisson's ratio at the intermediate point and at failure for each specimen category are summarised in Table 2.2. The overall average value was calculated to be approximately 0.6. This is close to the incompressibility value of 0.5. Of course, a Poisson's ratio above 0.5, which indicates volume loss under tension, is not possible in 3-d continua but it is seen in both woven and non-woven 2-d fabrics (Backer and Petterson (1960)). It has also been indicated by Kenedi et al (1964) that Poisson's ratio depends on active strain. An example is given for human abdominal skin where Poisson's ratio varies between 0.1 at low strains and 1.1 at higher strains. These values are only possible because the skin is treated on a macroscale as a homogeneous solid continuum while in fact it is a composite consisting of relatively stiff fibres in a soft matrix. Poisson's ratio is based on changes in width and length and is highly sensitive to the change in width which generally is small. Even small errors in these width measurements result in large variations in Poisson's ratio although the oversized specimens used in the present work help minimise this source of error.

Specimen	Poisson's ratio $\nu$	
	Intermediate	Failure
Frozen back - Longitudinal	0.58	0.61
Frozen back - Transverse	0.79	0.68
Fresh belly - Longitudinal	0.63	0.88
Fresh belly - Transverse	0.54	0.56
Fresh back - Longitudinal	0.31	0.34
Fresh back - Transverse	0.64	0.55

Table 2.2. Average values of Poisson's ratio at the intermediate point and at failure for each specimen category.

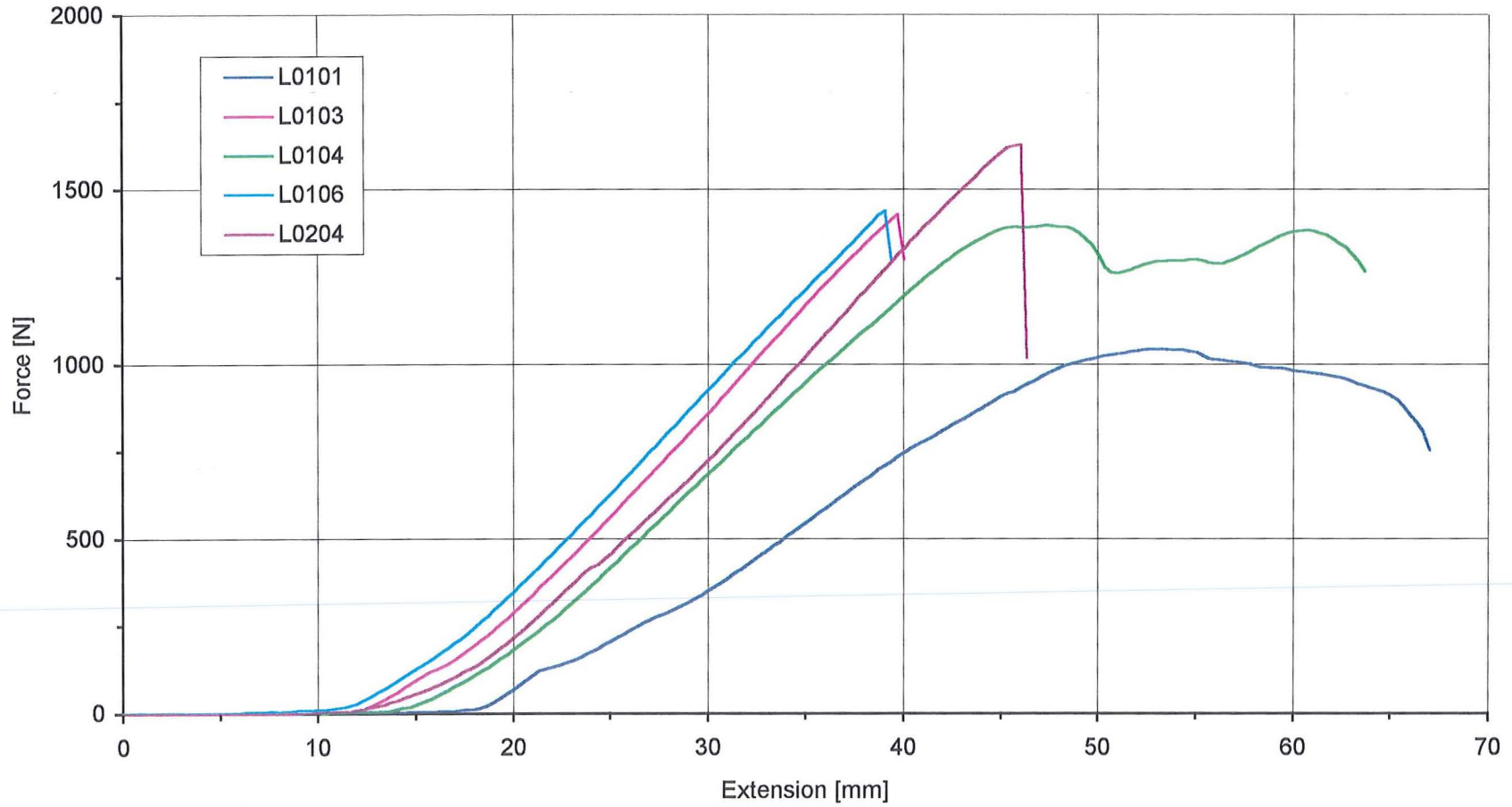


Figure 2.10. Tensile test on dumbbell shaped pig skin specimen - frozen back - longitudinal direction. Original in colour.

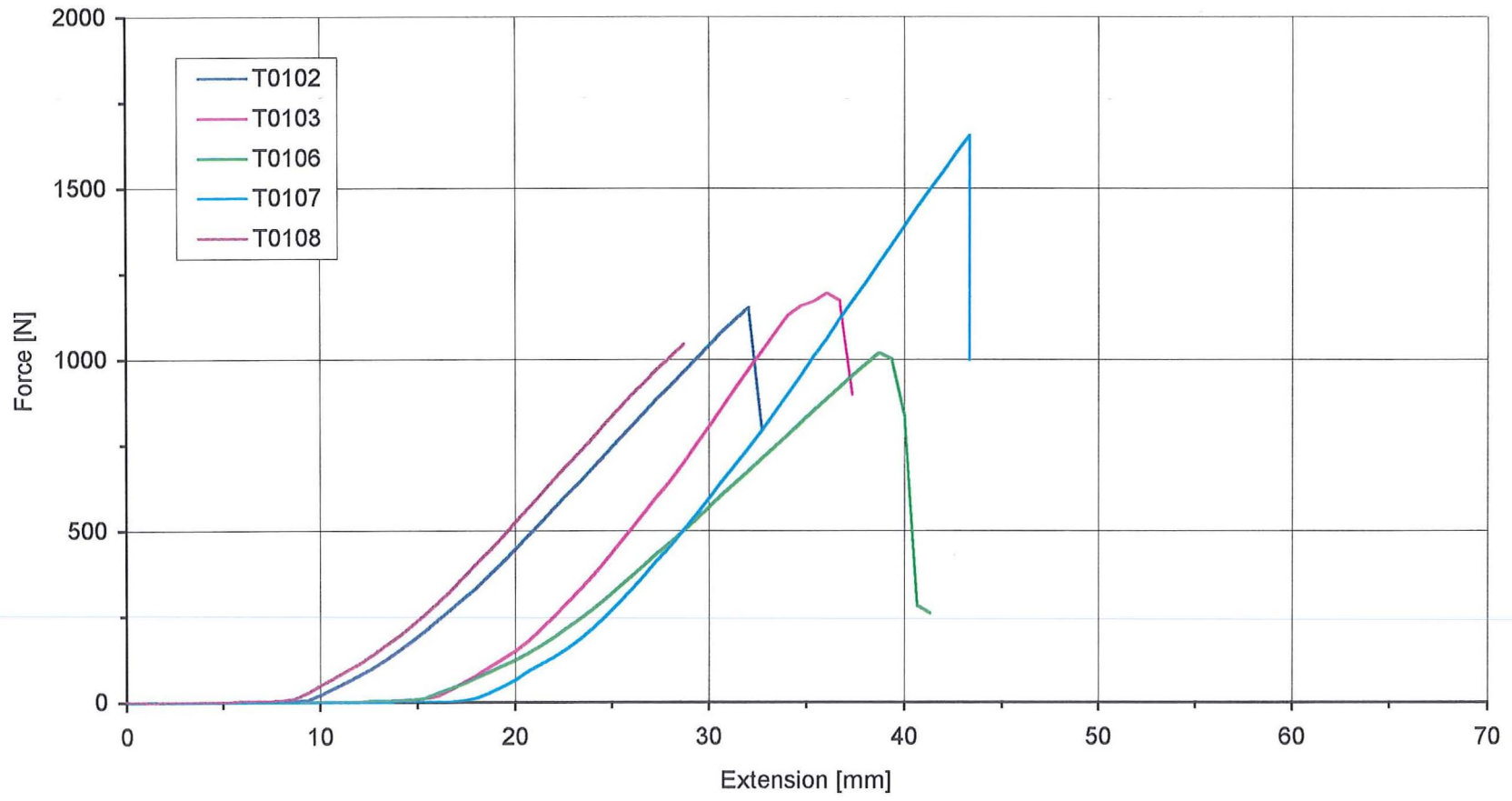


Figure 2.11. Tensile test on dumbbell shaped pig skin specimen - frozen back - transverse direction. Original in colour.

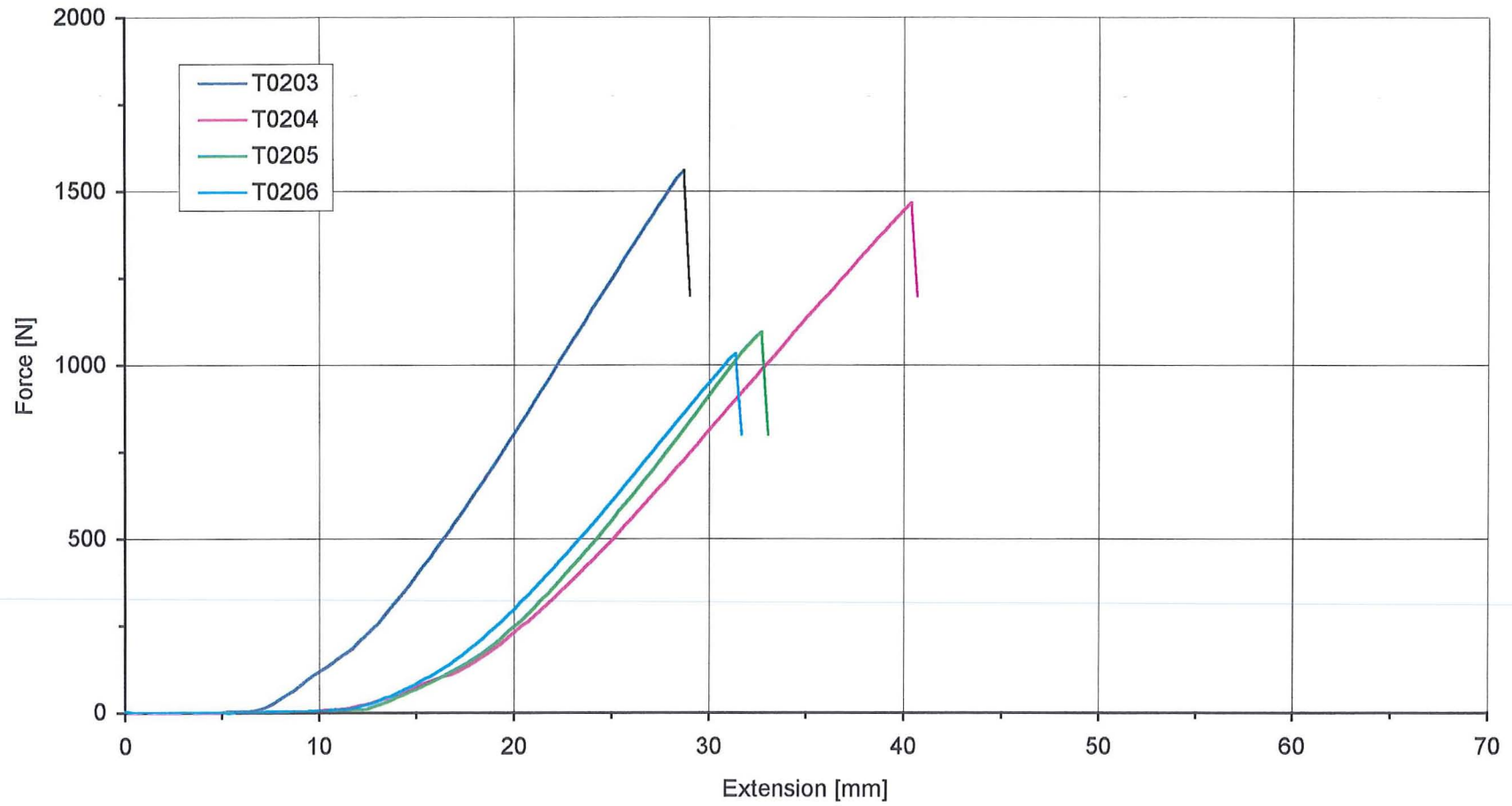


Figure 2.12. Tensile test on dumbbell shaped pig skin specimen - frozen back - transverse direction. Original in colour.

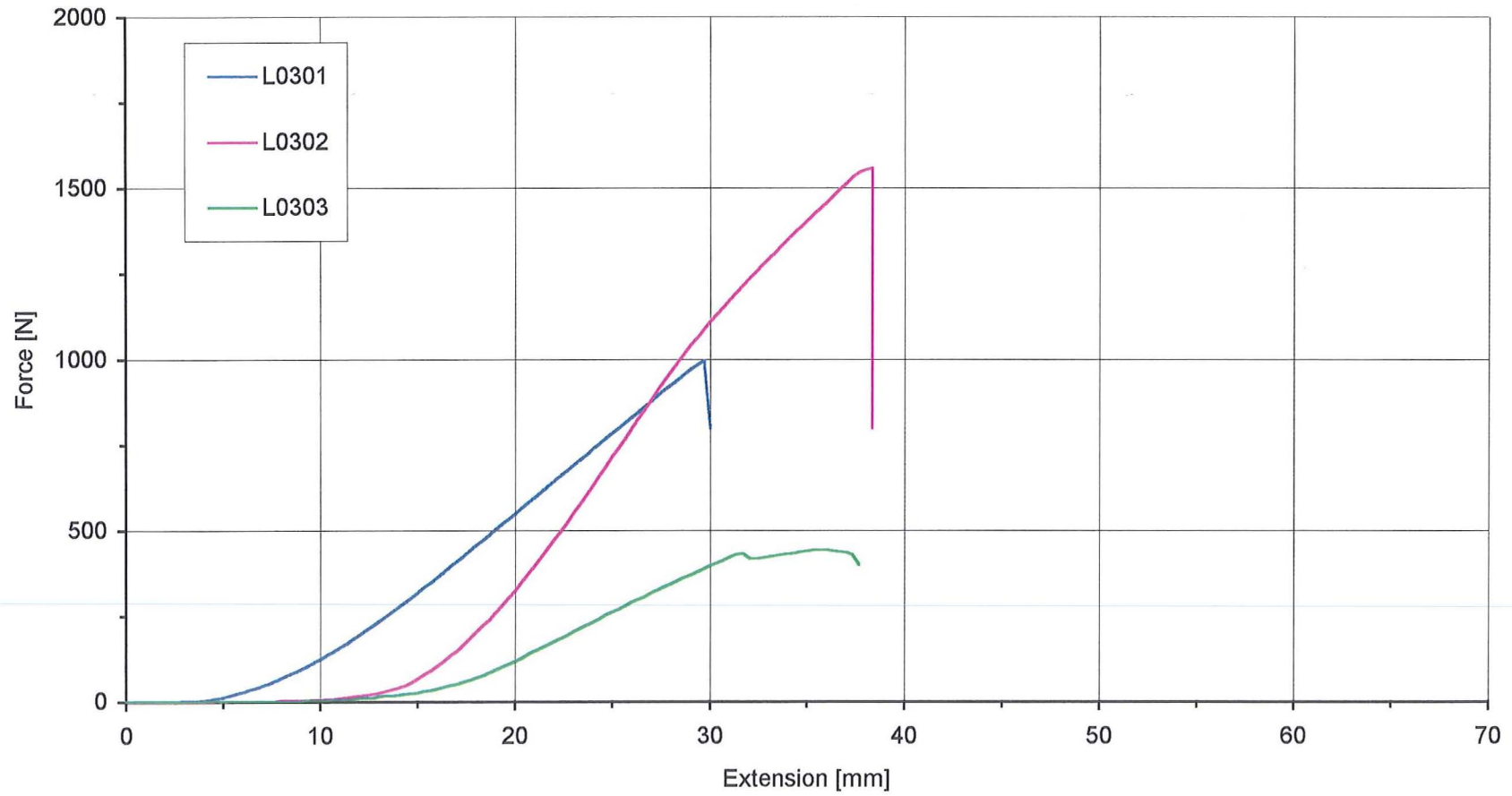


Figure 2.13. Tensile test on dumbbell shaped pig skin specimen - fresh belly - longitudinal direction. Original in colour.

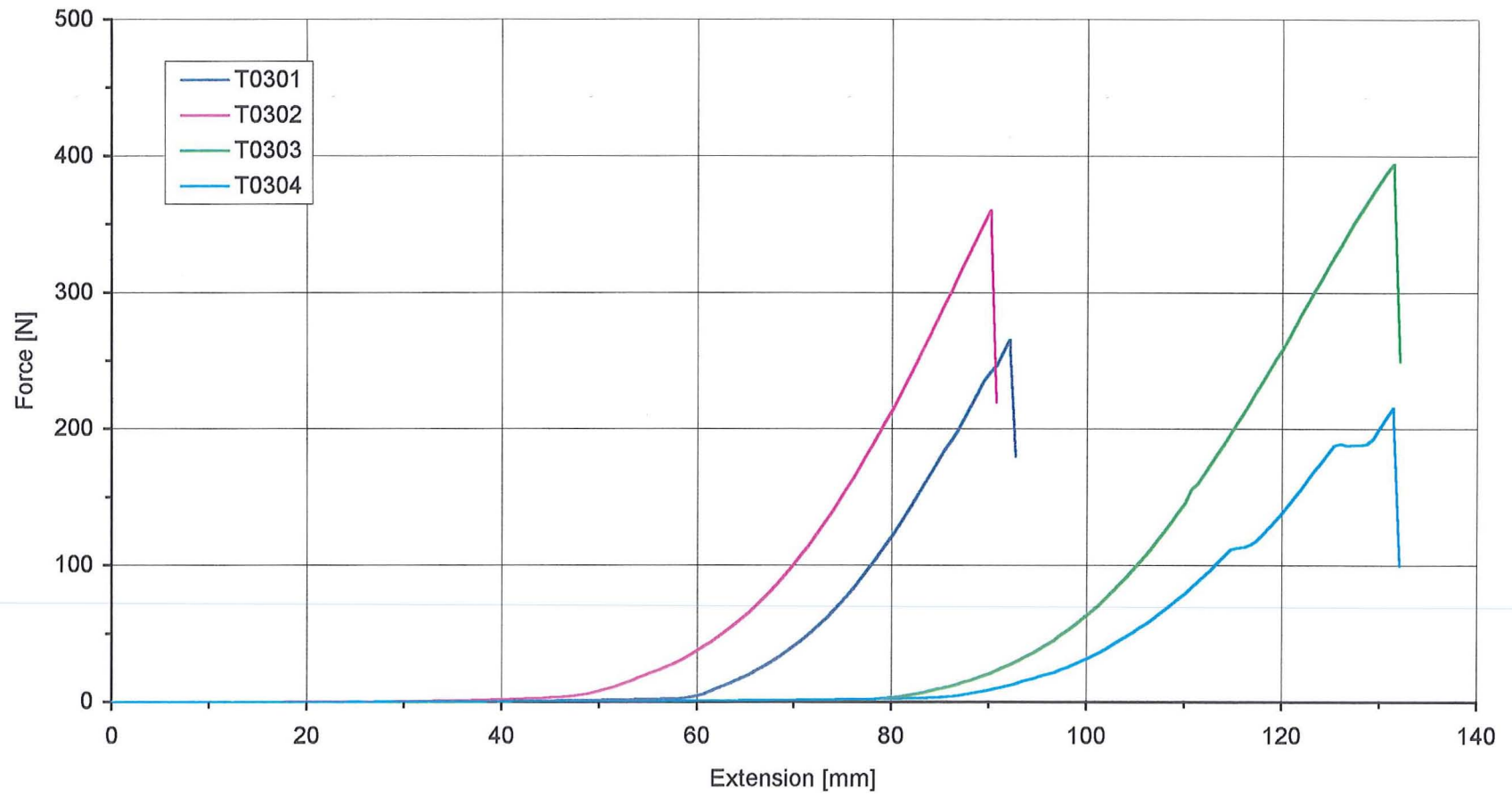


Figure 2.14. Tensile test on dumbbell shaped pig skin specimen - fresh belly - transverse direction. Original in colour.

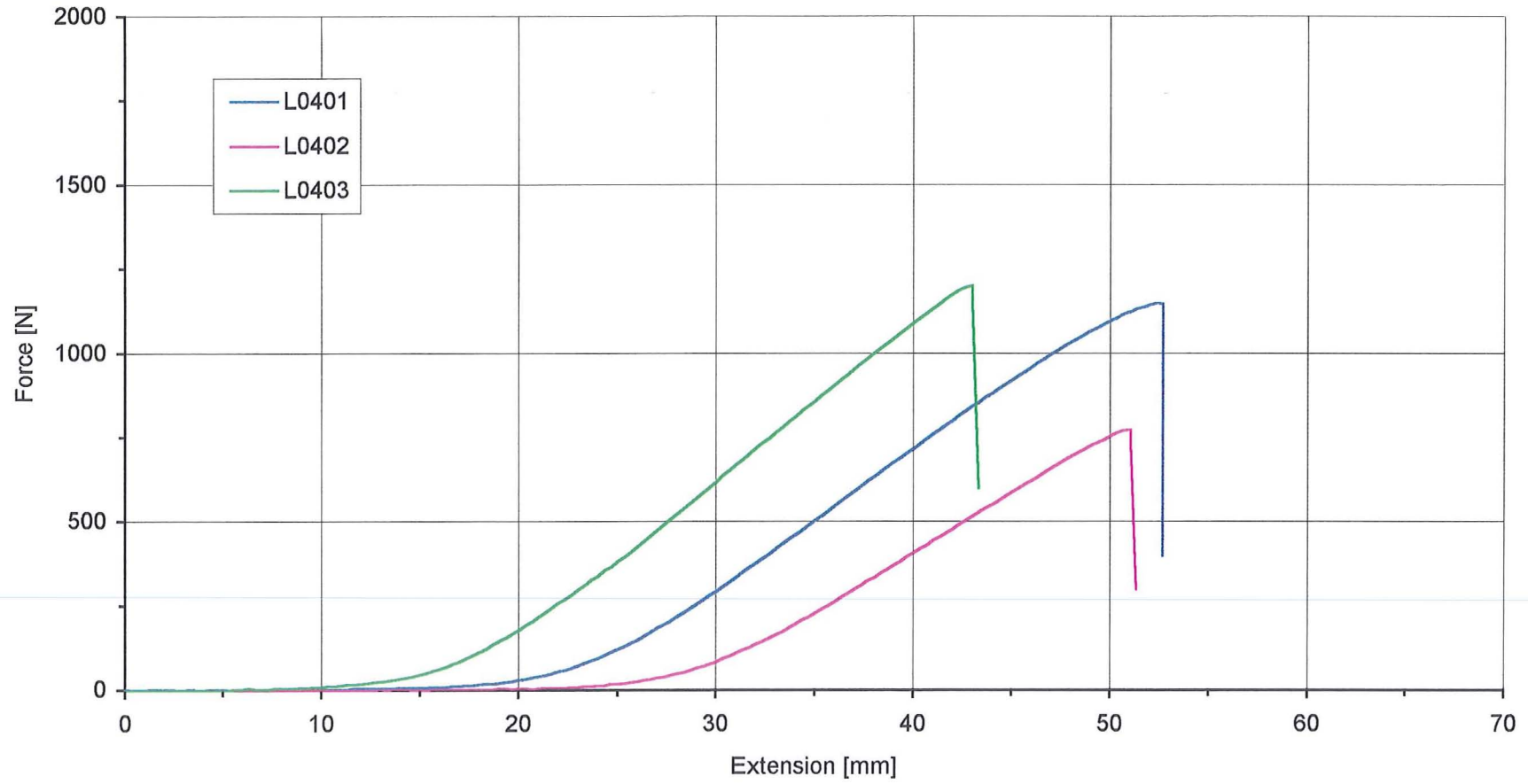


Figure 2.15. Tensile test on dumbbell shaped pig skin specimen - fresh back - longitudinal direction. Original in colour.

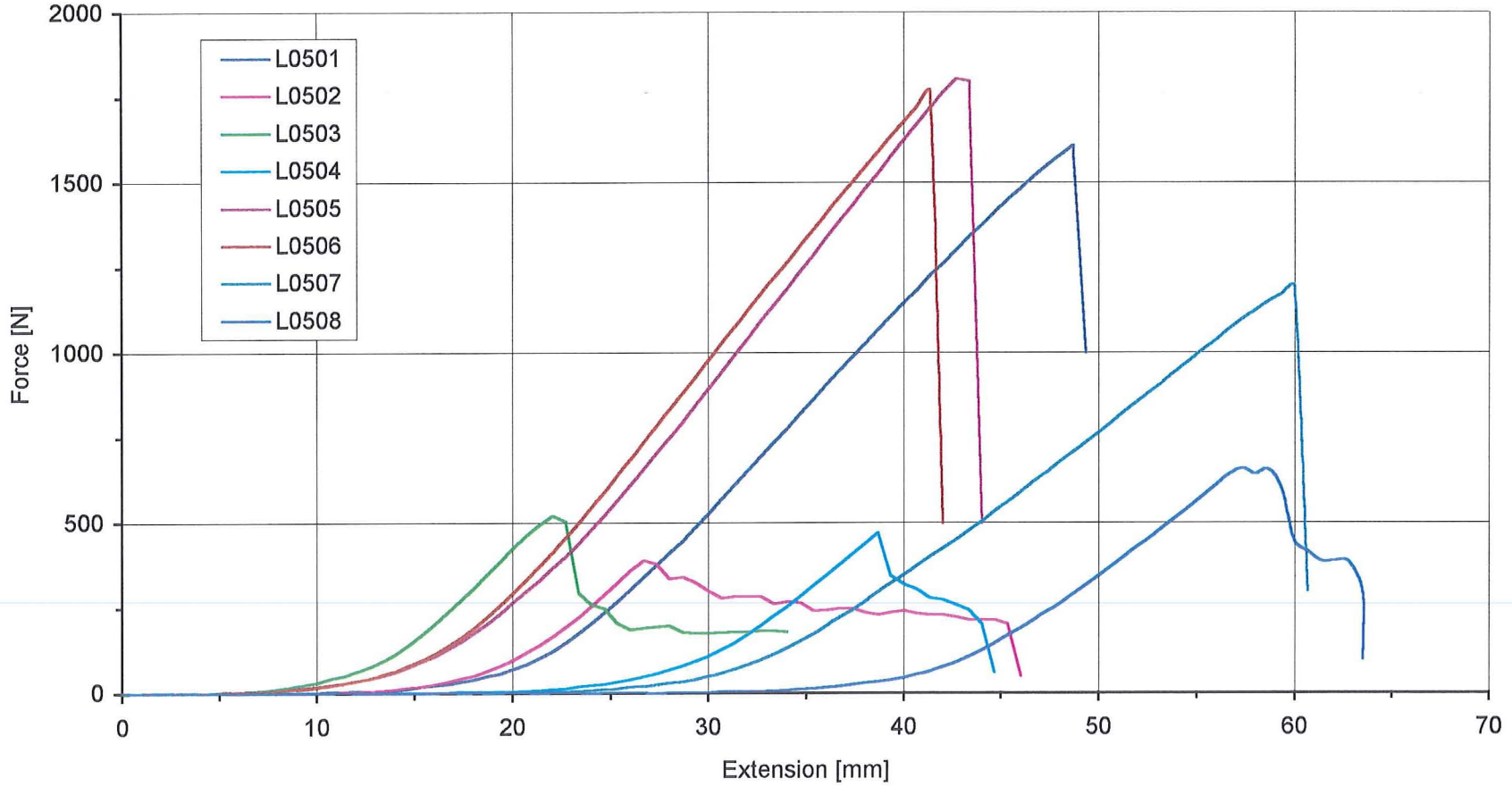


Figure 2.16. Tensile test on dumbbell shaped pig skin specimen - fresh back - longitudinal direction. Original in colour.

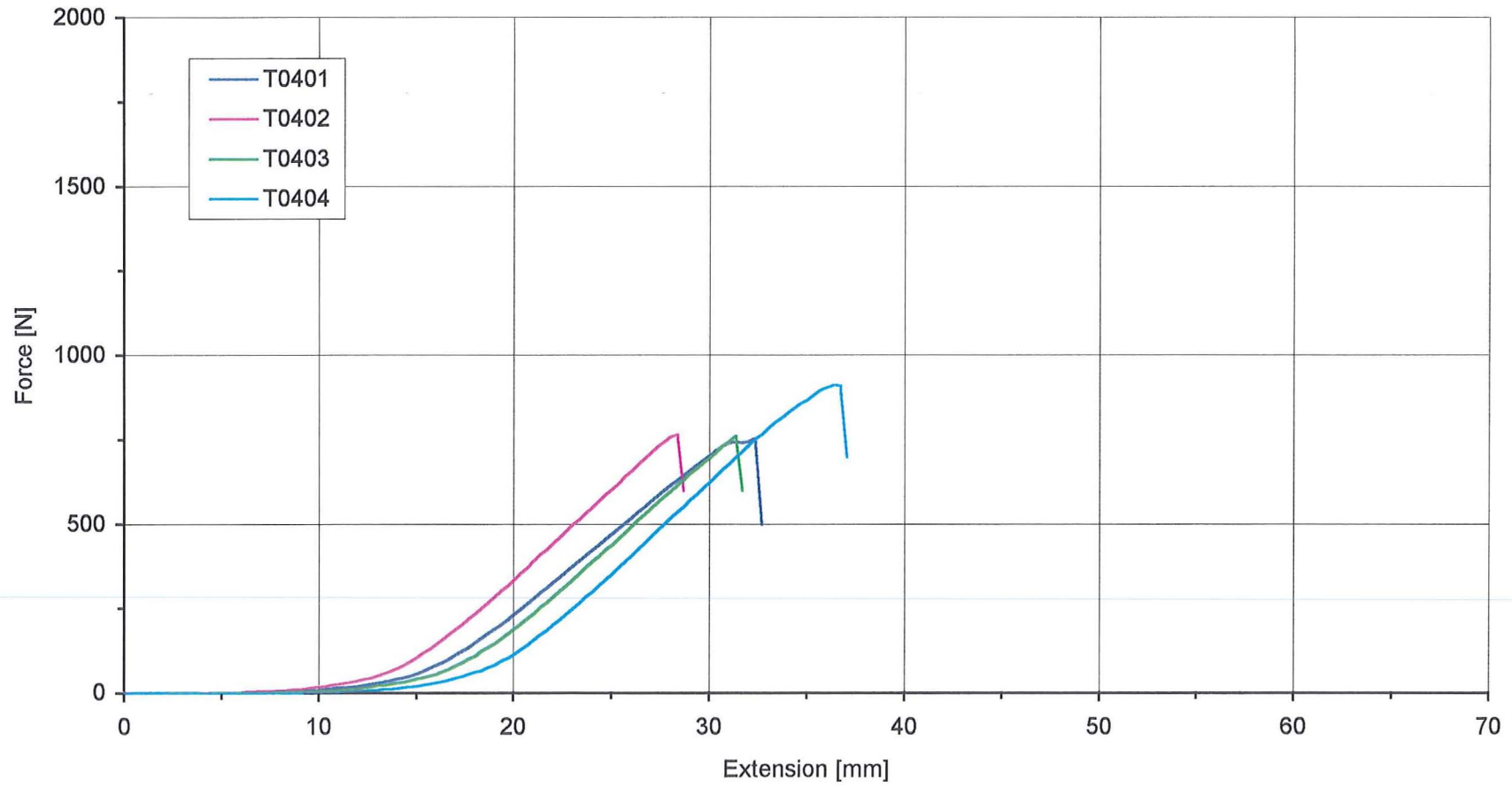


Figure 2.17. Tensile test on dumbbell shaped pig skin specimen - fresh back - transverse direction. Original in colour.

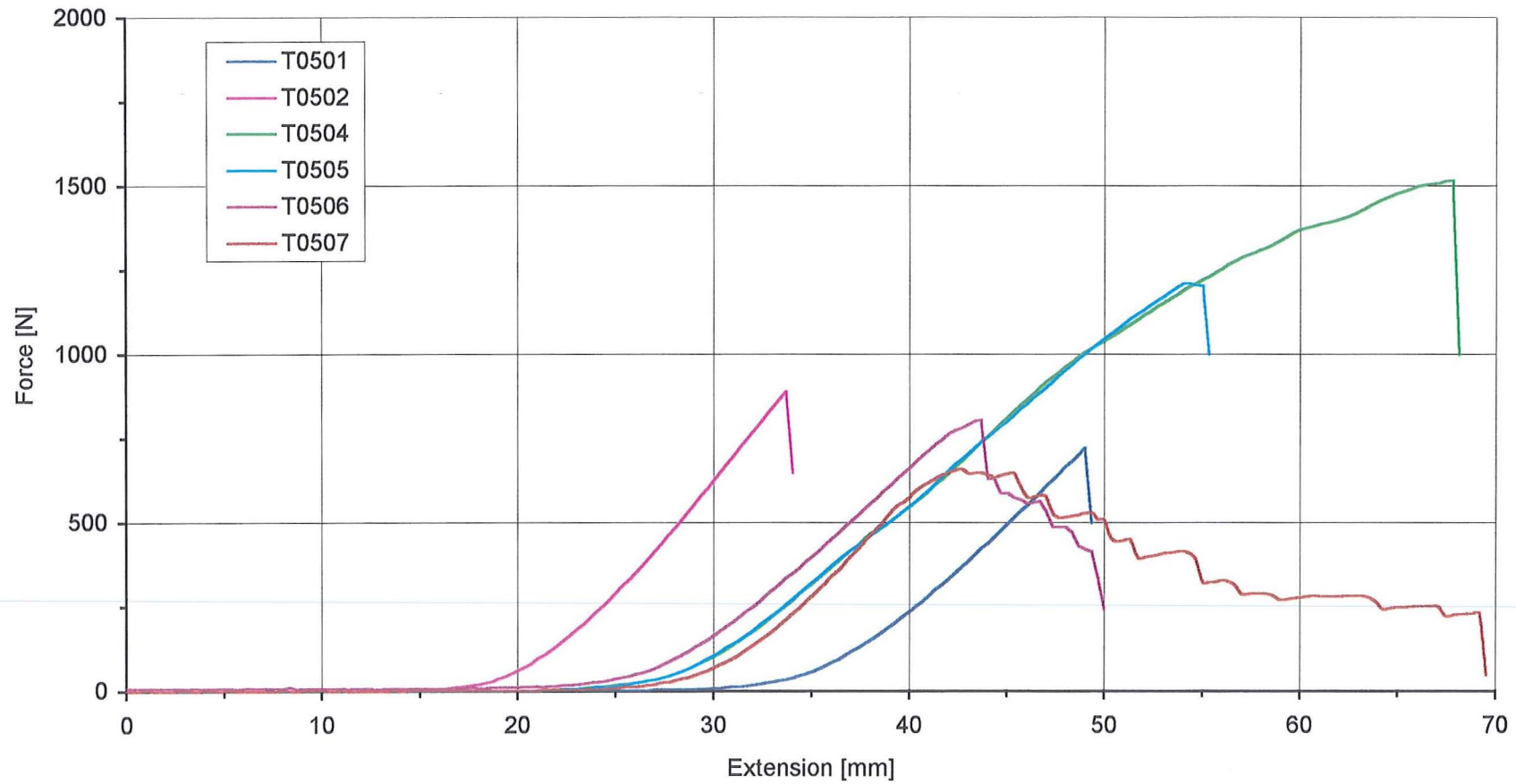


Figure 2.18. Tensile test on dumbbell shaped pig skin specimen - fresh back - transverse direction. Original in colour.

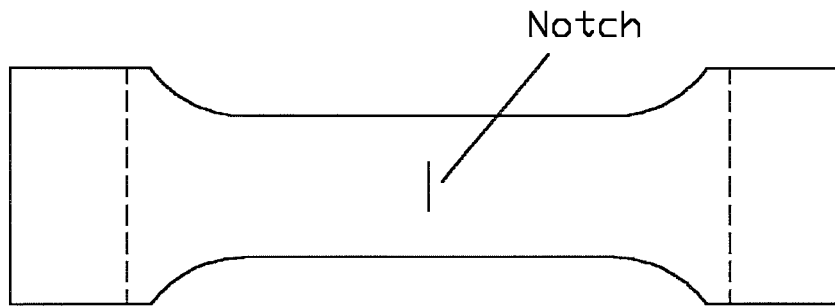


Figure 2.19 Dumbbell shaped specimen used for notch test.

### 2.3 Additional tests on selected skin simulant

Notch sensitivity tests, the response of the material to cyclic loading, and compressive loading tests in the thickness direction were also conducted but only on a small number of specimens. These tests were done to further characterise pig skin and verify the results against observations made by other investigators on real human skin.

#### 2.3.1 Notch tests

It is not yet clear whether biomaterials such as skin develop a stress or strain singularity ahead of a “crack-like” defect such as a knife incision. Certainly such materials are highly resistant to defects, as indeed their function requires. Additional work is required in this area but some indication of the ability of such materials to resist cracking may be obtained from tests on “pre-cracked” tensile specimens.

##### 2.3.1.1 Test programme

###### *Test rig*

The notch test utilised the basic tensile test apparatus.

###### *Specimen Preparation*

Tensile test specimens were prepared as described in section 2.2.1 from fresh back skin cut in the transverse direction. A straight notch was cut in the centre of the specimen perpendicular to the load direction as shown in Figure 2.19. Different sizes of notches were used to investigate notch sensitivity of pig skin.

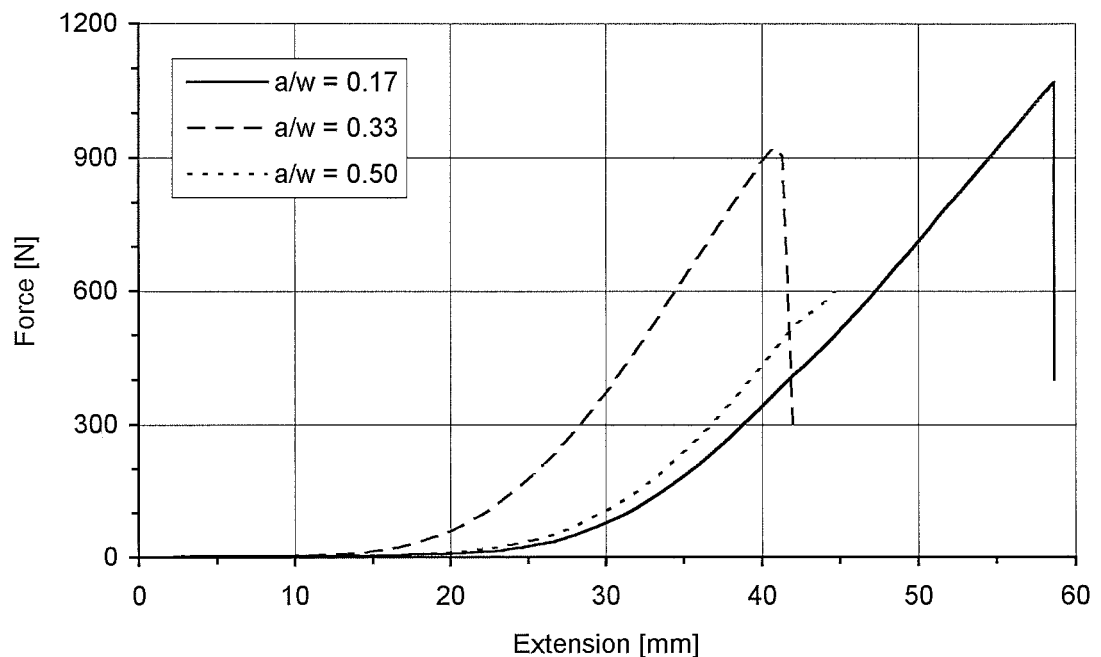


Figure 2.20. Notch test on dumbbell shaped pig skin specimen with various notch lengths. Notch length / specimen width ratio:  $a/w$ .

### *Test Protocol*

The test procedure was similar to the tensile test and an extension rate of 50 mm/min was again used here. Three specimens were tested with notch lengths of 5, 10, and 15 mm respectively. Data was stored computationally during each test.

### **2.3.1.2 Results and evaluation**

Force-extension curves obtained from notched tensile specimens are shown in Figure 2.20. The specimen with a notch length of 5 mm (notch-width ratio 0.17) failed at the transition between the narrow gauge section and the wider gripping area which indicates that the natural material defects play the greatest role at this notch size. Had the specimen been without any imperfections it would have failed at the notch where the cross-section is smallest. At a notch length of 10 mm (notch-width ratio 0.33) the specimen failed at the notch but still at a relatively high load. The largest notch of 15 mm (notch-width ratio 0.50) caused the specimen to fail at a reduced load. These results are based on single specimens and should therefore only be regarded as a general observation with some uncertainty as to the actual values. Nominal failure stresses calculated for the minimum cross-section at the notch are given in Table 2.3. These

stress values are based on an initial specimen width of 30 mm and a thickness of 2 mm. It should be noted that the failure stress for a notch-width ratio of 0.17 would have been slightly higher had the specimen failed at the notch as intended. Only a small reduction in failure stress could be observed in the notched specimens which indicates that stress is not raised significantly by the presence of a crack. This is supported by Atkins and Mai (1988) who state that most animal tissues are exceptionally resistant to cracking. The question is then why most of the tensile specimens failed at the transition between the waisted section and the gripping area. A possible answer could be that since skin is a fibrous material the loadbearing capacity will be practically unchanged at the necked section of the specimen under load. The geometric stress concentration caused by the transition will then have the final say in where the specimen fails. It is probably wrong to claim that skin is totally insensitive to stress concentrations, however, it seems that a highly flexible fibrous material such as skin is able to relocate the stress around a crack causing it to be of minimal notch sensitivity.

Notch-width ratio	Failure stress [MPa]
0.17	21
0.33	23
0.50	20

Table 2.3. Nominal failure stress for notched specimens.

### 2.3.2 The effect of cyclic loading

A single load/unload cycle will show the extent of hysteresis and a multi-cycle test was intended to verify so-called “conditioning” of the pig skin. This describes the tendency of the hysteresis loops to converge to a single attractor and has been reported by a number of authors as a feature of human skin (Cordio (1996), Peura (1993), Schneider (1982)).

### 2.3.2.1 Test programme

#### *Test rig*

The cyclic loading test was performed in a similar way to the uniaxial tensile test but with the machine set to perform cyclic load-unload paths.

#### *Specimen Preparation*

Tensile test specimens are used for the cyclic loading tests and were prepared as described in section 2.2.1. Fresh back skin cut in the transverse direction was exclusively used for cyclic loading.

#### *Test Protocol*

As before the specimen was inserted in the upper grips and the screws tightened. With the specimen hanging from the upper grips, the cross-head height was adjusted until the specimen was correctly positioned in the lower grips. The lower screws were then tightened. The single cycle test was conducted by extending the specimen at a constant extension rate of 10 mm/min until a load of 400 N was reached whereafter the cross-head returned to its original position also at 10 mm/min. The multi-cycle test was a x5 repetition of the single cycle, without any hold time between cycles. One single cycle test and one multi-cycle test was performed.

### 2.3.2.2 Results and evaluation

The mechanical response of pig skin to a single loading / unloading cycle is shown in Figure 2.21. The specimen was loaded to 400 N and unloaded immediately after with no hold-time. Curve 1 shows the typical response of skin to tensile loading and curve 2 shows the unloading response. It is clear that the unloading is not the reverse of the loading path which indicates the presence of hysteresis in pig skin.

Results from the multi-cycle test are shown in Figure 2.22. 5 loading / unloading cycles were imposed on the specimen, each cycle reaching a load of 400 N. The first cycle shows a degree of hysteresis which becomes less as the number of cycles increases. Cycles 4 and 5 have almost identical loading and unloading paths. At this stage the material is said to be “pseudo-elastic” which implies that practically all the elastic energy stored in the specimen under elongation is recovered when unloaded.

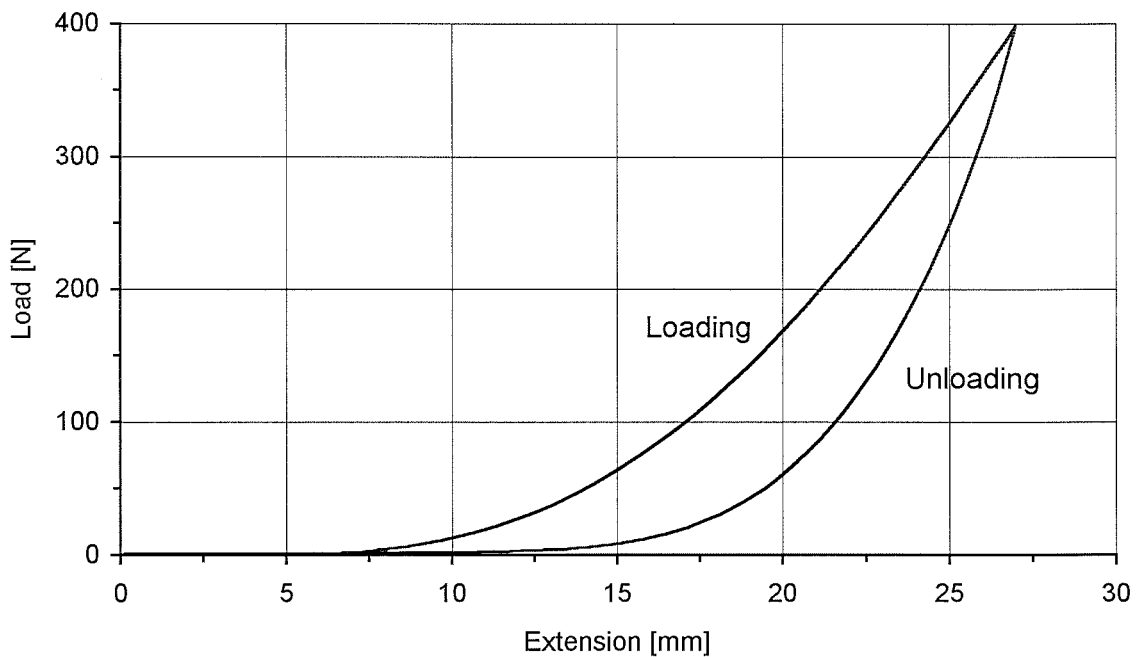


Figure 2.21. Load-extension response of pig skin under cyclic loading (single cycle).

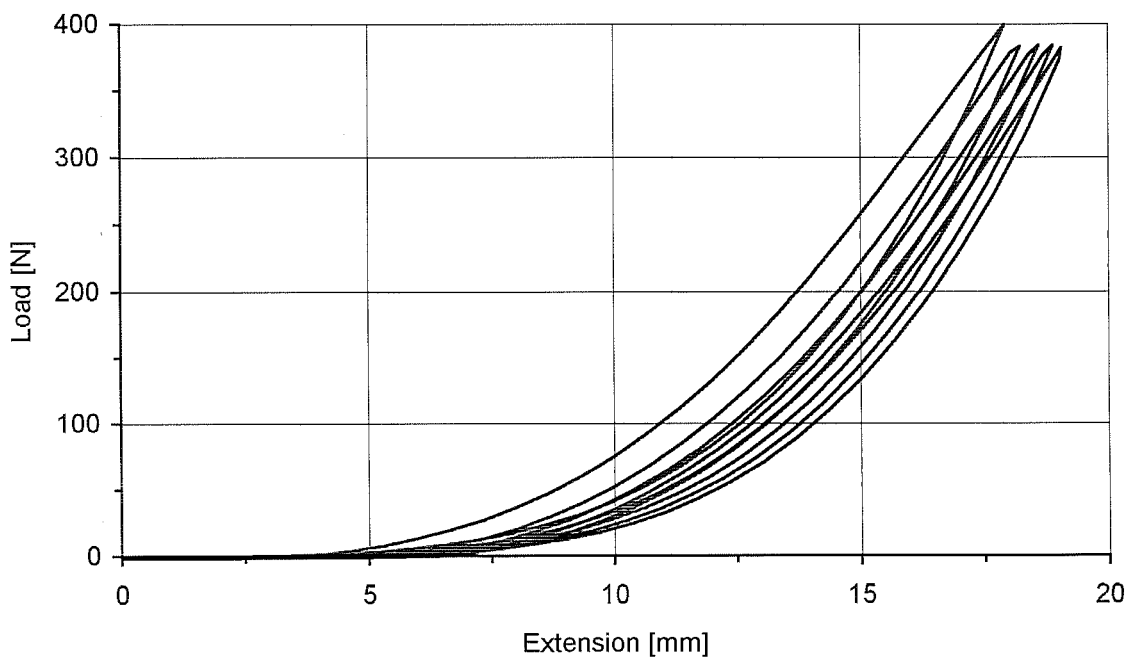


Figure 2.22. Load-extension response of pig skin under cyclic loading (5 cycles).

### 2.3.3 Through-thickness compression test

Through-thickness effects are largely ignored in the study of flexible membranes and in the case of a biomaterial such as skin no data were found on through-thickness mechanical properties. Tests were done on pig skin where results were needed for further characterization of this material and also for determining the constitutive material model used in computational modelling described in the following chapters.

#### 2.3.3.1 Test programme

##### *Test rig*

The compression test was conducted in the Lloyd Universal testing Machine by placing the pig skin specimen on a plane steel plate and applying a compressive load through a circular flat ended steel rod attached to the cross-head. Two sizes of compressors were used; 13 mm and 28 mm diameter. Engineering stress rather than true stress can be evaluated since the compressor was kept smaller than the specimen measures thus the compressed area was constant.

##### *Specimen Preparation*

Specimens were prepared as described in section 2.2.1 but were cut into a 30 x 30 mm square shape. Only fresh back skin was used for the compression test.

##### *Test Protocol*

The specimen was placed on a thick steel compression platen supported on the lower (fixed) cross-bar of the test machine. The upper platen was attached to the cross-head which was adjusted until the compressor just touched the specimen. The machine was programmed to a cross-head speed of 1 mm/min until a load of 7500 N was recorded on the 13 mm compressor. Using a new specimen the 28 mm compressor was loaded to 800 N also at 1 mm/min. The high load was applied via a 30 kN load cell to the small compression area to observe the behaviour under high stress and possible reach a yield or failure point of the pig skin. The low load was applied via a 1 kN load cell to the large compression area to obtain more accurate readings at low strains. After the maximum prescribed load was reached the cross-head returned to its initial position.

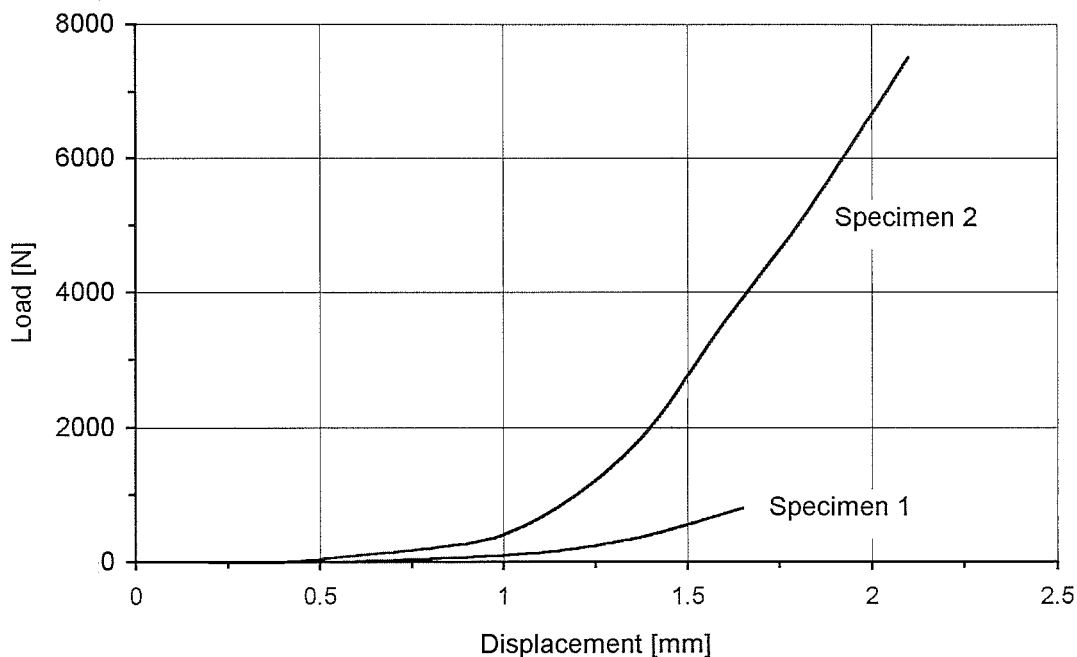


Figure 2.23. Load-displacement curves obtained for pig skin under compressive load.

### 2.3.3.2 Results and evaluation

Figure 2.23 shows the force-displacement curves obtained for pig skin under compressive load. Specimen 1 was tested by the 28 mm diameter compressor up to 800 N load and showed no visual permanent deformation after the pressure was released. Specimen 2 was tested by the 13 mm diameter compressor up to 7500 N load and due to the higher load, permanent deformation was evident after unloading. In general, the compressive behaviour of pig skin is very similar to its tensile behaviour, with initially large deformations taking place under little load. After a certain point, nearly linear stress-strain response is observed. No catastrophic failure was observed during the compression tests but it is likely that damage to the micro-structure of the skin occurred, especially for specimen 2. Fluid was expressed from both specimens during testing.

### 3 Stab-penetration test using sharp blades

The stab-penetration test is a highly simplified and idealised model of a real stabbing incident. An isolated system in the form of a target block representing a section of the whole human body will yield more consistent and hence comparative results, although the absolute values obtained might not exactly match those obtained from whole cadaver experiments. In the test a knife moving at relatively low velocity penetrates the target block. Although simple, this model enables the study of the effect of knife blade geometry on different types of target simulants.

While the main focus of this phase of the current work is to select a skin simulant, attention must also be given to the underlying material. Two prospective flesh simulants were tested. The first, Roma Plastilina, is a modelling clay used by the Home Office's Police Scientific Development Branch (Parker (1993)) as a witness and backing material in stab resistant body armour tests. This test involves projecting a knife from a gas gun towards the candidate armour and the modelling clay. The assumption is that the penetration depth of the knife is proportional to its initial kinetic energy. This is highly questionable and in particular it does not simulate what the author believes to be a common, quasi-static mode of attack in which the knife continues to be pushed into the victim well after initial penetration has occurred. In this case the knife continues to receive energy and momentum during the attack, in contrast to a projectile. The effect of skin is also absent from the PSDB test.

The second material tested was gelatine which is most conveniently available as domestic dessert jelly. This gelatine is used as a substitute for 10% ballistic gelatine which has been shown by Jason and Fackler (1990) to have a similar response to bullet penetration as pig leg muscle.

#### 3.1 Experimental programme

##### *Test rig*

The flesh simulant was placed in an open plastic container which measures 100 x 45 x 65 mm (length x width x height). The skin simulant was fixed against the top edges of the plastic container by a securing plate with a rectangular hole for the penetrators as shown in Figure 3.1. This securing plate has the secondary function of holding down the

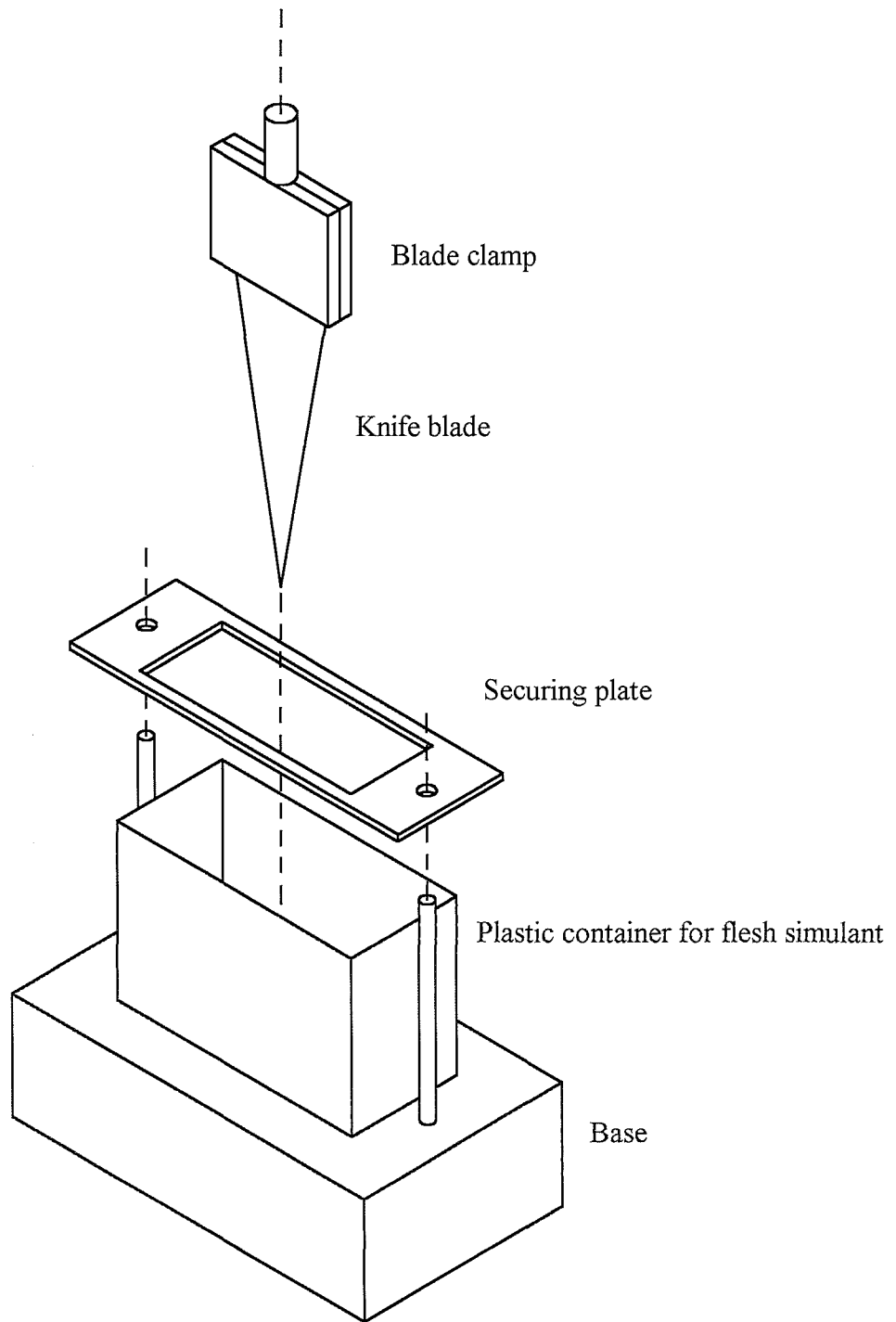


Figure 3.1. Test set-up for pilot stab-penetration test.

container while the penetrator is withdrawn from the target block.

The knives specified in PSDB 10/93 (Parker (1993)) are proprietary blades with the generic features of the Bowie knife. The Bowie knife is however a multi-purpose hunting tool, with only one edge sharpened along its full length. This edge is convex towards the blade tip. The other edge is sharpened along part of its length into a concave profile designed for skinning animals. The remainder of this edge, towards the handle, is blunted to allow hand pressure to be applied for heavier cutting tasks. The Bowie knife is then not particularly typical of the weapons, often bread knives, most frequently used in criminal attacks. Its asymmetric features also make it unnecessarily complex for either experimental testing (it is, for example, awkward to sharpen) or for simple computational modelling.

A number of simplified model blades were therefore devised as shown in Appendix 4. These were ground from high-quality steel strip, readily available in the engineering laboratory as power-hacksaw blades. The profiles were designed to highlight any effect of the sharpness of the blade tip and edge. The knife blade was held in a blade clamp (Figure 3.1) and attached to the cross-head of the Lloyd Universal Testing Machine via an adaptor.

### *Specimen Preparation*

For the stab-penetration tests, both skin simulants were prepared as described in section 2.1.1 but were cut into rectangular pieces slightly larger than the area of the plastic container (100 x 45 mm). The Roma Plastilina was prepared in two ways: a block of the as-received material was tested at room temperature while other blocks were softened (and slightly heated) by hand working and moulded into the container.

Gelatine was prepared by adding 50 ml of warm water to a 142 g pack of dessert jelly, this mix being chosen to give, on solidifying, a firm consistency typical of ballistic gelatine. The solution was poured into the plastic container and left to set.

### *Test Protocol*

The stab-penetration test was conducted on skin and flesh simulant alone and on combinations which included both. Roma Plastilina was tested alone in three ways:

- 1) in the unmoulded state
- 2) in the unmoulded state with a lubricant on the knife blade to simulate effects of body fluids
- 3) in a softened and moulded state.

In the lubricated case each knife blade was covered with Deb “Tufanega”, a type of handcleaner. Pig skin was not tested with all of the blade types but the other simulants were tested with all of the standard blades as shown in Table 3.1. The test procedure included fixing the plastic container containing the target simulant(s) under the securing plate (Figure 3.1). The knife blade was then mounted in the blade clamp and the cross-head brought down such that the blade tip was just above the target simulant. The knife blade was forced into the target simulant at a constant velocity of 8 mm/s to a depth of 45 mm, after which it was withdrawn at the same velocity. The maximum penetration force and the maximum withdrawal force was recorded for all the tests. The full force-displacement curve was also recorded for the pig skin and synthetic chamois alone.

Simulant	Blades	Remarks
Roma Plastilina	All	
Roma Plastilina	All	Lubricated
Roma Plastilina	All	Softened
Gelatine	All	
Gelatine+Chamois	All	
Chamois	3B	
Pig skin	3B	

Table 3.1. Target simulants subjected to stab-penetration test.

Sensitivity to velocity and repeatability was tested using blade 3B and moulded roma-plastilina only. Three repetitions of the stab-penetration test as described above was performed at different velocities (2 mm/s, 4 mm/s, and 8 mm/s). The full force-displacement curve was recorded both during entry and withdrawal of the knife blade.

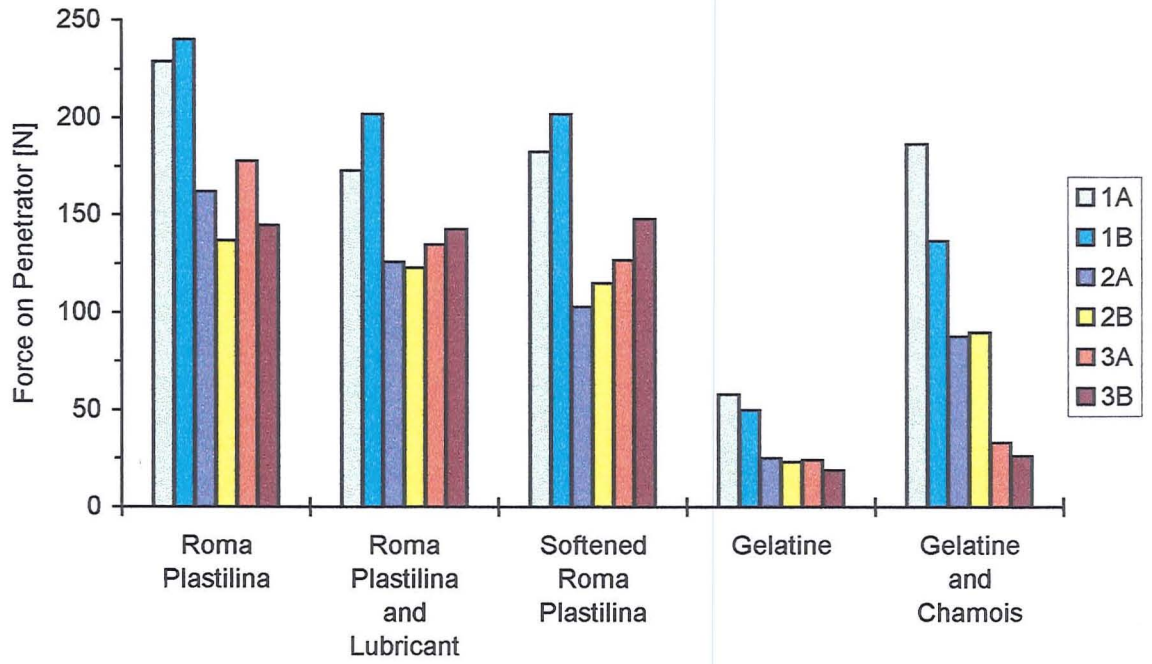


Figure 3.2. Maximum entry forces on standard knife blades for various target simulants. Original in colour.

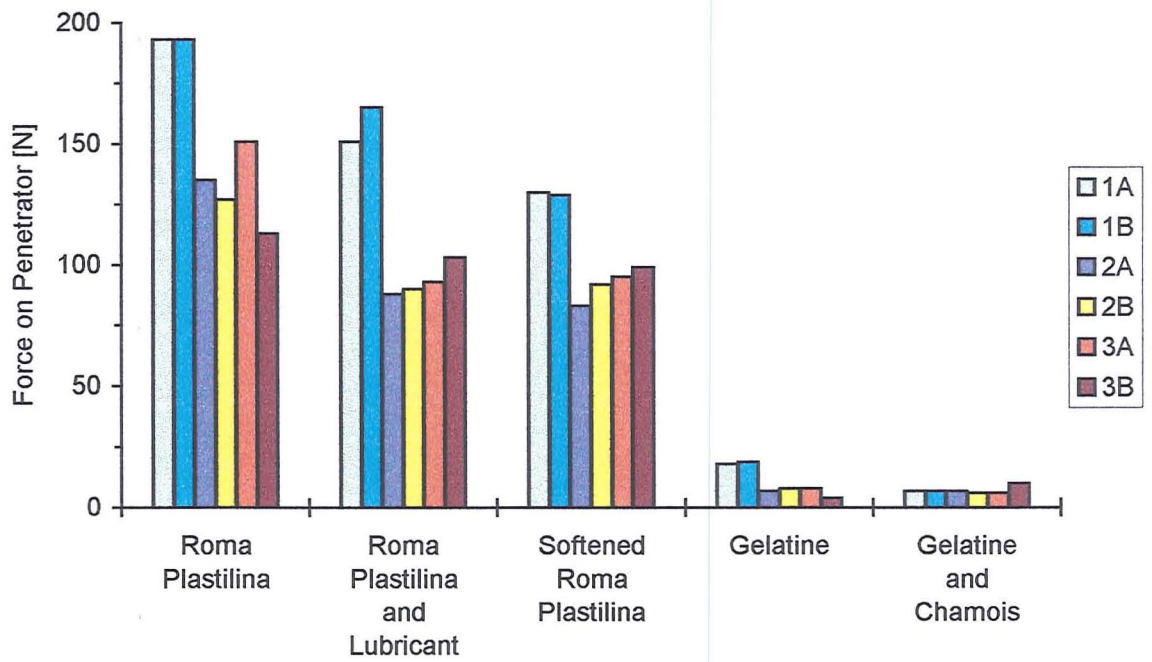


Figure 3.3. Maximum withdrawal forces on standard knife blades for various target simulants. Original in colour.

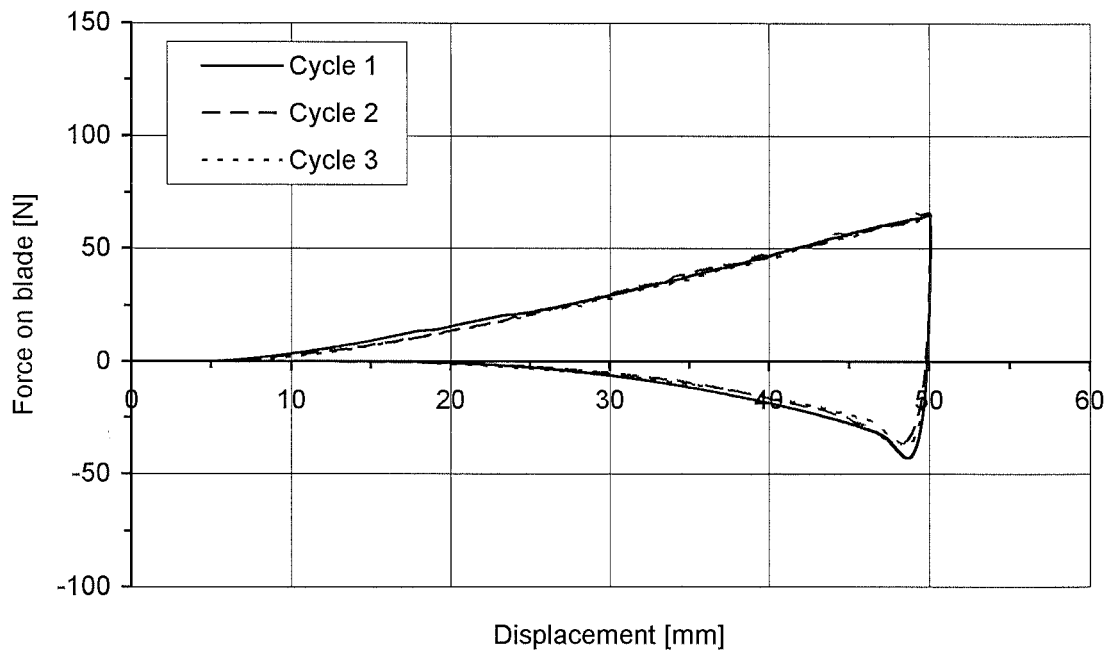


Figure 3.4. Entry and withdrawal force on blade 3B at 2 mm/s. Three repetitions on Roma Plastilina.

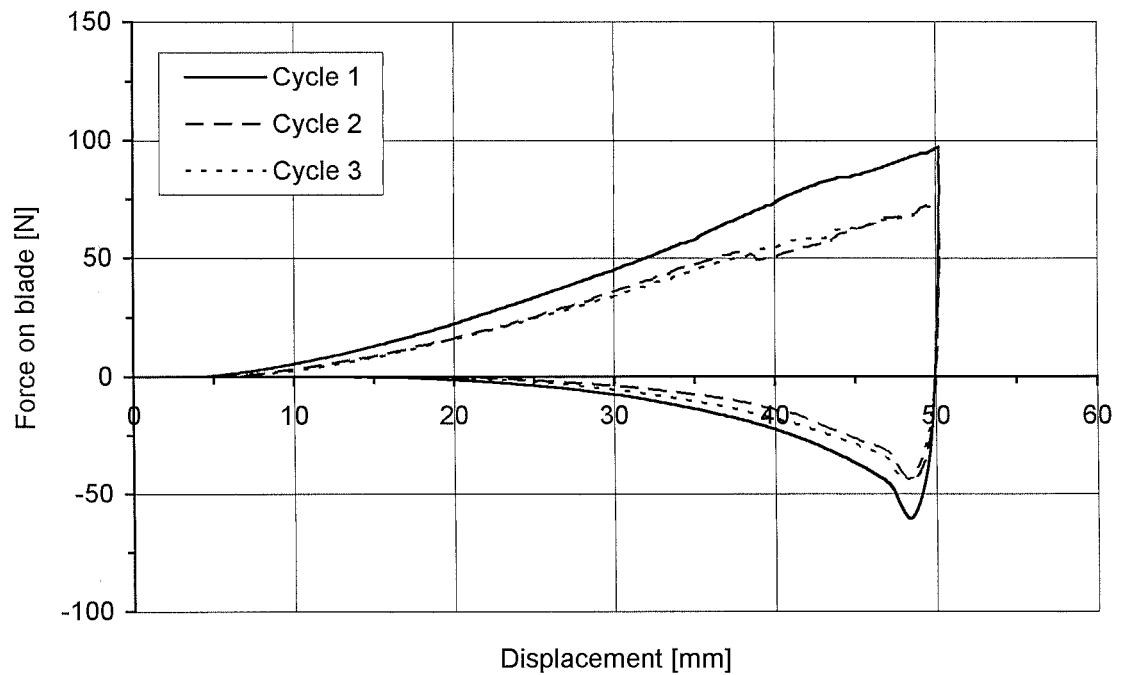


Figure 3.5. Entry and withdrawal force on blade 3B at 4 mm/s. Three repetitions on Roma Plastilina.

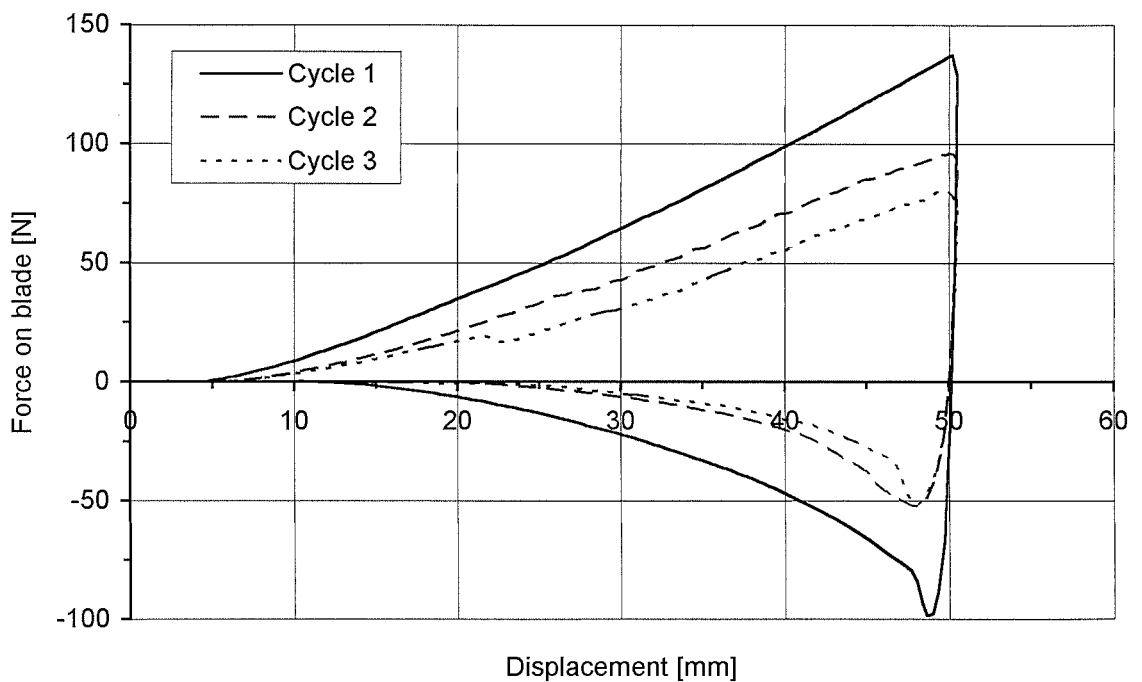


Figure 3.6. Entry and withdrawal force on blade 3B at 8 mm/s. Three repetitions on Roma Plastilina.

### 3.1.1 Results and evaluation

The results from those stab-penetration test which included all of the blades are shown in Figure 3.2. This gives the maximum penetration force measured on the knife blade as it enters the target simulant. Figure 3.3 gives the corresponding maximum force on the knife blade as it was withdrawn from the target.

Most of the results are in accord with both intuition and with Knight (1975) insofar as sharper blades require less force to penetrate the target. Lubricated Roma Plastilina yields slightly lower forces and it seems that softening and moulding has almost the same effect as lubrication. Yet the results for the three variants of Roma Plastilina were somewhat contradictory with the forces being higher for blades eg 1B with a pointed tip than for blades eg 1A with a blunt tip. The withdrawal forces for Roma Plastilina produced a similar pattern but with slightly lower forces. This might indicate that the main work exerted on the knife blade is due to friction both during entry and withdrawal. A reason for blunt tipped blades showing lower forces than blades with pointed tip could be that a “bow wave” of plastic clay, which fails to re-bond to the blade, is pushed aside during penetration by the blunt tip.

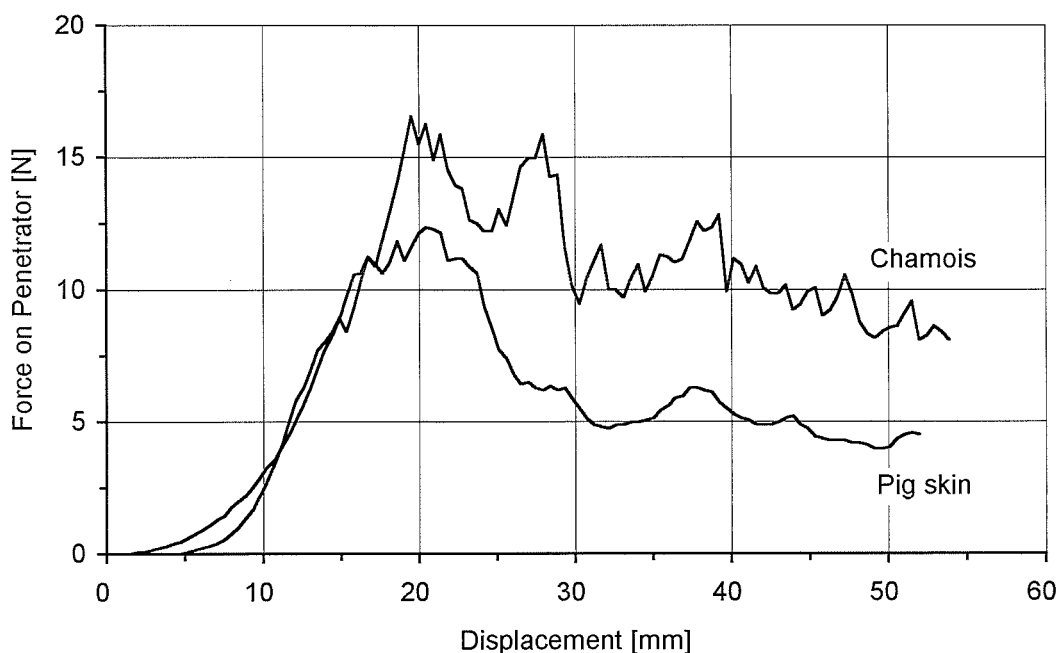


Figure 3.7. Pilot stab-penetration test on pig skin and chamois using knife blade 3B.

Entry and withdrawal forces for blade 3B at different velocities are shown in Figure 3.4 to Figure 3.6. The forces are dependent on the velocity as the maximum force consistently increase from 60 N at 2 mm/s to above 100 N at 8 mm/s. The repeatability is good at 2 mm/s but seems to deteriorate at higher velocities.

Gelatine alone shows much lower entry forces than Roma Plastilina and there is better intuitive agreement between blade type and force. Withdrawal forces are also lower than entry forces for gelatine. This tends to imply that the resistive force arises from material deformation and flow rather than friction as seems the case for Roma Plastilina. Gelatine covered with synthetic chamois shows a high and consistent dependence on blade type in which tip radius appears to play a significant role. Withdrawal forces are, as expected, not affected by the chamois layer.

A force-displacement curve was recorded for synthetic chamois and pig skin alone using blade 3B (pointed tip and sharp edges). These curves are shown in Figure 3.7. An important observation here is that chamois and pig skin performed almost equally well during the stab-penetration test where these two materials have been found to have quite different tensile strengths as described in section 2.1.1. An explanation could be that during initial penetration by a sharp pointed object the fibres are cut one at a time

and so the effects of fibre thickness and mesh density are minimised. In contrast, since pig skin has a much finer and more complex fibre mesh than chamois, one might expect the pig skin to perform better under tensile load.

### 3.2 Computational simulation

Computational simulation of the penetration of a deformable body is still at the limit of possibility and such analysis is by no means routine. The most appropriate technique for penetration analysis is currently the finite element method outlined in section 1.3 and while this is a well established method of structural analysis, particular difficulties are to be expected in the current work in the formulation of a material constitutive model for the target and in admitting penetration via element erosion or other means.

The finite element suite chosen for the analysis was Abaqus/Explicit, a commercial package specifically profiled for the nonlinear analysis of large deformation and contact/impact problems. An explicit integration method is used in which the field variables are updated in small enough time increments to allow piece-wise linear integration. The time increment is, by default, determined automatically in version 5.5, version 5.6, and version 5.7 used in the present work. Time incrementation is based on the eigenvalue of the entire model or the dilatational wave speed given as:

$$c_d = \sqrt{\frac{\lambda + 2\mu}{\rho}} \quad (5)$$

where  $\lambda$  and  $\mu$  are Lamé's constants and  $\rho$  is the density of the material (Abaqus Theory section 2.4.5). In version 5.6 and version 5.7 the time increment can also be controlled directly by the user. An event is analysed over a user-defined total time and so the CPU time is largely dependent on the number of time increments necessary to complete the event. Material properties such as density and stiffness affect the eigenvalue (or wave speed) as seen in equation (5) and thereby processing time. Lamé's constants represent the material stiffness thus a soft high density material will cause a low dilatational wave speed allowing large time increments thus lowering the processing time. A common way of lowering processing time is to artificially increase material density. However this stratagem is limited to quasi-static analyses where inertia and hence density do not

enter into the equation. The most important processing time factor is the number of elements in the model. Accuracy of the analysis is usually highly dependent on the number of elements or mesh refinement and, as in many other matters, time consumption and accuracy are compromising factors.

Abaqus takes a user-defined file as input. This input “deck” contains all of the so-called “model” information which includes geometry, material properties and boundary conditions which do not change during the analysis. This deck also contains “history” data which defines what is to happen to the model, eg the type of analysis (static, transient dynamic, thermal), the applied loading and any other boundary conditions which may change during the time for which the response is sought. Abaqus is capable of contact/impact analysis of freely moving, partially constrained and fully constrained bodies but possible contact surfaces need to be predefined to allow the program to monitor potential points of contact and so evaluate the corresponding forces. Material failure and penetration are facilitated by element erosion which deletes whole elements from the model once they reach a predefined failure point. This “whole element” factor leads to problems in itself, to be addressed later.

Results are written to a number of different output files during analysis. These results can be in the form of stresses, strains, displacements, velocities, accelerations and reaction forces, amongst others. Results can be displayed either directly in tabulated form or graphically through the Abaqus Post postprocessor. Results can be extracted for any number of user-specified time intervals during the event.

### **3.2.1 Material modelling**

Abaqus contains an internal library of material models which include linear-elasticity, hyperelasticity and a plasticity model applicable to traditional engineering materials such as steel. Most metals used in engineering applications are treated as isotropic and linear elastic which is adequate for eg most conventional design purposes. There are, however, also analyses which must incorporate plastic deformation, such as metal forming and dynamic impact simulations. The latter sometimes even require damage and failure of the material to be modelled, eg in ballistic penetration simulations.

Abaqus contains a generic material model capable of modelling the three stages of elasticity, plasticity, and failure for metals. With reference to a 3-d continuum element

the elastic stresses are updated via a symmetric isotropic stiffness matrix similar to equation (12) shown later in this section. If plasticity is included in the analysis, yield occurs by default once the Von Mises stress exceeds the user-defined yield stress. Other yield criteria can also be specified. Plasticity can be either perfect, ie all stress components remain constant during continued yielding or isotropic hardening can be included by user-specified stress-strain data points. Failure can be instantaneous at a given plastic strain or gradual by means of a damage evolution law also defined in terms of plastic strain at the onset of damage and at total failure. Passive strains during yield and failure are controlled by a flow rule employing a constant volume constraint. (Abaqus Theory version 5.7 section 4.2.1.) Certain stability criteria must be followed: There is a limitation to the ratio between plastic and elastic strain or in other words the plastic (dissipated) strain energy at failure must be several times greater than the elastic (recoverable) strain energy.

Hyperelasticity is commonly associated with elastomers which can undergo large deformations with little or no dissipation of strain energy. Elastomers are also characterised by near incompressibility, ie Poisson's ratio is close to 0.5. Rubber-like materials are widely used in industry and are often included in FEA. A generic hyperelastic material model is provided in Abaqus/Explicit based on an Ogden polynomial strain energy function. The stress-strain behaviour can also be given as a number of experimental stress-strain data points but a rather high number of data points is required to ensure stability. Passive strains are controlled by an incompressibility constraint. Both geometric and numerical stability are known problem areas for finite elements undergoing large deformation. Geometric stability can be maintained by re-meshing, which only became available in Abaqus/Explicit version 5.8 after the present work was finalised. Numerical stability has also been improved for the generic hyperelastic material model in version 5.8. Failure can, however, still not be simulated for hyperelastic materials probably due to a combination of: 1) lack of demand for modelling of continued failure of elastomers and 2) most importantly, difficulty in maintaining numerical stability as large amounts of elastic strain energy are released during failure.

Initial modelling of skin was attempted using the internal elastic-plastic model with appropriate properties. It was however realised that the model was not capable of the

large elastic strains associated with skin deformation and the analysis was prematurely terminated by Abaqus due to numerical instability. The hyperelastic model also looked promising but this essentially describes a material with a sigmoid stress-strain response. It has been pointed out by some authors that skin does not have such a response (Atkins and Mai (1988), Marks (1983)) but the hyperelastic model was investigated as a matter of course. The results showed that it did indeed become unstable well before the strain levels at which skin fails ( $\lambda = 1.2 \dots 1.6$ ) were reached. This attempt was made in Abaqus version 5.6 and later versions have, as mentioned, been improved with this respect. The lack of failure simulation was the key reason for not investigating this approach further.

In short, none of Abaqus' existing internal material models were suitable for modelling mechanical failure of skin and it was then necessary to employ a more complicated but more versatile method which requires a user-written constitutive model including:

- 1) the stress-strain behaviour of skin up to the point of rupture
- 2) a means of admitting penetration by element erosion

This model can be embedded into the Abaqus/Explicit package via the VUMAT (Vectorized User MATerial) facility. VUMAT is a subroutine shell provided within the Abaqus system. It is written in Fortran90 source code and so is visible to the user (Chivers and Sleightholme (1995)). The argument list provided matches the calling routine in the main Abaqus program and so the subroutine, with the user-defined constitutive model, may be linked into the analysis. The Abaqus input file is also able to read a variable list and pass these to VUMAT. Thus any number of material constants can be specified for insertion in the general constitutive model. In essence, VUMAT requires the user to update the stress tensor to take account of strain increments passed across from the main program.

The material model encoded in VUMAT was based on uniaxial tensile test results obtained from pig skin. Initially, results from the pilot tensile tests provided key values such as failure stress and strain for the model. By assuming the material to be a purely elastic isotropic continuum, the material model could be based on the generalised Hooke's law, which states that the stress tensor is linearly proportional to the strain

tensor thus:

$$\sigma_{ij} = C_{ijkl} e_{kl} \quad (6)$$

where  $\sigma_{ij}$  is the stress tensor,  $e_k$  is the strain tensor, and  $C_{ijk}$  is a tensor of elastic stiffness constants which, in linear elasticity, are stress and strain independent throughout the whole of the deformation history. This is usually only reasonable for small strains, eg in metallic structures.  $C_{ijkl}$  is a fourth order tensor with, potentially, 81 components but fortunately various symmetries usually apply to reduce this number. For example, if  $\sigma_{ij}$  is symmetric then:

$$C_{ijkl} = C_{jikl} \quad (7)$$

and so on. Indeed, for an isotropic, linear elastic material there are only two independent constants. There are of course more than two possible choices for the elastic constants but relationships exist such as:

$$E = 2G(1 + \nu) \quad (8)$$

These particular elastic constants are most useful when equation (6) is inverted and the strains are expressed explicitly in terms of the stresses. This, however, is not the case in VUMAT, which uses equation (6) itself. This is rather messy when written in terms of  $E$ ,  $\nu$  and  $G$  but takes on a particularly simple form when written in terms of the alternative elastic constants known as Lamé's constants  $\lambda$  and  $\mu$ . These are defined as:

$$\lambda = \frac{E\nu}{(1 + \nu)(1 - 2\nu)} \quad (9)$$

and:

$$\mu = G \quad (10)$$

although the latter is merely a change of notation. Then:

$$[\sigma] = [C] \times [\varepsilon] \quad (11)$$

where:

$$[C] = \begin{bmatrix} \lambda + 2G & \lambda & \lambda & 0 & 0 & 0 \\ & \lambda + 2G & \lambda & 0 & 0 & 0 \\ & & \lambda + 2G & 0 & 0 & 0 \\ & & & 2G & 0 & 0 \\ \text{Symm.} & & & & 2G & 0 \\ & & & & & 2G \end{bmatrix} \quad (12)$$

Expanding this into a form which may be directly encoded in VUMAT gives:

Direct stresses

$$\sigma_{xx} = \lambda(e_{xx} + e_{yy} + e_{zz}) + 2Ge_{xx}$$

$$\sigma_{yy} = \lambda(e_{xx} + e_{yy} + e_{zz}) + 2Ge_{yy} \quad (13)$$

$$\sigma_{zz} = \lambda(e_{xx} + e_{yy} + e_{zz}) + 2Ge_{zz}$$

Shear stresses

$$\sigma_{xy} = 2Ge_{xy}$$

$$\sigma_{yz} = 2Ge_{yz} \quad (14)$$

$$\sigma_{zx} = 2Ge_{zx}$$

Pig skin shows a non-linear stress-strain relationship and simply applying linear elastic theory based on the failure point would be too inaccurate. However, a bi-linear approach provides a good approximation to the actual stress-strain response and so Hooke's law can be applied in two stages (Figure 3.8). The key values derived from the experimental curve are:

the elastic modulus for the first linear section ( $E_1$ ),

the intermediate transition point (point A),

the elastic modulus for the second linear section ( $E_2$ ),

the failure stress (point B).

Poisson's ratio is also required but was not evaluated from the preliminary tensile tests, and an assumed value of 0.3 was used in the early computations. The later, more

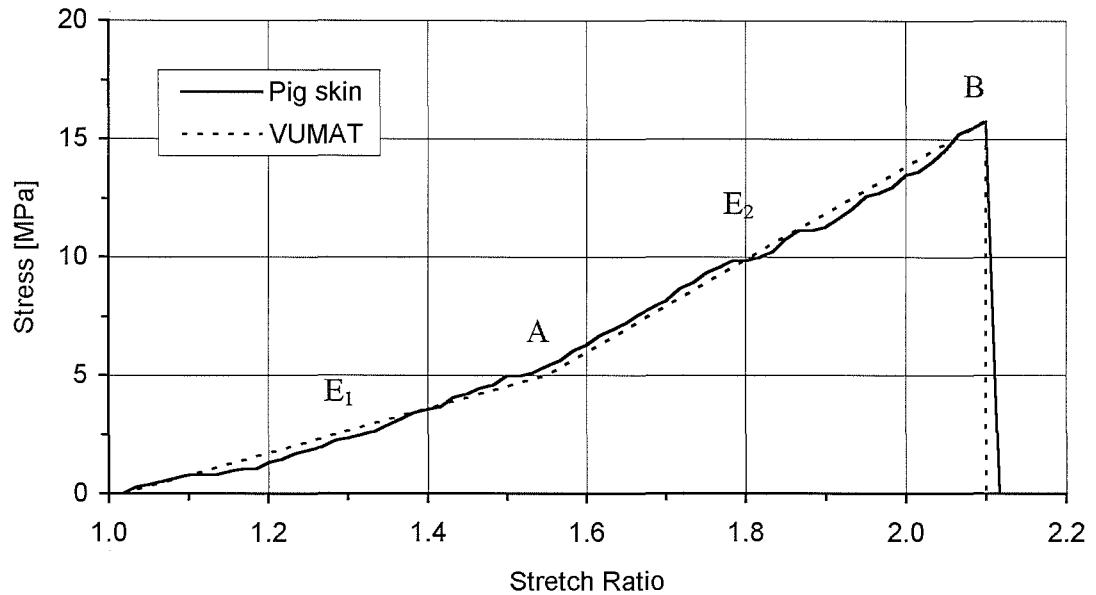


Figure 3.8. Bi-linear idealisation of pig skin for computational material model based on pilot tensile tests.

detailed tensile tests on pig skin suggested that Poisson's ratio was around 0.6 but that large variations existed (section 2.2.2). It has been suggested by Cook (1975) that skin might be incompressible, in which case Poisson's ratio would be 0.5. This value would, however, cause a zero division error in equation (9) and it was decided to continue with the value of 0.3. Abaqus works with true stress rather than the nominal stress which was obtained from the tensile test. Based on the assumed Poisson's ratio and the following relations the true stress was calculated at the intermediate point and at the failure point:

$$\lambda' = \frac{l_0 + \Delta l}{l_0} \quad (15)$$

$$\nu = \frac{\lambda'_y - 1}{\lambda'_x - 1} \quad (16)$$

where  $\lambda'$  is the stretch ratio (not to be confused with Lamé's constant  $\lambda$  - an unfortunate clash in the conventional notations),  $l_0$  is the original specimen dimension, and  $\Delta l$  is the change in specimen dimension. Finally the elastic modulus  $E_1$  and  $E_2$  were calculated based on true stress and strain:

$$E = \frac{\sigma_{true}}{\lambda' - 1} \quad (17)$$

The key values used directly in the material model are shown in Table 3.2. Assuming isotropy, failure under multiaxial stress can be triggered at a Von Mises stress which was updated continuously during the analysis. A sample of the actual user-programming in Fortran90 is given in Appendix 5.1.

Variable	Symbol (Fig. 3.1)	Value
Intermediate stress	$\sigma_A$	5.0 [MPa]
Intermediate strain	$\lambda'_A$	1.55
Failure stress	$\sigma_B$	16.0 [MPa]
Failure strain	$\lambda'_B$	2.1
Low elastic modulus	$E_1$	9.1 [MPa]
High elastic modulus	$E_2$	20.0 [MPa]
Poisson's ratio	$\nu$	0.3

Table 3.2. Key values used in the computational material model.

### 3.2.2. Mesh design and analysis

The stab-penetration test is an essentially 3-d problem in which the coupling between the vertical force on the slim knife blade and the horizontal forces induced in the skin membrane cannot be ignored. A 3-d model was therefore necessary and a scale model of the experimental stab-penetration test described in section 3.1 was created. Initially both the flesh and skin simulant were incorporated in the model but it was realised at an early stage that it would be more productive to focus on the skin alone at this stage. Flesh should at some point be considered in the model as it might have a load distributing ability influencing the penetration force but throughout this work only skin is considered. The model of skin only was used during development of the material model. Two different element types were analysed in a number of mesh configurations. The model was analysed in Abaqus/Explicit version 5.5.

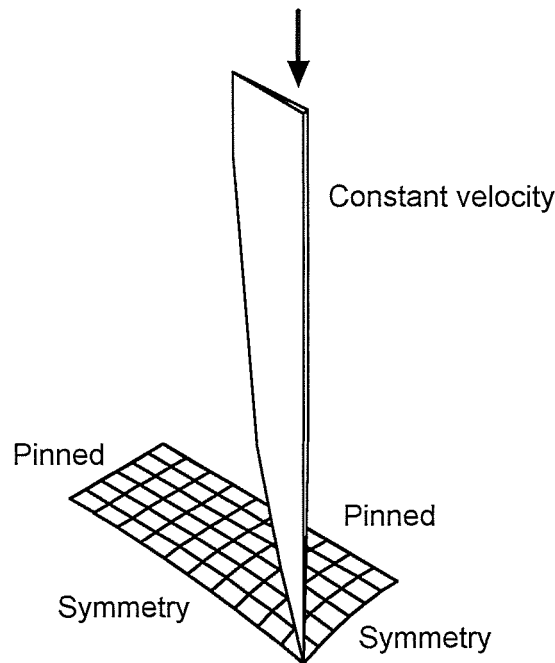


Figure 3.9. Boundary conditions on FE quarter model.

### *Target*

The target skin layer was modelled with similar dimensions to those used in the experimental test set-up described in section 3.1. Due to the four-fold symmetry (two symmetry planes) of the stab-penetration test, it was possible to analyse a quarter of the full model and so save in processing time. Boundary conditions were imposed on the nodes along all four edges of the quarter model (Figure 3.9). The outer edges of the skin, which in the experimental set-up was held against the top edges of the plastic container by a securing plate, were pinned in the FE-model. This allows free rotation but constrains all the translational freedoms. Nodes along the two planes of symmetry were assigned the relevant symmetry boundary conditions to restrict the appropriate rotational and translational freedoms (Abaqus/Explicit section 21.2.4). Two types of elements were used for modelling skin:

- 1) 4-noded quadrilateral membrane elements (M3D4R) with reduced integration and hourglass control.
- 2) 8-noded linear brick solid elements (C3D8R) with reduced integration and hourglass control.

The membrane elements have no bending stiffness and were used in a single layer 6 x 10 element configuration as shown in Appendix 7.1. These elements can indeed only be used in one layer which was assigned a section thickness of 2 mm corresponding to the total thickness of the test specimen. Within VUMAT, the two direct stresses and the one shear in the plane of the membrane were updated. To study the effect of element size, a bias was applied to the mesh density in both in-plane directions, with a finer mesh towards the point of impact. A bias value of 1 indicates equal element size in the model and bias values lower than 1 indicates an increasing mesh density in the immediate impact zone. All membrane elements were defined as a contact surface to allow generation of contact forces between knife and target once contact is established.

A similar mesh to that with membranes was used, but with solid elements 5 layers deep, as shown in Appendix 8.1. A mesh with the highest degree of bias (0.6) used with solid elements is shown in Appendix 8.3. In the solid elements, the full 3-d stress tensor, with three direct stresses and three shear stresses, must be updated in VUMAT. Instead of a contact surface, contact nodes were defined in the target to maintain generation of contact forces as failure and removal of elements progresses.

### *Penetrators*

A number of sharp knife-blade geometries were produced, corresponding to the blades used in the experimental stab-penetration test (Appendix 4). All the blades were double edged which means there are two planes of symmetry and again a quarter of the blade need be modelled. Rigid elements defined as contact surfaces were used for the blade. These are non-deforming and so there is no stress or strain recorded, which saves significantly on computing time. It does however preclude the recovery of blade tip stresses. These will ultimately be required but are not an essential feature of the current study. Both 3-noded triangular facet (R3D3) and 4-noded quadrilateral (R3D4) rigid elements were used to form the blade geometries. In Abaqus, rigid elements are collected and assigned to a rigid body. This is linked to a "reference node" at which the collective boundary conditions are prescribed. The blade was restricted to translational movements in the direction perpendicular to the target surface and element surfaces facing the target were defined as contact surfaces. The complete knife was moved towards the target at a constant velocity assigned to the reference node. The experimental knife velocity was 8 mm/s but by trial and error it was verified that a

velocity of 50 mm/s could be used in the FE-model. This did not affect the numerical results but considerably reduced the processing time.

### *Analysis protocol*

The two target configurations including membrane elements and solid elements respectively were used in the stab-penetration simulation with various degrees of mesh bias. Bias values ranged from 1.00, which is even element size, down to 0.45 which results in a highly refined mesh in the impact zone. Blade type 3B (pointed tip with sharp edges) geometry was eventually chosen as the benchmark for the analysis. The key result to be extracted from the simulation is the reaction force on the knife blade as it penetrates the target layer. This reaction force was monitored directly on the reference node controlling the knife blade. Since a quarter-model is used the computed reaction force is 1/4 of the actual force. However, the results presented later have been multiplied by 4 and may be directly compared with the experimentally obtained penetration forces. The analyses were carried out on an IBM RS 6000 workstation in Abaqus/Explicit version 5.5.

### **3.2.3 Results and evaluation**

Results from the computational stab-penetration test of the sharp-tipped knife using 60 membrane elements are presented in Figure 3.10 for bias values 1.00 to 0.75 and in Figure 3.11 for bias values 0.70 to 0.45. The curves show the total reaction force on a type 3B (pointed tip and sharp edges) penetrator plotted against displacement of the penetrator measured from the point of initial contact with the target. A steady decrease in penetration force is observed as the bias number decreases i.e. the element size in the impact zone decreases. This tendency is consistent down to a bias value of 0.55 where fluctuating inconsistent force readings appear. The quarter model using membrane elements is shown in Appendix 7 both in the undeformed state and as a Von Mises stress contour plot in the deformed state, prior to penetration, with a bias value of 0.90.

Equivalent results from the computational stab-penetration test using 5 x 60 solid elements are presented in Figure 3.12 for bias values 1.00 to 0.75 and in Figure 3.13 for bias values 0.70 to 0.50. The curves show the total reaction force on a type 3B (pointed tip and sharp edges) penetrator plotted against displacement of the penetrator measured from the point of initial contact with the target. A steady decrease in penetration force

is also observed for the solid elements as the bias number decreases, however, a fluctuating force reading is obtained for most bias values. The bias range 0.70 to 0.50 (0.55 excepted) produces similar penetration forces and a smooth curve leading to the point of penetration. The quarter model using solid elements is shown in Appendix 8.1 in the undeformed state and is shown in Appendix 8.2 as a Von Mises stress contour plot in deformed state prior to penetration with a bias value of 0.90.

The maximum penetration force with different mesh bias are shown in Figure 3.14 for both membrane elements and solid elements. There is a clear decrease in penetration force as the mesh density increases for the bias range 1.00 to 0.60. Below this range - for the membrane elements - some inconsistency is observed. The in-plane measures of the elements are probably too small compared to the thickness. Interlocking of the membrane elements due to large relative rotations is thought to cause this inconsistency. The analysis including solid elements could not be completed for bias values below 0.60 as Abaqus terminated the analysis before penetration occurred due to severe element distortion. Too high aspect ratio might also be the explanation here since the in-plane measures become small relative to the thickness or "height" of the elements for low bias values. For a given bias value the solid elements result in a much lower penetration force than the membrane elements which must be due to the five element layers used with the solid elements in contrast to the single membrane element layer. Even the solid elements result in a penetration force which is too high when compared with the experimental stab-penetration results. The tip-radius on blade 3B was not measured but was represented as an infinitely sharp wedge in the computational model. This will theoretically always result in a lower penetration force for a more refined target mesh although there seems to be some convergence towards a constant penetration force for a constant number of element layers as is the case for the model presented here.

Although membrane elements match the global behaviour of skin well due to the lack of bending stiffness, it remains a question whether this is the case when penetration by pointed objects is considered. Under the assumption that skin is a homogeneous material it seems more realistic to use solid elements which facilitate higher mesh refinement and allow multiple elements through the thickness of the skin. This enables a more detailed simulation where tip-radius of the penetrator can be included which is considered important since tip sharpness or more precisely tip-radius has been identified as a paramount factor regarding penetration force (Knight (1975)).

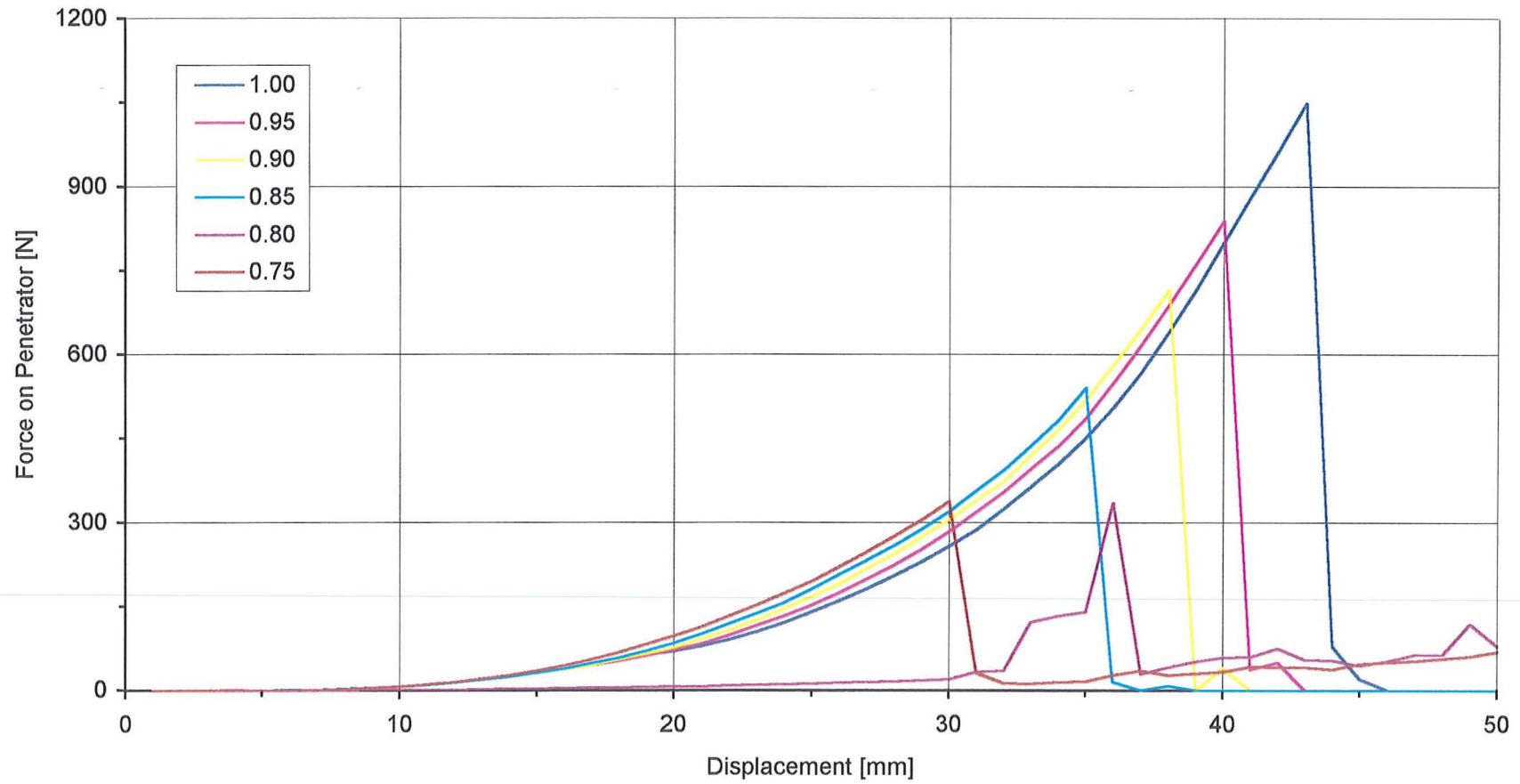


Figure 3.10. Computational stab-penetration test using 60 membrane elements and knife blade 3B (pointed tip and sharp edges). Bias values 1.00 to 0.75. Original in colour.

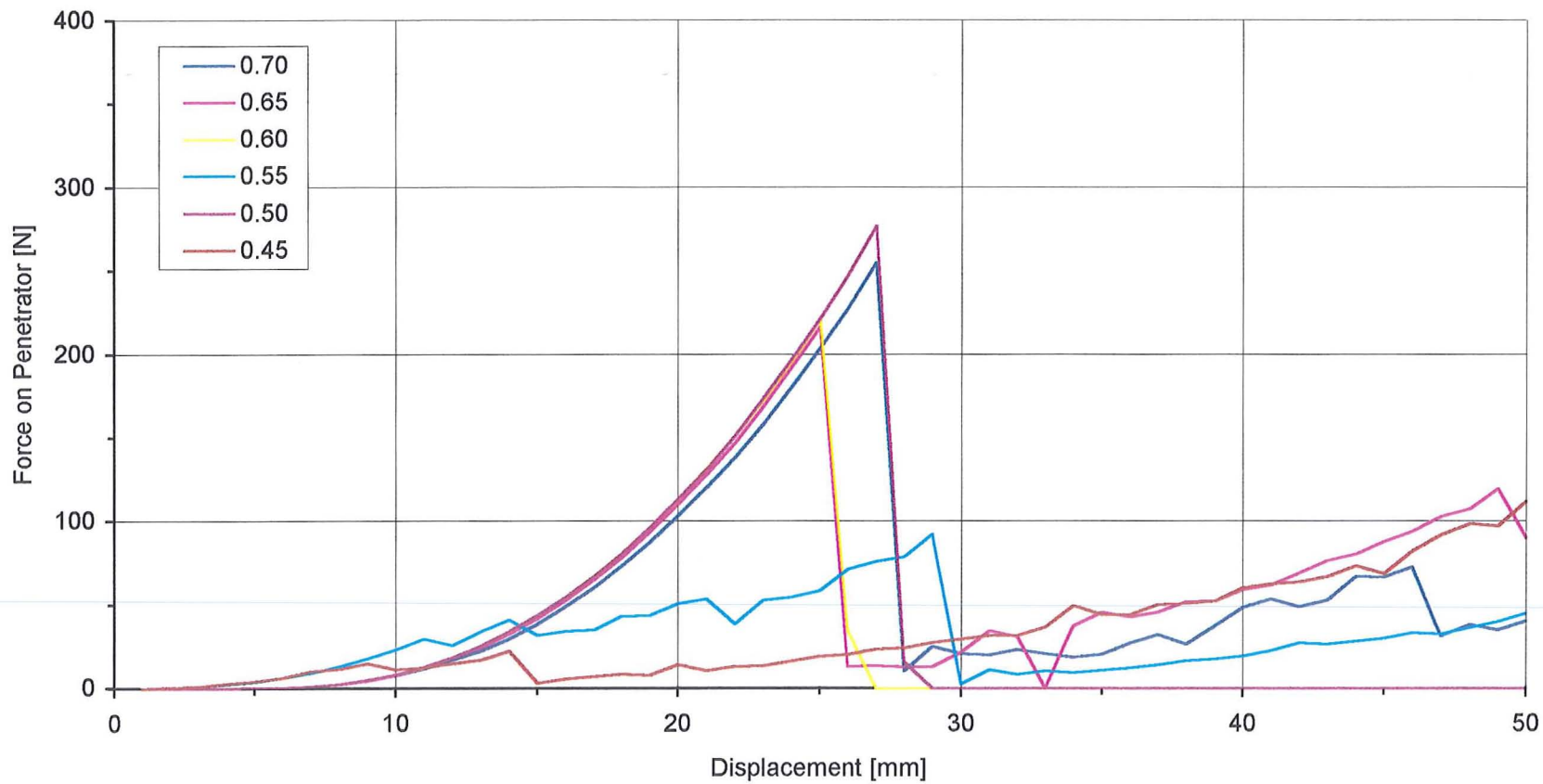


Figure 3.11. Computational stab-penetration test using 60 membrane elements and knife blade 3B (pointed tip and sharp edges). Bias values 0.70 to 0.45. Original in colour.

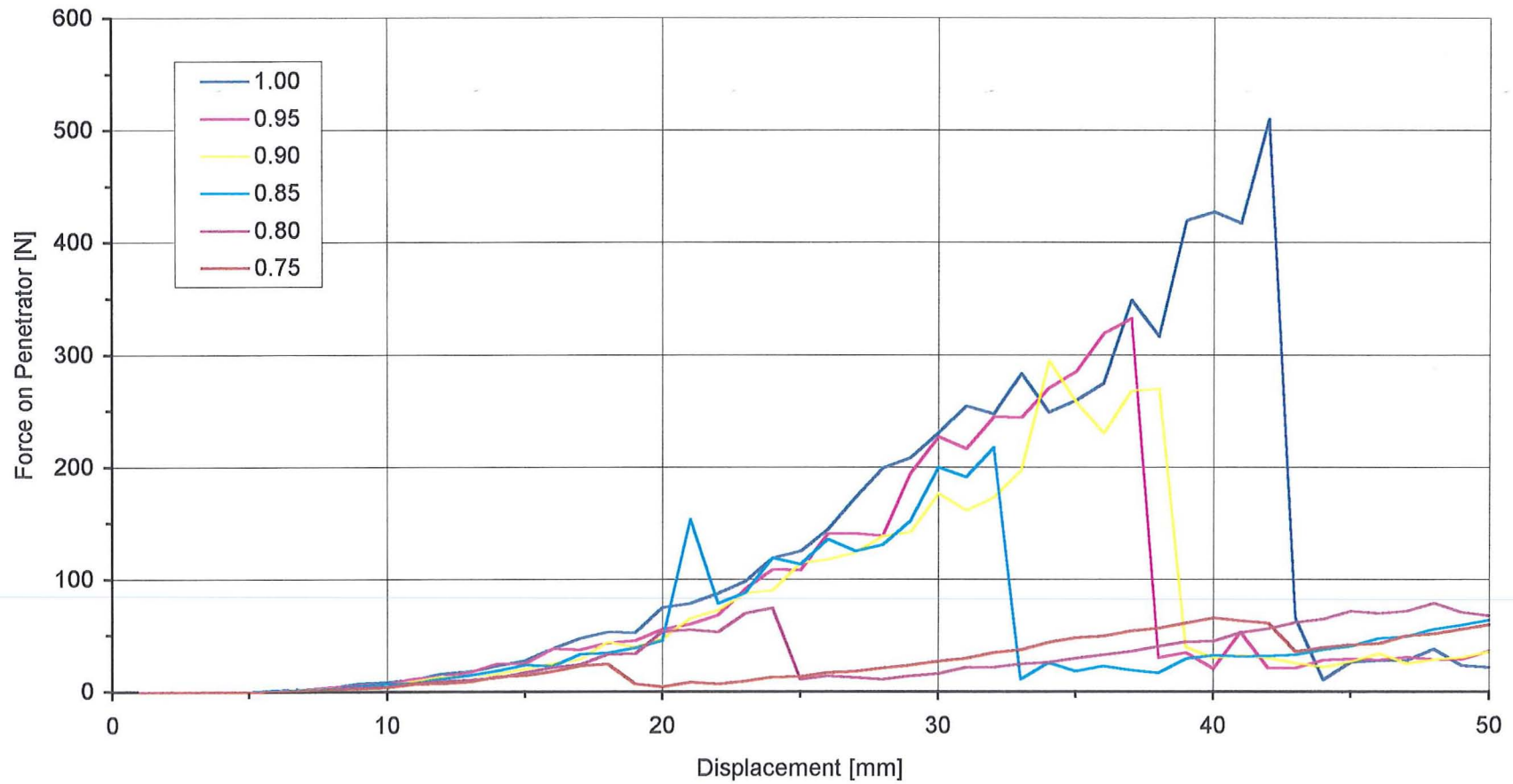


Figure 3.12. Computational stab-penetration test using 5 x 60 solid elements and knife blade 3B (pointed tip and sharp edges). Bias values 1.00 to 0.75. Original in colour.

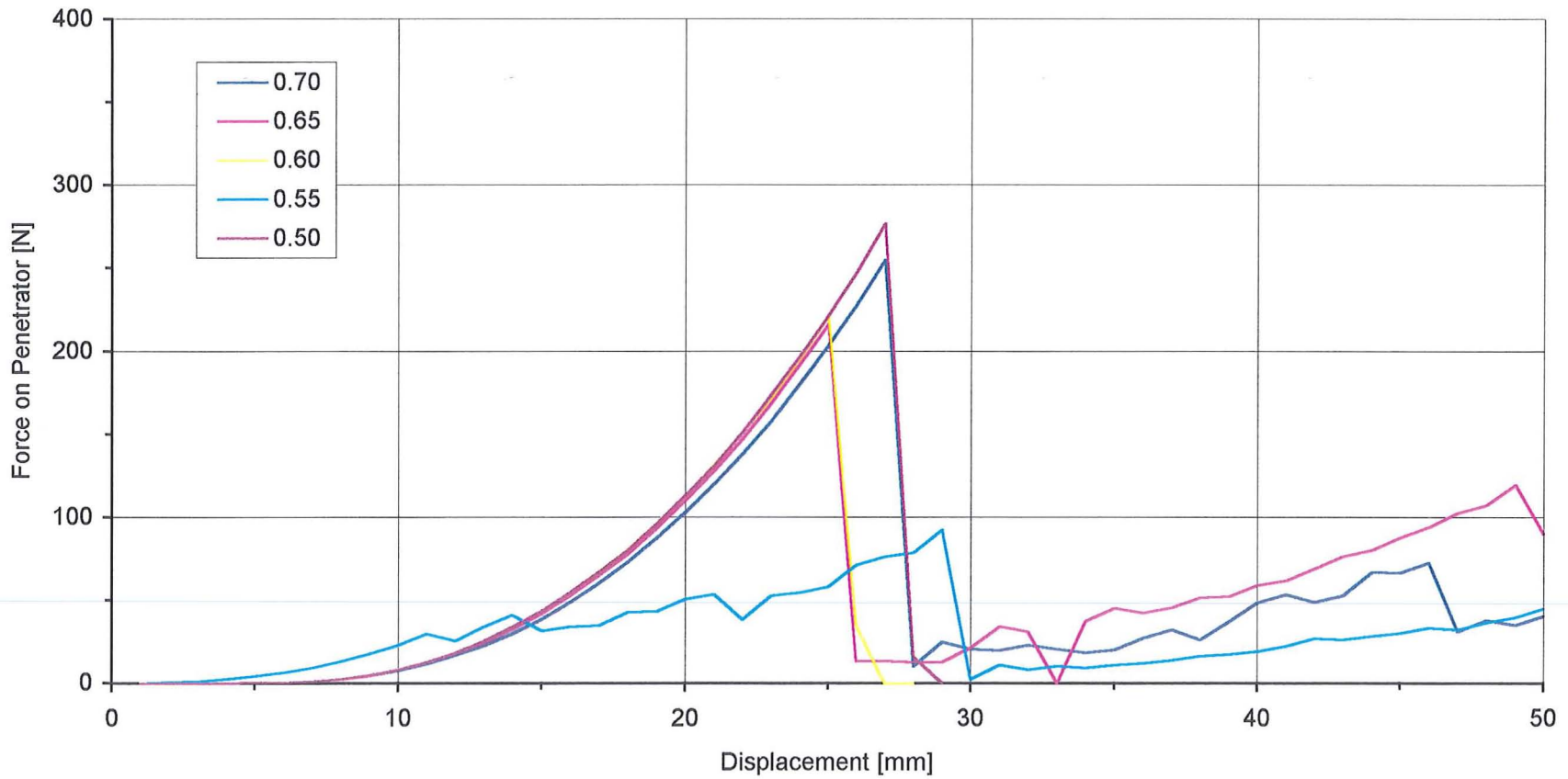


Figure 3.13. Computational stab-penetration test using 5 x 60 solid elements and knife blade 3B (pointed tip and sharp edges). Bias values 0.70 to 0.50. Original in colour.

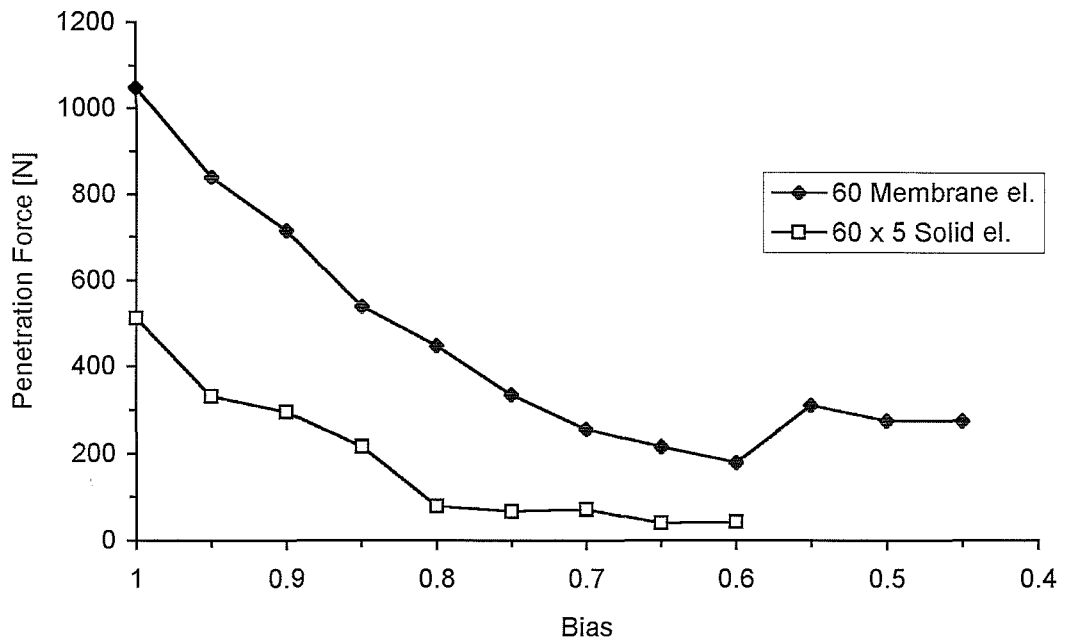


Figure 3.14. Maximum penetration force for membrane elements and solid elements with different mesh bias.

## 4 Stab-penetration test using blunt penetrators

Stab-penetration tests using sharp knives verified the fact that pointedness or tip-radius is of great importance in determining the maximum penetration force. As the tip-radius of these sharp blades is difficult to measure it was decided to study the effect of tip-radius using blunt penetrators with a range of “large” well defined tip-radii. Stab-penetration tests were conducted with rounded penetrators of various tip-radius to record any connection between tip-radius and maximum penetration force and hence point towards a theory which takes account of blade tip sharpness. From the FE-simulation of sharp blades it was learned that high mesh refinement was needed to avoid influence from element size. Axisymmetric modelling is therefore desirable as the computational cost is much smaller than for a full 3-d analysis. The test rig was designed with axisymmetric computational modelling in mind.

### 4.1 Experimental programme

#### *Test rig*

The stab-penetration test using blunt penetrators was conducted on the Lloyd Universal Testing Machine. The target specimen was secured in a fixture consisting of two matching square steel plates, each with 70 mm hole in the centre as shown in Figure 4.1. The mating surfaces were serrated to prevent slipping of the specimen and the plates were held together by 4 machine screws. A recess was turned in the lower plate which fits over a hollow tube. This provides clearance for the penetrators during testing and is a preparation for future experiments involving flesh simulants which would be placed inside the tube. The penetrator is a cylindrical steel rod with a hemispherical tip and is attached to the cross-head via an adapter in which the four different penetrator sizes fit. The adapter and penetrators are shown in Figure 4.2.

#### *Specimen preparation*

Specimens were prepared as described in section 2.2.1 but were cut into a 110 x 110 mm square shape. Only fresh back skin was used for the stab-penetration test.

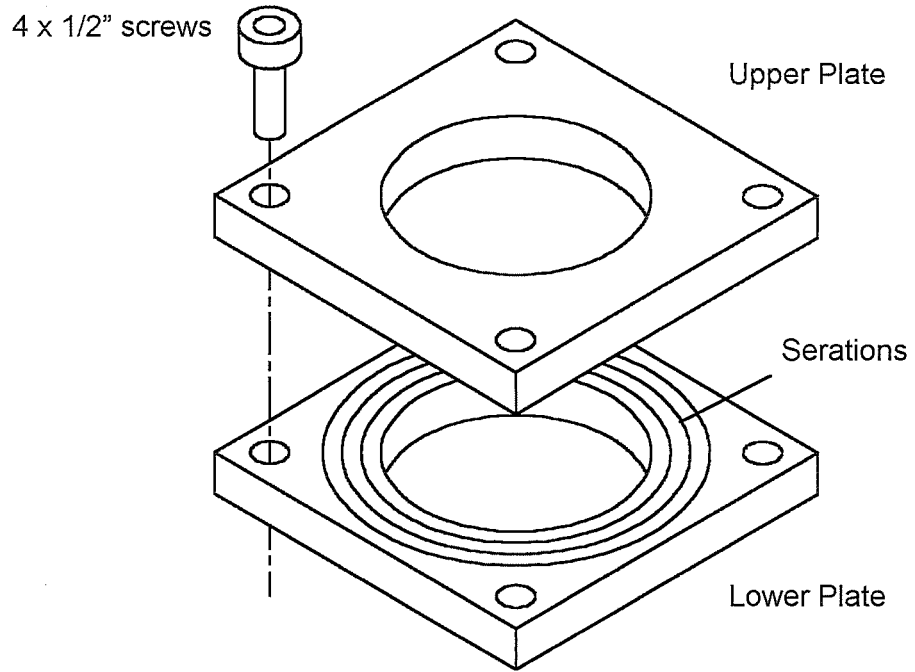


Figure 4.1. Skin specimen fixture for stab-penetration test using rounded penetrators. Plates: 110 x 110 x 12.7 mm with  $\varnothing 70$  mm hole.

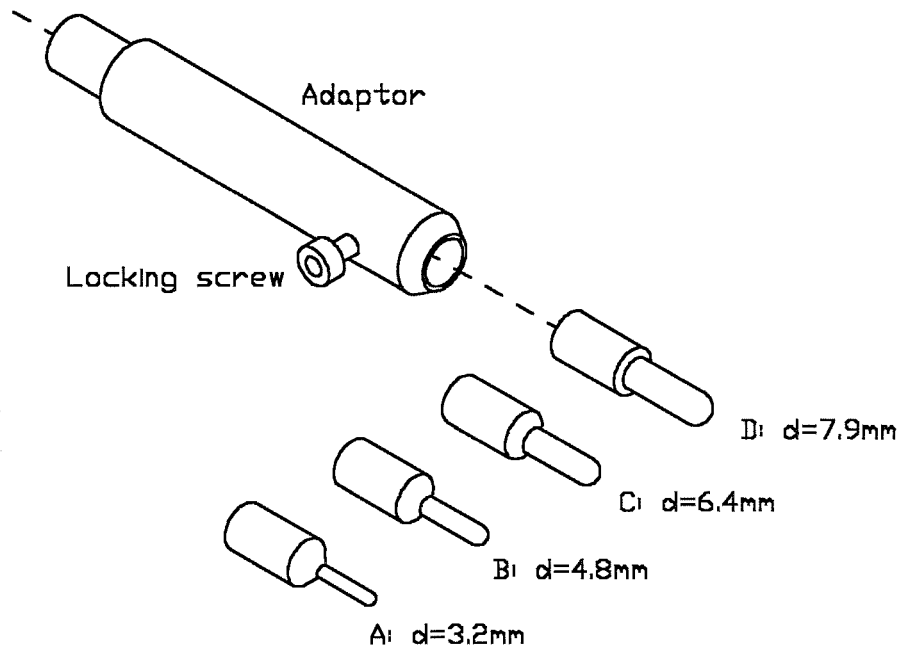


Figure 4.2. Hemispherical penetrators and adaptor used in stab-penetration test on pig skin.

### *Test protocol*

The specimen was secured in the fixture at a 45° angle to allow clearance for the four screws. With the outside of the skin facing the penetrator the fixture was placed on the hollow tube. The penetrator was mounted in the adapter and the cross-head was brought down until contact with the skin specimen was established. A constant cross-head speed of 50 mm/min was used and the cross-head returned automatically after penetration occurred. A total number of 24 experiments were conducted giving six repetitions per penetrator size. Each penetrator was tested on specimens originating from a combination of locations within the back skin pieces to account for material variations. Force-displacement curves were recorded during each test.

#### **4.1.1 Results and evaluation**

Force-displacement curves for each penetrator size are shown in Figure 4.4 to Figure 4.7. It was noticed during the tests that the failure and penetration occurred suddenly without any warning. This is reflected in the abrupt drop in penetration force on the curves. After removing the penetrator the puncture in the skin specimen left an almost linear crack with the length equal to the diameter of the penetrator. As expected there is a consistent increase in penetration force for increasing penetrator size. The displacement at the point of failure is nearly the same for the different penetrator sizes.

The stab-penetration test using rounded penetrators showed a consistent relation between penetrator diameter and maximum penetration force. This relation is shown in Figure 4.3 with a straight best fit line based on average values for each penetrator size as shown in Table 4.1. The best fit line is extrapolated down to a infinitesimal penetrator diameter where the penetration force is close to zero. From this it can be deduced that there must be a linear relationship between penetrator tip-radius and penetration force at least for penetrator sizes which are large compared to the skin thickness. The situation might be different when the penetrator tip-radius is small compared to the skin thickness i.e. for pointed knife blades. The problem is to measure the tip-radius for these pointed blades which was the main motivation for using the “large” rounded penetrators in this experiment. The fact that the best fit line does not exactly intersect the origin may be down to property variations of the pig skin. It can be speculated that the linear relationship is also valid for penetrators with very small tip-radius.

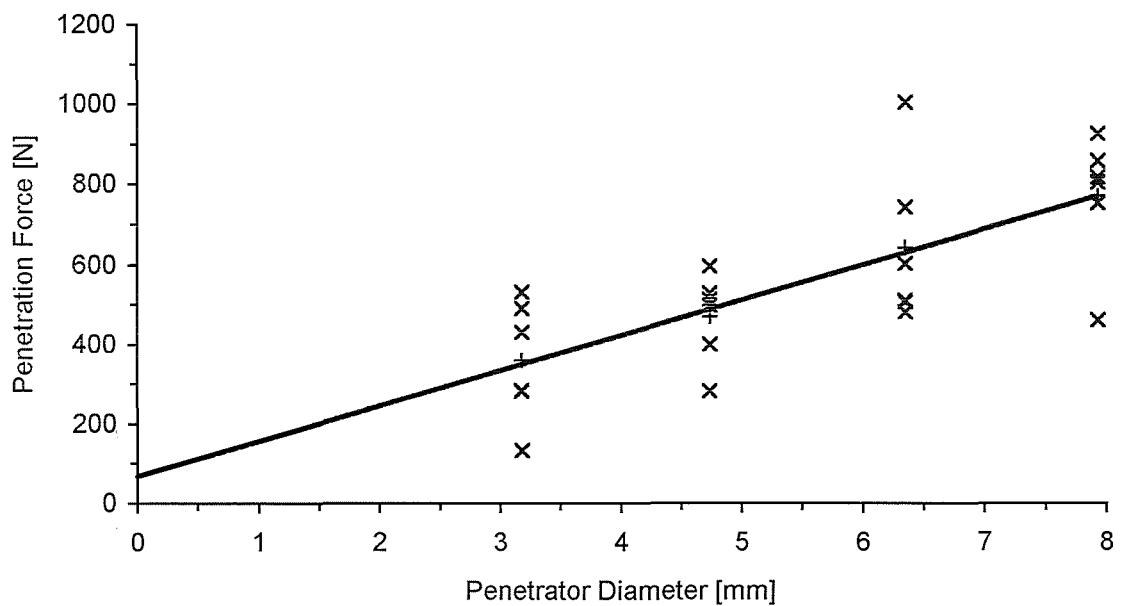


Figure 4.3. Maximum experimental penetration force versus penetrator diameter. Straight best fit line based on average values for each penetrator.

Knight (1975) and Green (1978) found the tip-sharpness to be a paramount factor when determining penetration forces for real knife blades. Here the difference in tip-radius between a sharp and a blunt blade must be in the order of micrometres and a doubling in tip-radius can easily occur when comparing a sharp and a blunt blade. Although not supported by actual figures, Knight stated that a blunt blade in many cases needed around double the force to penetrate compared to a sharp knife. This supports the linear relationship where a doubling of penetrator diameter causes a doubling in penetration force.

Penetration by the rounded penetrators occurred roughly at the same displacement for the four different penetrator sizes. Since the target fixture was the same for all penetrators, the in-plane strain in the target must be largely independent of penetrator size. This observation indicates that penetration possibly could be determined by in-plane strain which is largely independent of the penetrator size. The penetration force is then merely a function of the penetrator area in contact with the target material.

Spec.	Penetrator							
	A (3.18 mm)		B (4.75 mm)		C (6.35 mm)		D (7.93 mm)	
	RF [N]	u [mm]						
1	283	22	282	20	481	25	460	23
2	133	18	512	21	510	18	926	21
3	284	17	527	23	1005	24	817	20
4	490	19	496	21	742	25	858	20
5	430	20	596	21	507	18	752	20
6	531	19	399	19	602	24	804	20
Aver.	329.2	20.0	439.9	21.4	633.3	22.3	742.5	21.3

Table 4.1. Maximum experimental penetration force and penetrator displacement at failure for penetrator A, B, C, D.

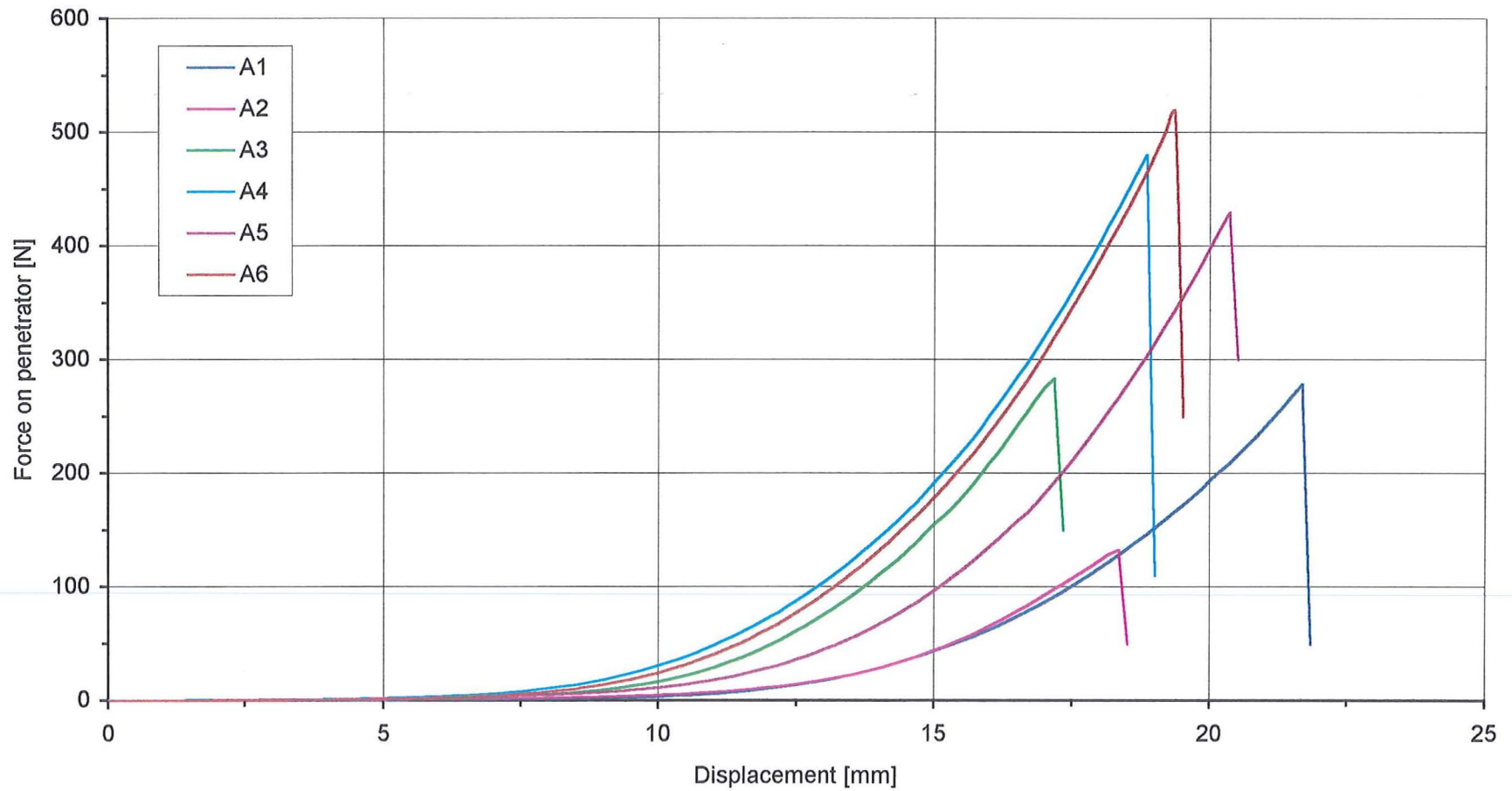


Figure 4.4. Experimental stab-penetration test on pig skin - Penetrator A (D=3.2mm). Original in colour.

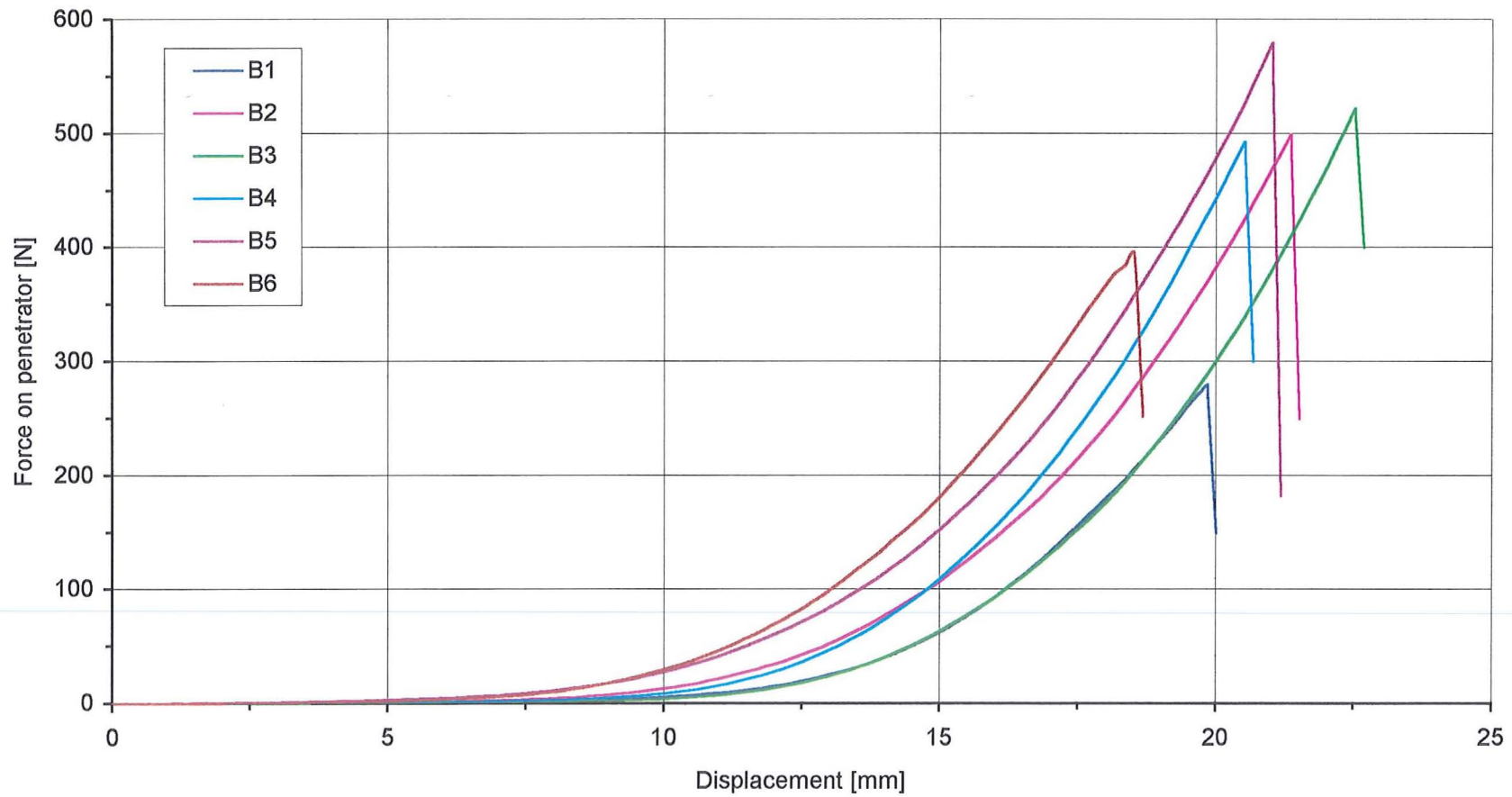


Figure 4.5. Experimental stab-penetration test on pig skin - Penetrator B (D=4.8mm).  
Original in colour.

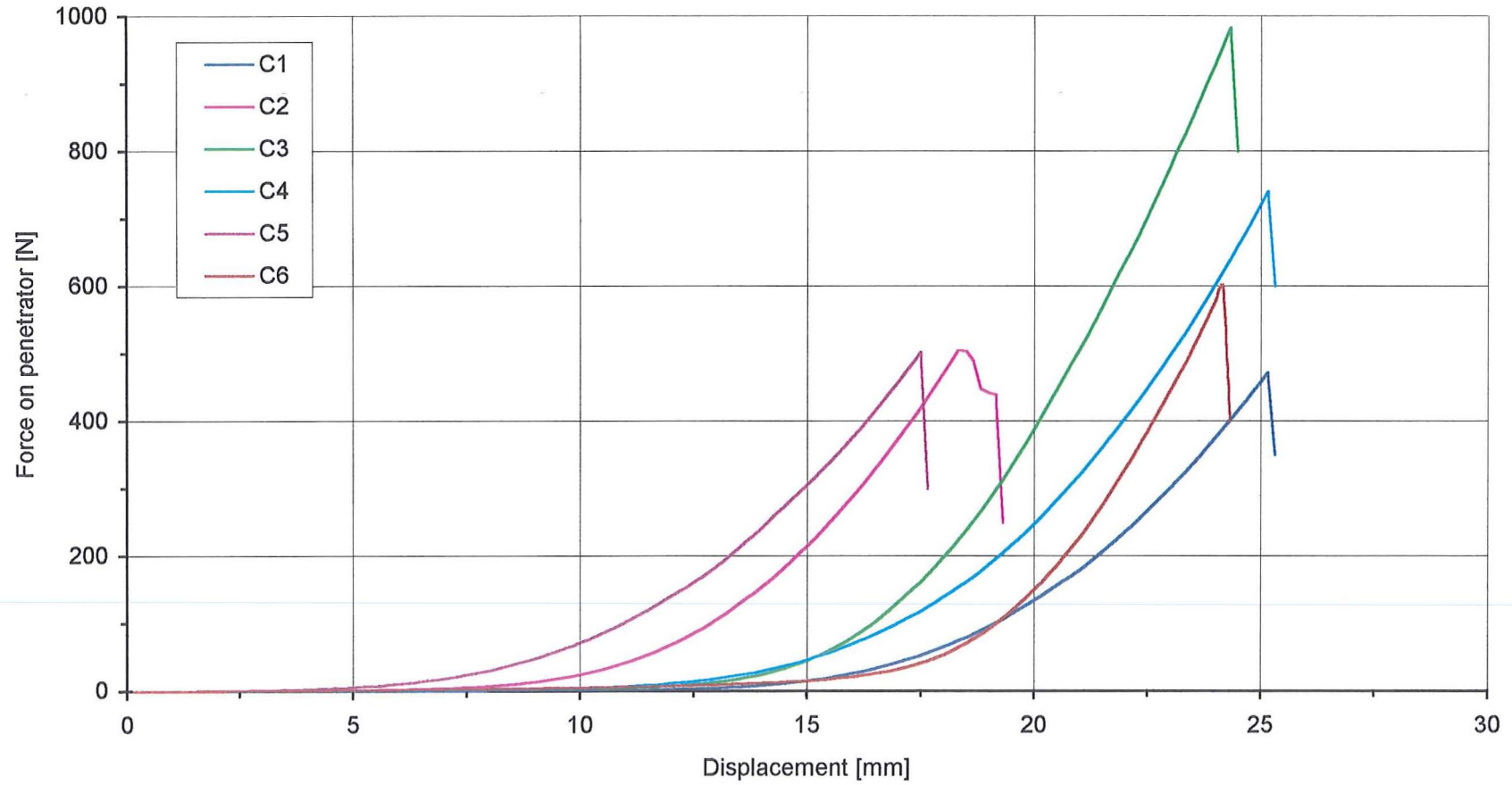


Figure 4.6. Experimental stab-penetration test on pig skin - Penetrator C (D=6.4mm).  
Original in colour.

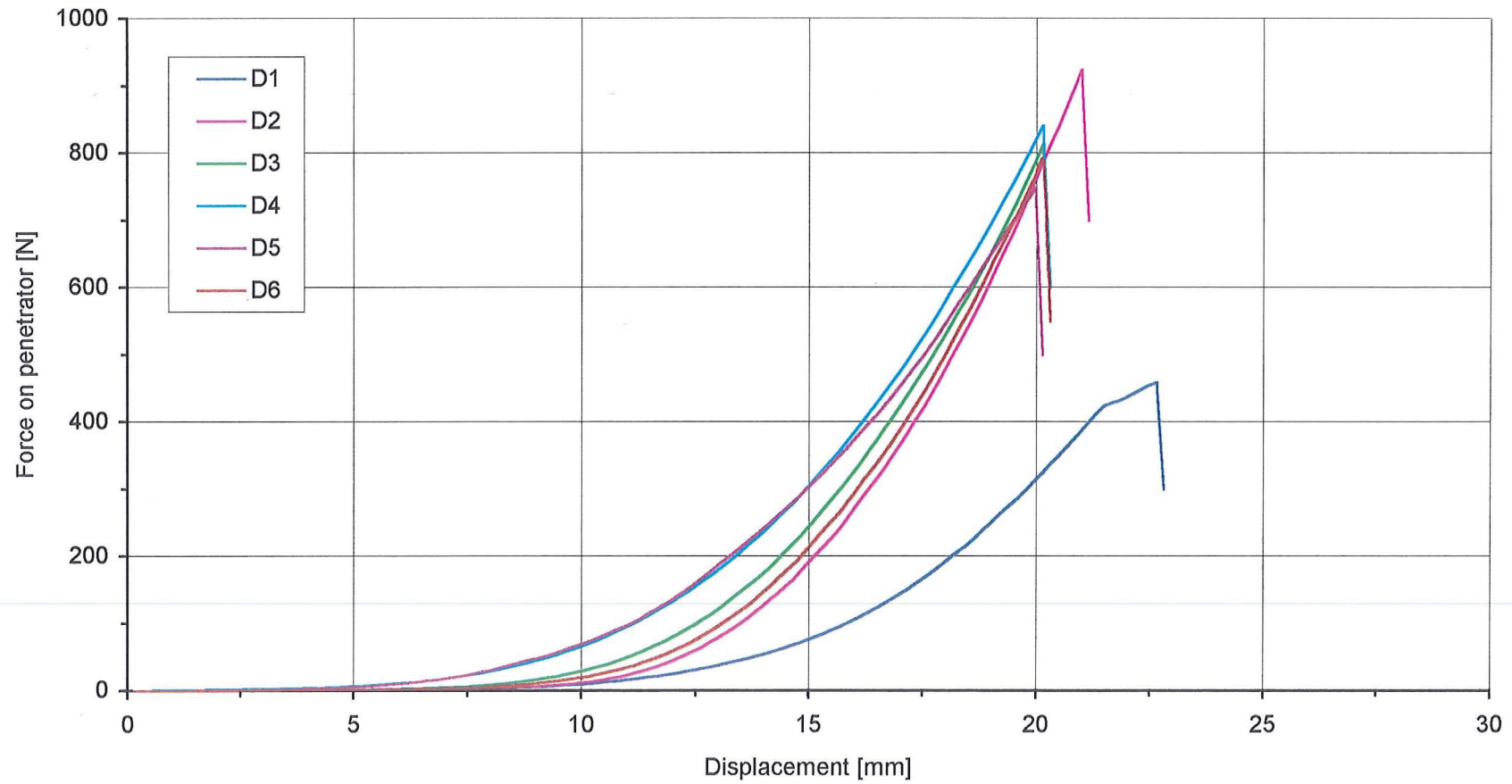


Figure 4.7. Experimental stab-penetration test on pig skin - Penetrator D (D=7.9mm).  
Original in colour.

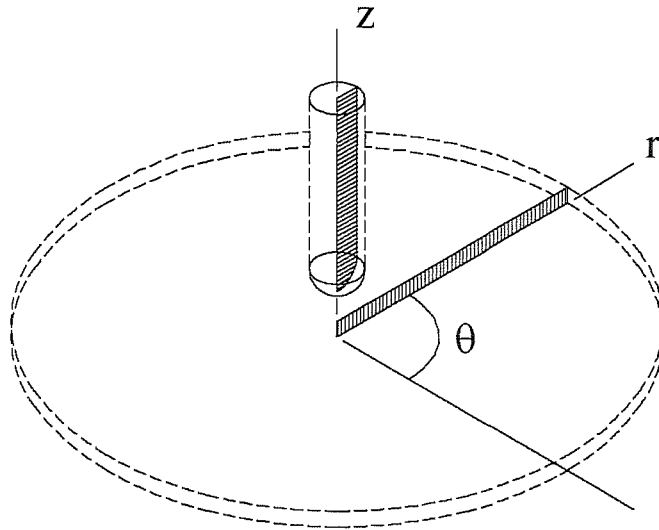


Figure 4.8. Radial plane defining the axisymmetric computational stab-penetration model.

## 4.2 Computational simulation

Unlike the sharp-tipped experiments, the stab-penetration tests using rounded penetrators, as previously mentioned, do admit axisymmetric modelling. Indeed, these experiments were designed with such modelling in mind, to provide useful results at less computational cost than a 3-d quarter model. Only a radial section of the model has to be defined geometrically and so mesh generation is effectively reduced to a 2-d problem in the  $(r,z)$ -plane (Figure 4.8). The axisymmetric model was analysed in Abaqus/Explicit version 5.6.

### 4.2.1 Material modelling

The material model used in connection with the axisymmetric model is similar to that used with the 3-d model including sharp blades (section 3.2.1). Minor adjustments were made to adapt the stress updates to the relevant directions associated with the axisymmetric elements.

#### 4.2.2 Mesh design and analysis

##### *Target*

The target represents the pig skin clamped in the fixture described in section 4.1. The radial section of the target is simply a rectangle which was meshed using MSC Patran v 8.0 Finite Element Pre/Post Processor for mesh generation. The axisymmetric model was set up to eliminate the dominating influence of element size by using penetrators with a finite tip-radius combined with a highly refined target mesh. By using a mesh generator it was possible to highly refine the mesh in the penetration zone and retain less refinement in the areas of reduced deformation gradient which are of minimal interest (Appendix 9.1). A total of 520 axisymmetric 4-noded quadrilateral elements with reduced integration and hourglass control (CAX4R) were used in the target. The normal, radial, and tangential direct stresses must be updated for this element type, together with the shear in the (r,z)-plane. Boundary conditions were imposed on the target nodes at the centre of revolution which were constrained in the radial direction and at the outer edge where the nodes were pinned. Nodes in the area of expected penetration were defined as contact nodes thus allowing contact forces to be generated between the penetrator and the target once contact is established. Contact analysis is time consuming and it is therefore desirable keep the number of contact nodes to a minimum.

##### *Penetrators*

The cylindrical penetrators with hemispherical tip were modelled with dimensions as described in section 4.1. As in the sharp-tipped model, the stress in the rounded penetrators was of no immediate interest and so rigid elements were used. The radial section of the penetrator is described geometrically by a quarter circle representing the tip and a straight line representing the cylindrical body of the penetrator. Rigid 2-noded axisymmetric elements (RAX2) were used with 10 elements forming the tip. This results in a  $9^\circ$  angle between elements. As in the sharp-tipped model, the penetrator elements were assigned to a rigid body controlled by a reference node which was constrained to translate only, perpendicular to the target surface. Element surfaces facing the target were defined as contact surfaces.

### *Analysis protocol*

The axisymmetric model was run with the 4 different penetrator sizes used in the experimental stab-penetration test. Again the key result is the reaction force on the penetrator as it is forced through the target layer. This reaction force is available at the reference node. In the axisymmetric model external forces such as the reaction force on the penetrator are given as the total value integrated around the circumference and the computational values can therefore be compared directly to the experimentally obtained penetration forces. The analyses were carried out on an IBM RS 6000 workstation.

### **4.2.3 Results and evaluation**

Results from the computational stab-penetration test of blunt penetrators using axisymmetric solid elements are presented in Figure 4.9. Only results for penetrator A and B are available as computational difficulties were encountered in the models including penetrator C and D and the analyses were terminated by Abaqus due to too high deformation speed to wave speed ratio (section 5.3.2). For penetrator A and B the force-displacement curves show similar characteristics to the experimental force-displacement curves (Figure 4.4 and Figure 4.5). The computed maximum penetration forces, however, are considerably lower than the experimental values but still the penetrator displacements at failure are the same for the two methods. The radial section of the axisymmetric model is shown Appendix 9 in the undeformed state and as a Von Mises stress contour plot in the deformed state prior to penetration.

Mesh refinement in the axisymmetric model is believed to have little or no influence on the results with the penetrator sizes used. The reason for the discrepancies between computed and experimental values must therefore be found in the general assumptions made or in the material model. Assuming skin to be a homogeneous solid knowing that it in reality is a fibrous material might be wrong. It was indicated in the stab-penetration test using sharp blades that there seem to be no direct connection between tensile strength and resistance to puncture for synthetic chamois and pig skin. The computational material model is based on tensile test results and yet applied to an analysis involving puncture.

Penetrator displacement at failure are similar for experimental and computed values and was experimentally found to be largely the same for the four different penetrator

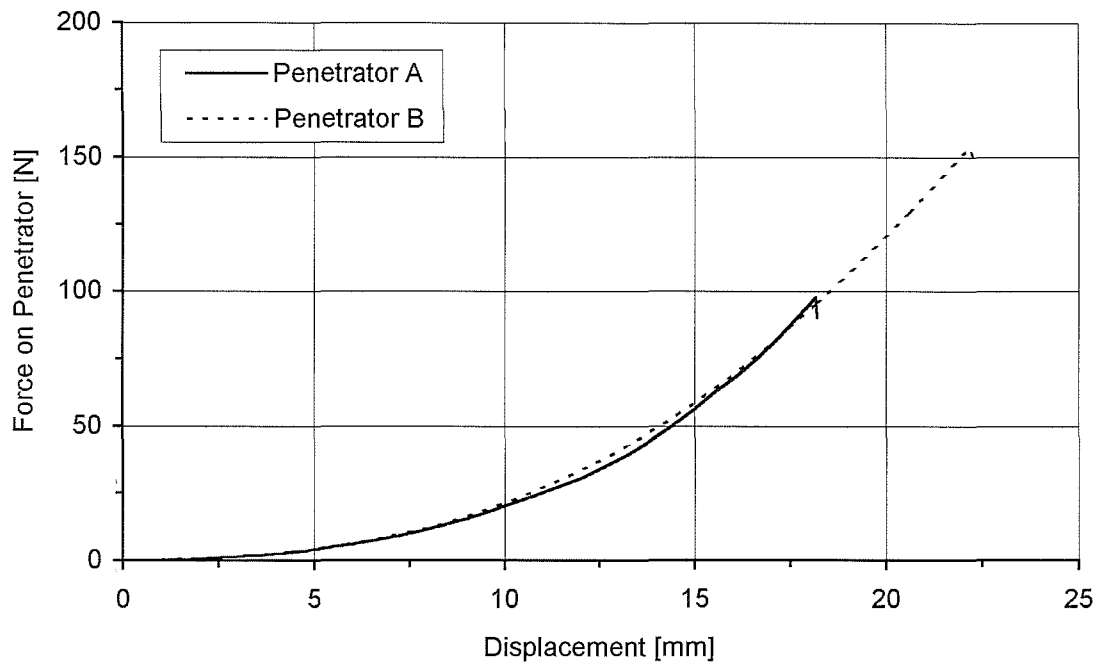


Figure 4.9. Computational stab-penetration test using axisymmetric model. Penetrator: A (D=3.2mm), B (D=4.8mm).

sizes. This is also the case for the computed values although values for only penetrator A and B have been obtained. As mentioned in section 4.1.1 penetration is possibly determined by in-plane strain in the pig skin which indicates that the computational material model has got the correct failure point in terms of strain. The stress based failure criteria might therefore be the cause of the discrepancies. At present, failure is determined by Von Mises stress based on all stress components updated for the axisymmetric solid elements. It is a question whether through-thickness stress actually contributes to failure during penetration. If not, it could be part of the explanation for the low computed penetration forces, a point to be investigated further.

## 5 Stab-penetration test with revised material models

Results from the axisymmetric finite element model described in section 4.2 did not match the experimental penetration forces as too low forces were predicted by the model. Furthermore numerical problems prevented completion of the analyses for the two largest penetrator sizes. The axisymmetric model is of minimal mesh sensitivity and it was felt that this model formed a good basis for further testing of the continuum finite element approach. Fundamental flaws were discovered in the initial bi-linear material model indicating that these might be the cause of the mismatch between computational and experimental ultimate penetration forces. Further work was therefore undertaken in terms of developing a material model that would result in a computational ultimate penetration force in agreement with the experimental value while maintaining stability during continued penetration.

### 5.1 Revised material models

Two versions of the final material model are presented in detail and applied to the axisymmetric stab-penetration test. A summary is given for the key stages of the material models developed successively from the initial version to the final revised versions. Concepts and problems encountered are briefly explained.

#### *Bi-linear isotropic with abrupt failure (initial model)*

This model proved to have some flaws in terms of encoding. Under general multiaxial loading, the bi-linear approach might result in different stiffness in different directions. This is especially so at high deviatoric strains, eg in uniaxial tension where the highly strained direction at some point will be in the high stiffness range and the other passive strains will be in the low stiffness range. Obviously the material cannot be assumed isotropic in this case as it has been. The abrupt failure with stress reset and element deletion in a single increment works well numerically. However, it seems to cause high force transients (acceleration) being applied to the adjacent elements which then halts the analysis due to high deformation rate to wave speed ratio as rupture of the specimen initiates.

*Non-linear isotropic with damage evolution and gradual failure*

An attempt to solve the force transient problem was made by introducing gradual stress reset during failure. The loading path was made non-linear by curve fitting an exponential expression as proposed by Kenedi et al (1964) to the experimental test data from pig skin. In fact the approach is piecewise linear as the stress update is linear for each strain increment. The elastic modulus is updated at each increment following the derivative of the fitted stress-strain curve. At this stage it was still not realised that deviatoric strains invalidate the isotropy assumption. The gradual stress reset was implemented by means of a damage evolution law. Once maximum strain was reached, the effective stiffness modulus decreased through zero to a negative maximum value. Gradual stress reset was found effective in one-dimensional problems but implementation in a multi-axial system is rather complicated. Damage will usually initiate in one local material direction and the problem is to control the stress reset in the passive directions ensuring all directions reach zero at the same time which is necessary to maintain a valid material description.

*Non-linear orthotropic with perfect plasticity, history dependent unloading, and abrupt failure*

During work on the previous model it was realised that the isotropy assumption for any non-linear material was invalid. The solution to this problem was to adopt an orthotropic approach to the stress update. As mentioned the analysis is incremental, allowing the use of an orthotropic Jacobian stiffness matrix for interrelating the three potentially different elastic moduli. These moduli are updated at each (small) strain increment resulting in a global nonlinear stress-strain relationship.

Perfect plasticity and abrupt stress reset replaced the gradual damage and stress reset. Avoiding the synchronisation problem of gradual stress reset, the plastic-abrupt failure still provides some degree of gradual load transfer through yield thus causing smaller force transients when the stress is reset in one increment at failure. After failure, remaining intact elements might have yielded a little and should unload elastically from the previous elastic-plastic strain state. This is implemented by storing the plastic strain during yield and using it as an offset elastic strain during unloading.

### 5.1.1 Material model with gradual failure

The approach used both in the intermediate stages described above and the final version is not directly derived from the experimental test data but more a combination of these and hypotheses on how the material is likely to behave when represented by solid continuum finite elements. The chosen method of using continuum elements is fully justified and straightforward when modelling global elastic behaviour similar to the experimental tests prior to failure. The real difficulty arises when modelling of failure or continued penetration is attempted. The analysis must remain stable during failure and removal of elements which often is hampered by numerical limitations (eg deformation rate to wave speed ratio). On a global level, the model must represent the real material accurately being nonlinear with abrupt failure. At finite element level - with several solid elements through the thickness - a single element must to some degree emulate the behaviour of the real material viewed at the same scale.

It is known that in skin some slipping occurs between the main loadbearing collagen fibres when close to failure (Wilkes et al (1973)). The author believes that at continuum finite element level this slipping can realistically be modelled as perfect plasticity. At present, the maximum plastic strain (slipping) is a pure guess. More plastic strain energy will provide higher damping during failure and yet it must not affect the global abrupt failure mode.

#### *Elastic response*

The stiffness is strain dependent due to the elastic stress-strain non-linearity. For a general stress state in 3-d space the three elastic moduli are potentially different which invalidates any assumption of isotropy. In an incremental analysis a linear elastic orthotropic Jacobian stiffness matrix can interrelate the potentially different stiffnesses which change at each strain increment.

For an orthotropic material the compliance matrix  $D$  is usually given and strain is expressed as a function of stress:

$$[\epsilon] = [D] \times [\sigma] \quad (18)$$

where

$$D = \begin{bmatrix} \frac{1}{E_1} & -\frac{\nu_{21}}{E_2} & -\frac{\nu_{31}}{E_3} & 0 & 0 & 0 \\ -\frac{\nu_{12}}{E_1} & \frac{1}{E_2} & -\frac{\nu_{32}}{E_3} & 0 & 0 & 0 \\ -\frac{\nu_{13}}{E_1} & -\frac{\nu_{23}}{E_2} & \frac{1}{E_3} & 0 & 0 & 0 \\ 0 & 0 & 0 & \frac{1}{G_{12}} & 0 & 0 \\ 0 & 0 & 0 & 0 & \frac{1}{G_{13}} & 0 \\ 0 & 0 & 0 & 0 & 0 & \frac{1}{G_{23}} \end{bmatrix} \quad (19)$$

If the following relationship is applied:

$$\frac{\nu_{ij}}{E_i} = \frac{\nu_{ji}}{E_j} \quad (20)$$

a simplification can be made as the compliance matrix  $D$  becomes symmetric:

$$D = \begin{bmatrix} \frac{1}{E_1} & -\frac{\nu_{12}}{E_1} & -\frac{\nu_{13}}{E_1} & 0 & 0 & 0 \\ & \frac{1}{E_2} & -\frac{\nu_{23}}{E_2} & 0 & 0 & 0 \\ & & \frac{1}{E_3} & 0 & 0 & 0 \\ & & & \frac{1}{G_{12}} & 0 & 0 \\ & \text{Symm.} & & & \frac{1}{G_{13}} & 0 \\ & & & & & \frac{1}{G_{23}} \end{bmatrix} \quad (21)$$

In VUMAT stress must be expressed as a function of strain:

$$[\sigma] = [C] \times [\varepsilon] \quad (22)$$

and the compliance matrix needs to be inverted to give the stiffness matrix. This

operation was carried out in Mathematica version 3.0 (Wolfram Research), a software capable of symbolic algebra. The compliance matrix  $D$  from above was inputted, inverted and simplified to give the stiffness matrix  $C$  which also is symmetric:

$$C = \begin{bmatrix} \frac{E_1^2(E_2 - E_3\nu_{23}^2)}{F} & \frac{E_1E_2(E_2\nu_{12} + E_3\nu_{13}\nu_{23})}{F} & \frac{E_1E_2E_3(\nu_{13} + \nu_{12}\nu_{23})}{F} & 0 & 0 & 0 \\ & \frac{E_2^2(E_1 - E_3\nu_{13}^2)}{F} & \frac{E_2E_3(E_2\nu_{12}\nu_{13} + E_1\nu_{23})}{F} & 0 & 0 & 0 \\ & & \frac{E_2E_3(E_1 - E_2\nu_{12}^2)}{F} & 0 & 0 & 0 \\ & & & G_{12} & 0 & 0 \\ & & & & G_{13} & 0 \\ & & & & & G_{23} \end{bmatrix}$$

$$\text{where } F = E_1(E_2 - E_3\nu_{23}^2) - E_2(E_2\nu_{12}^2 + E_3\nu_{13}(\nu_{13} + 2\nu_{12}\nu_{23})) \quad (23)$$

If Poisson's ratio is assumed the same in all directions before inversion

( $\nu = \nu_{12} = \nu_{13} = \nu_{23}$ ) the stiffness matrix again becomes slightly simpler:

$$C = \begin{bmatrix} \frac{E_1^2(E_2 - E_3\nu^2)}{F} & \frac{E_1E_2\nu(E_2 + E_3\nu)}{F} & \frac{E_1E_2E_3\nu(1 + \nu)}{F} & 0 & 0 & 0 \\ & \frac{E_2^2(E_1 - E_3\nu^2)}{F} & \frac{E_2E_3\nu(E_1 + E_2\nu)}{F} & 0 & 0 & 0 \\ & & \frac{E_2E_3(E_2\nu^2 - E_1)}{F} & 0 & 0 & 0 \\ & & & G_{12} & 0 & 0 \\ & & & & G_{13} & 0 \\ & & & & & G_{23} \end{bmatrix}$$

$$\text{where } F = E_1(E_2 - E_3\nu^2) - E_2\nu^2(E_2 + E_3 + 2E_3\nu) \quad (24)$$

*Stability:*

In Abaqus/Explicit version 5.6 section 9.2.1 stability criteria are stated for orthotropic materials in terms of the following in-equalities:

$$E_1, E_2, E_3, G_{12}, G_{13}, G_{23} > 0 \quad (25)$$

and

$$|v_{ij}| < \left( \frac{E_i}{E_j} \right)^{\frac{1}{2}} \quad (26)$$

if the relationship in equation (20) is applied. For orthotropic materials three different values of  $v$  are possible but for simplicity it is assumed that these values are the same. For skin the non-linear behaviour is modelled as piecewise linear which results in orthotropic behaviour. The three stiffness components are strain dependent thus a high stiffness is obtained at a high strain value and different stiffnesses are encountered at any strain state which is not hydrostatic. At, eg high uniaxial strain, there is a great difference between  $E_1$  and  $E_2$  as well as between  $E_1$  and  $E_3$ . This very common situation can violate the stability criterion especially for high values of  $v$ . Two measures could solve this problem: 1) Keep  $v$  small. 2) Keep the stress-strain relationship closer to linear.

It might not be correct to assume  $v$  to be constant over a large range of strain and with large differences between the stiffness in active and passive directions. Poisson's ratio could possibly be dependent on the difference between active and passive strain. This phenomenon has indeed been confirmed for human skin by Kenedi et al (1964) as mentioned in section 2.2.2. Also Stokes and Nied (1987) found Poisson's ratio strain dependent with the relationship:  $\lambda_2 = \lambda_1^{-n}$  ( $n = 0.4 \dots 0.5$ ) for flat sheet-like polycarbonate specimens subjected to large strains in uniaxial tension.

For stability reasons Poisson's ratio was kept constant at a value of 0.25. This value is indeed lower than what is suggested by the literature and the experimental findings. However, it was found more important to maintain a realistic degree of non-linearity of the stress-strain curve in return.

### *Plastic response*

Once the experimentally determined maximum stress is reached yield occurs simultaneously in all material directions. Stresses follow a conventional isotropic linear stress update with a very low stiffness and Poisson's ratio is unchanged. This approach reduces stability problems in the plastic range and as such can be regarded as isotropic hardening although the amount of hardening is negligible. A control routine ensures that

isotropic stress update only takes place during active yield and negative strain increments will result in return to orthotropic non-linear stress update during unloading.

#### *Gradual stress reset*

At a preset plastic strain level damage and gradual stress reset (softening) initiates. Softening results in a negative effective stiffness modulus and is in general unstable calling for fixed time incrementation. In a given 3-d stress state there are potentially six different stress values present at the onset of softening. Also for stability reasons it must be ensured that all stresses are reset to zero at the same time. The gradual stress reset has been tied to the time increments to maintain stability and synchronised stress reset to zero leading to deletion of the material point from the analysis.

#### *VUMAT encoding*

The revised material model was written in Fortran90 code based on similar procedures to those described in section 3.2.1. Compared to the initial bi-linear isotropic material model the revised model is more complex due to a multitude of control routines necessary for history dependence and gradual stress reset. Control routines have been used in preference to complicated analytical expressions due to the relative ease of debugging the control routines. The use of subroutines within the code has been avoided which, in the author's opinion, simplifies editing. A detailed description of the material model encoding is given below with reference to a complete Fortran file for axisymmetric elements (Appendix 5.2). Code extracts are shown in the main text in courier font and the letter "j" represents the four possible components for an axisymmetric element.

The non-linear elastic stress update is based on the exponential expression:

$$\sigma = a_k * e^{E_{\text{Elast}} * \epsilon_{\text{an}}}$$

where  $\sigma$  is the true Cauchy stress in uniaxial tension,  $a_k$  is a constant,  $e^{E_{\text{Elast}}}$  is the total elastic strain, and  $\epsilon_{\text{an}}$  is the exponent (also a constant). The two constants  $a_k$  and  $\epsilon_{\text{an}}$  were found by curve fitting the experimental stress-strain curve from pig skin. The stress-strain curve was differentiated to give the strain dependent elastic stiffness:

$$E_{\text{E}} = \epsilon_{\text{an}} * a_k * e^{E_{\text{Elast}} * \epsilon_{\text{an}}} * (\epsilon_{\text{an}} - 1)$$

Stiffness proportional damping was incorporated as an additional stiffness dependent on

the strain rate in each material direction:

$$EDamp = \beta_r * E * eRate$$

where  $\beta_r$  is a damping factor and  $eRate$  is the strain rate given by strain increment and time increment:

$$eRate = \text{ABS}(\text{strainInc}(i,j) / dt)$$

To avoid too great a difference between stiffnesses these are kept between  $E_{min} = 3.E7$  Pa and  $E_{max} = 1.1E8$  Pa. As long as the material is purely elastic the orthotropic stiffness matrix updates the stresses based on the three potentially different direct stiffnesses  $E1$ ,  $E2$ ,  $E3$ , and the shear stiffness  $E4$  (for axisymmetric elements).

Total strain is updated and stored as a state variable and once the yield stress  $sYield$  is exceeded in any one direction yield occurs in all directions and plastic strain is updated and stored as another state variable. Plastic stress is updated by an isotropic stiffness matrix with low stiffness. Damping is also applied here based on the average strain rate for the material point. Further stretching leads to gradual failure which initiates at a plastic strain of 0.1. At the onset of tensile unloading the stress state is stored and an unloading factor is calculated for each direction to ensure synchronised stress reset:

$$f_j = \text{const} * \text{stressNew}(i,j) / sYield$$

All variables which are not updated in each increment throughout the analysis must be stored as a state variable. The unloading constant  $\text{const}$  is dependent on the average strain rate and the time increment is multiplied with the unloading factor before subtraction from the stress at the beginning of the increment in order to make the synchronised stress reset independent from time increment size.

Once the absolute value of a stress component is less than 1.E6 Pa a failure flag is set to one. In near pure uniaxial stress states small passive stresses are kept at 10 Pa for stability during yield and unloading. Failure flags must be set to one in all directions before the material point is deleted from the analysis. If compressive strain increments are encountered at any point during active yield or unloading elastic orthotropic stress update will be reactivated. The stress at which unloading initiated is stored as a state variable which acts as a new failure point.

### 5.1.2 Material model with abrupt failure

During analyses using the above model with gradual failure, problems were encountered as an element entered the plastic region. Deformation speed could not be controlled during yielding thus preventing continued penetration analysis. This is discussed further in section 5.3.2. To enable continued penetration analysis the plasticity and gradual failure was removed and an elastic approach with abrupt failure was looked into again, but with other means of ensuring a stable analysis as described below.

#### *Elastic response*

A non-linear orthotropic elastic stress update similar to that of the gradual failure model described in section 5.1.1 was used. Stiffness dependent damping was also maintained as this worked well to ensure mesh stability at high strains.

#### *Abrupt failure*

Direct stress was again used as failure criterion. Once any of the direct stress components exceeds the failure stress, all stress components are reset to zero in a single increment and the material point is deleted from the model.

#### *Stability*

The bulk viscosity of the material can be controlled by a generic Abaqus command (\*BULK VISCOSITY). Linear bulk viscosity damps out "ringing" in the highest element frequency and quadratic bulk viscosity prevent elements from collapsing under high loading rates and is only applied under compressive volumetric strain (Abaqus/Explicit version 5.7 section 6.2.1). Mass proportional damping (\*DAMPING) introduces damping forces caused by absolute velocities of the model. This simulates the model moving in a viscous fluid (Abaqus/Explicit version 5.7 section 11.1.1).

The actual values of the damping factors necessary to ensure a stable analysis were not investigated in detail due to time constraints. Continued penetration was found possible with a linear bulk viscosity parameter of 0.6 (default: 0.06), a quadratic bulk viscosity parameter of 1.8 (default: 1.2), and a mass proportional damping factor of 10 s<sup>-1</sup> (default: 0 s<sup>-1</sup>). The generic stiffness proportional damping cannot be used in combination with VUMAT and is therefore still incorporated directly in the material model.

### *VUMAT encoding*

The encoding for the material model with abrupt failure is a much simplified version of the model with gradual failure (section 5.1.1) where the elastic stress update is re-used. The complete Fortran90 encoding is shown in Appendix 5.3 for the orthotropic material model with abrupt failure.

## **5.2 Test and verification**

### **5.2.1 Single element**

The simplest method of evaluating a material model is the application of the model to a single element. A single membrane element with dimensions similar to the pilot tensile test specimen (section 2.1.1) was stretched to failure using displacement control. Basic features such as yield and softening as well as the uniaxial non-linear stress-strain curve could be verified and tuned. Since stiffness dependent damping was introduced, which essentially causes rate dependence, different stretch ratios were applied to the single element model. The stress-strain response for the material model with gradual failure is shown in Figure 5.1 at different strain rates. Stiffness proportional damping is only supposed to damp out “ringing” of the elements thus only very high strain rates should cause significant damping. As can be seen in Figure 5.1 stiffening due to damping is only prominent at high strain rates ( $1000 \text{ s}^{-1}$ ) and in particular in the plastic range. Limitations are imposed on the damping stiffness for stability reasons. At low strain rates ( $10 \text{ s}^{-1}$ ) practically no damping is seen as the stress-strain curve here coincides with those of even lower strain rates. All following tests on the single element were carried out at ( $10 \text{ s}^{-1}$ ) or lower. The material model with abrupt failure (not shown) has exactly the same elastic response as the model with gradual failure.

The elastic - plastic - unloading response was tested by stretching the element into the plastic range, unloading until compression occurred, then re-loading until failure was complete. A stress-strain curve of this cycle is shown in Figure 5.2 for the gradual failure model. The abrupt failure model is shown in Figure 5.3 when simply loaded to failure.

Various combinations of biaxial loading were also tested for the gradual failure model. Figure 5.4 shows the active and slightly lower passive stress versus time when the element is loaded to failure biaxially. This verifies synchronised yield and synchronised gradual stress reset during failure.

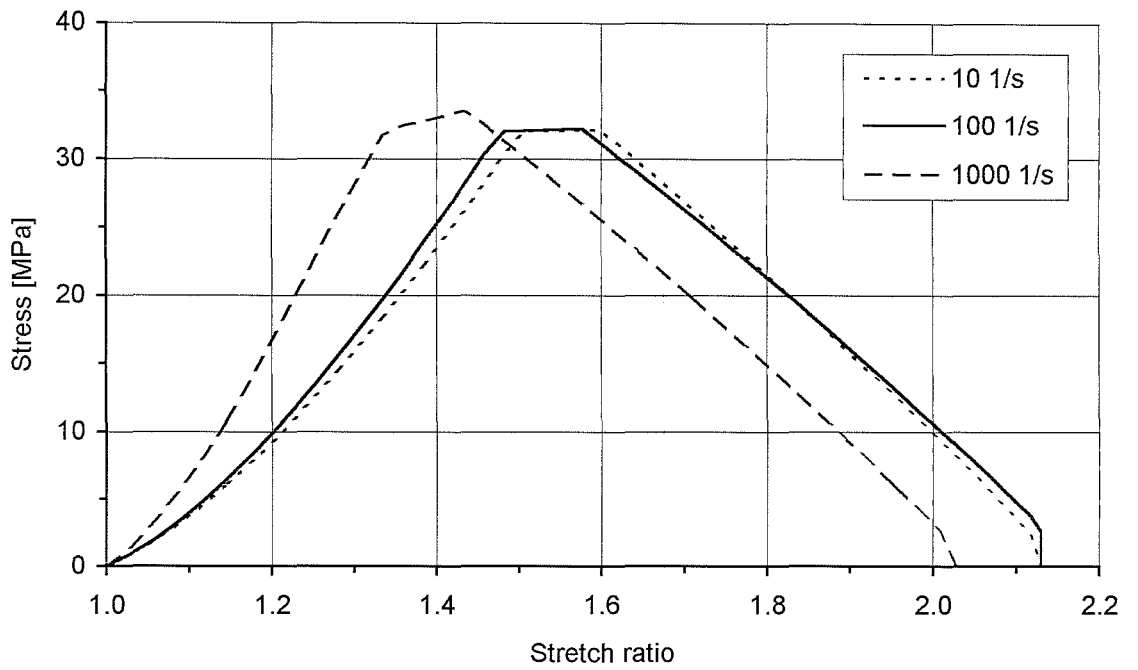


Figure 5.1. Constant strain rate loading to complete failure at different strain rates for gradual failure model.

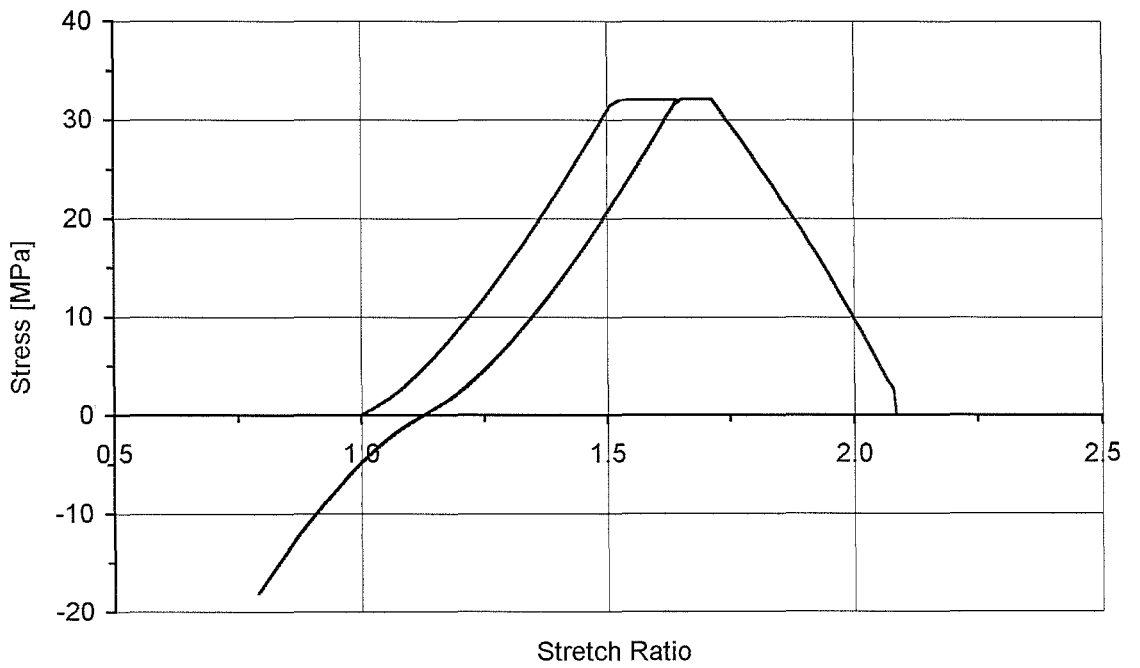


Figure 5.2. Single membrane element stretched to yield, compressed, and re-loaded to failure with gradual failure model.

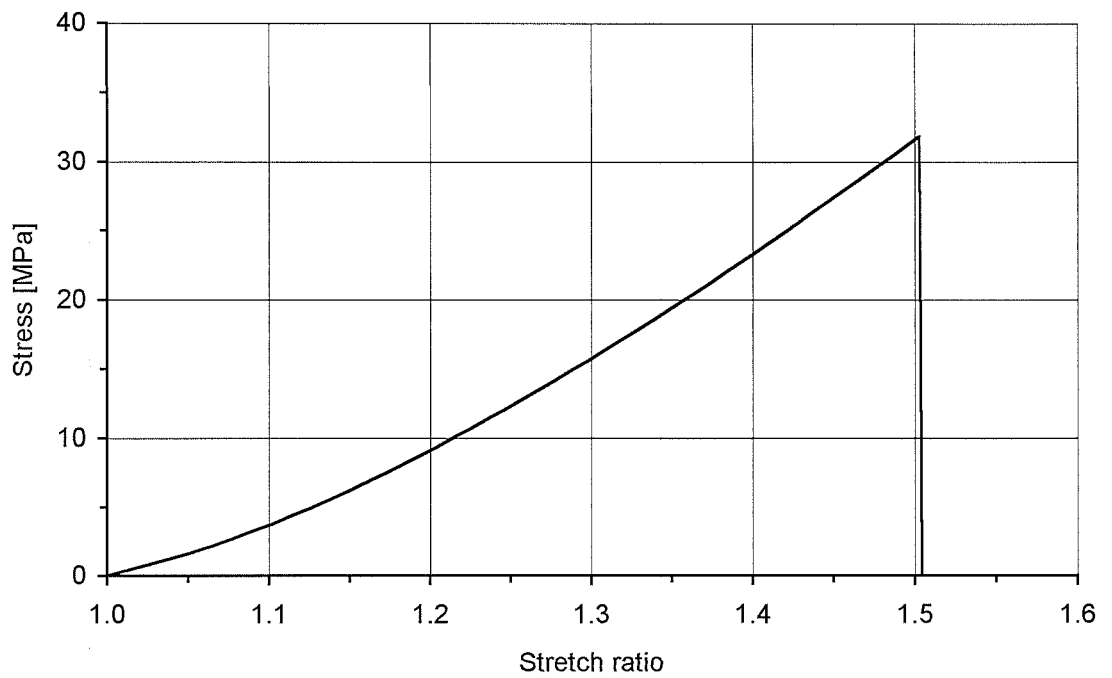


Figure 5.3. Single membrane element stretched to failure with abrupt failure model.

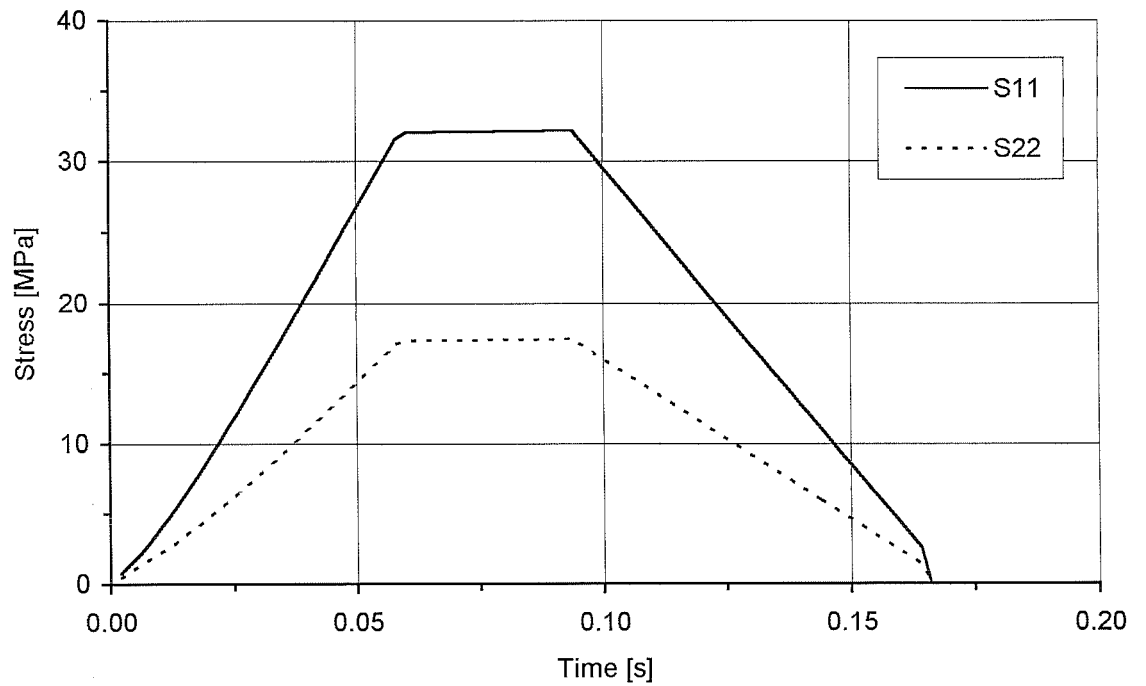


Figure 5.4. Stress-time curves of biaxially loaded single membrane element showing synchronised failure

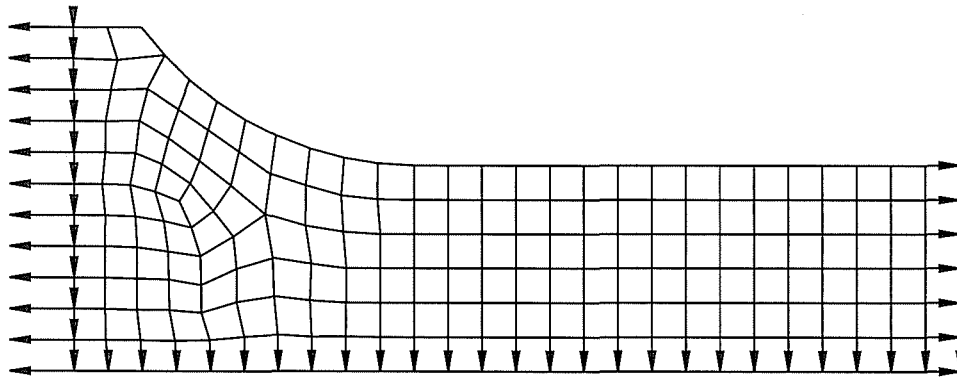


Figure 5.5. Quarter mesh of dumbbell shaped tensile specimen.

### 5.2.2 Multi element model

During the development phase it was realised that a multi-element model was needed to verify the exact global behaviour during and after failure. This is particularly so for Abaqus/Explicit since this code performs a fully dynamic analysis taking mass accelerations into account. During failure of hyperelastic materials large strain energy quantities are released and transferred to the neighbouring elements. This event can obviously not be traced in a single element model.

#### *Mesh and boundary conditions*

Due to the questionable assumption of material homogeneity the multi element model was meshed to the exact dimensions of the dumbbell shaped tensile test specimen described in section 2.2. Reaction force and displacement could be directly monitored and compared against the experimental force-displacement data. This measure was taken since the relation between nominal stress-strain and true stress-strain was not known with sufficient accuracy. Final adjustments could be made to the constitutive model in terms of ultimate stress and strain. Due to two-fold symmetry a quarter model (Figure 5.5) was meshed with 178 four-noded membrane elements, using MSC Patran v 8.0 Finite Element Pre/Post Processor. A thickness of 2 mm, matching that of pig skin, was assigned to the elements. Symmetry boundary conditions were applied to the relevant sides and a constant velocity of 40 mm/s was applied to the free end of the specimen resulting in a strain rate of  $0.6 \text{ s}^{-1}$ .

*Results from multi-element model*

Comparison between experimental tensile data and the computational analysis are made in terms of reaction force and displacement at the displaced end of the specimen. Both reaction force and displacement from the FE quarter model were multiplied by two to enable direct comparison with experimental force-displacement curves. Results from the material model with gradual failure are shown in Figure 5.6 and for the abrupt failure model the results are shown in Figure 5.7. Both models result in an ultimate force of around 1400 N which is in good agreement with the experimentally obtained forces for fresh back skin which was used for the stab-penetration experiments (Figure 2.15 - Figure 2.18). The computational results were obtained with an ultimate true direct stress of 32 MPa as can be seen in Figure 5.1 to Figure 5.4 for the tests on a single element.

The gradual failure model resulted in slightly higher ultimate force and displacement than the abrupt failure model. Stiffening due to damping during yield explains this behaviour for the gradual failure model. Non-linearity is, however, not as pronounced in the computational tensile test results as they are in the experimental force-displacement curves. The non-linearity could be increased, however, with the potential risk of lowering the material stability.

Another basic purpose of the multi-element model was to visually monitor the mesh distortion as failure occurred. This was done by viewing the displaced mesh in Abaqus Post. A contour plot of tensile stress just prior to failure is shown in Appendix 10. It is noticed that the highest stress is found near the transition between the narrow gauge section and the wider gripping area. Failure occurred at this location and shows that the specimen geometry is not ideal. This is in accord with the fact that a number of specimen failed at the transition during experimental testing.

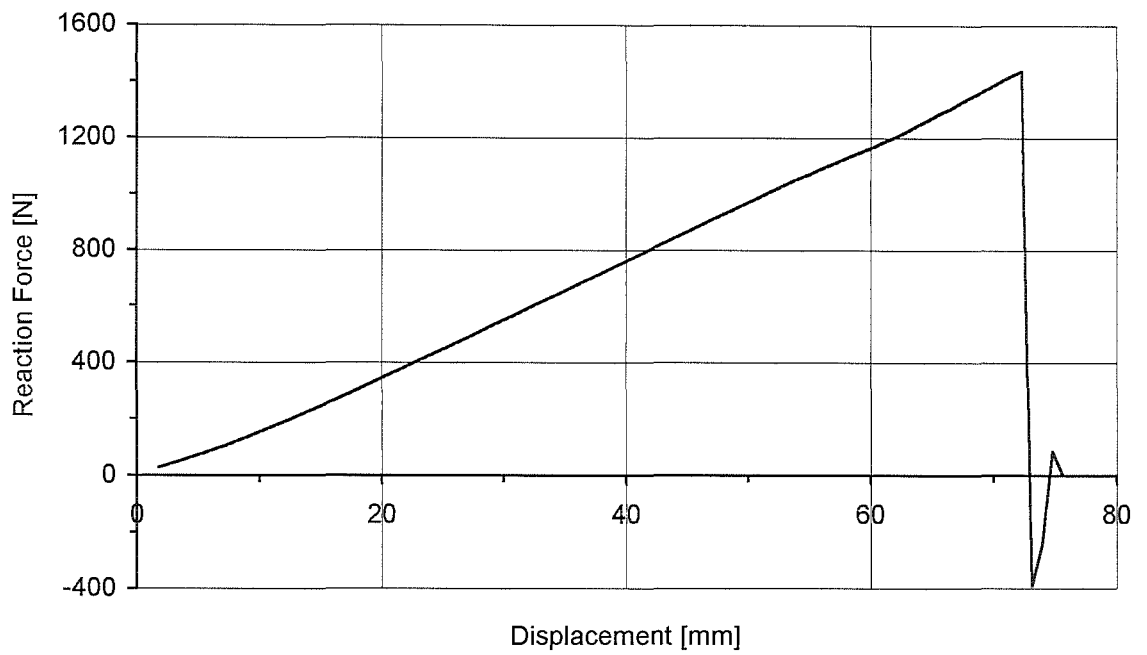


Figure 5.6. Force-displacement curve for computational tensile test with dumbbell shaped specimen and gradual failure material model.

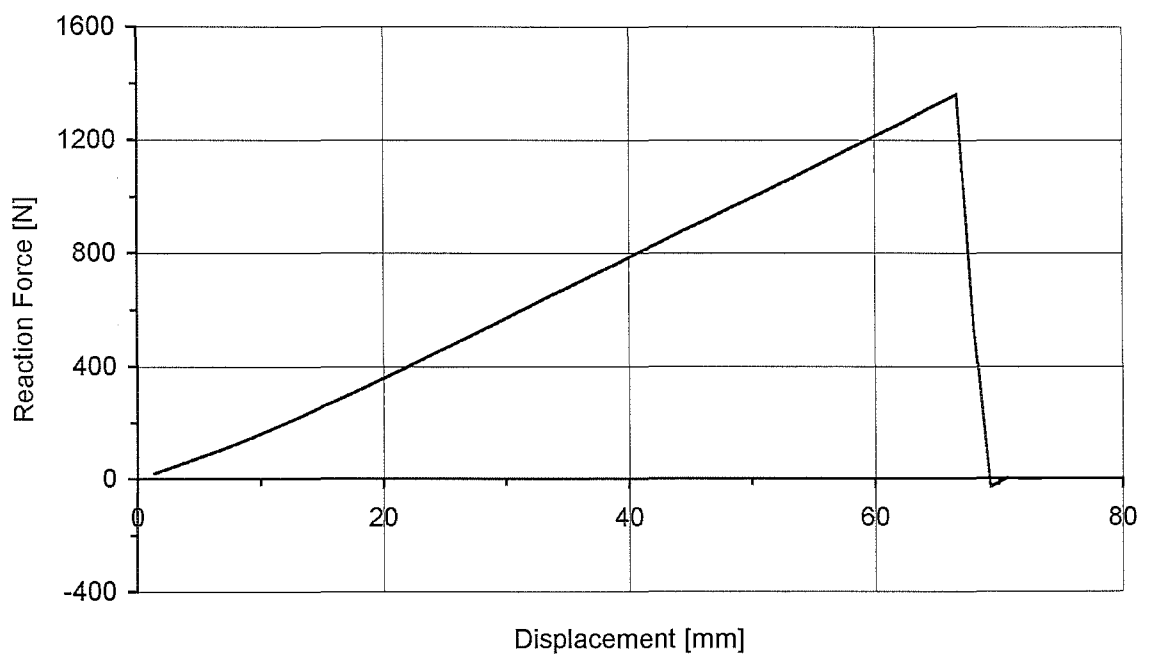


Figure 5.7. Force-displacement curve for computational tensile test with dumbbell shaped specimen and abrupt failure material model.

### 5.3 Application to axisymmetric stab-penetration model

#### 5.3.1 Mesh design and analysis

At this stage the axisymmetric stab-penetration model was updated to Abaqus version 5.7 level. The main change was the introduction of an analytical rigid surface representing the punch thus replacing the rigid elements used in the initial model. The analytical rigid surface is simple to define and should be more efficient for contact analysis and reduce "noise" introduced by the facets associated with elements (Abaqus/Explicit version 5.7 section 2.3.3). The rigid surface is still linked by a reference node to a rigid body where boundary conditions are applied to the reference node. A sample input file is shown in Appendix 6 for the revised axisymmetric stab-penetration model with penetrator A.

#### *Target*

The initial target mesh had the smallest elements situated in the transition between high and low mesh density areas (Appendix 9.1). As the stable time increment size is determined by the smallest element it was desirable to have a uniform element size in the refined impact zone. The mesh was optimised by using tied contact between the highly refined impact zone and the rest of the target resulting in a sudden change in mesh density but allowing a well formed mesh with all rectangular elements. Generic Abaqus mesh generation commands were used for the geometrically simple mesh enabling easy adjustment to the mesh. Slightly different meshes were used for the four penetrators in terms of the refined mesh area size. Additional elements were used for penetrator D to keep the refined element size roughly the same for all penetrators. A total of 440 elements form the target mesh for penetrator D and 380 elements for the other penetrator sizes. As in the previous Patran generated mesh the first 20 columns of nodes in the impact zone were defined as contact nodes. Boundary conditions were applied as before with x-symmetry on the nodes in the centre of the disk shaped specimen and nodes at the perimeter were pinned. Meshes used for the four penetrator sizes are shown in Appendix 11 as undeformed plots and were shared by the two revised material models.

### *Analysis protocol*

A ramp velocity function was used as displacement control for the punch allowing contact to be established between target and punch before the full constant velocity of 80 mm/s was reached. This measure was taken to work around the deformation speed problem which occurred in particular as contact was established. The chosen velocity is indeed higher than that used in the experiments, however, it was necessary to keep total analysis time within reasonable limits to make progress. As relatively high damping factors are used to maintain stability the higher velocity might influence the results, a point for further investigation. It was noticed that highly compressed surface elements in the impact zone could undergo sudden distortion due lack of friction. A small amount of friction ( $\mu=0.01$ ) was introduced at the punch / target interface to enhance mesh stability just prior to failure. The analyses were performed in two steps using automatic time incrementation and mass scaling in the first step which typically lasted 0.2 s. Mass scaling was used to keep the time increment above 0.4  $\mu$ s. If the stable time increment size goes below this limit the mass of the critical elements is increased (Abaqus/Explicit section 21.17.1). In the second step lasting 0.02 s fixed time increments were used without mass scaling to capture the sudden rupture of the target with a high number of restarts written in a short time interval. The analyses with the revised material models were carried out on a Sun SPARC station 4 workstation.

### **5.3.2 Results and evaluation for gradual failure**

Results from the computational stab-penetration test were successfully obtained for all four penetrator sizes. Force-displacement curves are shown in Figure 5.8. The point of rupture was reached in all cases, however, continued penetration could not be simulated due to excessive deformation speed in the failing elements. This is discussed in more detail below. The maximum penetration force for each penetrator increases gradually from 200 N for penetrator A to 360 N for penetrator C. Penetrator D shows a maximum value of 280 N which is much less than expected. If the linear relationship between penetration force and penetrator diameter indicated by penetrator A, B, C should be followed, the force for penetrator D should be around 420 N. Contour plots of direct stress are shown in Appendix 11 for all four penetrator sizes. A plot is shown for each penetrator size in the undeformed state and at the last increment written before

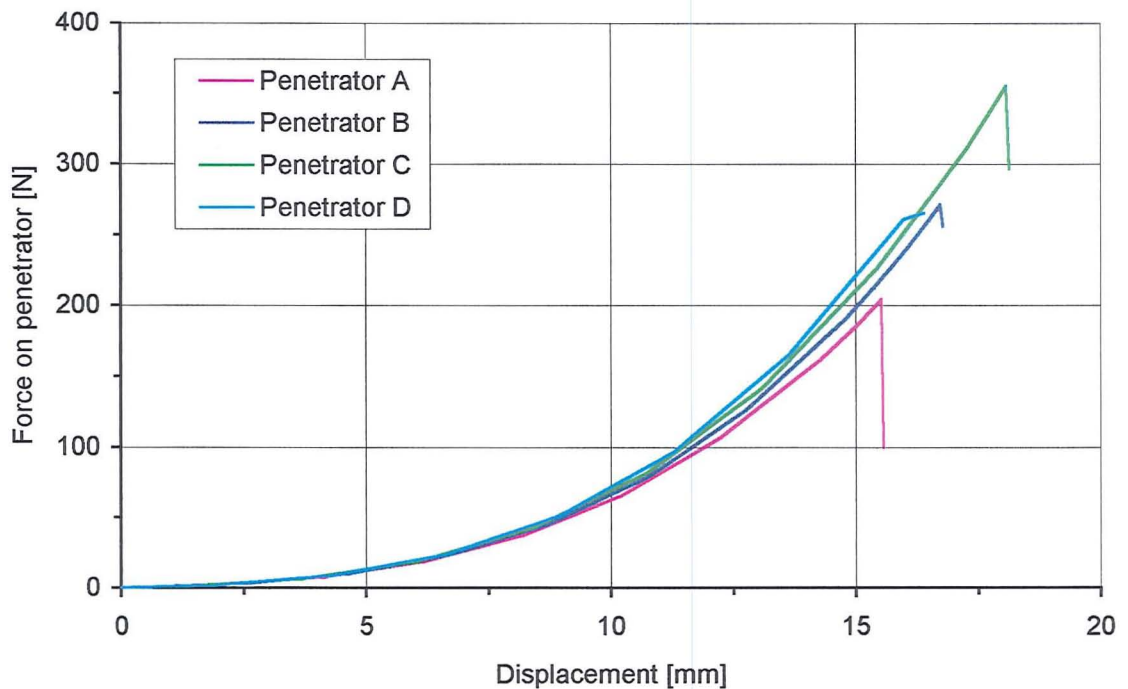


Figure 5.8. Computational stab-penetration test using axisymmetric FE model with orthotropic material model with gradual failure. Original in colour.

the analysis was halted. Radial stress (S11) is the highest and thereby the failure determining stress for penetrator A, B, C. Hoop stress (S33) is the highest for penetrator D. Failed elements are included in the contour plots and are seen as the highly distorted elements. These elements are excluded from the numerical analysis at this point and carry no stress but are still displayed graphically in Abaqus Post.

#### *Stable time increment*

The stable time increment is by default determined automatically by Abaqus. This is based on density and stiffness of the material and since the material is non-linear the stiffness increases with higher strain thereby lowering the stable time increment. During elastic stress update the automatic time incrementation works satisfactorily, but during the plastic stress update the material becomes very soft and the time increment increases beyond the stability limit. One way of avoiding this problem is to use fixed time increments. To ensure a stable analysis the fixed time increment must be set on the safe side, ie lower than the optimum increment size, which leads to longer total analysis time. The analysis can be divided into two steps where the first is using automatic time incrementation and the second uses fixed incrementation. However, finding the

appropriate time mark initiating the second step is a matter of trial and error. Also finding the increment size which will allow a stable analysis following the prescribed stress strain path is a matter of trial and error. This increment size is usually orders of magnitude lower than the stable increment size in the elastic region.

#### *Deformation speed to wave speed ratio*

A problem which was often encountered during the finite element analyses was that of too high deformation speed to wave speed ratio. This ratio must be below a certain value to maintain a stable analysis and once this value is exceeded Abaqus terminates the analysis. The wave speed is determined by model dimensions, material stiffness, and density. Soft tissue has a high density relative to the stiffness, especially at low strains, which results in a low wave speed for the material. The upper limit for deformation speed is therefore rather limited for soft tissue and in computational modelling of this material tough restrictions must be imposed on the velocities applied in impact / contact analysis. An artificially high bulk modulus can be applied in the analysis which can help prevent elements collapsing during sudden loading. This introduces a rate dependence which stiffens the element at high strain rates thus allowing higher deformation speed. Obviously an artificially high bulk modulus can influence the dynamic response of the material and cause “false” results and should therefore be set as low as possible while still ensuring a stable analysis.

Stiffness proportional damping was introduced both in the elastic and plastic region. In the elastic region a small amount of damping worked satisfactory eliminating most oscillations which were otherwise prominent at high strains. Damping in the plastic range was introduced in an attempt to avoid too high deformation speed in a yielding element. For this to be effective a relatively high amount of damping is needed and high levels of stress are reached in the yielding element prior to failure. Any strain localisations in the model are thereby spread to a larger area or localised failure might not occur at all. This poses a dilemma between: a) Omitting plasticity with excessive deformation speed in elements adjacent to a failing element. b) Including plasticity with excessive deformation speed in the failing element itself. The introduction of plasticity and gradual stress reset has not been successful in solving the deformation speed problem during failure simulation but has merely moved it from surrounding elements to the failing element itself.

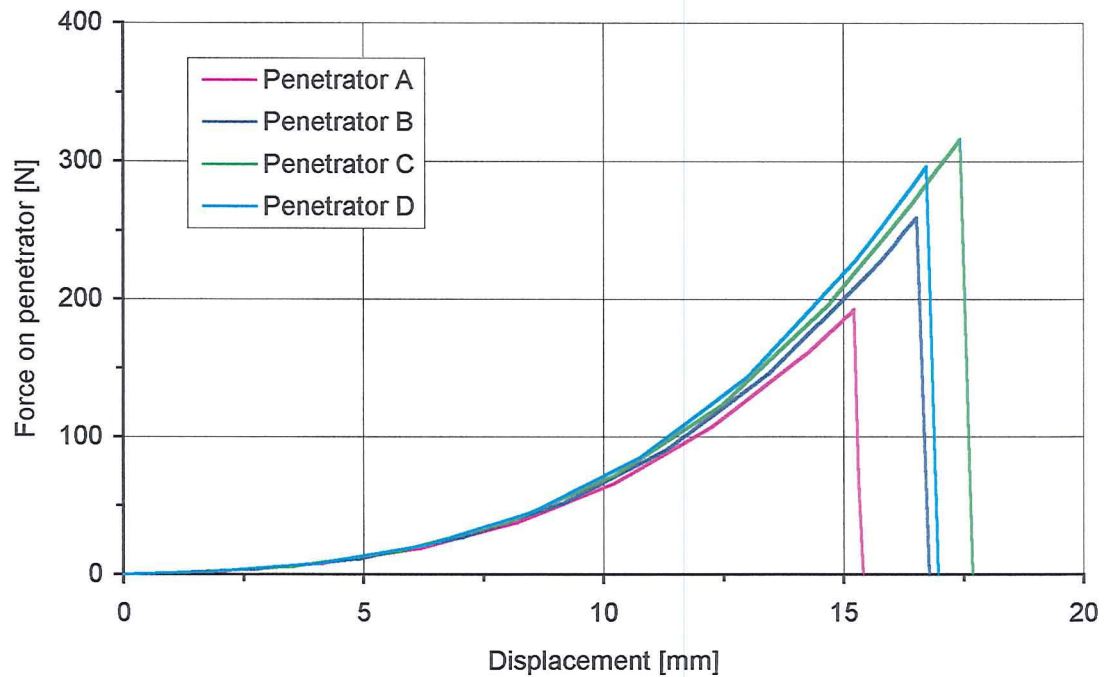


Figure 5.9. Computational stab-penetration test using axisymmetric FE model with orthotropic material model with abrupt failure. Original in colour.

### 5.3.3 Results and evaluation for abrupt failure

Eliminating the wavespeed problems encountered with plasticity and gradual failure was successful in terms of being able to simulate continued penetration. The analyses for all four penetrator sizes continued until the total analysis time was completed. Force-displacement curves are shown in Figure 5.9. Contour plots of direct stress are shown in Appendix 12 for all four penetrator sizes. A plot is shown for each penetrator size at the last increment prior to rupture and the first increment after rupture with failed elements removed. Contrary to the gradual failure model, hoop stress (S33) is the highest and thereby the failure determining stress for penetrator A, B, C, and radial stress (S11) is the highest for penetrator D. Maximum penetration forces are similar in pattern and magnitude to the values obtained with gradual failure. The similar magnitudes were indeed expected as the failure criterion is the same for the two material models.

The fact that penetrator D shows a too low value might suggest that the failure mechanisms of skin are not fully determined by simple maximum direct stress. It is noted that the highest direct stress component differs between penetrator D and the other three penetrator sizes. The computed penetration forces are in general lower than the experimental values but the linear trend is apparent when penetrator D is disregarded

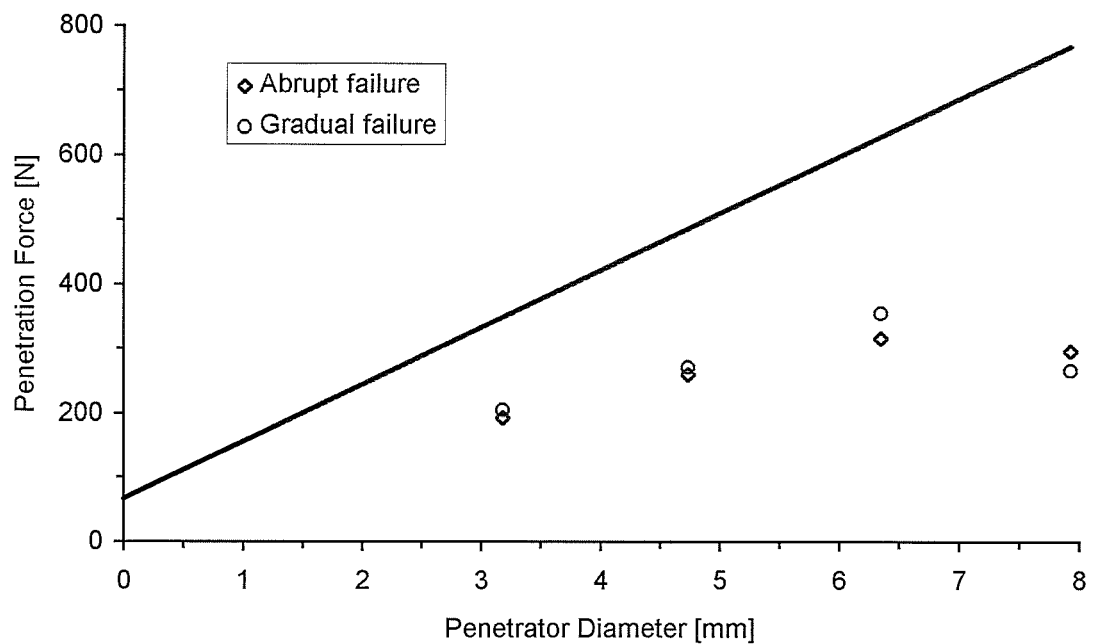


Figure 5.10. Maximum penetration force from axisymmetric models plotted against straight line fit from experimental values.

(Figure 5.10). The failure stress was found by matching experimental and computational force-displacement curves from dumbbell shaped tensile specimen. The maximum stress value deduced therefrom is highly sensitive to the specimen thickness which was not measured accurately. In cases where the specimen was slightly thinner than assumed the maximum stress would be found lower than it actually is. This could well explain the too low computational predictions of the penetration force.

### *Damping*

It was found that by increasing the quadratic bulk modulus artificially as well as increasing the mass proportional damping factor continued failure could be modelled successfully. The added viscosity ensured that loading rates are controlled on elements adjacent to a failing element and the higher bulk modulus has a rate dependent stiffening effect thus allowing higher loading rates without exceeding the maximum deformation speed to wave speed ratio. The damping factors were not optimised analytically and might be set higher than necessary thus influencing force-displacement readings at the point of rupture.

## 6 Discussion and conclusions

### 6.1 Characteristics of tissue simulants

#### *Skin simulants*

Synthetic chamois was tested as a skin simulant but was found to be too directionally dependent and around three times weaker than human skin in terms of tensile strength. High moisture content in the synthetic chamois caused a slight increase in both failure stress and strain which is contrary to real skin.

Pig skin was tested as the other human skin simulant. From the results of the experiments conducted, pig skin was found to have almost the same mechanical properties as human skin. It exhibited a comparable tensile behaviour similar to that of human skin. Although it has some disadvantages, e.g. non-uniform mechanical properties, material being perishable implying time constraints on test routines, pig skin was chosen as the most suitable skin simulant.

The inconsistencies in mechanical properties associated with pig skin have to some degree been accounted for by using average values obtained from multiple specimens. The emphasis, in terms of numbers of specimens, was put on the uniaxial tensile test of pig skin and the stab-penetration test using blunt penetrators. Additional tests such as notch sensitivity, cyclic loading, and compressive loading were only carried out on a small number of specimens. Numerical results from these additional tests are not statistically reliable although qualitative conclusions are sound.

Pig skin showed large directional effects in the belly region while near in-plane isotropy was observed at the back. Abrupt failure at around 22 MPa nominal stress and a stretch ratio of 1.4 was found as average values with rather large variations between samples. Characteristics such as hysteresis, low notch sensitivity, and incompressibility were also observed. These characteristics are all in accord with the findings by other investigators who have studied real human skin (Daly (1966), Schneider (1982)). It is therefore concluded that pig skin is a realistic simulant for human skin.

#### *Flesh simulants*

Roma Plastilina and gelatine were used as flesh simulants in the stab-penetration test with a range of knife blades with different tip geometries. In this test Roma Plastilina showed

poor agreement between penetration force and blade geometry. The material absorbs the work done during penetration primarily by friction between the material and the blade flanks. Furthermore, the force needed to continue penetration increases strongly with depth. It was therefore concluded that Roma Plastilina is not a suitable flesh simulant which is supported by Jason and Fackler (1990).

Gelatine was also tested as a flesh simulant and showed good agreement between penetration force and blade geometry. Sharp pointed blades needed much less force than blunt blades and the penetration force was less dependent on penetration depth. Gelatine is a good and realistic flesh simulant in connection with low velocity knife penetration.

The combination of gelatine covered with pig skin showed a realistic response to the range of knife profiles tested. It was verified that skin provides most of the penetration resistance as the penetration force dropped drastically after puncture of the skin and was hardly influenced by the underlying flesh simulant. This observation is in agreement with Knight (1975) who made similar observations on human cadavers.

## **6.2 Experimental stab-penetration test**

### *Sharp blades*

Based on the pilot tests it appears that penetration resistance is not very dependent on the UTS of the materials concerned. Pig skin has a tensile strength three to four times higher than that of synthetic chamois and yet the penetration force for the two materials was found almost similar. This observation was made while using the most pointed and most sharp edged knife blade. The significant parameters determining penetration forces might therefore be different from those determining tensile strength and it is likely that fibrous materials in particular show this behaviour.

Under tensile load, mainly the fibres and the fibre-matrix bonding determine the failure load, whereas the fibres will be pushed aside during penetration by a pointed object, and be cut one by one causing the penetration force to be influenced more by the weaker matrix. The smooth surface produced by a sharp knife blade must be the result of cutting of the main load bearing collagen fibres without significant straining and is probably determined by shear stress in the individual fibres. Although it has not been investigated in the present work, the layout and type of fibres and matrix material are

thought to play a more important role in a given materials resistance to penetration rather than just the tensile strength of the individual materials. It is also necessary to identify a suitable method for quantifying the sharpness of a given knife blade.

### *Blunt penetrators*

The stab-penetration test using blunt penetrators indicated that there exists a linear relationship between penetrator tip-radius and penetration force. Penetrator displacement at puncture was identical for the different penetrator sizes thus penetration could possibly be determined by in-plane strain which is largely independent of penetrator size. Penetration by the blunt penetrators is probably governed by tearing of the skin rather than cutting. Tearing of skin is mainly due to fibre pull-out, ie failure of the fibre-matrix bonds. The rough edges of the cracks or tears produced by the blunt penetrators support that.

The conclusions from the experimental stab-penetration tests are: 1) Penetration force is highly dependable on tip-radius of the penetrator. 2) There exists no direct relationship between tensile strength and puncture resistance for the materials tested.

## **6.3 Computational modelling**

### *3-d model with sharp blades*

Computational modelling of the stab-penetration test using sharp blades predicted too high penetration forces. Mesh refinement was here found to be the key factor as smaller elements in the target caused a decrease in penetration force. For membrane elements there is a limit to mesh refinement due to aspect ratio of the elements which only can be arranged in a single layer representing the skin. Solid elements can be used in any number of layers and allows very high mesh refinement and was therefore chosen for further analyses including blunt rounded penetrators.

Although membrane elements match the global behaviour of skin well due to the lack of bending stiffness, it remains a question whether this is the case when penetration by pointed objects is considered. Under the assumption that skin is a homogeneous material it seems more realistic to use solid elements which facilitate higher mesh refinement and allow multiple elements through the thickness of the skin. This enables a more detailed simulation where tip-radius of the penetrator can be included which is

considered important since pointedness or more precisely tip-radius has been identified as a paramount factor regarding penetration force.

For computational modelling, skin has been assumed a homogeneous material and the material model was developed based on tensile test results. This appears reasonable since the global behaviour of real skin and the mathematical model match well. However, it is now believed that this global behaviour might not suffice for simulating damage and failure caused to a fibrous material by a pointed object. The penetration force will be highly dependent on the micro structure of the target material and skin must indeed be regarded as a fibrous material when viewed on a micro scale. The more pointed a penetrator is the more significant is the microstructure. The rounded penetrators used in the experimental and computed stab-penetration test should then be less sensitive to the microstructure and yield more consistent results.

#### *Axisymmetric model with blunt penetrators*

Computational modelling using the initial bi-linear material model predicted much too low penetration forces and was hampered by numerical difficulties. These problems were mainly due to errors in the material model and the Von Mises yield criterion was indeed not suitable for a fibrous material such as skin. The axisymmetric model with high mesh refinement was thought to be a good basis for further development and verification of the computational material model.

Revision of the material model resulted in some advances. Modelling of continued penetration is now possible with the orthotropic material model with abrupt failure. Both mass proportional damping and stiffness dependent damping were necessary for stabilising the analysis. Although not successful in modelling continued penetration the more complex plastic-damage model might still be of interest for future investigation. It is believed to be a more accurate model of soft tissue undergoing failure as fibre slippage is known to occur prior to complete failure. Finding a robust method of incorporating rate control during yield is the main point to be addressed here. Both revised material models provided similar penetration forces and a linear relation between force and penetrator tip-radius was evident except for penetrator D which showed a much lower penetration force than expected.

The failure criterion based on maximum direct stress appears to be much more realistic for skin compared to the Von Mises yield criterion initially used. The fact that penetrator D shows a too low value might, however, suggest that the failure mechanisms of skin are not fully determined by maximum direct stress. It is likely that both in-plane direct stresses have a combined effect on failure, ie biaxial loading should be considered.

Removal of whole elements during failure posed some problems, however, only in the relatively coarse meshes used in 3-d models with sharp blades. High mesh refinement as used in the axisymmetric model with blunt penetrators eliminated these problems, although a larger area of the target failed than was suggested by the experiments. Further adjustment to the damping factors for the target material might reduce the number of failed elements. Viscoelasticity has largely been ignored in the present work for simplicity reasons. Treating skin as viscoelastic might solve a number of the numerical problems encountered during finite element analyses. A number of viscoelastic constitutive models have been proposed as pointed out by Lanir (1983). However, all models consider only strain levels encountered in vivo and failure is therefore not mentioned.

It is concluded that modelling of continued knife penetration via finite element method is possible but analysis is time consuming due to the high mesh refinement required. Minor adjustments to the material model should enable accurate prediction of penetration forces for blunt penetrators. Accuracy of the predicted penetration force is, however, still too low for typical knife blade sharpnesses to be of practical use as mesh sensitivity is significant.

## **7 Recommendations and future work**

### **7.1 Experimental work**

Present work has provided rough failure values for pig skin in terms of global ultimate stress and strain under uniaxial tension. As mentioned in section 1.4 skin is a complex material and many variables were ignored in this study. Future work should include a more detailed study of skin to eliminate or quantify variables such as anisotropy, age, preservation, and temperature. Thickness variation of the material should also be considered in more detail as this parameter can influence results greatly. In a fully dynamic FE simulation viscoelasticity and rate dependence are important and should be investigated experimentally. Micro mechanical properties with respect to failure should be investigated provided the micro mechanical FE modelling approach mentioned below is taken up. In this context a close study of the failure surfaces could yield information on whether cutting or tearing (fibre pull-out) actually takes place. Skin specimens should be subjected to biaxial loading and the effect on failure values should be studied. A suitable method of quantifying the sharpness and pointedness of a knife blade is needed for further advances in penetration modelling with sharp blades. A possible method could be the use of a reference target material subjected to the stab-penetration test. There are, however, very high repeatability requirements for such a reference material.

Although a crack must be pre-defined, a fracture mechanics approach to knife penetration should be looked into. In this connection a search for other skin simulants could be based on toughness rather than tensile stress.

### **7.2 Continuum modelling**

Continuum finite element modelling of knife penetration is not fully investigated at this stage. The main area to be further studied is that of constitutive modelling. At present, rate dependence has been introduced successfully to stabilise the analysis as failure occurs. Future work should possibly concentrate on a fully dynamic approach to material modelling and the effects of various damping factors should be clarified. This would hopefully enable modelling with higher, more realistic, impact velocities. The failure criterion should be investigated further with respect to biaxial loading and failure.

The revised material model should eventually be tested with sharp blades again. The effect of underlying tissue such as flesh and bone should be investigated in more detail and should possibly be incorporated in the computational model at some stage.

### **7.3 Alternative approaches**

#### *Discrete elements*

Discrete element modelling has been looked into by using PFC2d software which is capable of 2-dimensional modelling. A sharp blade has successfully penetrated a target of discrete elements bonded together. The issue that arises when using discrete elements is the link between macro and micro material behaviour. A theory describing this link is needed to obtain the relevant properties for the breakable bonds holding the target particles together. Data needed for the breakable bonds are normal and shear stiffness and strength. In order to simulate the stab-penetration test with realistic forces a 3-d model is necessary.

#### *Nodal release (spot welds) in Abaqus/Explicit*

Following the concept of breakable bonds in discrete modelling a finite element model with breakable bonds was tried modelled in Abaqus for the sharp blade only. Breakable bonds were here intended to model spot welds connecting two contact surfaces. Normal and shear strength must be defined and complete damage can be given as either a time to failure or a displacement. Also a bead size must be specified. As in PFC2d a connection between macro and micro properties is sought. A fracture mechanics approach could be adopted governing failure of the bonds (spot welds). The model was, however, abandoned at an early stage due to problems at the contact interface at the two target faces and the penetrator surface.

#### *Micro modelling*

Modelling of skin by means of 1-d truss elements in a diamond shaped layout as proposed by Daly (1966) should be investigated. This will simplify constitutive modelling significantly as only 1-d failure has to be considered. Also the elastic behaviour of collagen fibres is simple to describe. The downside of this approach is great complications in terms of specifying the mesh. Fibre length and diameter must be

determined and it must be considered how many layers or plies are necessary to simulate real skin. A 3-d mesh could possibly be built by interlinking the diamond shaped substructures through the thickness. Fibre dimensions greater than those of real skin are likely to disguise the effect of weapon tip sharpness, however, this is also the case with continuum elements. Finite element modelling to this detail is actually a step away from the concepts of simplification of real events via modelling and is computationally expensive. High computing power is, on the other hand, continuously becoming available at a lower cost. Complex detailed meshing with a simple material model might then yield better results than the opposite configuration with a complicated material model applied on a simple mesh.

## List of references

Abaqus/Explicit User's Manual, version 5.5 (1995) to version 5.7 (1998). Hibbitt, Karlsson & Sorensen.

Abaqus/Post Manual, version 5.5 (1995) to version 5.7 (1998). Hibbitt, Karlsson & Sorensen.

Abaqus Theory Manual, version 5.5 (1995) to version 5.7 (1998). Hibbitt, Karlsson & Sorensen.

Atkins A.G. & Mai Y-W (1988), Elastic and Plastic Fracture - metals, polymers, ceramics, composites, biological materials. Ellis Horwood series in mechanical engineering.

Backer S. and Petterson D.R. (1960), Some Principles of Non-Woven Fabrics. Text. Res. J. 30, 704-711.

Backman M. and Goldsmith W. (1978), The mechanics of penetration of projectiles into targets. Int. J. Eng. Sci. 16, 1-99.

Barbenel J.C., Evans J.H., and Finlay J.B. (1973), Stress-strain-time relations for soft connective tissues. Perspectives in Bioengineering (edited by Kenedi R.M.), University Park Press, pp.165-172.

Barbenel J.C. (1994), University of Strathclyde, Private communication.

Bathe K.J. (1982), Finite element procedures in engineering analysis, Prentice-Hall Inc., Englewood Cliffs, New Jersey.

Bleetman A. (1997), Police - The Voice of the Service, April 1997, p. 20-21.

- Calvano N.J. (1993), A Study to Determine the Most Important Parameters for Evaluating the Resistance of Soft Body Armor to Penetration By Edged Weapons, U.S. Department of Justice, Washington DC.
- Camps & Cameron (1971), Practical forensic medicine, 2nd edition, Hutchinson Medical, London.
- Chivers I. and Sleightholme J. (1995), Introducing FORTRAN 90. Springer-Verlag London Limited.
- Cook T.H. (1975), The Mechanical Characterization of Skin in Vivo. PhD Thesis, Stevens Institute of Technology, Castle Point, New Jersey.
- Cordio K.B. (1996), Determination of Mechanical Properties of Skin Using Quasi-static Biaxial Testing. Thesis, Worcester Polytechnic Institute, Massachusetts.
- Daly C.H. (1966), The Biomechanical Characteristics of Human Skin. PhD thesis, University of Strathclyde, Scotland.
- Flanagan C.L., Hernandez M.J., Hollister S.J., Taylor J.E. (1995), A two-dimensional computational model of soft tissue mechanics using a stiffening finite strain extremum principle. BED-Vol.31, Advances in bioengineering, ASME, pp. 101-102.
- Flynn D.M. (1989), Development of a Nonlinear Finite Element Based Method to Determine Incremental Material Properties of Two-dimensional Planar Sheets. PhD thesis, Worcester Polytechnic Institute, Massachusetts.
- Fung Y.C. (1993), Biomechanics - Mechanical Properties of Living Tissues, 2nd edition, Springer, New York.
- Gradwohl R.B.H. (1976), Gradwohl's Legal Medicine, 3rd edition.

Green M.A. (1978), Stab Wound Dynamics - A Recording Technique for Use in Medico-legal Investigations. *J. Forens. Sci. Soc.* 18, 161-163.

Hamouda A.M.S., Hashmi M.S.J. (1996), Modelling the impact and penetration events of modern engineering materials: characteristics of computer codes and material models. *Journal of Materials Processing Technology*, Vol.56, No.1-4, pp.847-862.

Hetherington J.G. (1995), Energy and Momentum Changes During Ballistic Perforation. *Int. J. Impact Engng* 18, 319-337.

Jansen L.H. & Rottier P.B. (1958a), Some Mechanical Properties of Human Abdominal Skin Measured on Excised Strips. *Dermatologica* 117, 65-83.

Jansen L.H. & Rottier P.B. (1958b), Comparison of the Mechanical Properties of Strips of Human Abdominal Skin Excised from Below and from Above the Umbilic. *Dermatologica* 117, 252-258.

Jason A. and Fackler M.L. (1990), Body Armor Standards - A Review and Analysis, Center for Ballistic Analysis, San Pablo, California, USA. Final report - second edition.

Kenedi R.M., Gibson T. and Daly C.H. (1964), The Effects of Unidirectional Tension. Structure and Function of Connective and Skeletal Tissue, Proceedings of an Advanced Study Institute Organized under the Auspices of NATO, St. Andrews.

Knight B. (1975), The Dynamics of Stab Wounds. *Forensic Science*, 6, 249-255.

Lanir Y. (1983), Constitutive equations for fibrous connective tissues. *Journal of Biomechanics*, vol. 16, no. 1, 1-12.

Lanir Y. and Fung Y.C. (1974a), Two-dimensional mechanical properties of rabbit skin: I. Experimental system. *J. Biomech.* 7, 29-34.

- Lanir Y. and Fung Y.C. (1974b), Two-dimensional mechanical properties of rabbit skin: II. Experimental results. *J. Biomech.* 7, 171-182.
- Lissenden C.J., Herakovich C.T. (1995), Numerical modelling of damage development and viscoplasticity in metal matrix composites. *Computer Methods in Applied Mechanics and Engineering*, Vol.126, No.3-4, pp.289-303.
- Marks R. (1983), *Mechanical Properties of the Skin*. Biochemistry and physiology of the skin (edited by Goldsmith I.) vol. 2, Oxford University Press.
- Nielson P.M.F. et al (1991), Biaxial testing of membrane biomaterials: Testing equipment and procedures. *J. Biomechanical Engineering*, 113, 295-300.
- Oden J.T. (1983), Comments on some problems in computational penetration mechanics. *Lecture Notes in Engineering*, 3, pp.149-165. Springer-Verlag, Berlin, West Ger and New York, NY, USA.
- Park H.C., Youn S.K. (1998), Finite element analysis and constitutive modelling of anisotropic nonlinear hyperelastic bodies with convected frames. *Computer Methods in Applied Mechanics and Engineering*,
- Parker G. (1993), *Stab Resistant Body Armour Test Procedure*, UK Home Office Police Scientific Development Branch publication 10/93.
- Peura G.D (1993), *Determination of Anisotropic Material Properties of Soft Tissue*. MSc thesis, Worcester Polytechnic Institute, Massachusetts.
- Reihnsner R., Balogh B., Menzel E.J. (1995), Two-dimensional elastic properties of human skin in terms of an incremental model at the in vivo configuration. *Med. Eng. Phys.* Vol. 17, No. 4, pp. 304-313.

Ridge M.D. & Wright V. (1966a), Mechanical properties of skin: A bioengineering study of skin structure. *J. Appl. Physiol.* 21(5), 1602-1606.

Ridge M.D. & Wright V. (1966b), The Directional effects of skin. *J. Invest Dermatol.* 46, p.341-346.

Roylance D. and Wang S.S., (1980), Penetration Mechanics of Textile Structures. *Ballistic Materials and Penetration Mechanics*. Ed. Laible R.C. Elsevier Scientific Publishing Company.

Shim V.P.W., Tan V.B.C., Tay T.E. (1995), Modelling deformation and damage characteristics of woven fabric under small projectile impact. *International Journal of Impact Engineering*, Vol.16, No.4, pp.585-605.

Schneider D.C. (1982), Viscoelasticity and Tearing Strength of the Human Skin. PhD Thesis, University of California.

Simpson Keith (1979), *Forensic Medicine*, 8th edition.

Soh J.S. (1998), Impact resistance of bioceramics. MSc thesis. University of Glasgow, Scotland.

Stokes V.K. and Nied H.F. (1987), Lateral strain effects during the large extension of polycarbonate. Constitutive modelling for nontraditional materials. Presented at the Winter Annual Meeting of the ASME, Boston, Massachusetts, December 13-18, 1987 (ed. Stokes V. and Krajcinovic D.)

Vincent J.F.V. (1982), *Structural Biomaterials*. The Macmillan Press Ltd.

Vincent J.F.V. (1992), *Biomechanics, Materials, A practical Approach*. Oxford University Press.

Walsh T.F., Lee B.L., Song J.W. (1996), Penetration failure mechanisms of woven textile composites. Proceedings of the American Society for Composites.

Wilkes G.L., Brown I.A., and Wildnauer R.H. (1973), The biomechanical properties of skin. CRC Critical Reviews in Bioengineering, 453-495.

Wilkins M.L. (1984), Modelling the behaviour of materials. Theoretical foundation for large-scale computations of nonlinear material behaviour. Ed: Nemat-Nasser S., Asaro R.J., Hegemier G.A. Martinus Nijhoff Publishers.

Zhong Z.H. (1993), Finite Element Procedures for Contact-impact Problems, Oxford University Press.

## Appendices

- 1 Collated data from 34 case studies of stabbing incidents.
  - 1.1 Location of stab wounds.
  - 1.2 Size of wounds and knives used.
  
- 2 Force-extension curves from pilot tensile tests.
  - 2.1 Pig skin tested on Hounsfield Tensometer.
  - 2.2 Dry chamois tested on Hounsfield Tensometer parallel to fibre direction.
  - 2.3 Wet chamois tested on Hounsfield Tensometer parallel to fibre direction.
  - 2.4 Dry chamois tested on Lloyd Universal Testing Machine parallel to fibre direction.
  - 2.5 Dry chamois tested on Lloyd Universal Testing Machine 45 degrees to fibre direction.
  - 2.6 Wet chamois tested on Lloyd Universal Testing Machine 45 degrees to fibre direction.
  
- 3 Tensile test results from dumbbell shaped pig skin specimens.
  - 3.1 Frozen back - longitudinal direction.
  - 3.2 Frozen back - transverse direction.
  - 3.3 Fresh belly - longitudinal direction.
  - 3.4 Fresh belly - transverse direction.
  - 3.5 Fresh back - longitudinal direction.
  - 3.6 Fresh back - transverse direction.
  
- 4 Standard knife blades with varying tip pointedness and edge sharpness.
  
- 5 Fortran90 file.
  - 5.1 Bi-linear material model with abrupt failure.
  - 5.2 Orthotropic material model with gradual failure.
  - 5.3 Orthotropic material model with abrupt failure.

- 6 Sample Abaqus input file for the revised axisymmetric stab-penetration model with penetrator A.
- 7 Quarter model using 60 membrane elements and knife blade 3B (pointed tip and sharp edges).
  - 7.1 Undeformed plot with 0.90 mesh bias.
  - 7.2 Von Mises stress contour plot in deformed state prior to failure with 0.90 mesh bias.
- 8 Quarter model using 5 x 60 solid elements and knife blade 3B (pointed tip and sharp edges).
  - 8.1 Undeformed plot with 0.90 mesh bias.
  - 8.2 Von Mises stress contour plot in deformed state prior to failure with 0.90 mesh bias.
  - 8.3 Undeformed plot with 0.60 mesh bias.
- 9 Radial section of axisymmetric model with bi-linear material model.
  - 9.1 Undeformed plot (penetrator A).
  - 9.2 Von Mises stress contour plot in deformed state prior to failure (penetrator A).
  - 9.3 Von Mises stress contour plot in deformed state prior to failure (penetrator B).
- 10 Tensile stress contour plot of quarter model of dumbbell shaped specimen in deformed state prior to failure.

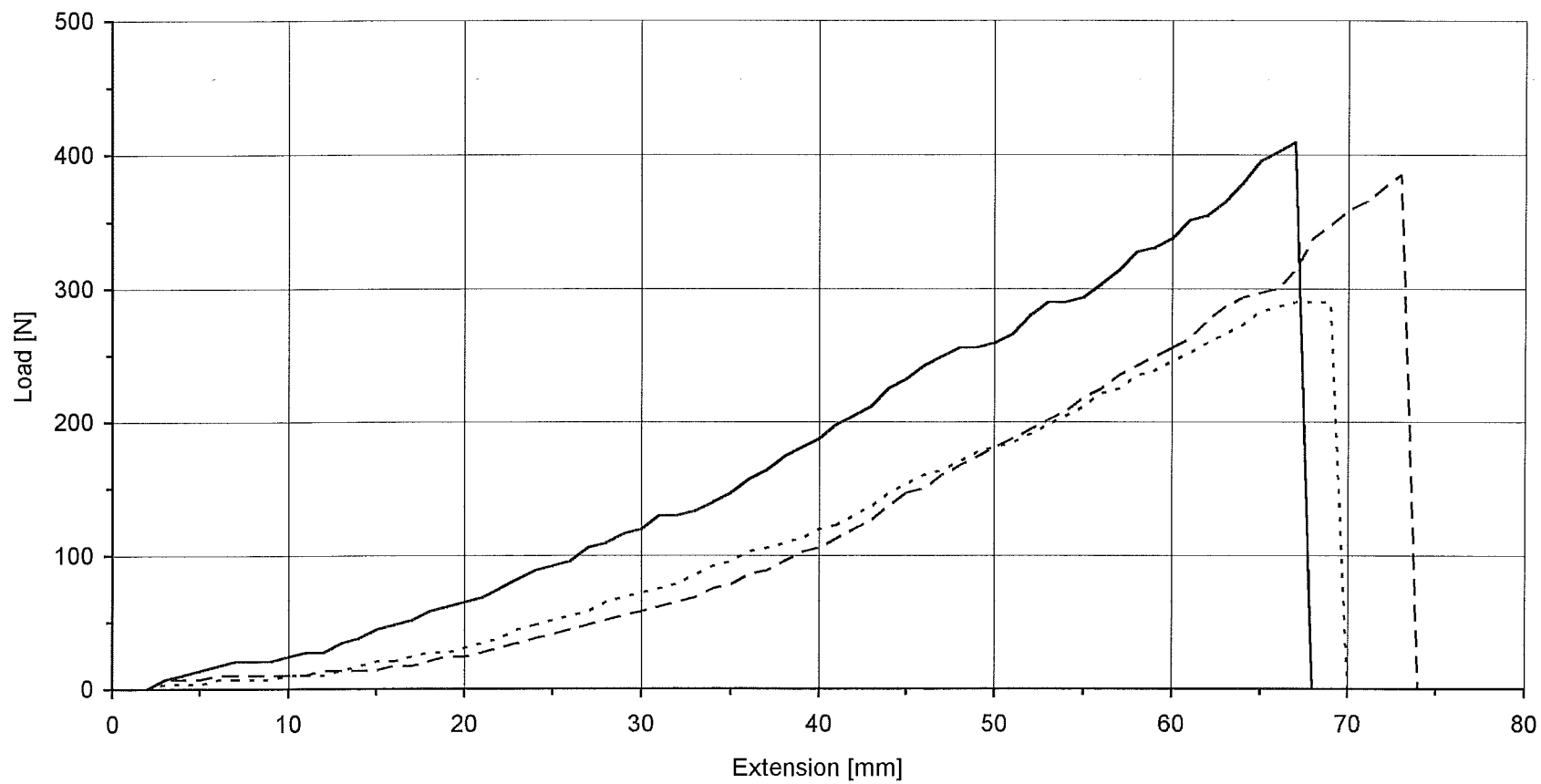
- 11 Radial section of axisymmetric model with orthotropic material model with gradual failure.
  - 11.1 Undeformed plot (penetrator A).
  - 11.2 Hoop stress contour plot in deformed state prior to failure (penetrator A).
  - 11.3 Undeformed plot (penetrator B).
  - 11.4 Hoop stress contour plot in deformed state prior to failure (penetrator B).
  - 11.5 Undeformed plot (penetrator C).
  - 11.6 Hoop stress contour plot in deformed state prior to failure (penetrator C).
  - 11.7 Undeformed plot (penetrator D).
  - 11.8 Hoop stress contour plot in deformed state prior to failure (penetrator D).
  
- 12 Radial section of axisymmetric model with orthotropic material model with abrupt failure.
  - 12.1 Hoop stress contour plot in deformed state prior to failure (penetrator A).
  - 12.2 Hoop stress contour plot in deformed state after failure (penetrator A).
  - 12.3 Hoop stress contour plot in deformed state prior to failure (penetrator B).
  - 12.4 Hoop stress contour plot in deformed state after failure (penetrator B).
  - 12.5 Hoop stress contour plot in deformed state prior to failure (penetrator C).
  - 12.6 Hoop stress contour plot in deformed state after failure (penetrator C).
  - 12.7 Radial stress contour plot in deformed state prior to failure (penetrator D).
  - 12.8 Radial stress contour plot in deformed state after failure (penetrator D).

Case	Pers. data		Cause of d.		Clothing No. layers	Bone cut through	Location and number of wounds						
	Sex	Age	Stab	Other			Chest	Neck / head	Abdomen	Back	Extremit.	Other	Total
1	m	18	1		?		1						1
2	m	31	1		?	1	1			1			2
3	m	17	1		2		1	2					3
4	m	28	1		?	1	2		1		2		5
5	m	28	1		2	1	1						1
6	f	31	1		1			1	1				1
7	m	35	1		0	1	2	1					3
8	m	27	1		0	1	1	5					6
9	m	22	1		?		3	2		1			6
10	f	17	1		2		5	3			5		13
11	m	21	1	1	1	1	14	3	1	12			30
12	f	28	1		?	1	4	1	1	5	1		12
13	m	33	1		?	1	1			1		1	3
14	m	51	1		1		1						1
15	m	20	1		?		1						1
16	m	31	1		?		1	1					2
17	m	21	1		?		1						1
18	m	26	1	1	1	1	2						2
19	m	48	1		1	1	4				1		5
20	m	31	1		1	1	2	1	2				5
21	m	26	1		2		1		2				3
22	f	84		1	2		2		1				3
23	m	43		1	1		3						3
24	m	33	1		1	1	1						1
25	m	26	1		?	1				1			1
26	m	23	1		?	1	7						7
27	f	36	1		?		4				2		6
28	m	34	1		?	1	1						1
29	m	41	1		2		5	4			2		11
30	m	21	1		3	1						1	1
31	m	25	1		0	1	1						1
32	f	19	1		?	1	6		5				11
33	m	55	1		2	1	3						3
34	m	32	1		?	1	1						1
Total						20	83	23	14	21	13	2	156
Average		31					2.4	0.7	0.4	0.6	0.4	0.1	4.6
Percentage						59%	53%	15%	9%	13%	8%	1%	

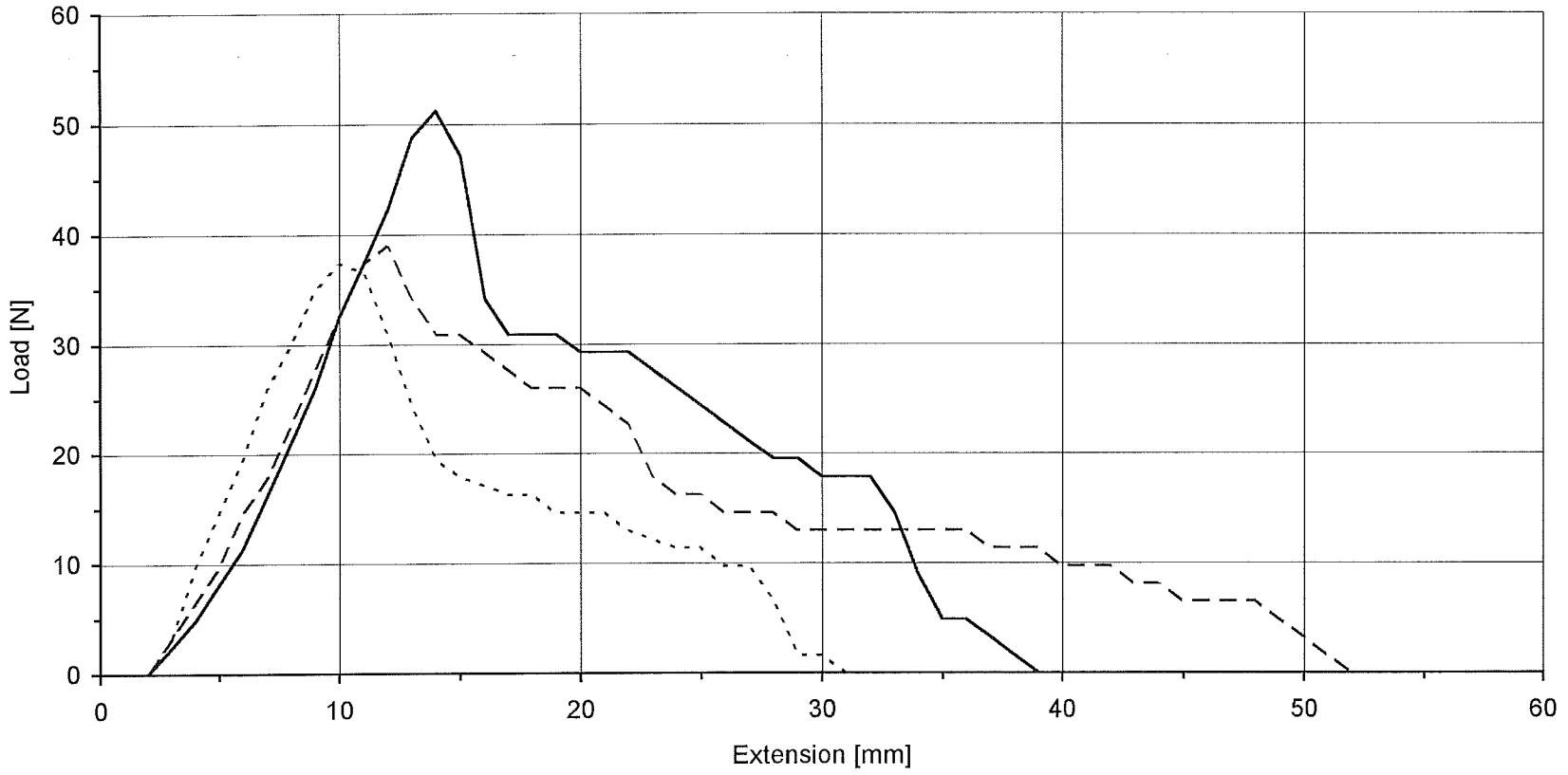
Appendix 1.1. Collated data from 34 case studies of stabbing incidents.  
Location of stab wounds.

Case	Wound length [mm]		Wound depth [mm]		Knife blade [mm]		No. sharp edges	Remarks
	Min	Max	Min	Max	Width	Length		
1	13	13	127	127	13	121	1	
2	13	16	190	203	19	184	1	
3	13	25	38	140	13	89	1	
4	11	29	64	165	6	120	1	
5	44	44	127	127	35	190	1	
6	13	20	38	50	25	216	1	
7	19	29	89	102	19	105	1	
8	13	38	?	203	20	165	1	
9	8	25	25	76	15	76	1	
10	6	22	?	127	16	89	1	< 1st blade broken
11	6	76	?	?	50	238	1	
12	6	50	?	?	25	152	1	
13	20	32	?	?	19	114	1	
14	16	16	76	76	34	162	1	
15	16	16	89	89	18	102	1	
16	10	20	114	152	25	127	1	
17	19	19	152	152	19	102	1	
18	38	101	?	?	44	216	1	
19	10	38	?	?	25	203	1	
20	6	16	76	152	13	114	1	
21	22	25	?	165	38 ?	152	1	
22	13	42	?	80	40	200	1	Same weapon
23	18	42	?	?	40	200	1	
24	23	23	120	120	15	153	1	
25	20	20	150	150	23	175	2	
26	35	35	130	150	29	150	1	
27	20	25	100	140	23	150	1	
28	22	22	?	?	?	?	1	
29	15	40	15	170	?	?	?	
30	40	40	100	100	25	228	1	
31	35	35	x	?	20	114	1	
32	15	35	?	?	?	?	?	
33	22	41	152	178	19	152	1	
34	50	50	102	102	35	146	1	
Aver.	19.1	32.9	98.8	131.8	23.3	148.9		
Max	50	101	190	203	50	238		
Min	6	13	15	50	6	76		

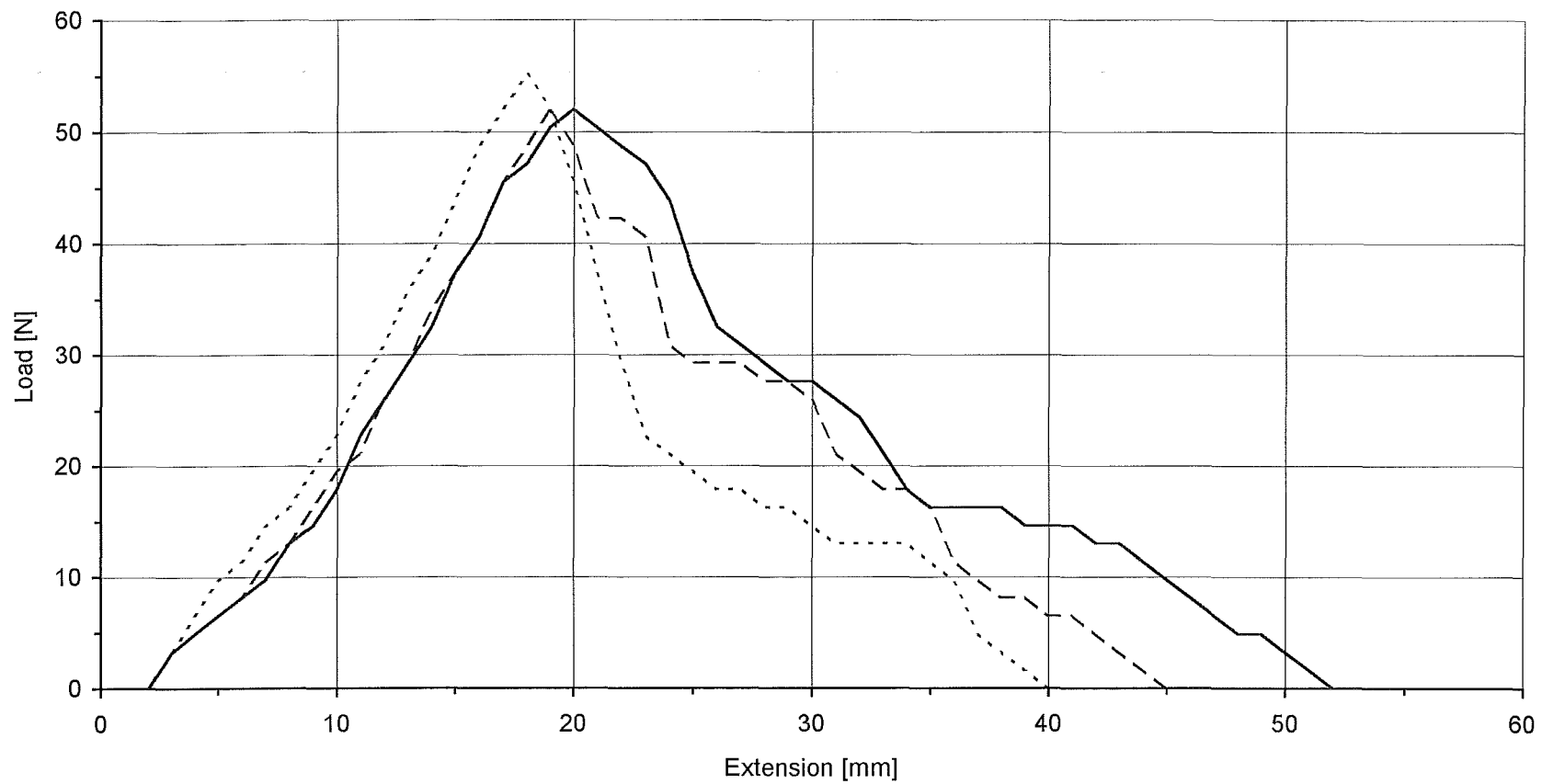
Appendix 1.2. Collated data from 34 case studies of stabbing incidents. Size of wounds and knives used.



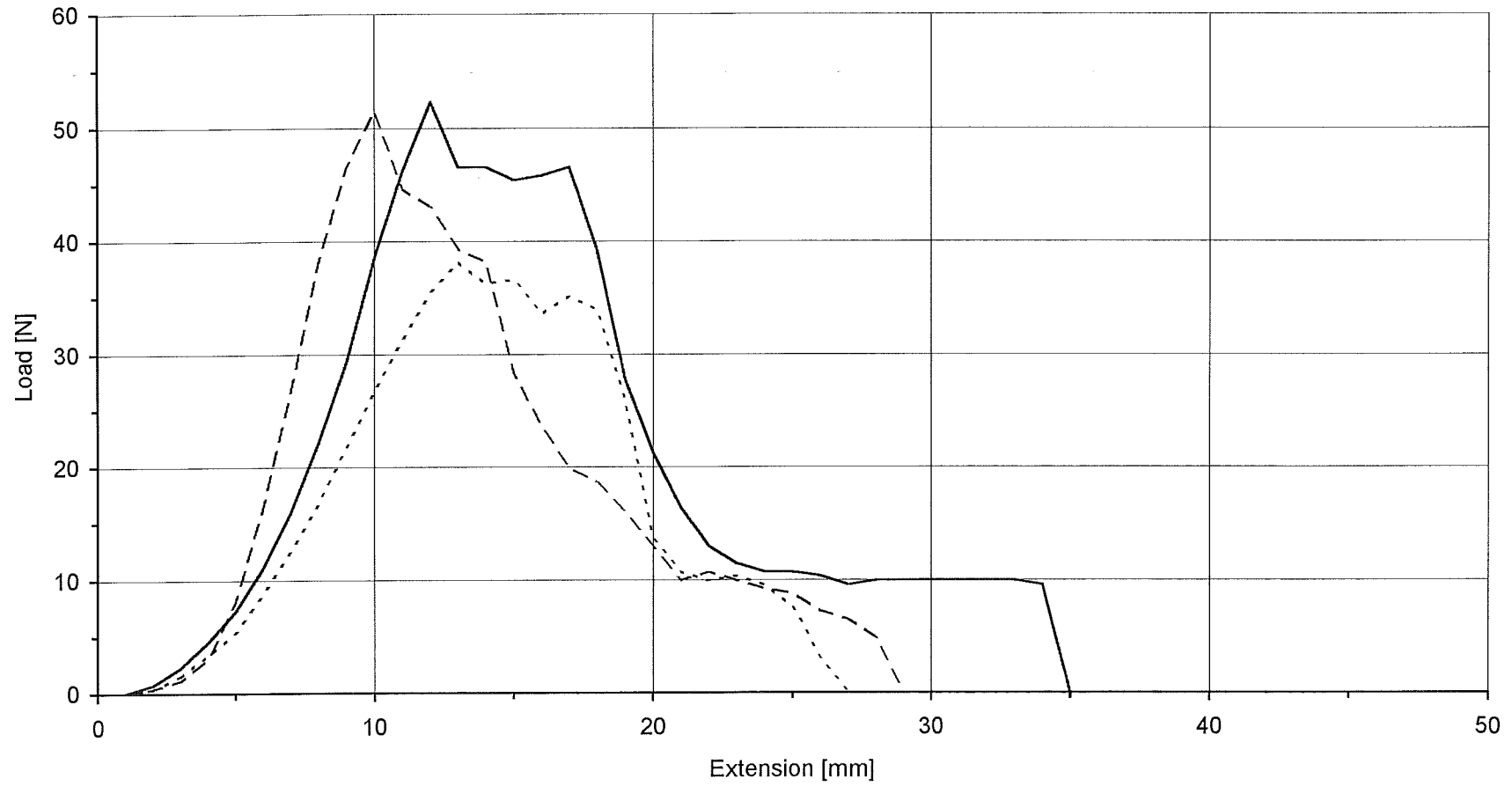
Appendix 2.1 Force-extension curves from pilot tensile tests. Pig skin tested on Hounsfield Tensometer.



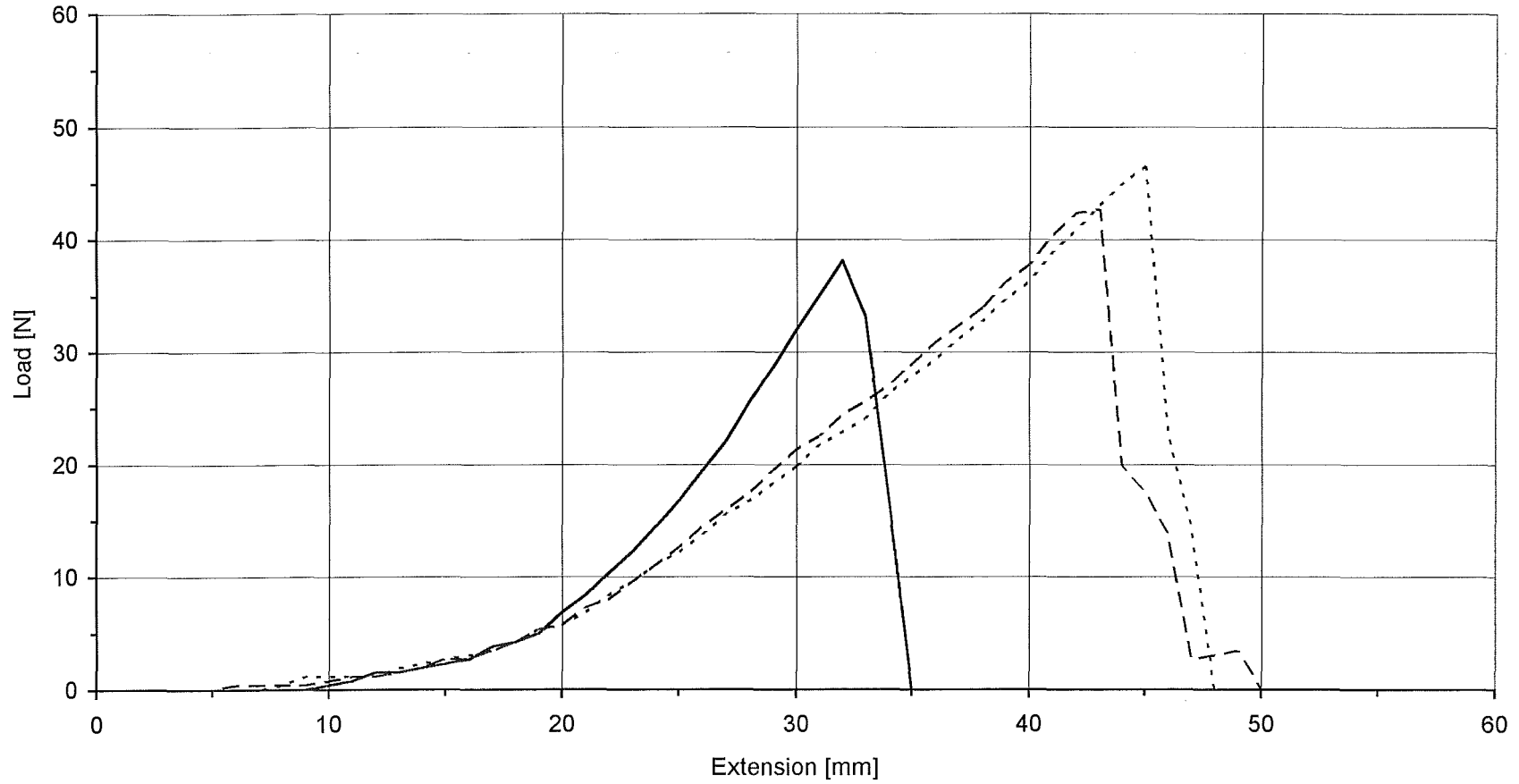
Appendix 2.2 Force-extension curves from pilot tensile tests. Dry chamois tested on Hounsfield Tensometer parallel to fibre direction.



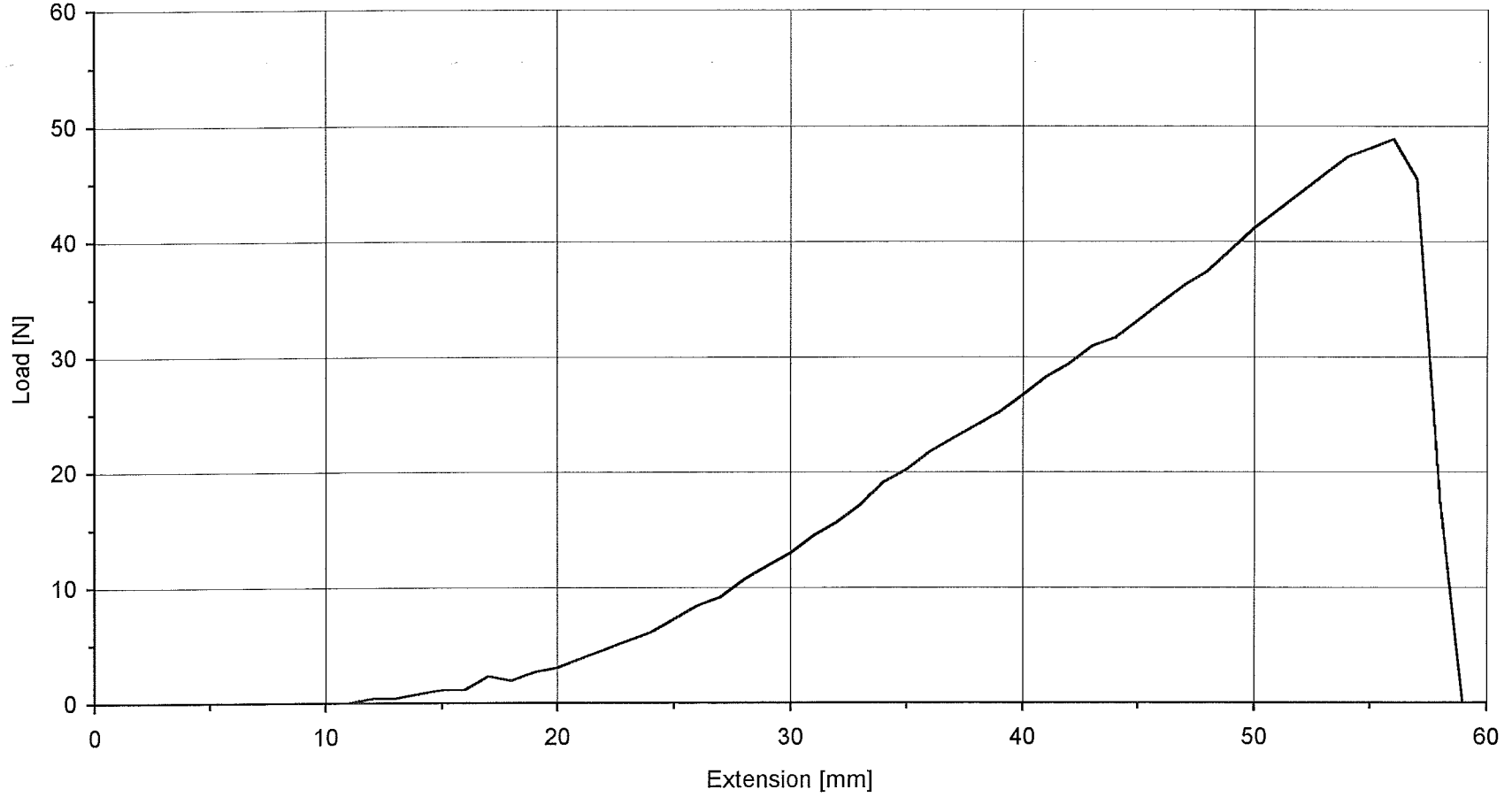
Appendix 2.3 Force-extension curves from pilot tensile tests. Wet chamois tested on Hounsfield Tensometer parallel to fibre direction.



Appendix 2.4 Force-extension curves from pilot tensile tests. Dry chamois tested on Lloyd Universal Testing Machine parallel to fibre direction.



Appendix 2.5 Force-extension curves from pilot tensile tests. Dry chamois tested on Lloyd Universal Testing Machine 45 degrees to fibre direction.



Appendix 2.6 Force-extension curves from pilot tensile tests. Wet chamois tested on Lloyd Universal Testing Machine 45 degrees to fibre direction.

	Specimen	Initial	Intermediate	Failure	Max Load	Max Elong	Remarks	nu-inter	nu-failure	Nom stress	True stress
		Width [mm]			[N]	[mm]				[MPa]	[MPa]
22.01.97	L0101	27	25	20	1442	40		0.41	0.71	27	36
	L0102						Slips at vice				
	L0103	29	29	29	1195	32		0.00	0.00	21	21
	L0104	27	22	16	1435	40		1.02	1.12	27	45
	L0105						Slips at vice				
30.01.97	L0106	28	28	27	1657	26		0.00	0.15	30	31
	L0201						Slips at vice				
	L0202						Slips at vice				
	L0203						Slips at vice				
	L0204	30	21	17	1634	45		1.47	1.06	27	48
Max		30	29	29	1657	45		1.47	1.12	30	48
Min		27	21	16	1195	26		0.00	0.00	21	21
Average		28	25	22	1473	37		0.58	0.61	26	36

Appendix 3.1. Tensile test results from dumbbell shaped pig skin specimens - frozen back - longitudinal direction.

	Specimen	Initial	Intermediate	Failure	Max Load	Max Elong	Remarks	nu-inter	nu-failure	Nom stress	True stress
23.01.97	T0101						Slips at vice				
	T0102	28	26	24	1172	28	Soaked in water	0.56	0.56	21	24
	T0103	26	25	22	1202	34		0.25	0.50	23	27
	T0104						Slips at vice				
	T0105						Slips at vice				
	T0106	28	25	19	1025	38		0.62	0.93	18	27
	T0107	28	27	27	1659	43		0.18	0.09	30	31
	T0108	28	24	21	1053	28		1.12	0.98	19	25
30.01.97	T0201						Fat/slips				
	T0202						Fat/>2kN				
	T0203	29	26	25	1563	29		0.78	0.52	27	31
	T0204	29	23	23	1490	40		1.14	0.57	26	32
	T0205	30	28	24	1101	30		0.49	0.73	18	23
	T0206	30	22	20	1041	30		1.96	1.22	17	26
Max		30	28	27	1659	43		1.96	1.22	30	32
Min		26	22	19	1025	28		0.18	0.09	17	23
Average		28	25	23	1256	33		0.79	0.68	22	27

Appendix 3.2. Tensile test results from dumbbell shaped pig skin specimens - frozen back - transverse direction.

	Specimen	Initial	Intermediate	Failure	Max Load	Max Elong	Remarks	nu-inter	nu-failure	Nom stress	True stress
		Width [mm]			[N]	[mm]				[MPa]	[MPa]
26.02.97	L0301	27	25	20	1002	30	snaps at waist	0.54	0.95	19	25
	L0302	26	24	20	1563	36	snaps at trans	0.47	0.71	30	39
	L0303	29	25	20	446	35	snaps at trans	0.87	0.98	8	11
Max		29	25	20	1563	36		0.87	0.98	30	39
Min		26	24	20	446	30		0.47	0.71	8	11
Average		27	25	20	1004	34		0.63	0.88	19	25

Appendix 3.3. Tensile test results from dumbbell shaped pig skin specimens - fresh belly - longitudinal direction.

	Specimen	Initial	Intermediate	Failure	Max Load	Max Elong	Remarks	nu-inter	nu-failure	Nom stress	True stress
		Width [mm]			[N]	[mm]				[MPa]	[MPa]
26.02.97	T0301	27	20	13	267	95	snaps at vice	0.60	0.60	5	10
	T0302	28	22	14	363	92	snaps at vice	0.51	0.60	6	13
	T0303	26	18	10	395	130	snaps at vice	0.52	0.52	8	20
	T0304	26	18	10	221	130	snaps at vice	0.52	0.52	4	11
Max		28	22	14	395	130		0.60	0.60	8	20
Min		26	18	10	221	92		0.51	0.52	4	10
Average		27	20	12	312	112		0.54	0.56	6	14

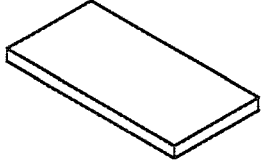
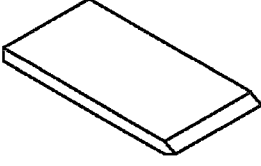
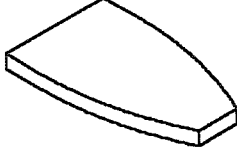
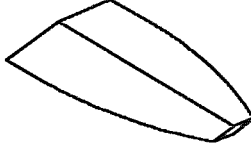
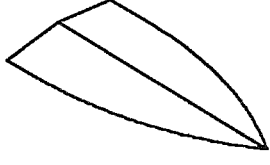
Appendix 3.4. Tensile test results from dumbbell shaped pig skin specimens - fresh belly - transverse direction.

	Specimen	Initial	Intermediate	Failure	Max Load	Max Elong	Remarks	nu-inter	nu-failure	Nom stress	True stress
		Width [mm]			[N]	[mm]				[MPa]	[MPa]
28.02.97	L0401	29	28	24	1151	54	snaps at waist	0.14	0.35	20	24
	L0402	30	26	23	778	52	snaps at waist	0.56	0.49	13	17
	L0403	29	28	24	1202	54	snaps at trans	0.14	0.35	21	25
12.03.97	L0501	30	25	28	1611	51	Snaps at trans (wide)	0.72	0.14	27	29
	L0502	28	28	28	401	28	Tear at trans (narrow)	0.00	0.00	7	7
	L0503	29	29	29	538	23	Tear at trans (narrow)	0.00	0.00	9	9
	L0504	30	28	25	476	37	Tear at trans (narrow)	0.40	0.50	8	10
	L0505	29	27	22	1833	45	Snaps at trans (wide)	0.34	0.59	32	42
	L0506	29	28	25	1778	22	Snaps at trans (wide)	0.34	0.69	31	36
	L0507	30	25	22	1201	58	Snaps at trans (narrow)	0.63	0.51	20	27
	L0508	27	26	25	551	58	Tears at trans (narrow)	0.14	0.14	10	11
Max		30	29	29	1833	58		0.72	0.69	32	42
Min		27	25	22	401	22		0.00	0.00	7	7
Average		29	27	25	1047	44		0.31	0.34	18	21

Appendix 3.5. Tensile test results from dumbbell shaped pig skin specimens - fresh back - longitudinal direction.

	Specimen	Initial	Intermediate	Failure	Max Load	Max Elong	Remarks	nu-inter	nu-failure	Nom stress	True stress
28.02.97	T0401	30	25	23	759	33	snaps at trans	1.11	0.78	13	17
	T0402	29	25	22	767	29	snaps at trans	1.05	0.92	13	17
	T0403	30	25	22	771	33	snaps at trans	1.11	0.89	13	18
12.03.97	T0404	29	25	19	916	38	snaps at trans	0.80	1.00	16	24
	T0501	29	27	25	735	50	Snaps at trans	0.30	0.30	13	15
	T0502	30	28	27	900	34	Snaps at trans	0.43	0.32	15	17
	T0503				1433		Slipped at vice				
	T0504	27	25	24	1522	68	Snaps at trans	0.24	0.18	28	32
	T0505				1211		Tear at vice				
	T0506	29	27	26	806	42	Tear at trans	0.36	0.27	14	16
	T0507	27	25	24	659	42	Tear at trans	0.39	0.29	12	14
	T0508				840		Tear at vice				
	Max		30	28	27	1522	68		1.11	1.00	28
Min		27	25	19	659	29		0.24	0.18	12	14
Average		29	26	24	943	41		0.64	0.55	15	19

Appendix 3.6. Tensile test results from dumbbell shaped pig skin specimens - fresh back - transverse direction.

No	Description	Figure
1A	Square-ended blade with blunt edge	
1B	Square-ended blade with sharp edge	
2A	Blunt-tipped blade with blunt edges	
2B	Blunt-tipped blade with sharp edges	
3A	Pointed blade with blunt edges	
3B	Pointed blade with sharp edges	

Appendix 4. Standard knife blades with varying tip pointedness and edge sharpness.



```
C Update stress tensor using the relevant E-modulus
C
      stressNew(i,1)=stressOld(i,1)+twoG*strainInc(i,1)+ala*trace
      stressNew(i,2)=stressOld(i,2)+twoG*strainInc(i,2)+ala*trace
      stressNew(i,3)=stressOld(i,3)+twoG*strainInc(i,3)+ala*trace
      stressNew(i,4)=stressOld(i,4)+twoG*strainInc(i,4)
      stressNew(i,5)=stressOld(i,5)+twoG*strainInc(i,5)
      stressNew(i,6)=stressOld(i,6)+twoG*strainInc(i,6)
      stateNew(i,1)=1 !Material point active
    else
      stressNew(i,1) = 0.0
      stressNew(i,2) = 0.0
      stressNew(i,3) = 0.0
      stressNew(i,4) = 0.0
      stressNew(i,5) = 0.0
      stressNew(i,6) = 0.0
      stateNew(i,1)=0 !Material point deleted
    endif
C
100  continue
C
      return
      end
```

Appendix 5.1. Fortran90 file. Bi-linear material model with abrupt failure.

```

subroutine vumat(
C Read only (unmodifiable) variables -
  1 nblock, ndir, nshr, nstatev, nfieldv, nprops, lanneal,
  2 stepTime, totalTime, dt, cmname, coordMp, charLength,
  3 props, density, strainInc, relSpinInc,
  4 tempOld, stretchOld, defgradOld, fieldOld,
  5 stressOld, stateOld, enerInternOld, enerInelasOld,
  6 tempNew, stretchNew, defgradNew, fieldNew,
C Write only (modifiable) variables -
  7 stressNew, stateNew, enerInternNew, enerInelasNew)
C
  include 'vaba_param.inc'
C
  dimension props(nprops), density(nblock), coordMp(nblock),
  1 charLength(nblock), strainInc(nblock,ndir+nshr),
  2 relSpinInc(nblock,nshr), tempOld(nblock),
  3 stretchOld(nblock,ndir+nshr), defgradOld(nblock,ndir+nshr+nshr),
  4 fieldOld(nblock,nfieldv), stressOld(nblock,ndir+nshr),
  5 stateOld(nblock,nstatev), enerInternOld(nblock),
  6 enerInelasOld(nblock), tempNew(nblock),
  7 stretchNew(nblock,ndir+nshr), defgradNew(nblock,ndir+nshr+nshr),
  8 fieldNew(nblock,nfieldv), stressNew(nblock,ndir+nshr),
  9 stateNew(nblock,nstatev), enerInternNew(nblock),
  1 enerInelasNew(nblock)
C
  character*8 cmname
C
C234567890123456789012345678901234567890123456789012345678901234567890123
C
  sYield = 3.2E7 ! True yield stress.
  ak     = 80.E6 ! Stress-Strain constant.
  an     = 1.4   ! Exponent.
  anu    = 0.25  ! Poisson's ratio.
  Emin   = 3.0E7 ! Minimum elastic stiffness.
  Emax   = 1.1E8 ! Maximum elastic stiffness.
  beta_r = 1.0E-3 ! Damping factor.
C
C stateNew(i,1) = Total strain in 1-direction
C stateNew(i,2) = Total strain in 2-direction
C stateNew(i,3) = Total strain in 3-direction
C stateNew(i,4) = Total strain in 4-direction
C stateNew(i,5) = Plastic strain in 1-direction
C stateNew(i,6) = Plastic strain in 2-direction
C stateNew(i,7) = Plastic strain in 3-direction
C stateNew(i,8) = Failure indicator for material point
C stateNew(i,10) = Yield indicator (>1 once yield has occurred)
C stateNew(i,11) = Backstress in 1-direction
C stateNew(i,12) = Backstress in 2-direction
C stateNew(i,13) = Backstress in 3-direction
C stateNew(i,14) = Failure flag in 1-direction
C stateNew(i,15) = Failure flag in 2-direction
C stateNew(i,16) = Failure flag in 3-direction
C stateNew(i,17) = Active plasticity flag in 1-direction
C stateNew(i,18) = Active plasticity flag in 2-direction
C stateNew(i,19) = Active plasticity flag in 3-direction
C stateNew(i,20) = f1
C stateNew(i,21) = f2
C stateNew(i,22) = f3
C stateNew(i,23) = f4
C
C Loop on the number of data blocks.
C
  do 100 i = 1,nblock
C
C Update total strain for all strain components and check if
C active yielding occurs. If so, update offset strain. Yield occurs
C once sYield is reached in any one direction. Negative strain
C results in an infinite non-linear response.

```

Appendix 5.2. Fortran90 file. Orthotropic material model with gradual failure.

```

stateNew(i,1) = stateOld(i,1) + strainInc(i,1)
deltae1 = ABS(stateNew(i,1)) - ABS(stateOld(i,1))
eElast1 = ABS(stateNew(i,1) - stateOld(i,5))
EE1 = an*ak*eElast1**(an-1.)
eRate1 = ABS(strainInc(i,1)/dt)
EDamp1 = beta_r*EE1*eRate1
E1 = EE1 + EDamp1
if (E1 .lt. Emin) E1 = Emin
if (E1 .gt. Emax) E1 = Emax
C
stateNew(i,2) = stateOld(i,2) + strainInc(i,2)
deltae2 = ABS(stateNew(i,2)) - ABS(stateOld(i,2))
eElast2 = ABS(stateNew(i,2) - stateOld(i,6))
EE2 = an*ak*eElast2**(an-1.)
eRate2 = ABS(strainInc(i,2)/dt)
EDamp2 = beta_r*EE2*eRate2
E2 = EE2 + EDamp2
if (E2 .lt. Emin) E2 = Emin
if (E2 .gt. Emax) E2 = Emax
C
stateNew(i,3) = stateOld(i,3) + strainInc(i,3)
deltae3 = ABS(stateNew(i,3)) - ABS(stateOld(i,3))
eElast3 = ABS(stateNew(i,3) - stateOld(i,7))
EE3 = an*ak*eElast3**(an-1.)
eRate3 = ABS(strainInc(i,3)/dt)
EDamp3 = beta_r*EE3*eRate3
E3 = EE3 + EDamp3
if (E3 .lt. Emin) E3 = Emin
if (E3 .gt. Emax) E3 = Emax
C
stateNew(i,4) = stateOld(i,4) + strainInc(i,4)
EE4 = an*ak*ABS(stateNew(i,4))**(an-1.)
eRate4 = ABS(strainInc(i,4)/dt)
EDamp4 = beta_r*EE4*eRate4
E4 = EE4 + EDamp4
if (E4 .lt. Emin) E4 = Emin
if (E4 .gt. Emax) E4 = Emax
C
eRateA = (eRate1+eRate2+eRate3+eRate4) / 4
C
if ((stateOld(i,17) .lt. 0.5) .and.
& (stateOld(i,18) .lt. 0.5) .and.
& (stateOld(i,19) .lt. 0.5)) then
C
C Stiffness matrix components for a 3-d orthotropic material.
C
factor = E1*(E2-E3*anu**2)-E2*anu**2*(E2+E3+2*E3*anu)
C
C11 = E1**2*(E2-E3*anu**2) / factor
C22 = E2**2*(E1-E3*anu**2) / factor
C33 = -E2*E3*(E2*anu**2-E1) / factor
C
C12 = E1*E2*anu*(E2+E3*anu) / factor
C13 = E1*E2*E3*anu*(1+anu) / factor
C23 = E2*E3*anu*(E1+E2*anu) / factor
C
C21 = C12
C31 = C13
C32 = C23
C
C44 = E4 / (1+anu)
C

```

C Update stress as non-linear elastic provided no yield occurs. If  
 C sYield is reached in any one direction plasticity is imposed in all  
 C directions. Plasticity with some hardening is imposed until the  
 C plastic strain reaches 0.1 in any direction. Hereafter, stress is  
 C lowered proportionally to the individual pre-yield level in terms of  
 C time increments. The material point is deleted as the active stress  
 C approaches zero and passive stress is, when small, kept at a constant  
 C level for passive stress-strain control in uniaxial cases.

```

C
      stressNew(i,1)=stressOld(i,1)+C11*strainInc(i,1)
& +C12*strainInc(i,2)+C13*strainInc(i,3)
      stressNew(i,2)=stressOld(i,2)+C21*strainInc(i,1)
& +C22*strainInc(i,2)+C23*strainInc(i,3)
      stressNew(i,3)=stressOld(i,3)+C31*strainInc(i,1)
& +C32*strainInc(i,2)+C33*strainInc(i,3)
      stressNew(i,4)=stressOld(i,4)+C44*strainInc(i,4)
C
      stateNew(i,10) = stateOld(i,10)
      stateNew(i,11) = stateOld(i,11)
      stateNew(i,12) = stateOld(i,12)
      stateNew(i,13) = stateOld(i,13)
      stateNew(i,20) = stateOld(i,20)
      stateNew(i,21) = stateOld(i,21)
      stateNew(i,22) = stateOld(i,22)
      stateNew(i,23) = stateOld(i,23)
      else
& if ((stateOld(i,5) .lt. 0.1) .and.
&      (stateOld(i,6) .lt. 0.1) .and.
&      (stateOld(i,7) .lt. 0.1)) then
      trace = strainInc(i,1)+strainInc(i,2)+strainInc(i,3)
      const = 1.5E8 * eRateA
      EE = 5.E5
      EDamp = 1.E-5*EE*eRateA
      E = EE + EDamp
      if (E .gt. Emin) E = Emin
      twoG = E/(1.+anu)
      ala = anu*twoG/(1.-2.*anu)
      stressNew(i,1)=stressOld(i,1)+twoG*strainInc(i,1)+ala*trace
      stressNew(i,2)=stressOld(i,2)+twoG*strainInc(i,2)+ala*trace
      stressNew(i,3)=stressOld(i,3)+twoG*strainInc(i,3)+ala*trace
      stressNew(i,4)=stressOld(i,4)+twoG*strainInc(i,4)
      stateNew(i,20) = const * stressNew(i,1) / sYield
      stateNew(i,21) = const * stressNew(i,2) / sYield
      stateNew(i,22) = const * stressNew(i,3) / sYield
      stateNew(i,23) = const * stressNew(i,4) / sYield
      else
      stateNew(i,20) = stateOld(i,20)
      stateNew(i,21) = stateOld(i,21)
      stateNew(i,22) = stateOld(i,22)
      stateNew(i,23) = stateOld(i,23)
      stressNew(i,1) = stressOld(i,1) - stateNew(i,20)*dt
      stressNew(i,2) = stressOld(i,2) - stateNew(i,21)*dt
      stressNew(i,3) = stressOld(i,3) - stateNew(i,22)*dt
      stressNew(i,4) = stressOld(i,4) - stateNew(i,23)*dt
      if (ABS(stressNew(i,1)) .lt. 2.E6) stateNew(i,14) = 1.
      if (ABS(stressNew(i,2)) .lt. 2.E6) stateNew(i,15) = 1.
      if (ABS(stressNew(i,3)) .lt. 2.E6) stateNew(i,16) = 1.
      if (ABS(stressOld(i,1)) .lt. 10.) stressNew(i,1)=stressOld(i,1)
      if (ABS(stressOld(i,2)) .lt. 10.) stressNew(i,2)=stressOld(i,2)
      if (ABS(stressOld(i,3)) .lt. 10.) stressNew(i,3)=stressOld(i,3)
      if (ABS(stressOld(i,4)) .lt. 10.) stressNew(i,4)=stressOld(i,4)
      endif
      stateNew(i,10) = stateOld(i,10) + 1.
      stateNew(i,11) = ABS(stressNew(i,1))
      stateNew(i,12) = ABS(stressNew(i,2))
      stateNew(i,13) = ABS(stressNew(i,3))
      endif
C

```

Appendix 5.2. Fortran90 file. Orthotropic material model with gradual failure.

```

        if (stateNew(i,10) .lt. 0.5) then
            stateNew(i,11) = sYield
            stateNew(i,12) = sYield
            stateNew(i,13) = sYield
        endif
C
        if ((ABS(stressNew(i,1)) .ge. stateNew(i,11)) .and.
&         (stateNew(i,1) .gt. 0.2) .and.
&         (deltae1 .gt. 0.)) then
            stateNew(i,17) = 1.
        else
            stateNew(i,17) = 0.
        endif
C
        if ((ABS(stressNew(i,2)) .ge. stateNew(i,12)) .and.
&         (stateNew(i,2) .gt. 0.2) .and.
&         (deltae2 .gt. 0.)) then
            stateNew(i,18) = 1.
            stateNew(i,6) = stateOld(i,6) + strainInc(i,2)
        else
            stateNew(i,18) = 0.
        endif
C
        if ((ABS(stressNew(i,3)) .ge. stateNew(i,13)) .and.
&         (stateNew(i,3) .gt. 0.2) .and.
&         (deltae3 .gt. 0.)) then
            stateNew(i,19) = 1.
        else
            stateNew(i,19) = 0.
        endif
C
        if ((stateNew(i,17) .gt. 0.5) .or.
&         (stateNew(i,18) .gt. 0.5) .or.
&         (stateNew(i,19) .gt. 0.5)) then
            stateNew(i,5) = stateOld(i,5) + strainInc(i,1)
            stateNew(i,6) = stateOld(i,6) + strainInc(i,2)
            stateNew(i,7) = stateOld(i,7) + strainInc(i,3)
        else
            stateNew(i,5) = stateOld(i,5)
            stateNew(i,6) = stateOld(i,6)
            stateNew(i,7) = stateOld(i,7)
        endif
C
C If all failure flags become one, all stresses are reset and the
C material point is deleted. Otherwise the material point is active.
C
        if ((stateNew(i,14) .gt. 0.5) .and.
&         (stateNew(i,15) .gt. 0.5) .and.
&         (stateNew(i,16) .gt. 0.5)) then
            stressNew(i,1) = 0.
            stressNew(i,2) = 0.
            stressNew(i,3) = 0.
            stressNew(i,4) = 0.
            stateNew(i,8) = 0 ! Material point deleted.
        else
            stateNew(i,8) = 1 ! Material point active.
        endif
C
100  continue
C
        return
        end

```

```

subroutine vumat(
C Read only (unmodifiable) variables -
  1 nblock, ndir, nshr, nstatev, nfieldv, nprops, lanneal,
  2 stepTime, totalTime, dt, cmname, coordMp, charLength,
  3 props, density, strainInc, relSpinInc,
  4 tempOld, stretchOld, defgradOld, fieldOld,
  5 stressOld, stateOld, enerInternOld, enerInelasOld,
  6 tempNew, stretchNew, defgradNew, fieldNew,
C Write only (modifiable) variables -
  7 stressNew, stateNew, enerInternNew, enerInelasNew)
C
  include 'vaba_param.inc'
C
  dimension props(nprops), density(nblock), coordMp(nblock),
  1 charLength(nblock), strainInc(nblock,ndir+nshr),
  2 relSpinInc(nblock,nshr), tempOld(nblock),
  3 stretchOld(nblock,ndir+nshr), defgradOld(nblock,ndir+nshr+nshr),
  4 fieldOld(nblock,nfieldv), stressOld(nblock,ndir+nshr),
  5 stateOld(nblock,nstatev), enerInternOld(nblock),
  6 enerInelasOld(nblock), tempNew(nblock),
  7 stretchNew(nblock,ndir+nshr), defgradNew(nblock,ndir+nshr+nshr),
  8 fieldNew(nblock,nfieldv), stressNew(nblock,ndir+nshr),
  9 stateNew(nblock,nstatev), enerInternNew(nblock),
  1 enerInelasNew(nblock)
C
  character*8 cmname
C
C234567890123456789012345678901234567890123456789012345678901234567890123
C
  sFail = 3.2E7 ! True failure stress.
  ak = 80.E6 ! Stress-Strain constant.
  an = 1.4 ! Exponent.
  anu = 0.25 ! Poisson's ratio.
  Emin = 3.0E7 ! Minimum elastic stiffness.
  Emax = 1.1E8 ! Maximum elastic stiffness.
  beta_r = 1.0E-3 ! Damping factor.
C
C stateNew(i,1) = Total strain in 1-direction
C stateNew(i,2) = Total strain in 2-direction
C stateNew(i,3) = Total strain in 3-direction
C stateNew(i,4) = Total strain in 4-direction
C stateNew(i,8) = Failure indicator for material point
C
C Loop on the number of data blocks.
C
  do 100 i = 1,nblock
C
C Provided failure stress has not been reached the strain is
C updated and stored. The elastic modulus is updated as nonlinear
C with strain dependence. Stiffness proportional damping is added
C in terms of a rate dependent stiffness component.
C If the failure stress has been exceeded by any direct stress
C component all stress components are reset to zero and the material
C point is deleted from the analysis.
C
  if ((stressOld(i,1) .lt. sFail) .and.
& (stressOld(i,2) .lt. sFail) .and.
& (stressOld(i,3) .lt. sFail)) then
C
  stateNew(i,1) = stateOld(i,1) + strainInc(i,1)
  eElast1 = ABS(stateNew(i,1))
  EE1 = an*ak*eElast1**(an-1.)
  eRate1 = ABS(strainInc(i,1)/dt)
  EDamp1 = beta_r*EE1*eRate1
  E1 = EE1 + EDamp1
  if (E1 .lt. Emin) E1 = Emin
  if (E1 .gt. Emax) E1 = Emax
C

```

Appendix 5.3. Fortran90 file. Orthotropic material model with abrupt failure.

```

stateNew(i,2) = stateOld(i,2) + strainInc(i,2)
eElast2 = ABS(stateNew(i,2))
EE2 = an*ak*eElast2**(an-1.)
eRate2 = ABS(strainInc(i,2)/dt)
EDamp2 = beta_r*EE2*eRate2
E2 = EE2 + EDamp2
if (E2 .lt. Emin) E2 = Emin
if (E2 .gt. Emax) E2 = Emax
C
stateNew(i,3) = stateOld(i,3) + strainInc(i,3)
eElast3 = ABS(stateNew(i,3))
EE3 = an*ak*eElast3**(an-1.)
eRate3 = ABS(strainInc(i,3)/dt)
EDamp3 = beta_r*EE3*eRate3
E3 = EE3 + EDamp3
if (E3 .lt. Emin) E3 = Emin
if (E3 .gt. Emax) E3 = Emax
C
stateNew(i,4) = stateOld(i,4) + strainInc(i,4)
EE4 = an*ak*ABS(stateNew(i,4))**(an-1.)
eRate4 = ABS(strainInc(i,4)/dt)
EDamp4 = beta_r*EE4*eRate4
E4 = EE4 + EDamp4
if (E4 .lt. Emin) E4 = Emin
if (E4 .gt. Emax) E4 = Emax
C
C Stiffness matrix components for a 3-d orthotropic material.
C
factor = E1*(E2-E3*anu**2)-E2*anu**2*(E2+E3+2*E3*anu)
C
C11 = E1**2*(E2-E3*anu**2) / factor
C22 = E2**2*(E1-E3*anu**2) / factor
C33 = -E2*E3*(E2*anu**2-E1) / factor
C
C12 = E1*E2*anu*(E2+E3*anu) / factor
C13 = E1*E2*E3*anu*(1+anu) / factor
C23 = E2*E3*anu*(E1+E2*anu) / factor
C
C21 = C12
C31 = C13
C32 = C23
C
C44 = E4 / (1+anu)
C
stressNew(i,1)=stressOld(i,1)+C11*strainInc(i,1)
& +C12*strainInc(i,2)+C13*strainInc(i,3)
stressNew(i,2)=stressOld(i,2)+C21*strainInc(i,1)
& +C22*strainInc(i,2)+C23*strainInc(i,3)
stressNew(i,3)=stressOld(i,3)+C31*strainInc(i,1)
& +C32*strainInc(i,2)+C33*strainInc(i,3)
stressNew(i,4)=stressOld(i,4)+C44*strainInc(i,4)
C
stateNew(i,8) = 1 ! Material point active.
else
stressNew(i,1) = 0.
stressNew(i,2) = 0.
stressNew(i,3) = 0.
stressNew(i,4) = 0.
stateNew(i,8) = 0 ! Material point deleted.
endif
C
100 continue
C
return
end

```

Appendix 5.3. Fortran90 file. Orthotropic material model with abrupt failure.

```

**CONST. VELOCITY PENETRATION
**AXISYMMETRIC MODEL
**ROUNDED PUNCH R=1.6mm
**CIRCULAR PIGSKIN SPECIMEN
**0.01 FRICTION BETWEEN PENETRATOR AND SKIN
*PREPRINT, CONTACT=NO, ECHO=NO, HISTORY=NO, MODEL=NO
*RESTART, WRITE, NUMBER INTERVAL=30
*NODE
  10000, 0.000, 0.000
  12500, 0.004, 0.000
  10012, 0.000, 0.002
  12512, 0.004, 0.002
*NGEN, NSET=LEFT1
  10000, 10012, 1
*NGEN, NSET=RIGHT1
  12500, 12512, 1
*NFILL, BIAS=0.95, NSET=BLOCK1
  LEFT1, RIGHT1, 25, 100
*NSET, NSET=R11
  12000,
  12001,
  12002,
  12003,
  12004,
  12005,
  12006,
  12007,
  12008,
  12009,
  12010,
  12011,
  12012,
*NFILL, BIAS=0.95, NSET=TARG1
  LEFT1, R11, 20, 100
*NODE
  20000, 0.004, 0.000
  22000, 0.035, 0.000
  20004, 0.004, 0.002
  22004, 0.035, 0.002
*NGEN, NSET=LEFT2
  20000, 20004, 1
*NGEN, NSET=RIGHT2
  22000, 22004, 1
*NFILL, NSET=BLOCK2
  LEFT2, RIGHT2, 20, 100
*ELEMENT, TYPE=CAX4R
  10000, 10000, 10100, 10101, 10001
  20000, 20000, 20100, 20101, 20001
*ELGEN, ELSET=BLOCK1
  10000, 25,100,1, 12,1,25
*ELGEN, ELSET=BLOCK2
  20000, 20,100,1, 4,1,20
*ELSET, ELSET=SKINE
  BLOCK1, BLOCK2
*NODE
  2222, 0.000, 3.7E-3
*RIGID BODY, REF NODE=2222
*BOUNDARY
  2222, 1,1
  LEFT1, 1,1
  RIGHT2, 1,2

```

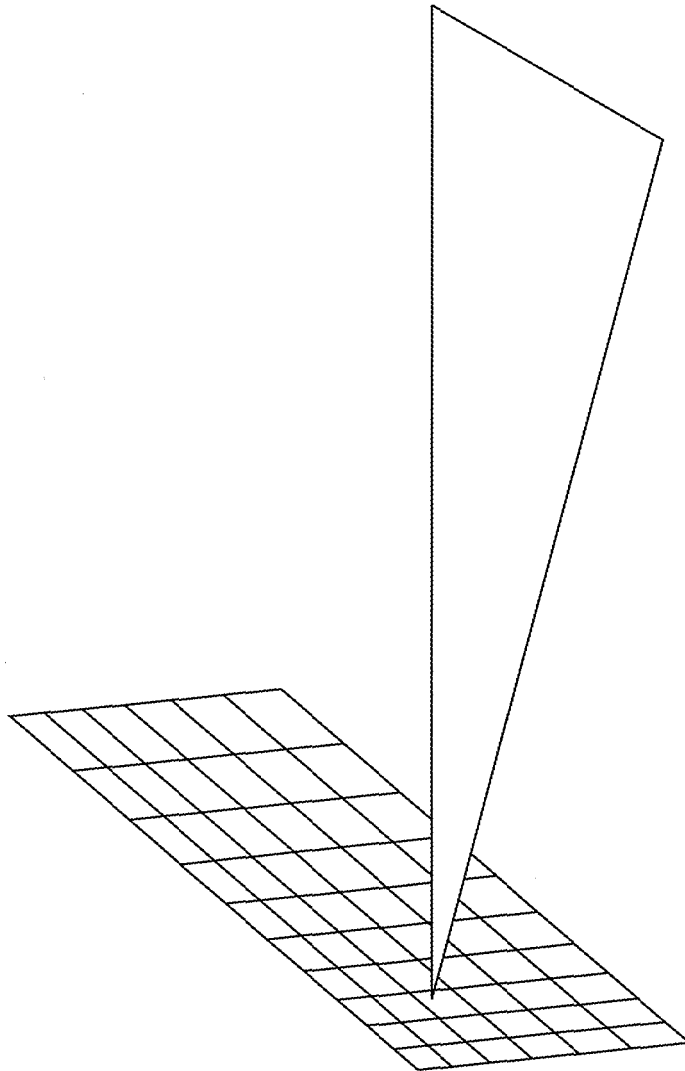
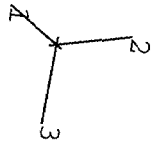
Appendix 6. Sample Abaqus input file for the revised axisymmetric stab-penetration model with penetrator A.

```

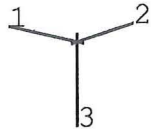
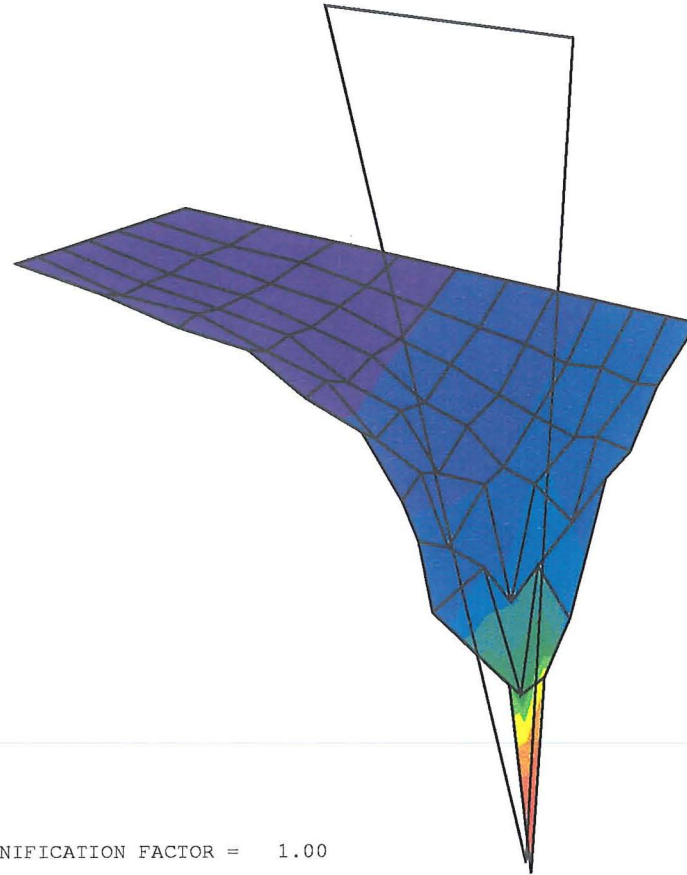
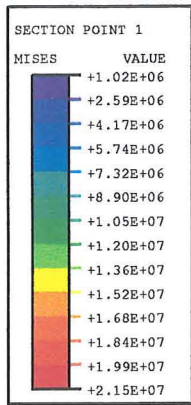
*SOLID SECTION, ELSET=SKINE, MATERIAL=PIG
*MATERIAL, NAME=PIG
*DAMPING, ALPHA=10.
*DENSITY
1000.
*USER MATERIAL, CONSTANTS=0
*DEPVAR, DELETE=8
8
*AMPLITUDE, NAME=RAMP
0.0,0.0, 0.01,1.0, 0.1,1.0
*STEP
*DYNAMIC, EXPLICIT
, 0.19
*BULK VISCOSITY
0.6, 1.8
*VARIABLE MASS SCALING, DT=4.E-7, TYPE=BELOW MIN, FREQUENCY=1000
*BOUNDARY, AMPLITUDE=RAMP, TYPE=VELOCITY
2222, 2, 2, -0.08
*****
**DEFINITION OF PUNCH A (R=1.6mm)**
*RIGID SURFACE, TYPE=SEGMENTS, NAME=KNIFs, REF NODE=2222
START, 1.6E-3, 14.5E-3
LINE, 1.6E-3, 3.7E-3
CIRCL, 0.0, 2.1E-3, 0.0, 3.7E-3
*****
*CONTACT NODE SET, NAME=CNS1
RIGHT1,
*SURFACE DEFINITION, NAME=SURF2
20000, S4
20020, S4
20040, S4
20060, S4
*CONTACT PAIR, TIED, ADJUST=1.E-6
SURF2, CNS1
*CONTACT NODE SET, NAME=SCNS
TARG1,
*SURFACE INTERACTION, NAME=PUNCH
*FRICTION
0.01
*CONTACT PAIR, INTERACTION=PUNCH
KNIFs, SCNS
*END STEP
*STEP
*DYNAMIC, EXPLICIT, DIRECT USER CONTROL
4.E-8 , 0.01
*BOUNDARY, TYPE=VELOCITY
2222, 2, 2, -0.08
*END STEP

```

Appendix 6. Sample Abaqus input file for the revised axisymmetric stab-penetration model with penetrator A.

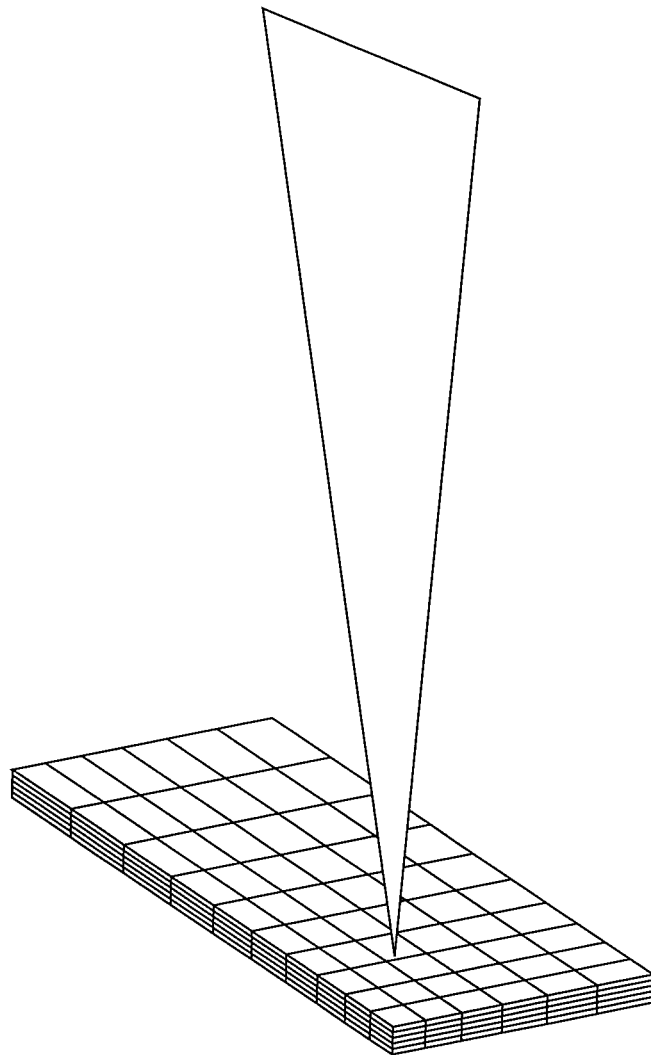
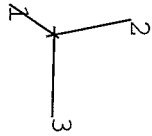


Appendix 7.1 Quarter model using 60 membrane elements and knife blade 3B (pointed tip and sharp edges). Undeformed plot with 0.90 mesh bias.

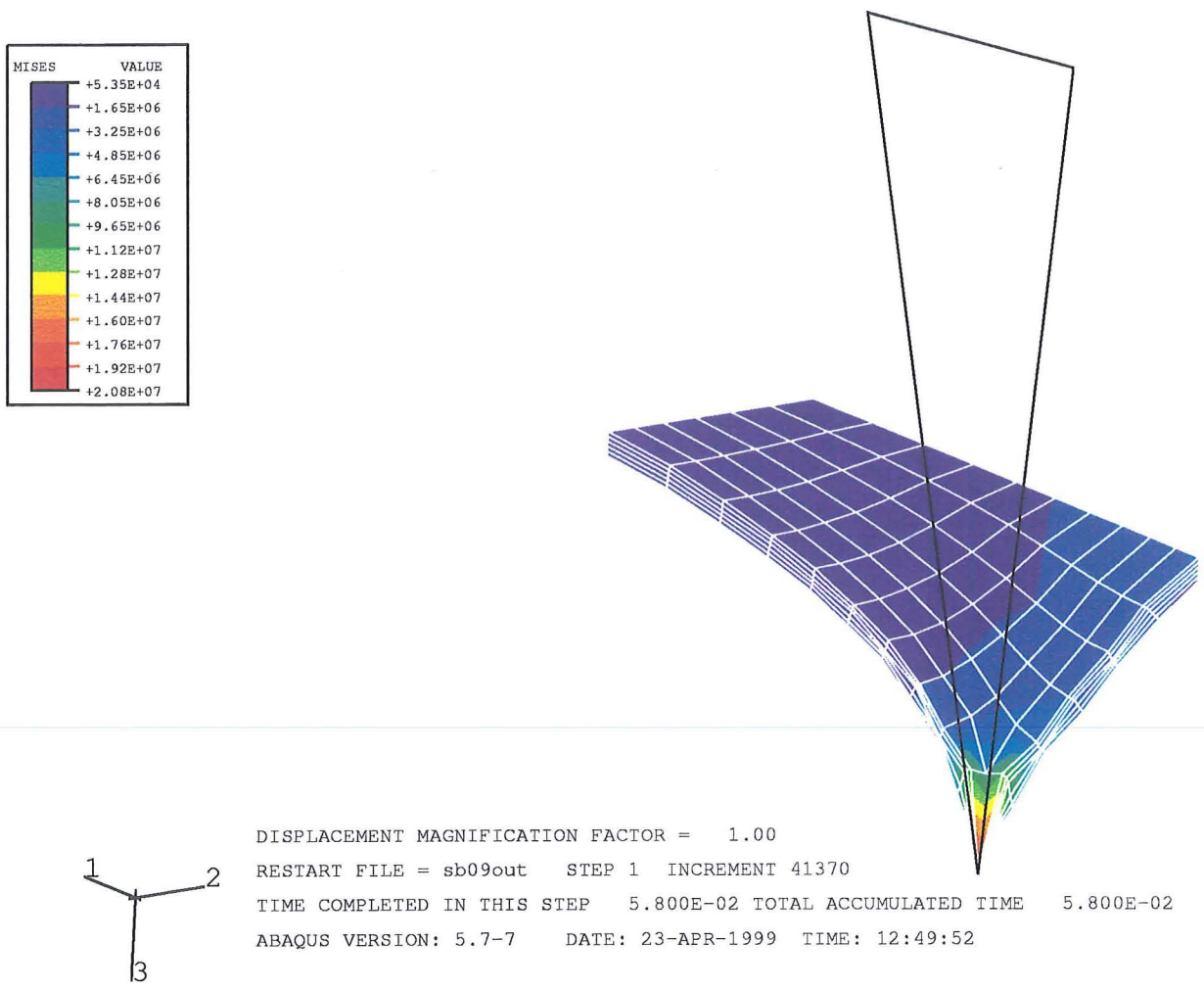


DISPLACEMENT MAGNIFICATION FACTOR = 1.00  
 RESTART FILE = b09out STEP 1 INCREMENT 13841  
 TIME COMPLETED IN THIS STEP 9.800E-02 TOTAL ACCUMULATED TIME 9.800E-02  
 ABAQUS VERSION: 5.7-7 DATE: 23-APR-1999 TIME: 12:29:47

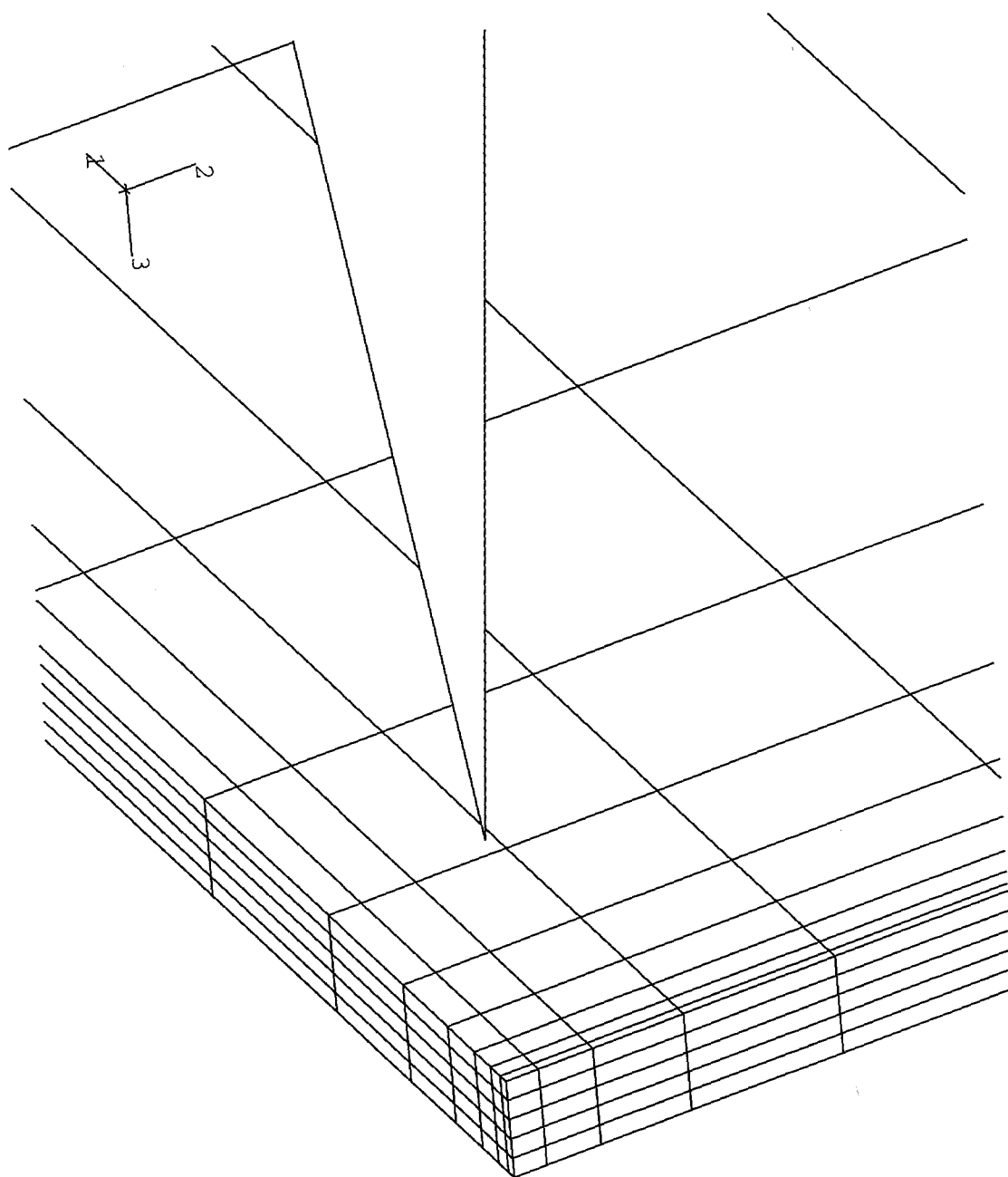
Appendix 7.2 Quarter model using 60 membrane elements and knife blade 3B (pointed tip and sharp edges). Von Mises stress contour plot in deformed state prior to failure with 0.90 mesh bias. Original in colour.



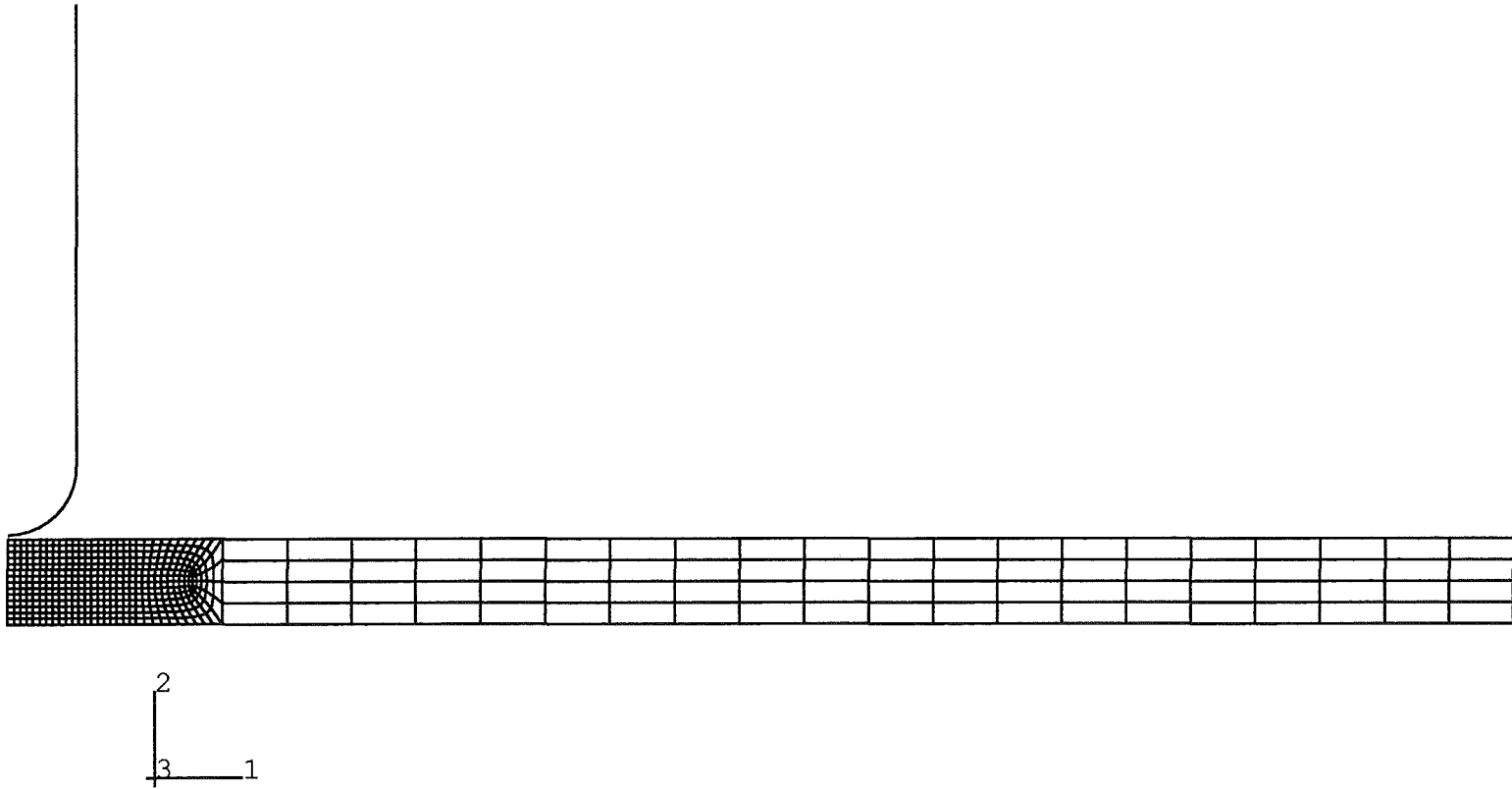
Appendix 8.1 Quarter model using 5 x 60 solid elements and knife blade 3B (pointed tip and sharp edges). Undeformed plot with 0.90 mesh bias.



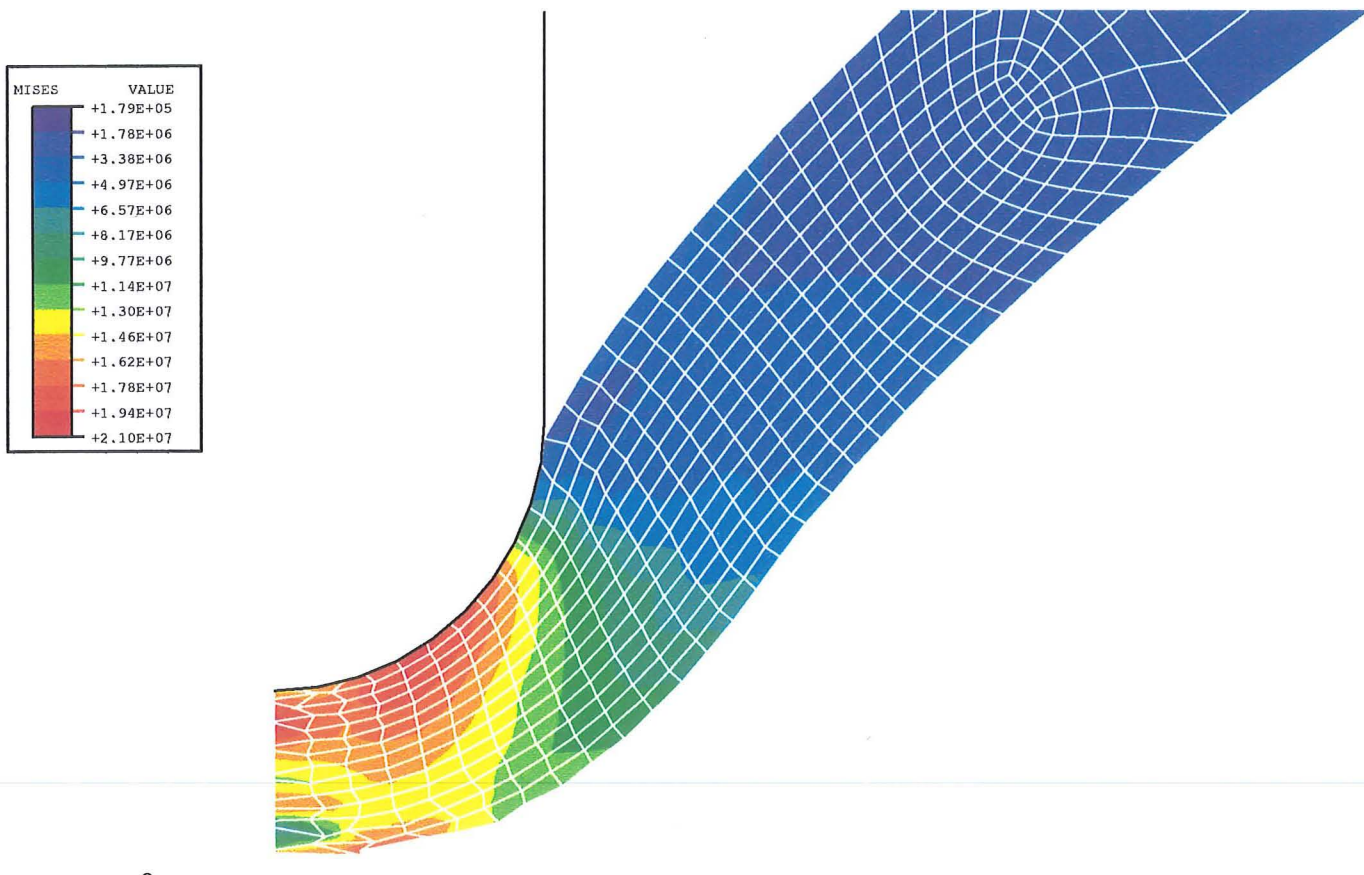
Appendix 8.2 Quarter model using 5 x 60 solid elements and knife blade 3B (pointed tip and sharp edges). Von Mises stress contour plot in deformed state prior to failure with 0.90 mesh bias. Original in colour.



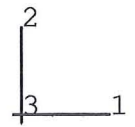
Appendix 8.3 Quarter model using 5 x 60 solid elements and knife blade 3B (pointed tip and sharp edges). Undeformed plot with 0.60 mesh bias.



Appendix 9.1 Radial section of axisymmetric model with bi-linear material model. Undeformed plot (penetrator A).

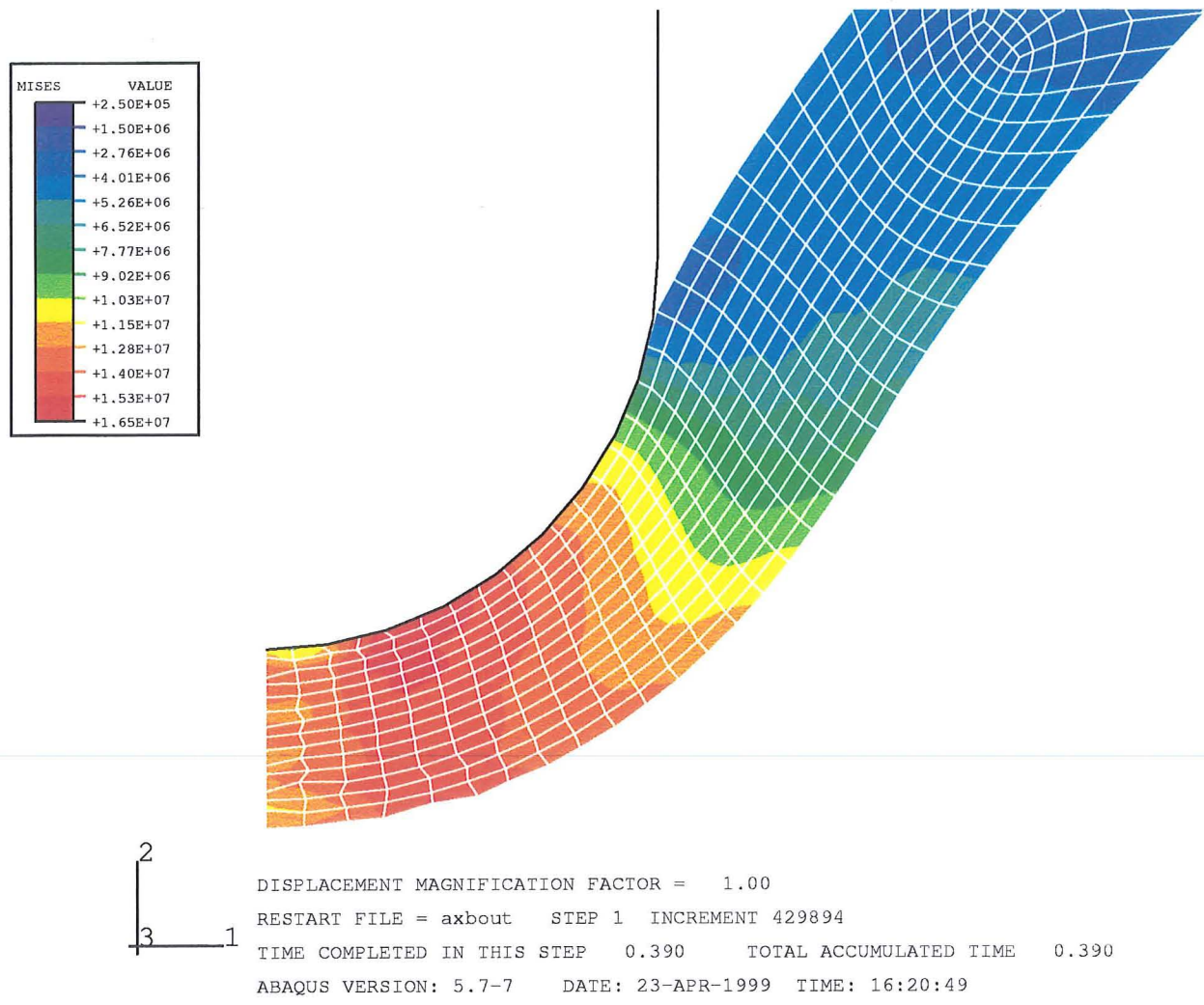


MISES	VALUE
	+1.79E+05
	+1.78E+06
	+3.38E+06
	+4.97E+06
	+6.57E+06
	+8.17E+06
	+9.77E+06
	+1.14E+07
	+1.30E+07
	+1.46E+07
	+1.62E+07
	+1.78E+07
	+1.94E+07
	+2.10E+07

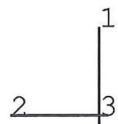
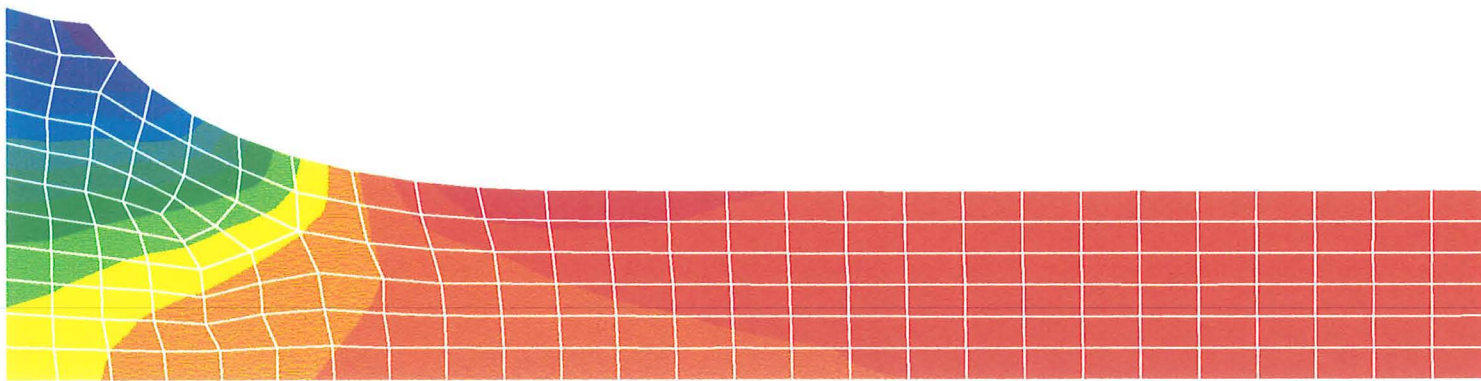
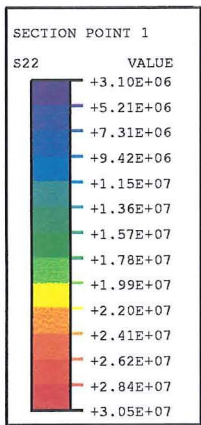


DISPLACEMENT MAGNIFICATION FACTOR = 1.00  
RESTART FILE = axaout STEP 1 INCREMENT 351439  
TIME COMPLETED IN THIS STEP 0.330 TOTAL ACCUMULATED TIME 0.330  
ABAQUS VERSION: 5.7-7 DATE: 23-APR-1999 TIME: 16:03:17

Appendix 9.2 Radial section of axisymmetric model with bi-linear material model.  
Von Mises stress contour plot in deformed state prior to failure (penetrator A). Original in colour.

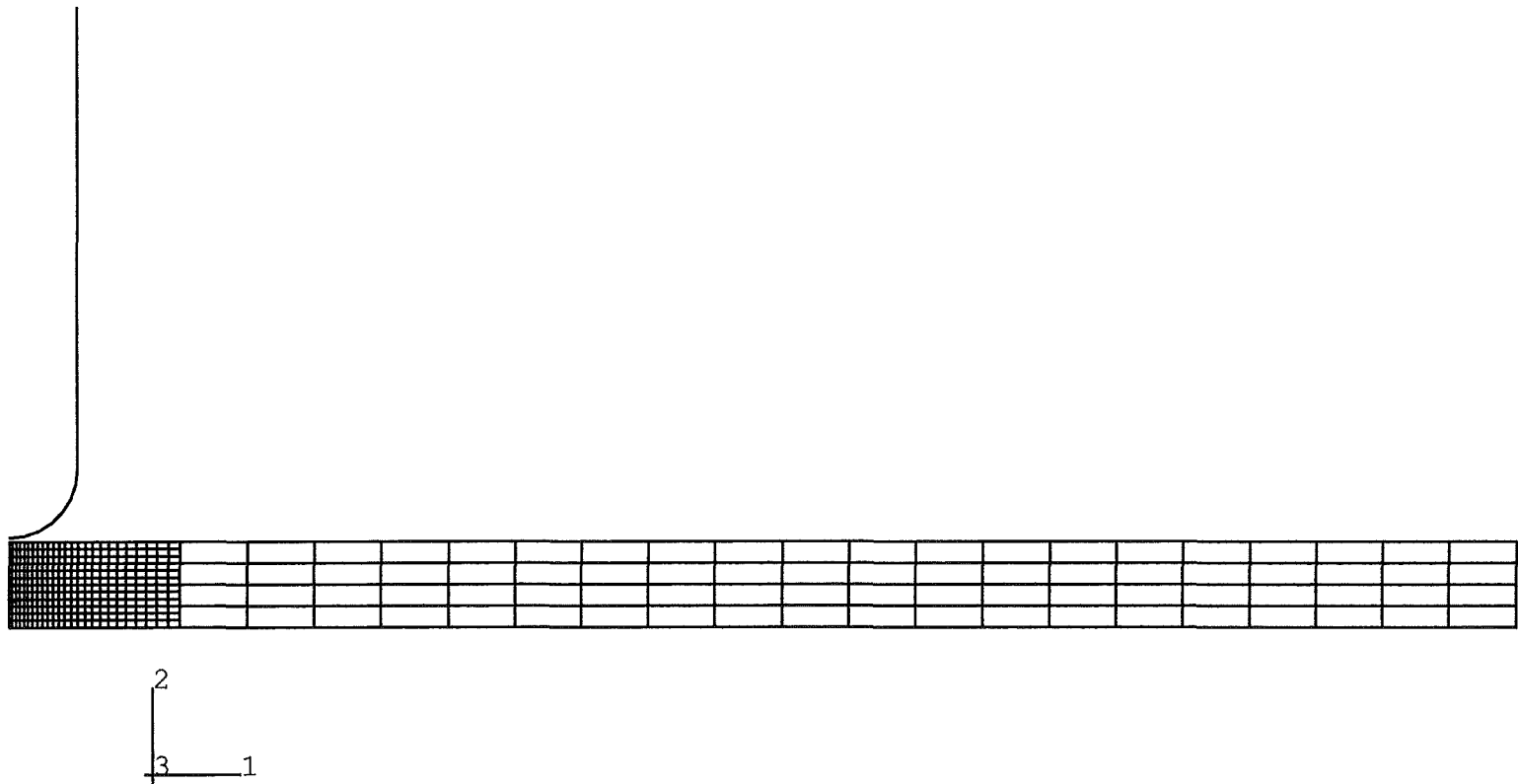


Appendix 9.3 Radial section of axisymmetric model with bi-linear material model.  
Von Mises stress contour plot in deformed state prior to failure (penetrator B). Original in colour.

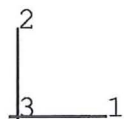
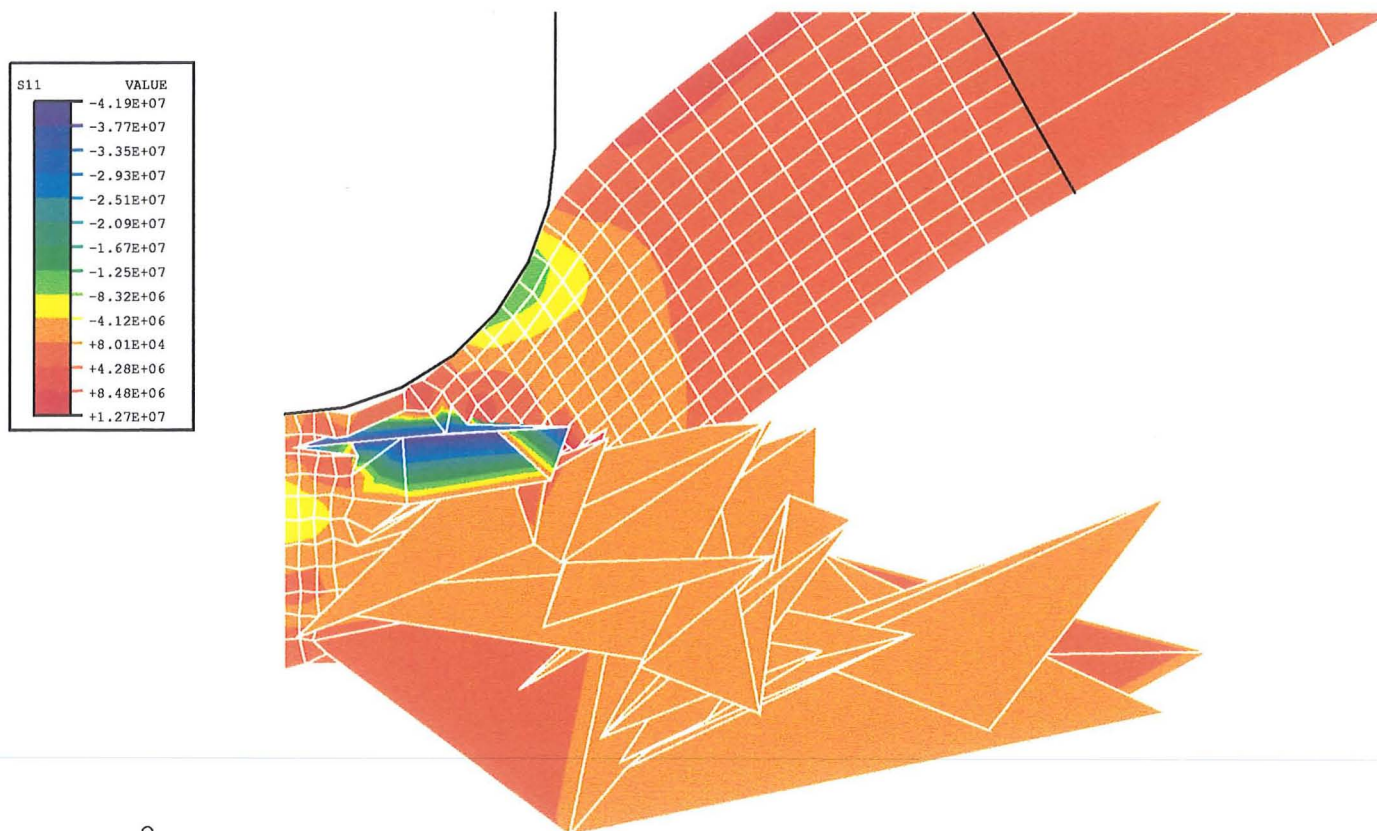


DISPLACEMENT MAGNIFICATION FACTOR = 1.00  
RESTART FILE = dbmemout STEP 1 INCREMENT 272138  
TIME COMPLETED IN THIS STEP 0.833 TOTAL ACCUMULATED TIME 0.833  
ABAQUS VERSION: 5.7-7 DATE: 23-APR-1999 TIME: 14:25:13

Appendix 10. Tensile stress contour plot of quarter model of dumbbell shaped specimen in deformed state prior to failure. Original in colour.

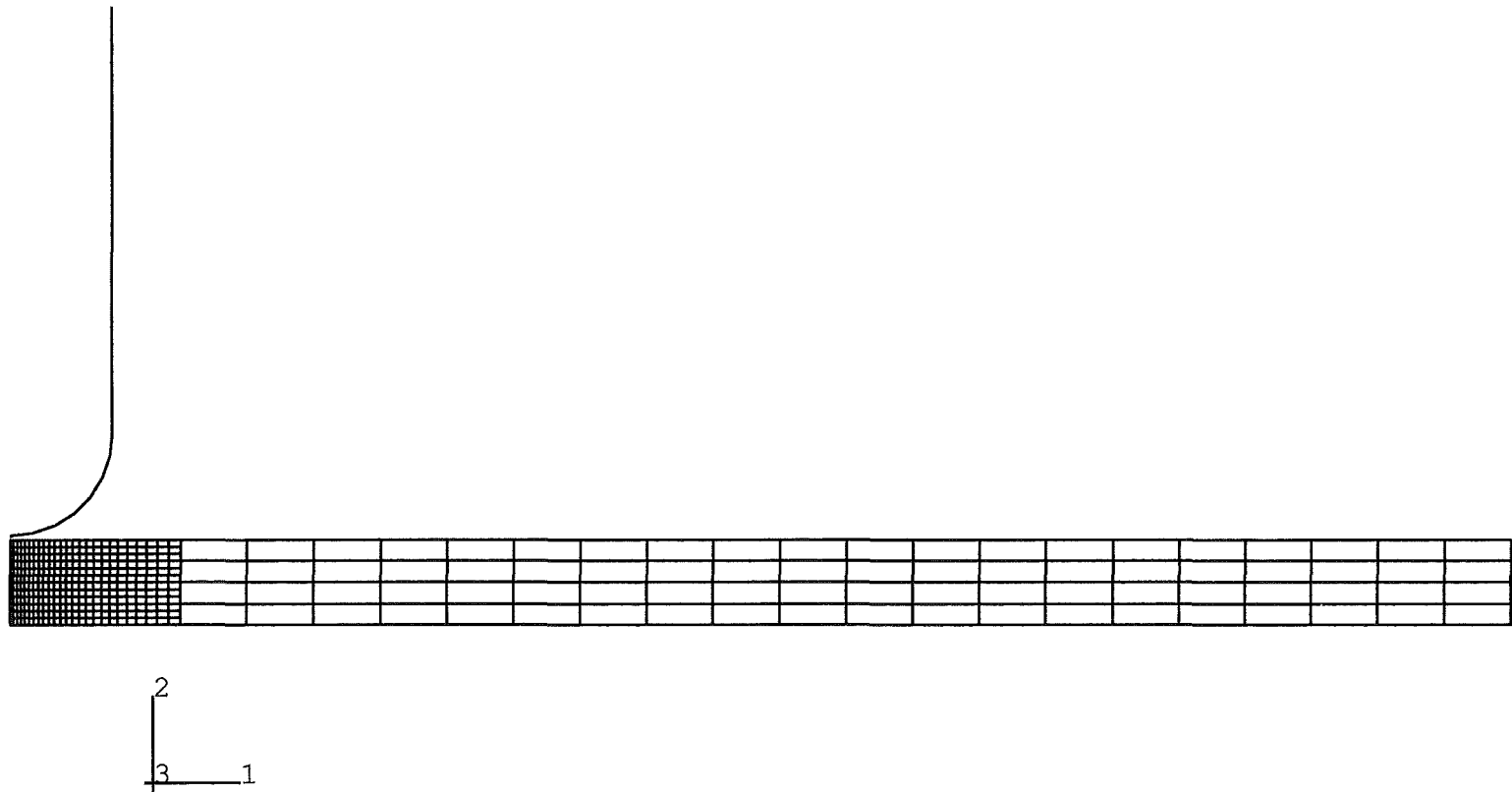


Appendix 11.1 Radial section of axisymmetric model with orthotropic material model with gradual failure. Undeformed plot (penetrator A).

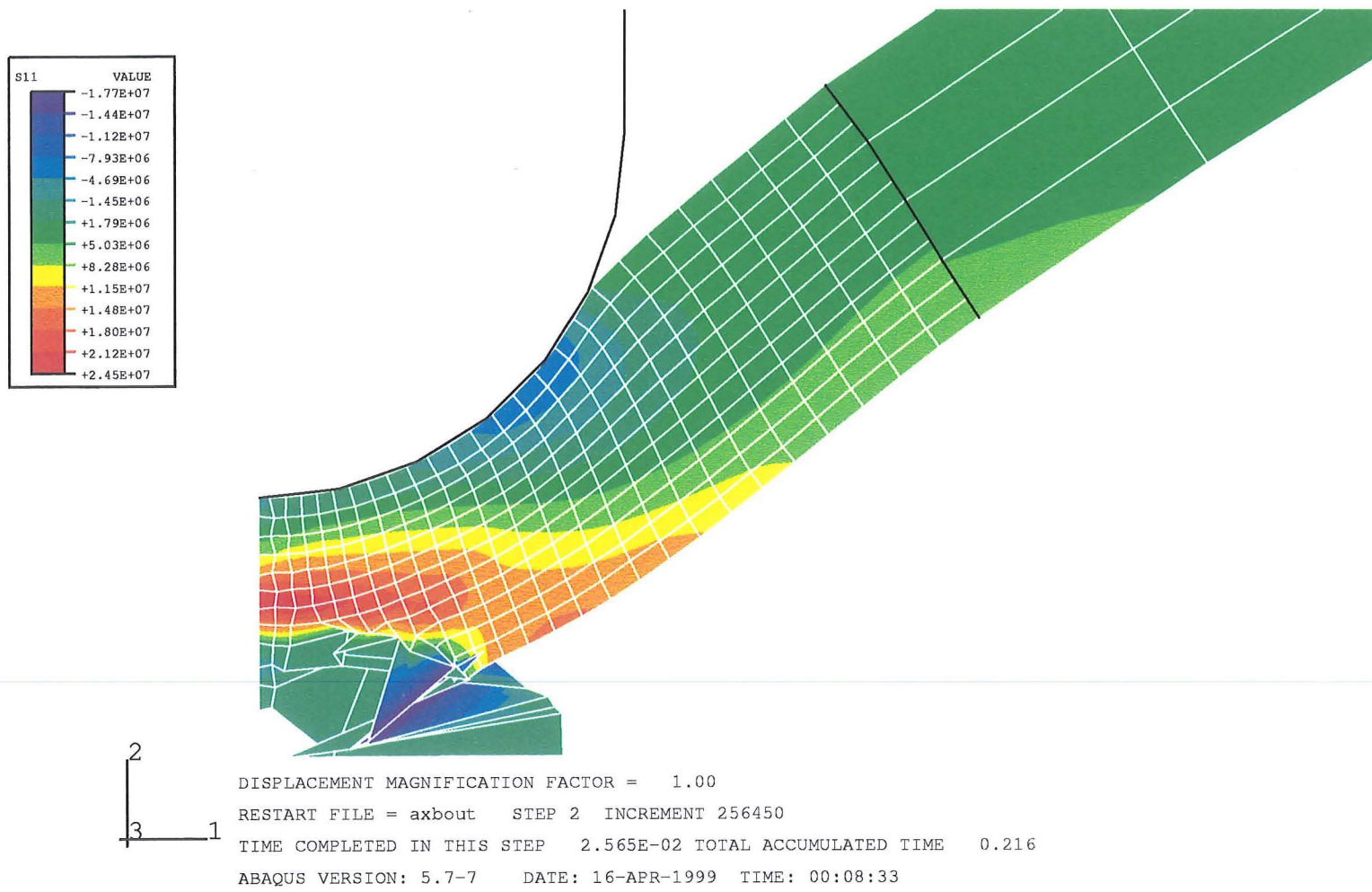


DISPLACEMENT MAGNIFICATION FACTOR = 1.00  
 RESTART FILE = axaout STEP 2 INCREMENT 94883  
 TIME COMPLETED IN THIS STEP 9.488E-03 TOTAL ACCUMULATED TIME 0.199  
 ABAQUS VERSION: 5.7-7 DATE: 15-APR-1999 TIME: 09:40:26

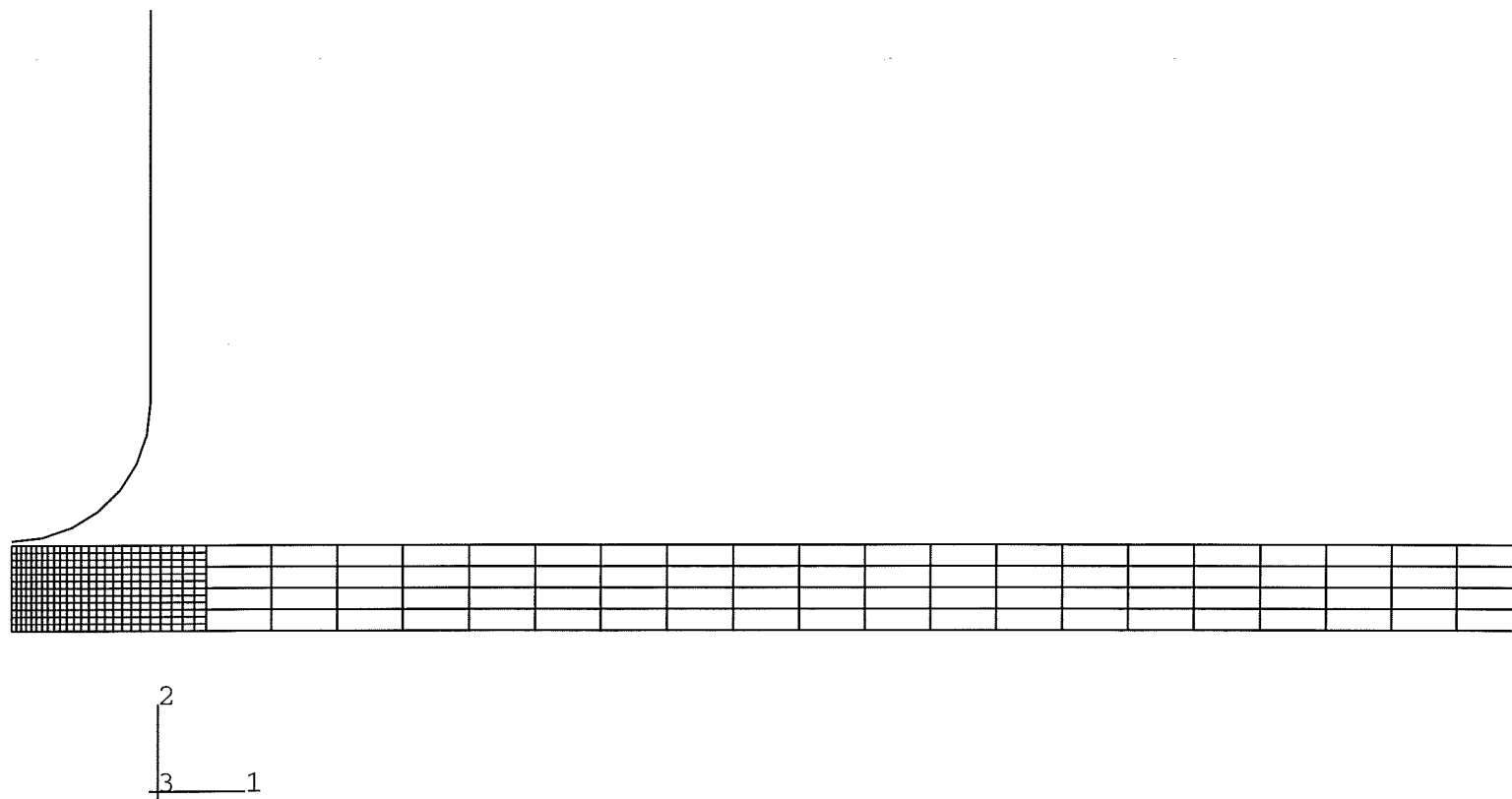
Appendix 11.2 Radial section of axisymmetric model with orthotropic material model with gradual failure. Radial stress contour plot in deformed state during failure (penetrator A). Original in colour.



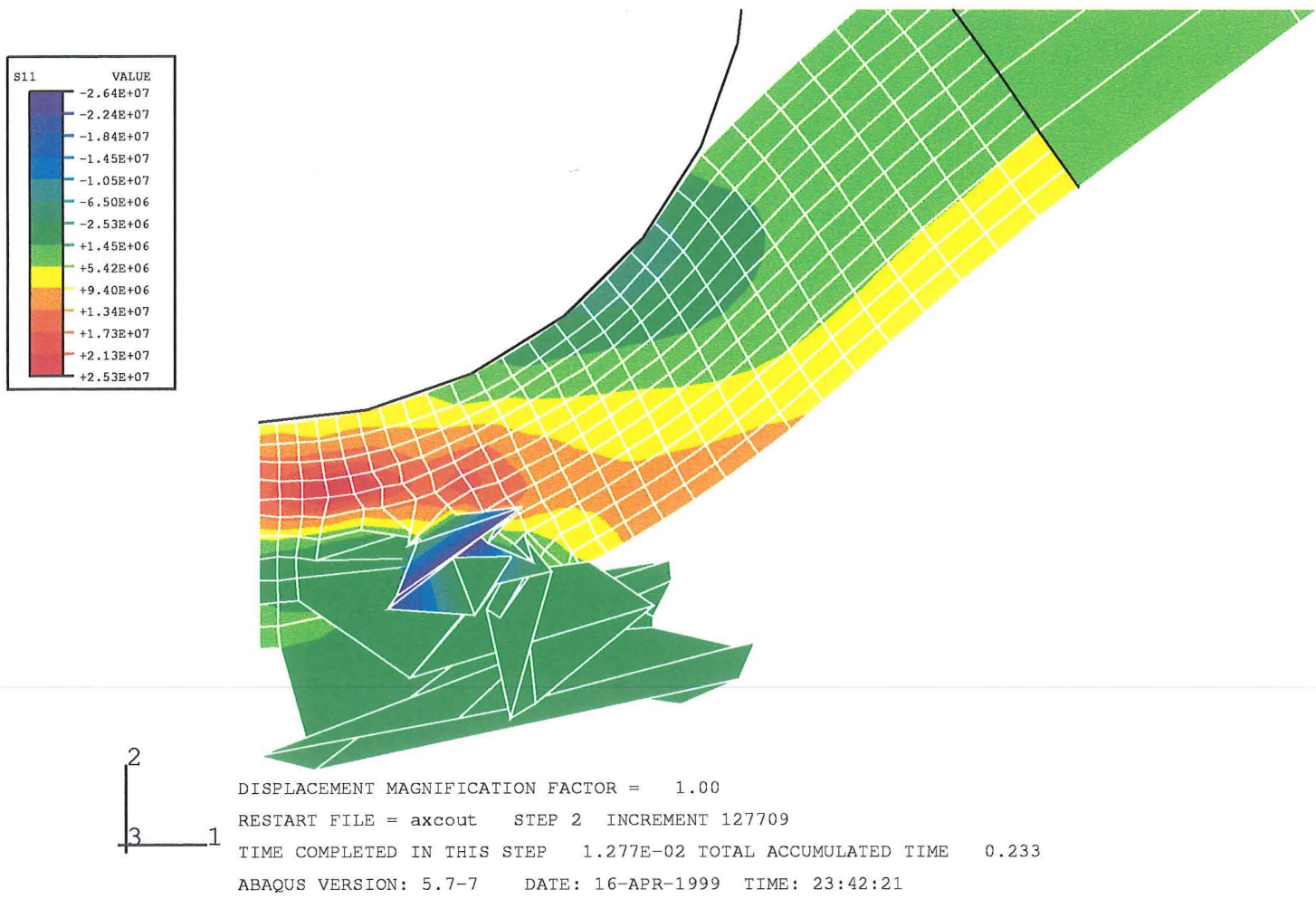
Appendix 11.3 Radial section of axisymmetric model with orthotropic material model with gradual failure. Undeformed plot (penetrator B).



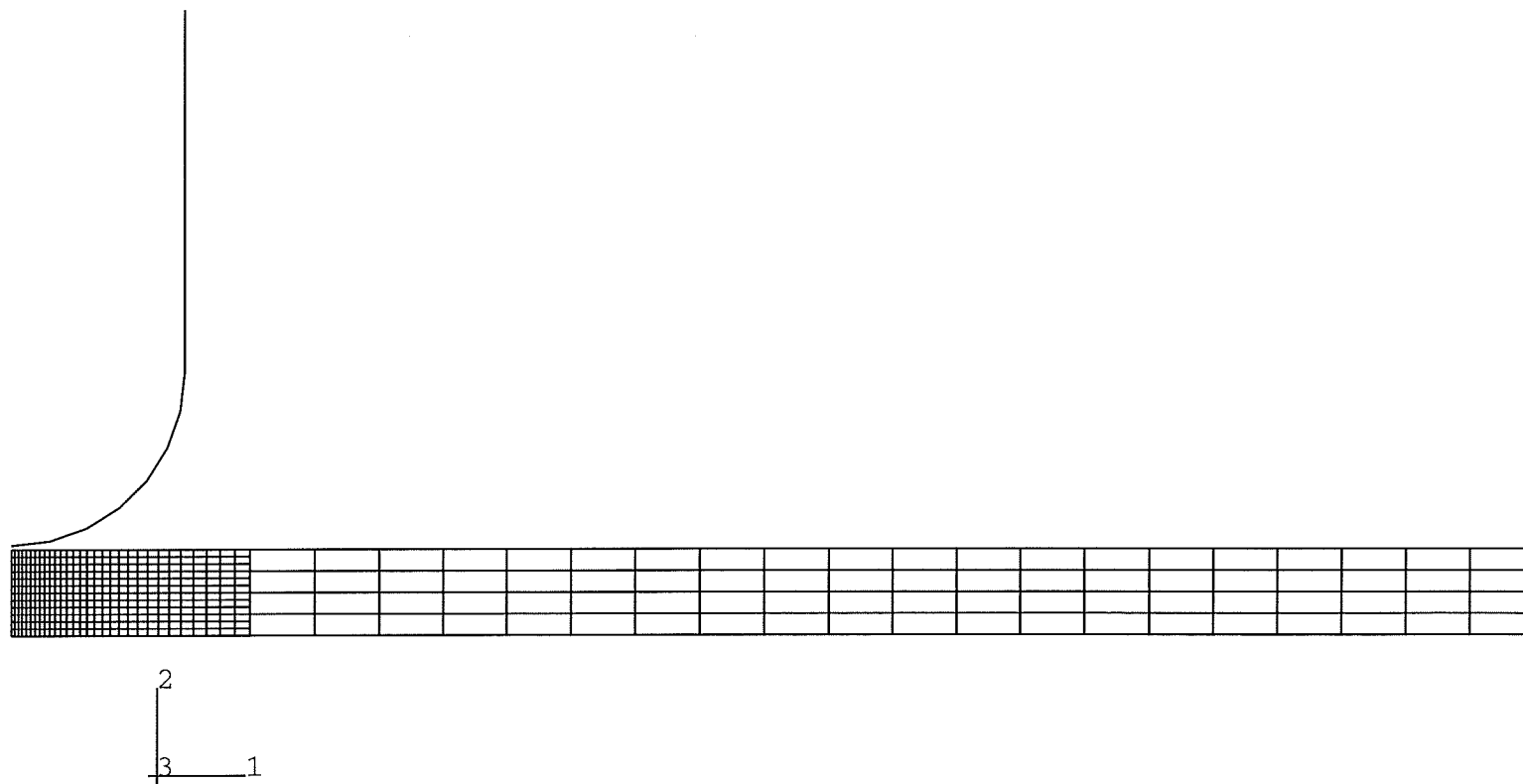
Appendix 11.4 Radial section of axisymmetric model with orthotropic material model with gradual failure. Radial stress contour plot in deformed state during failure (penetrator B). Original in colour.



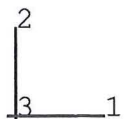
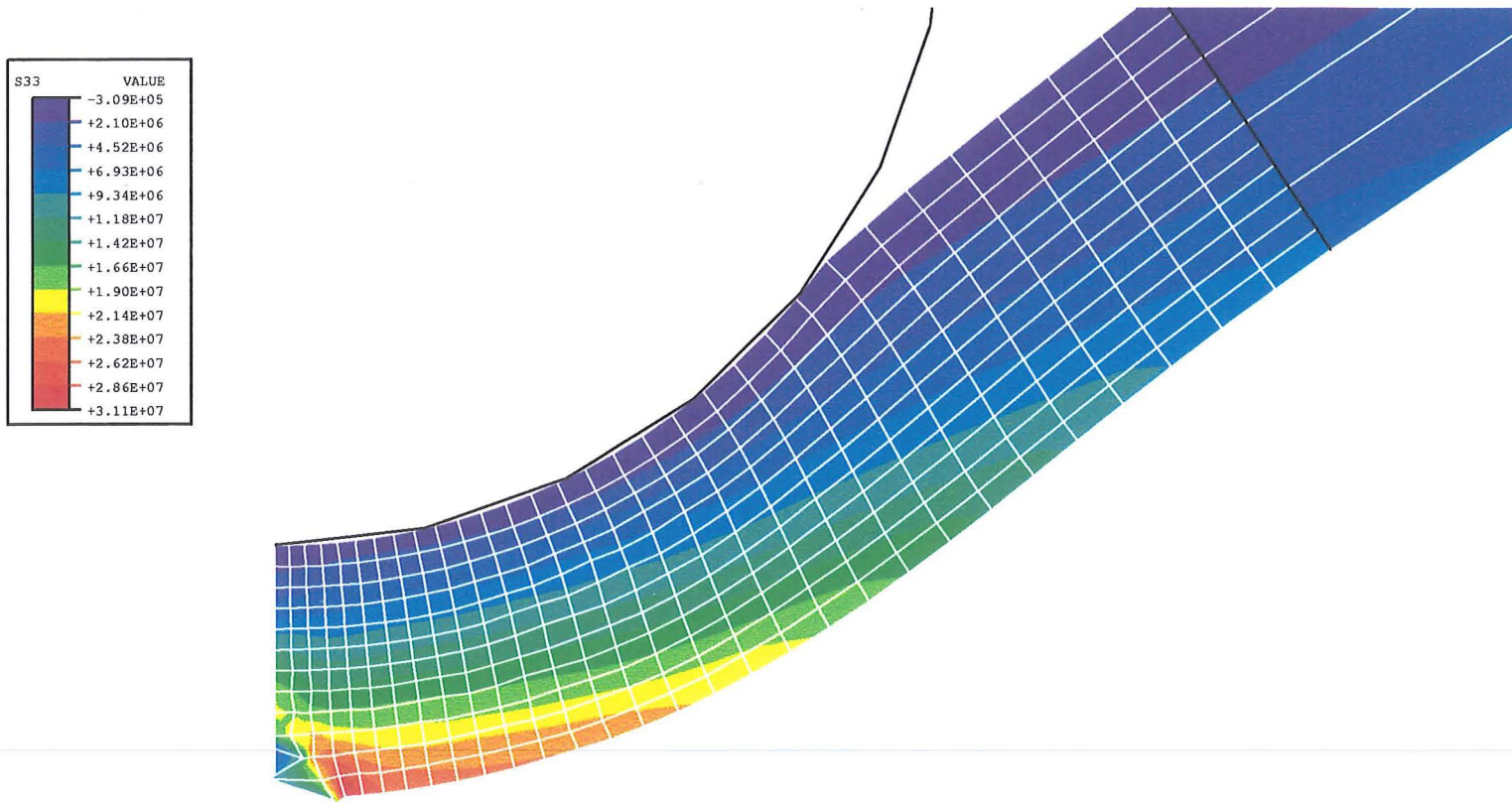
Appendix 11.5 Radial section of axisymmetric model with orthotropic material model with gradual failure. Undeformed plot (penetrator C).



Appendix 11.6 Radial section of axisymmetric model with orthotropic material model with gradual failure. Radial stress contour plot in deformed state during failure (penetrator C). Original in colour.

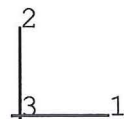
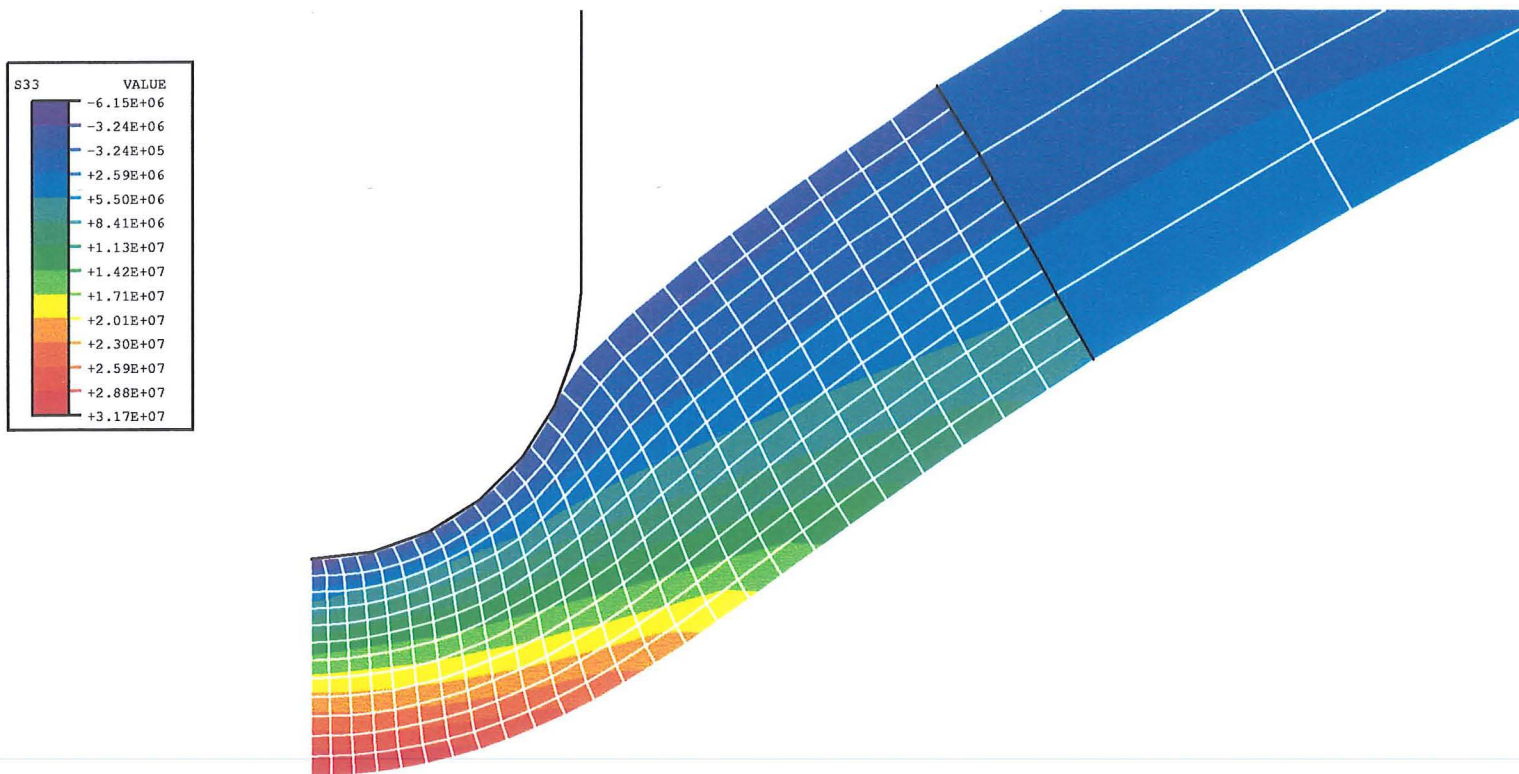


Appendix 11.7 Radial section of axisymmetric model with orthotropic material model with gradual failure. Undeformed plot (penetrator D).



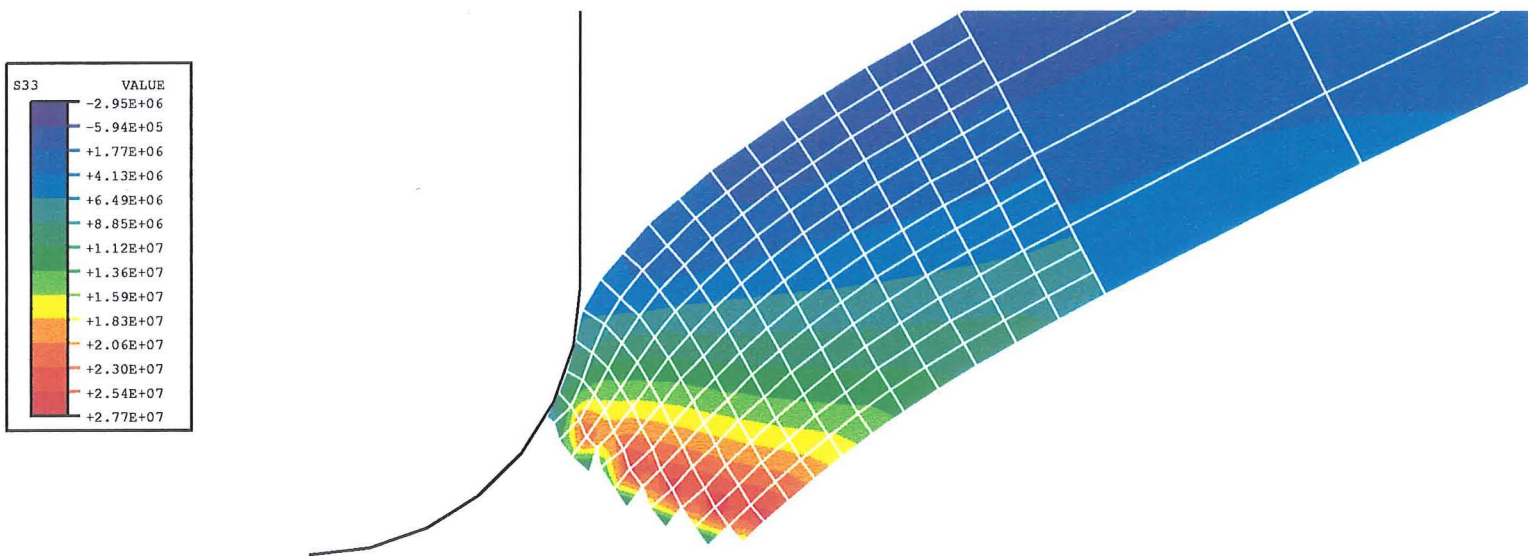
DISPLACEMENT MAGNIFICATION FACTOR = 1.00  
RESTART FILE = axdout STEP 2 INCREMENT 109130  
TIME COMPLETED IN THIS STEP 1.091E-02 TOTAL ACCUMULATED TIME 0.221  
ABAQUS VERSION: 5.7-7 DATE: 20-APR-1999 TIME: 12:30:29

Appendix 11.8 Radial section of axisymmetric model with orthotropic material model with gradual failure. Hoop stress contour plot in deformed state during failure (penetrator D). Original in colour.

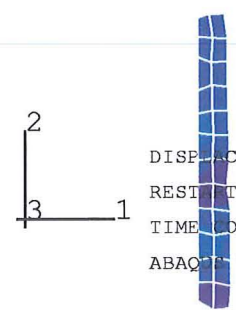


DISPLACEMENT MAGNIFICATION FACTOR = 1.00  
 RESTART FILE = axaout STEP 2 INCREMENT 183332  
 TIME COMPLETED IN THIS STEP 7.333E-03 TOTAL ACCUMULATED TIME 0.197  
 ABAQUS VERSION: 5.7-7 DATE: 07-APR-1999 TIME: 22:47:21

Appendix 12.1 Radial section of axisymmetric model with orthotropic material model with abrupt failure. Hoop stress contour plot in deformed state prior to failure (penetrator A). Original in colour.

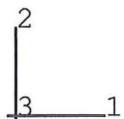
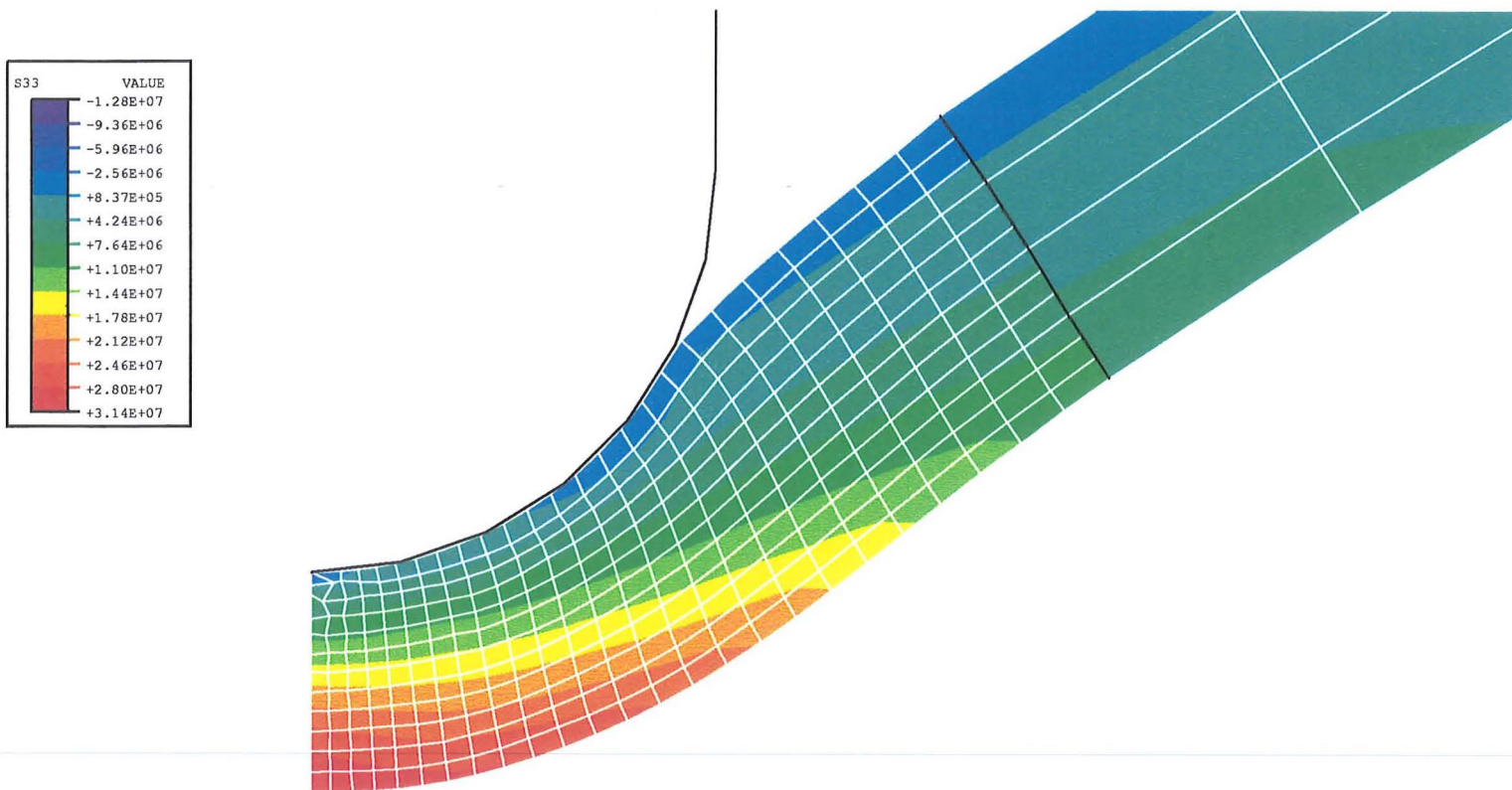


S33	VALUE
	-2.95E+06
	-5.94E+05
	+1.77E+06
	+4.13E+06
	+6.49E+06
	+8.85E+06
	+1.12E+07
	+1.36E+07
	+1.59E+07
	+1.83E+07
	+2.06E+07
	+2.30E+07
	+2.54E+07
	+2.77E+07



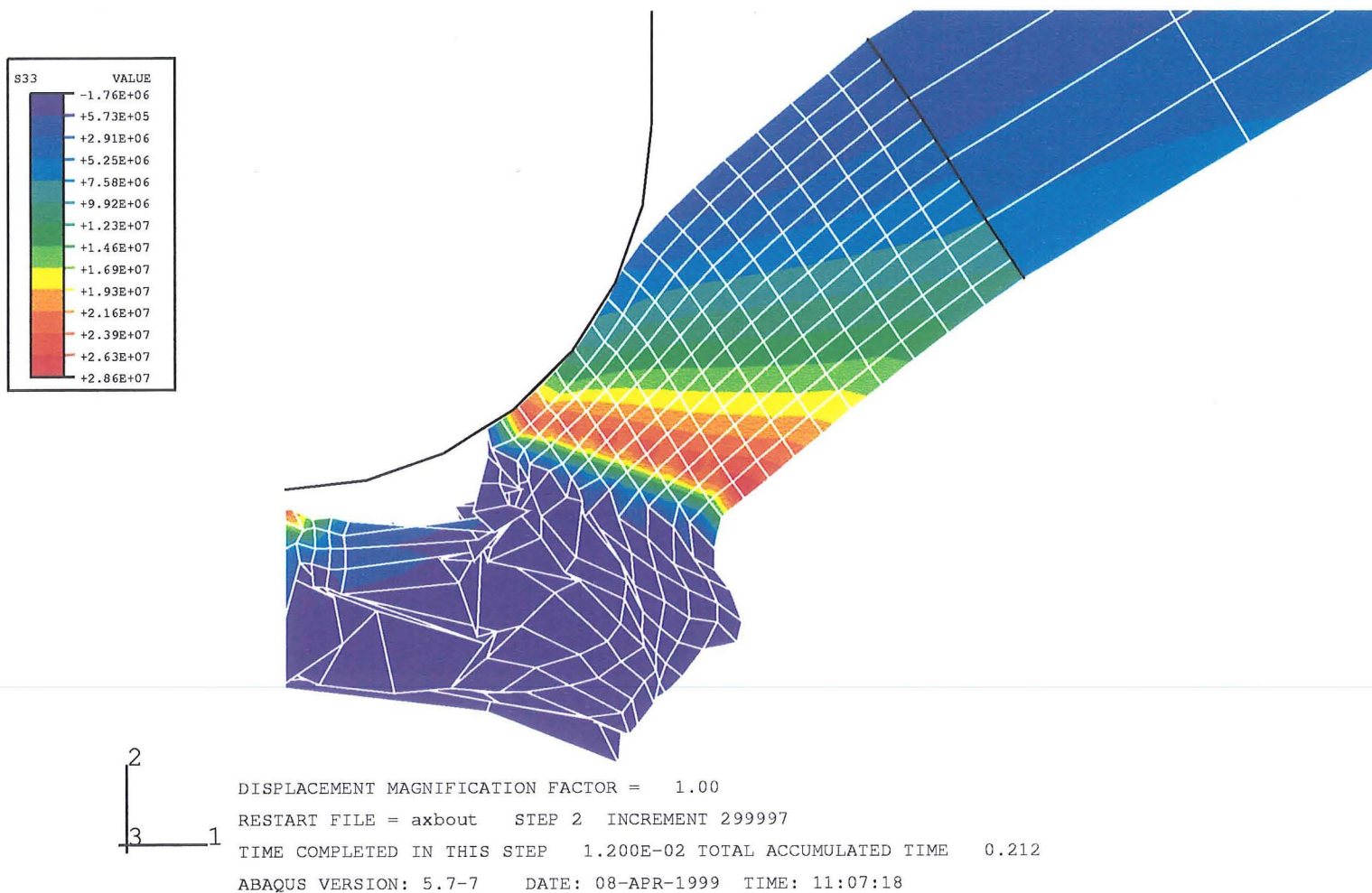
DISPLACEMENT MAGNIFICATION FACTOR = 1.00  
 RESULT FILE = axaout STEP 2 INCREMENT 191666  
 TIME COMPLETED IN THIS STEP 7.667E-03 TOTAL ACCUMULATED TIME 0.198  
 ABAQUS VERSION: 5.7-7 DATE: 07-APR-1999 TIME: 22:47:21

Appendix 12.2 Radial section of axisymmetric model with orthotropic material model with abrupt failure. Hoop stress contour plot in deformed state after failure (penetrator A). Original in colour.

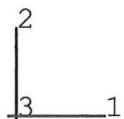
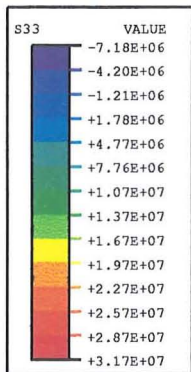
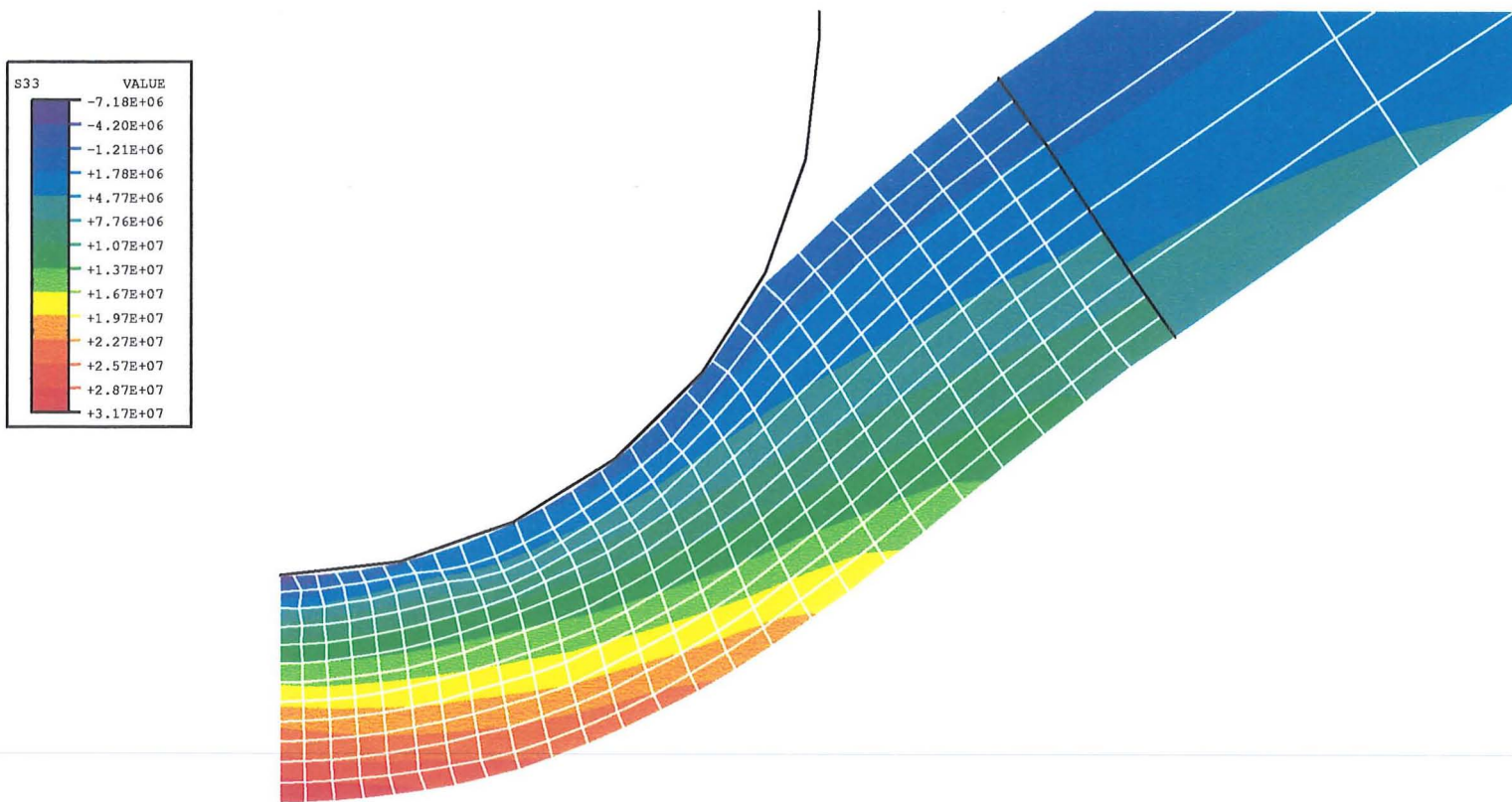


DISPLACEMENT MAGNIFICATION FACTOR = 1.00  
 RESTART FILE = axbout STEP 2 INCREMENT 283331  
 TIME COMPLETED IN THIS STEP 1.133E-02 TOTAL ACCUMULATED TIME 0.211  
 ABAQUS VERSION: 5.7-7 DATE: 08-APR-1999 TIME: 11:07:18

Appendix 12.3 Radial section of axisymmetric model with orthotropic material model with abrupt failure. Hoop stress contour plot in deformed state prior to failure (penetrator B). Original in colour.

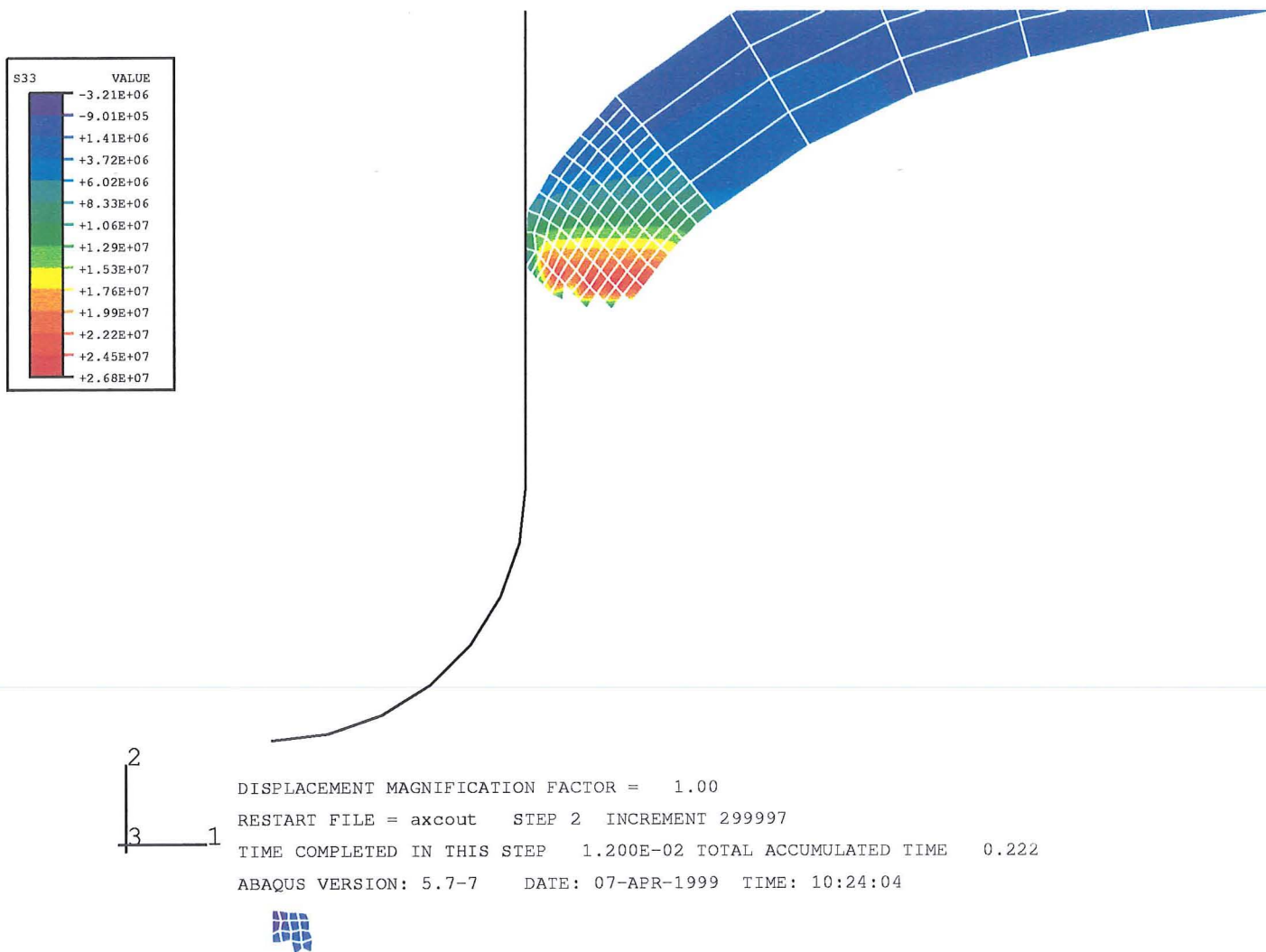


Appendix 12.4 Radial section of axisymmetric model with orthotropic material model with abrupt failure. Hoop stress contour plot in deformed state after failure (penetrator B). Original in colour.

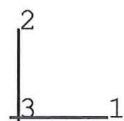
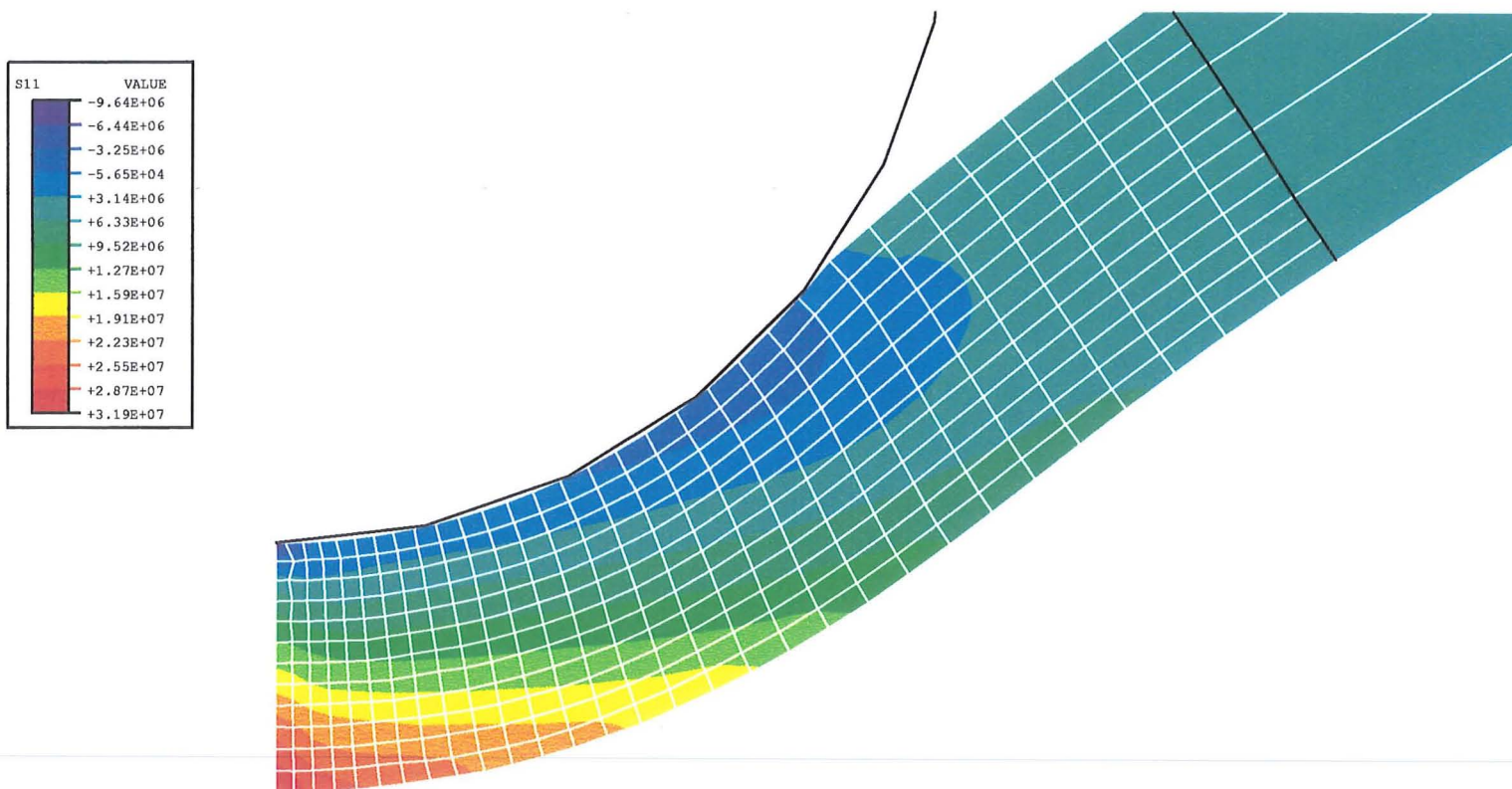


DISPLACEMENT MAGNIFICATION FACTOR = 1.00  
 RESTART FILE = axcout STEP 2 INCREMENT 283331  
 TIME COMPLETED IN THIS STEP 1.133E-02 TOTAL ACCUMULATED TIME 0.221  
 ABAQUS VERSION: 5.7-7 DATE: 07-APR-1999 TIME: 10:24:04

Appendix 12.5 Radial section of axisymmetric model with orthotropic material model with abrupt failure. Hoop stress contour plot in deformed state prior to failure (penetrator C). Original in colour.

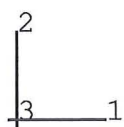
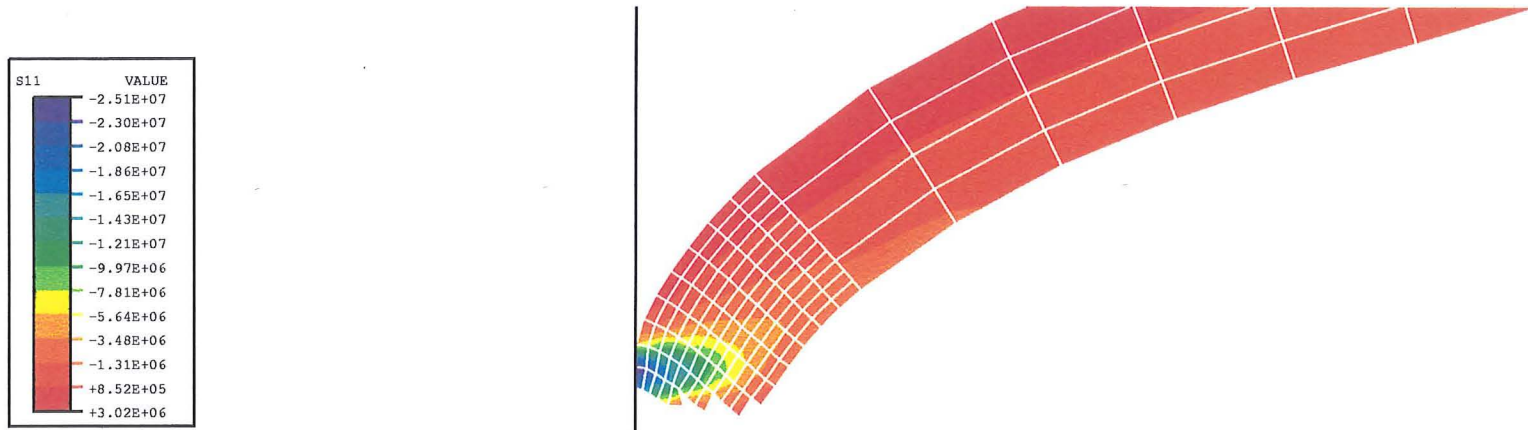


Appendix 12.6 Radial section of axisymmetric model with orthotropic material model with abrupt failure. Hoop stress contour plot in deformed state after failure (penetrator C). Original in colour.



DISPLACEMENT MAGNIFICATION FACTOR = 1.00  
 RESTART FILE = axdout STEP 2 INCREMENT 133333  
 TIME COMPLETED IN THIS STEP 5.333E-03 TOTAL ACCUMULATED TIME 0.215  
 ABAQUS VERSION: 5.7-7 DATE: 08-APR-1999 TIME: 08:41:52

Appendix 12.7 Radial section of axisymmetric model with orthotropic material model with abrupt failure. Radial stress contour plot in deformed state prior to failure (penetrator D). Original in colour.



DISPLACEMENT MAGNIFICATION FACTOR = 1.00  
RESTART FILE = axdout STEP 2 INCREMENT 149999  
TIME COMPLETED IN THIS STEP 6.000E-03 TOTAL ACCUMULATED TIME 0.216  
ABAQUS VERSION: 5.7-7 DATE: 08-APR-1999 TIME: 08:41:52

Appendix 12.8 Radial section of axisymmetric model with orthotropic material model with abrupt failure. Radial stress contour plot in deformed state after failure (penetrator D). Original in colour.